Thermal-Hydraulic Analysis of Cross-Shaped Spiral Fuel in High Power Density BWRs

by

Thomas M. Conboy
B.S., Engineering Physics
University of California, Berkeley, 2005

Submitted to the Department of Nuclear Science & Engineering
in partial fulfillment of the Requirements for the Degree of

Master of Science in Nuclear Science & Engineering

at the

MASSACHUSETTS INSTITUTE of TECHNOLOGY

May 24, 2007
[June 2007]

Author.....
Thomas M. Conboy, MIT
Department of Nuclear Science & Engineering

Certified by.....
Dr. Pavel Hejzlar, MIT
Principal Research Scientist
Thesis Co-Supervisor

Certified by.....
Dr. Mujid S. Kazimi, MIT
Professor of Nuclear Science & Engineering
Thesis Co-Supervisor

Accepted by.....
Dr. Jeffrey Coderre, MIT
Professor of Nuclear Science & Engineering
Chairman, Department Committee on Graduate Students

Thermal-Hydraulic Analysis of Cross-Shaped Spiral Fuel in High Power Density BWRs

by

Thomas M. Conboy

Submitted to the Department of Nuclear Science & Engineering in May 2007, in partial fulfillment of the Requirements for the Degree of Master of Science at the Massachusetts Institute of Technology.

Abstract

Preliminary analysis of the cross-shaped spiral (CSS) fuel assembly suggests great thermal-hydraulic upside. According to computational models, the increase in rod surface area, combined with an increase in coolant turbulence and inter-channel mixing will allow for a greater than 25% uprate in total core power, without loss of safety margin. Proper design of the rod dimensions can limit circumferential heat-flux to a peak-to-average ratio of 1.88. Non-uniformities in heat flux due to its unusual geometry seem to particularly ally CSS fuel to the BWR core, where limiting conditions are less likely to be locally influenced. Furthermore, the increase in cooling surface and reduction in central pin thickness is expected to drop fuel centerline temperature an estimated 200°C under nominal operating conditions, a reduction which rises to 300°C at 125% of nominal power conditions.

In addition to these advantages, the absence of grid spacers within the CSS fuel assembly is expected to lower pressure losses, aiding natural convection and core stability. Spacers typically account for 25-30% of the total core pressure drop. Experimental measurements of hydraulic losses for 1.5-meter-long model CSS rods in 4x4 arrays show a larger pressure drop at the same flow velocity than for bare cylindrical rods. However, this results in a CSS-bundle turbulent friction factor which is only 90% of the expected value given its hydraulic diameter. The effect of twist pitch on this pressure drop and friction factor is negligible in the range of twists examined.

Combined with the elimination of grid spacers, this results in a 40% reduction in core hydraulic loss from the reference case (neglecting entrance and exit plates). All told, the use of CSS rods should reduce total core pressure drop at nominal power by 9%, in spite of a reduction in core flow area. At 125% of nominal power, this becomes a 16% increase in pressure drop in comparison to the reference core at nominal power.

Thesis Supervisors: Dr. Pavel Hejzlar, Prof. Mujid Kazimi

Acknowledgments

This research could not have been completed without the technical and financial assistance of my supervisors Dr. Pavel Hejzlar and Prof. Mujid Kazimi, the tireless support of Dr. Thomas McKrell, and the experienced hand of Yakov Ostrovsky.

Table of Contents

List of Figures

List of Tables

1. Introduction

1.1 Background

One of the primary driving factors in economics and safety of BWR design is thermal-hydraulic performance of the fuel. Because of this, much research over the past few decades has been directed towards the achievement of optimal BWR fuel design and configuration. During this period, appreciable gains in power-density as well as safety margin have been realized through a gradual shift to smaller cylindrical fuel rod diameters and expansion of array size.

Due to the costs of new plant construction, power uprating of existing nuclear reactors looks to be an area of extensive research for years to come. Similarly, the increased focus on economics and safety in design of future reactors puts a larger focus on alternatives that might provide more dramatic increases in margin, in addition to higher power output. To this end, advanced fuel design is a more active area of research today.

Several new fuel types and assembly geometries, offering creative alternatives to the traditional BWR assembly geometry, have recently been proposed [1]. Among these is the cross-shaped spiral (CSS) rod fuelled assembly. Though used in Russian submarine power cores in the 3-petal variety, they have only recently been tested for VVER application [2]. Similar 4-petal rods have been investigated for use in PWRs [3]. Cross-shaped spiral fuel rods have never been used commercially in either the VVER or PWR, nor investigated under BWR conditions.

1.2 Objective

The goal of this research is to design a cross-shaped spiral (CSS) fuel rod assembly optimized for the BWR core, and to complete a preliminary steady-state analysis of the unique thermal-hydraulic phenomena associated with this fuel type. This should result in

a well-informed evaluation of the potential of CSS fuel for application to high-power-density BWRs.

1.3 Motivation

The Cross-Shaped Spiral fuel rod cross-section is illustrated in Figure 1, and is seen to resemble a cross (or a 4-petaled flower). In a fuel assembly, CSS rods would slide into an assembly in a tight bundle such that the petals of neighboring pins contact each other at their outer-most extent in a self-supporting lattice, without the presence of grid spacers. However, to allow for cross-flow, each rod is axially twisted. Thus the contact with neighboring rods occurs at only several locations along the height of the fuel (Figure 1.1).

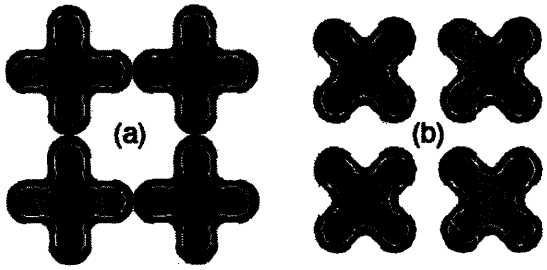

Figure 1.1: (a) and (b) show CSS rod gap variation axially.

Potential advantages of this design raise much optimism from a thermal-hydraulic perspective. These cross-shaped rods possess a larger surface area, resulting in increased cooling and a reduced average surface heat flux. In addition, the thin petal-like extensions reduce the thermal resistance between the hot central region of the fuel pellet and bulk coolant flow, decreasing the maximum fuel temperature in comparison to a cylindrical fuel rod under the same operating conditions.

It is further recognized that a rod's spiral twist will impart upon the flowing coolant an additional radial velocity component, increasing turbulence and mixing within an assembly, and increasing the rate of droplet deposition, possibly extending the presence of annular flow. In this regard, the CSS fuel concept has a potential advantage over other approaches in raising power density in BWR cores, which are ulimately limited by the

proportional increase in mass flux required and the resulting detriment to CPR [4]. These factors would seem to combine to raise the assembly Minimum Critical Power Ratio (MCPR) in comparison to the reference assembly MCPR, providing a margin for increased power density.

In addition to these thermal advantages, the absence of grid spacers within the CSS fuel assembly is expected to lower core pressure losses, aiding natural convection and core stability and lowering pumping power. Spacers typically account for at least 25-30% of the total core pressure drop; the rest is comprised of losses at the inlet an outlet plates, frictional loss along the rod bundle, and the unavoidable gravity/acceleration loss terms.

There are potential drawbacks, however. This radial flow could do more harm than good if the resultant secondary flow served to lower the breakthrough velocity to turbulent wave undercut, increasing the rate of entrainment from the annular film on the rods. This would impede the smooth circumferential flow that is characteristic of high quality rod-bundle flow, and would lead to premature dryout.

It is also inevitable that the pin's surface heat flux, while lower on average, will be larger at the "elbow" of two adjoining petals than elsewhere. Radial heterogeneity in the fuel cross-sectional shape may also lead to heat flux abnormalities due to slow-neutron shielding, and should be separately investigated. The full extent of these effects must be evaluated.

Other concerns about this design, which have to do with fuel performance at higher power, cladding integrity at corners, or difficulty in manufacturing, will not be fully addressed in this study as it is focused only on thermal-hydraulic aspects of performance.

1.4 Scope

The scope of this work is to provide a first-order estimate of the aforementioned benefits and drawbacks of the CSS fuel. The fuel is kept near BWR-typical design parameters in

terms of pin and array size, fuel and moderator volume, while maintaining a worthwhile increase in surface area and a twisted shape.

To quantify power uprate potential, it is necessary to compare safety margins between the CSS design and a reference "standard" BWR assembly model. For this, typical design parameters and operating conditions are chosen, with details provided in Chapter 2. The Critical Power Ratio (CPR) is used to quantify the safety margin during steady-state operation, as is common practice for cylindrical rod-fuelled BWRs.

This analysis will also, in a detailed manner, investigate several unique features including "elbow" region heat-flux peaking, and temperature variations as well as neutronic consequences of the distinctively-shaped cross-section.

Computational analysis of these various thermal properties will be supplemented by experimental measurements of the frictional pressure drop due to 4x4 bundles of prototype CSS fuel rods of varying twist pitch; this is described in Chapters 5 and beyond.

2. Fuel and Assembly Design

2.1 The Reference Assembly

The CSS (Cross-Shaped Spiral) fuel assembly is based on a modification of the BWR "reference" assembly (Figure 2.1). This reference assembly adopts its dimensions from the General Electric BWR6 assembly design [1], featuring a 9x9 array of cylindrical fuel rods. The rods themselves consist of oxide pellets housed in Zircalloy cladding, allowing for a modest Helium gas gap. Central to the assembly are two large water rods that provide much of the in-assembly moderation; their presence displaces 7 fuel rods from the array, leaving a total of 74.

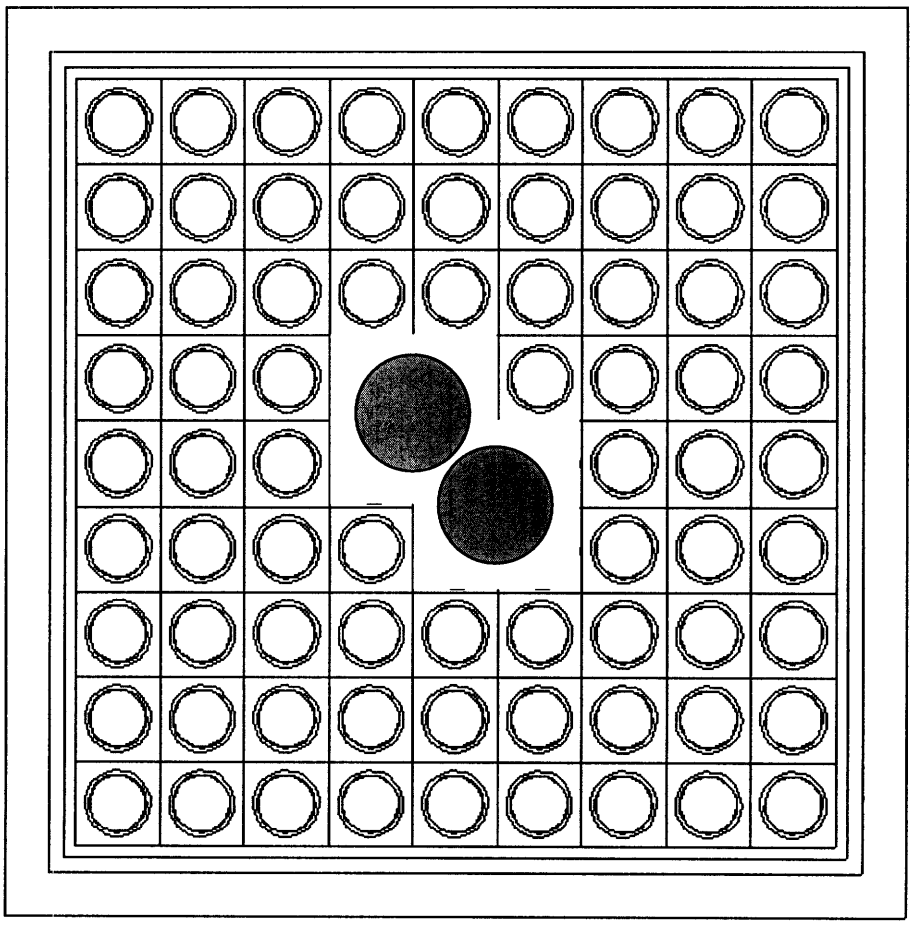

Figure 2.1: Reference BWR Fuel Assembly (to-scale)

Consistent with BWR design, the assembly is closed within a rigid duct, which allows for no exchange with neighboring assemblies. Within these walls, the rods are provided with stability against vibrations by an axial series of 7, equally spaced gridspacers, equipped with mixing veins for critical quality enhancement.

Though precise dimensions of the GE/6 fuel rod cannot be provided due to proprietary concerns, a cross-sectional cut of the assembly (as in Figure 1) reveals a coolant flow area between rods of 93.8 cm^2, a moderator area of 51.7 cm^2, and a fuel area of 53.0 cm^2. Knowing the areas of these regions, along with assumptions regarding coolant, moderator and fuel densities, allows one to find the assembly Hydrogen-to-Heavy Metal Atomic Ratio (H/HM).

The H/HM ratio in a reactor core is generally seen a good description of the neutron spectrum within an average assembly, and is therefore taken in this study as one of several key design constraints. It is found by comparing the number of atoms of Hydrogen in the coolant and moderator to the number of Uranium atoms in the fuel for a given assembly:

$$\frac{H}{HM} = \frac{\frac{2\rho_m N_A V_m}{M_{H_2O}} + \frac{2\rho_c N_A V_c}{M_{H_2O}}}{f_U \frac{\rho_{UO_2} N_A V_{UO_2}}{M_U}} \qquad \text{(Eqn. 2.1)}$$

For which the following variables are defined:

ρ_m, ρ_c, ρ_{UO2} = respective average densities of moderator, coolant and uranium dioxide.

V_m, V_c, V_{UO2} = respective volumes of moderator, coolant, and fuel. (Here, a cross-sectional area is taken, acknowledging the constant axial dimensions).

M_{H20}, M_U = molecular weight of water and uranium

f = the mass fraction of Uranium in UO_2, taken as 0.8815

N_A = Avagadro's number, 6.022 x 10^{23}

This distinguishes between two different sources of hydrogen in the following way: moderator – defined as water from within the water rods and inter-assembly bypass region, and coolant – lower density water from within the flow area. Assuming an axially-averaged coolant density of 0.435 g/cc, an average moderator density of 0.735 g/cc, and a UO_2 density of 10.42 g/cc, the reference core has an H/HM value of 4.3.

2.2 CSS Fuel Design

2.2.1 Design Criteria

In order to minimize the effort required for optimization of the CSS fuel type, several characteristics were adopted directly from the reference; this includes the fuel volume, rod cladding and gas gap thicknesses, the assembly box dimensions, and the approximate assembly H/HM ratio.

As a rule, changes in the flow area were permitted but kept limited as not to increase coolant mass-flux. Slight losses in moderative power due to diminished flow area were compensated for with equivalent increases in water rod volume. However, such changes to the bypass flow in water rods were also minimized to prevent void reactivity and stability issues.

Matching array size, fuel volume, and approximate H/HM ratio between the reference case and the CSS assembly ensures similar neutronic behavior in terms of optimal poison and enrichment pin-loading schemes to limit local peaking. Likewise, maintaining clad and gas gap thickness values from the reference case diminishes concerns regarding pin integrity in terms of internal or external pressure-related stresses on the CSS rods.

As previously described, the CSS rods fill an assembly in a tight bundle such that the petals of neighboring pins contact each other at their outer-most extent in a self-supporting lattice, without the presence of grid spacers. The fuel petals come into contact

with one-another once for every 90° axial-twist, and remain out of contact until the next 90° twist has been completed further along the length of the pin.

In order to match the number of support planes in existing BWRs, the CSS rod would need to complete a minimum of two full turns along the height of the core, resulting in a total of 8 contact points. This is a marked reduction in twist-pitch from previous studies [2], but is necessary to ensure the practicability of loading oxide pellets into traditional Zircalloy cladding tubes. Cross-shaped fuel pellets would be difficult to thread into very sharply-twisted cladding. Manufacturing of CSS-type fuel has been topically addressed for PWR fuel [3], and should be at least as feasible in the production of BWR rods which are typically larger in diameter. The issue of mechanical support and vibration is also briefly investigated in [3], which makes the assumption that pacers and CSS fuel-petal contact is equivalent from a support standpoint.

These material and geometry design choices therefore help to place the focus of this study on a side-by-side thermal-hydraulic comparison of the CSS fuel-type and a standard reference design, rather than any other factors.

2.2.2 Spiral Pin 1

With fixed values for the array dimensions and assembly box size, as well as fuel volume and other given dimensions, the only degrees of freedom for the CSS cross-sectional shape are the fuel petal-thickness, and the radius of curvature at the joint of any two fuel-petals – the "elbow". A larger elbow radius requires a broader central region, and a reduction in petal thickness for a given fuel volume. Sensing that elbow radius could prove to be a sensitive parameter, this was chosen as the value to be specified *a priori*.

As a first design, the fuel pellet was modeled such that the elbow region radius of curvature would match the curvature at the outer lobe of a petal, as per previous work on PWR CSS fuel [3].

Geometric relations (Table 2.1) were developed for this CSS fuel shape, dubbed Spiral Pin 1 (SP1) to allow one to analytically determine the surface area, fuel volume, and local coolant flow area. Characteristic values of the pitch (P), petal length (D), petal-lobe radius of curvature (r), cladding plus gap thickness (δ) are illustrated in Figure 2.2.

Pin pitch in this design, and any other proposed CSS assembly, is increased slightly from the reference case. This is because typical BWR fuel assemblies have a larger gap between the outermost pins and the assembly duct than the space between any two pins. The CSS assembly, which must span the entire assembly space from duct-to-duct with fuel rods to ensure self-support, must therefore carry a larger pitch.

Table 2.1: Geometric Relations for CSS Assembly SP1 Calculations

(a)	Outer clad perimeter (clad surface area / rod height)	$8D + 2\pi\delta - (24 - 6\pi)r$
(b)	Fuel surface area (fuel volume / rod height)	$8Dr - (8 - \pi)\, r^2$
(c)	Total CSS rod surface area (rod volume / rod height)	$[(\pi - 8)\, r^2 + (6\pi\delta - 24\delta + 8D)r + (\pi\delta^2 + 8D\delta)]$
(d)	Coolant Flow Area (unit cell water volume / height)	$P^2 - [(\pi - 8)\, r^2 + (6\pi\delta - 24\delta + 8D)r + (\pi\delta^2 + 8D\delta)]$

These equations differ slightly from the equations introduced in [3] for an identical fuel rod shape (proportionally) because these include a correction; the previous formulae assumed 90-degree angles at the fuel elbow rather than a curved slope. Surface and volume are marginally impacted.

P and δ, which represent pin pitch and the combined gap thickness respectively, are fixed constraints as mentioned for all rod designs. Therefore, the fuel petal length D is also known, since the following relation holds:

$$P = 2(D + \delta) \qquad \text{(Eqn. 2.2)}$$

Fixing the fuel volume per unit length to equal the reference case allows the final unknown, r, to be found using the equation from Table 2.1-b. With all variables known, it becomes trivial to solve for CSS perimeter, rod cross-sectional surface area, and local subchannel flow area, filling out the rest of Table 2.1. For a single CSS rod, the value of wetted perimeter becomes 4.9 cm, an increase of 40% over the cooling surface of the reference rods. The total pin cross-sectional area rises 11.6% to 1.1 cm^2, while the local subchannel flow area also increases by 1%. Local subchannel flow area is slightly increased even as total flow area drops and total pin cross-section increases, since CSS-model subchannels make use of the entire assembly, whereas the reference assemblies leave a wider gap between the assembly and the duct wall. This result and others are summarized in Table 2.3, at the end of this section.

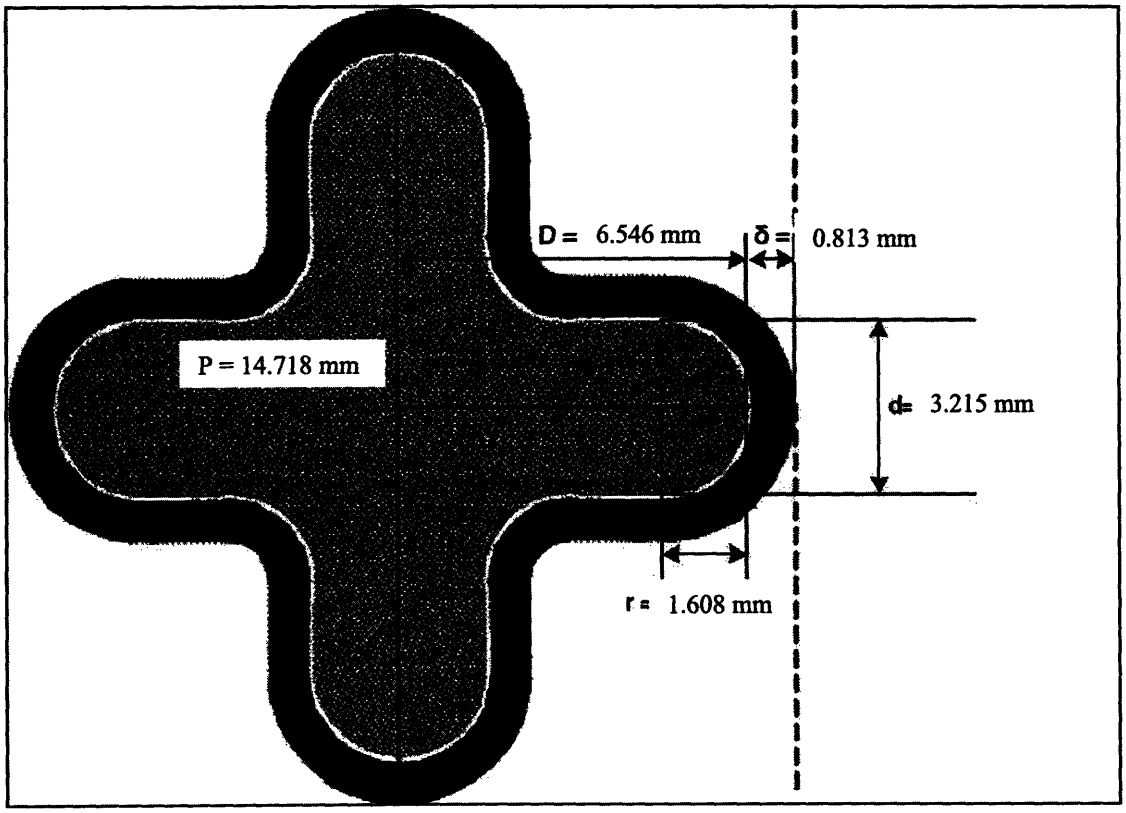

Figure 2.2: Scale depiction of the SP1 design, with characteristic lengths defined.

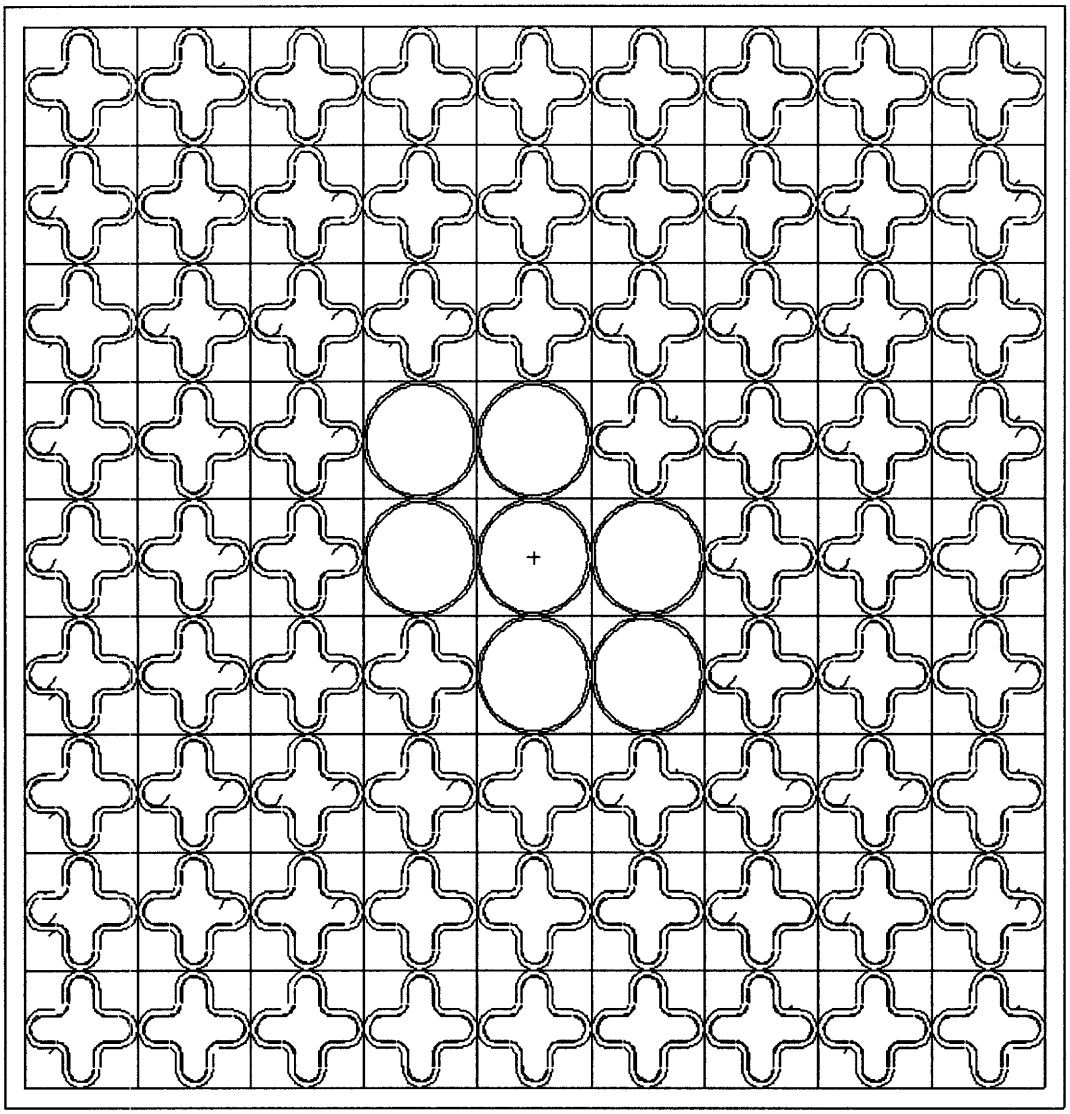

Figure 2.3: The full 9x9 assembly, spanned by CSS SP1 fuel rods

On the whole, the CSS-SP1 fuel rods have the effect of reducing the coolant flow area for the entire assembly by 12%, due to the 40% increase in cladding and gas gap volume that accompanies the rise in surface area. As a result, coolant mass flux will be proportionally greater than that within the reference assembly at the same core power and mass flow.

This is an early indication of the looming struggle to balance the effects of increasing surface area (and therefore cladding volume) to take advantage of a larger cooling surface, but in the process, diminishing flow area – which causes a rise in coolant

velocity and therefore negatively impacting pressure drop and the two-phase critical quality to the limit of critical power.

The flow area, moderator area, and fuel area for this assembly (Figure 2.3) taken on the values 82.1 cm^2, 54.7 cm^2, and 53.0 cm^2 respectively (Table 2.3), resulting in an H/HM ratio for this assembly of 4.2. This is a little low, but not far off the reference value of 4.3. It is likely that the use of a different formation of water rods, such one or two large, central rectangular blocks, could be used to increase the H/HM ratio with little impact on other thermal-hydraulic characteristics. This is done in some modern BWR assemblies, including in designs by AREVA. However this scheme was not modeled in this case, in the interest of simplicity.

With all measurements defined, determining the assembly hydraulic diameter also becomes trivial. Using the definition of hydraulic diameter for non-tubular channels:

$$D_e = \frac{4A_f}{P_w} \qquad \text{(Eqn. 2.3)}$$

One finds the CSS SP1 Assembly to have a hydraulic diameter of 0.66 cm, much smaller than the reference value of 1.13 cm. This is an indication that frictional pressure drop for this assembly could be quite large, even without grid spacers.

2.2.3 Spiral Pin 2

A second CSS design was modeled, with a larger radius of curvature at the elbow region. While dropping the overall surface area in comparison to SP1, the increase in cooling surface at the elbow itself was expected to help alleviate heat flux peaking concerns of the CSS fuel design concept. This effect is discussed fully in Section 3.2.

For this design, the pellet was modeled such that the elbow region radius of curvature would double the curvature at the outer lobe of a petal. To be clear, the curvature

mentioned here is at the elbow of the fuel-pellet itself, not the outer curvature of the rod at the cladding surface. This is almost the largest possible curve that can be accommodated without fundamentally changing the cross-sectional shape.

As was accomplished for SP1, an effort was made to obtain a set of relationships between the lengths P, D, r, and delta defined in Figure 2.2, and the outer clad perimeter, fuel surface volume/unit length, rod surface volume/unit length, and local channel flow area, summarized in Table 2.2.

Table 2.2: Geometric Relations for CSS SP2 Assembly Calculations

(a)	Outer clad perimeter (clad surface area / rod height)	$4\pi(r + \delta) + 2\pi(2r - \delta) + 8(D - 4r)$
(b)	Fuel surface area (fuel volume / rod height)	$2\pi r^2 + 5(2r)^2 + 8r(D - 4r)$
(c)	Total CSS rod surface area (rod volume / rod height)	$[(4 + 2\pi)(r + \delta)^2 + (4 - \pi)(2r - \delta)^2 + 8(r + \delta)(D - 2r - \delta)]$
(d)	Coolant Flow Area (unit cell water volume / height)	$P^2 - [(4 + 2\pi)(r + \delta)^2 + (4 - \pi)(2r - \delta)^2 + 8(r + \delta)(D - 2r - \delta)]$

The radius of curvature at the elbow of the pellet is 2r, therefore the radius of curvature at the cladding surface elbow is 2r-δ. This dimension ends up being 2.109 mm, as compared to the 0.81 mm for SP1. Solving for the rest of the parameters (by fixing the fuel volume at the reference value) gives SP2 dimensions that are very comparable to that for SP1.

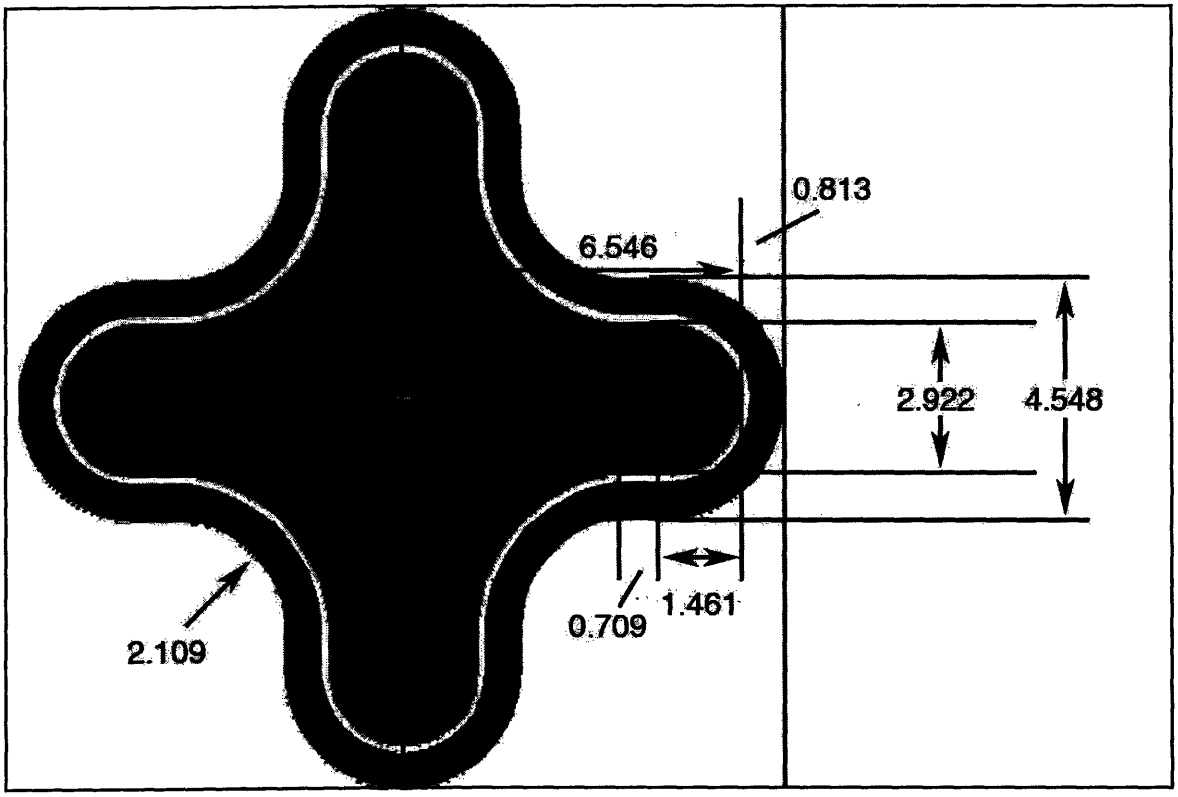

Figure 2.4: Scale depiction of the SP2 design.

The result is a fuel rod that matches the reference fuel mass yet possesses a 35% larger cooling surface. This has the effect of increasing the total cross-sectional footprint of the CSS rod by 6.7%, but also increases local subchannel flow area by 5.8% for the same reason that SP1 creates this effect.

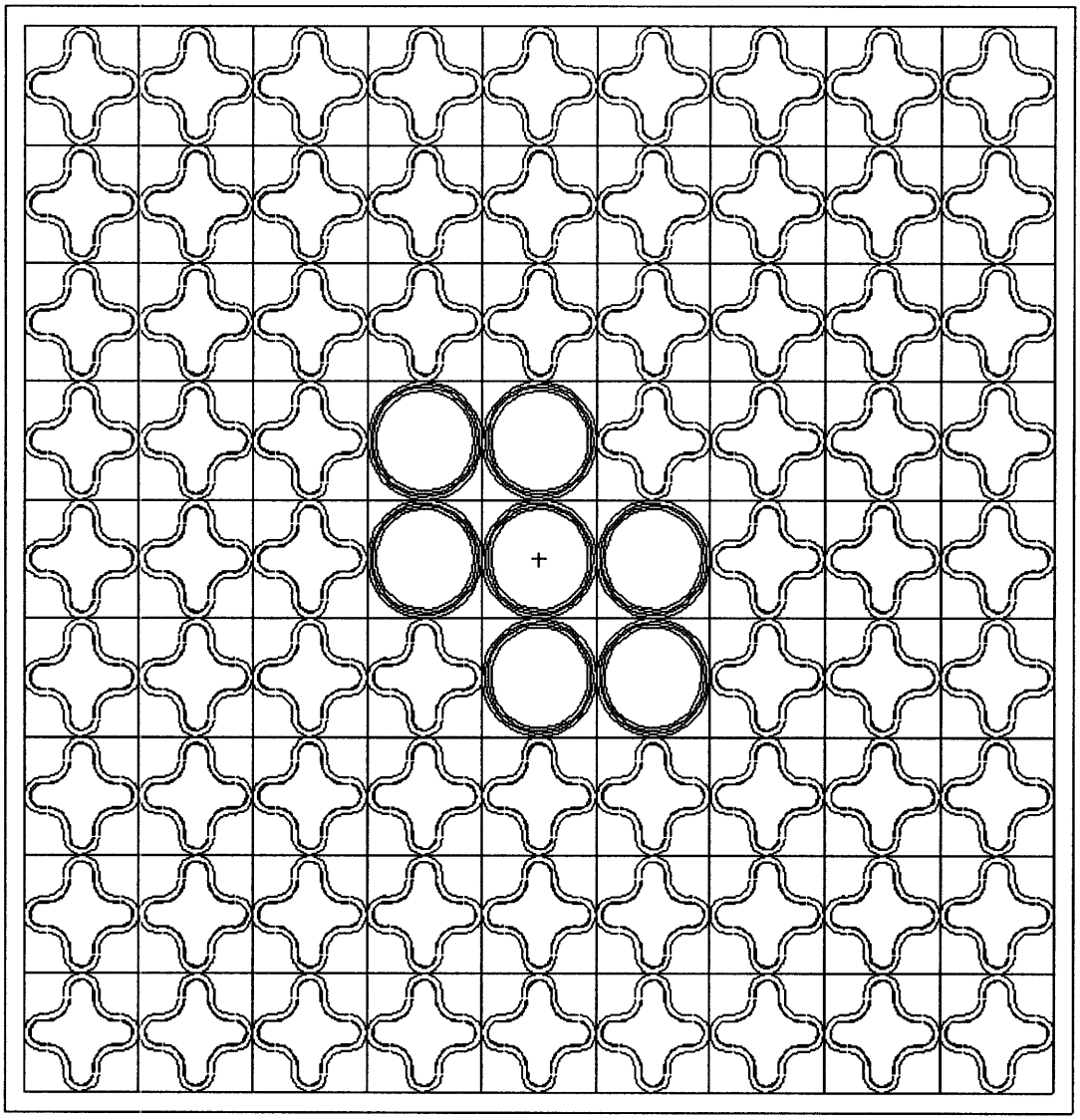

Figure 2.5: The full 9x9 assembly, spanned by CSS SP2 fuel rods

Over the entire assembly, this results in an 8% decrease in flow area. While this decrease is undesirable, it represents a significant improvement over the SP1 assembly in this regard. Still, the SP2 assembly is characterized by a reduction in clad surface area in comparison to SP1, and therefore will face a higher average surface heat flux, and higher maximum fuel temperature.

The flow area, moderator area, and fuel area for this SP2 assembly (Figure 2.5) take on the values 85.7 cm^2, 54.7 cm^2, and 53.0 cm^2 respectively (Table 2.3), resulting in an H/HM ratio for this assembly of 4.2.

Finally, the smaller wetted perimeter, as well as the larger flow area, combine to give the SP2 assembly a hydraulic diameter of 0.72 which is still well below the reference, but a significant improvement over the SP1 case.

2.3 Summary of Design Dimensions

2.3.1 Summary of Pin Dimensions

A summary of the fuel rod parameters mentioned for the three fuel geometries through Chapter 2 is displayed here for ease of comparison:

Table 2.3: Fuel Rod Design Comparison

	Fuel cross-sectional area (cm^2)	**Total pin cross-sectional area (cm^2)**	**Local subchannel flow area (cm^2)**	**Pin surface perimeter (cm)**
Ref.	0.736	0.981	1.058	3.511
SP1	0.736 (+0%)	1.095 (+11.6%)	1.071 (+1.2%)	4.919 (+40.1%)
SP2	0.736 (+0%)	1.047 (+6.7%)	1.119 (+5.8%)	4.744 (+35.1%)

The SP2 design seems favorable to SP1 in the categories excluding pin surface perimeter, where SP1 holds an inherent 5% advantage. This includes the total pin cross-sectional area, as well as it's inverse – the local subchannel flow area.

2.3.2 Summary of Assembly Dimensions

A summary of the parameters mentioned for the three assemblies through Chapter 1 is displayed here for ease of comparison:

Table 2.4: Fuel Assembly Design Comparison

	Fuel cross-sectional area (cm^2)	**Tot. Pin cross-sectional area (cm^2)**	**Total assembly flow area (cm^2)**	**Total wetted perimeter (cm)**	**Assembly Hydraulic diameter (cm)**	**Assembly H/HM ratio**	**Total Moderator area (cm^2)**
Ref.	52.98	72.59	93.88	328.44	1.13	4.3	51.66
SP1	52.98	81.03	82.10	499.24	0.66	4.2	54.68
SP2	52.98	77.48	85.70	486.27	0.72	4.2	54.68

Similar to the comparison between individual fuel rods, the SP2 assembly holds the edge over SP1 in most of the columns in Table 2.4: it boasts a larger flow area, smaller pin cross-sectional area, and larger hydraulic diameter. The SP1 assembly dominates the wetted perimeter category, which could turn out to be a double-edged sword: though this means the largest cooling surface and therefore the lowest average surface heat-flux, this will also likely mean the highest frictional hydraulic losses. The pressure drop situation for SP1 will be further magnified by the fact that flow area is smaller, requiring a higher mass flux than the other assemblies at the same power rating.

Clearly, the benefits and drawbacks of the characteristics shown for each assembly in Table 4 must be analyzed using a computational tool (or experimental methods); this is precisely what is attempted in a large part of the remaining work (detailed in Chapter 2.1). The thermal-hydraulic code VIPRE was employed to conduct a full-scale comparative analysis.

3. Methodology

3.1 Core Performance Modeling

3.1.1 Selection of a Computational Tool

Two parameters were identified as key measures of thermal-hydraulic peformance: the Critical Power Ratio (CPR) and core pressure drop. Though there are many ways to evaluate these using established correlations, it has been accepted widely within the nuclear systems analysis community that the use of the EPRI-developed Thermal-Hydraulics code VIPRE [5] (Versatile Internals and Component Program for Reactors) can be an accurate and easy to apply means to perform these calculations.

VIPRE is a subchannel code which predicts 3D velocity, pressure, and thermal energy fields within discrete axial nodes of user-defined coolant channels, and temperature profiles within user-defined heated elements (nuclear fuel rods). This is accomplished by solving finite-difference equations for mass, momentum, and energy conservation for any interconnected array of coolant channels, using the assumption of incompressible yet thermally-expandable flow. VIPRE is thus applicable to single and two-phase flow in pressurized and boiling water reactors.

Compared to similar codes, VIPRE is particularly flexible, allowing for redundant geometry definiton, and is therefore ideal for the unusual modeling required for CSS fuel. Additionally, VIPRE has a robust set of void-drift correlations, helping the simulation of complex two-phase effects typical of BWR subchannel analysis. The version used here, VIPRE01mod02, is especially applicable, with an updated two-phase friction multiplier and modern CPR and CHFR correlations.

3.1.1 Application of VIPRE to BWR Core Analysis

To ensure correct analysis of a reactor core, one would in general want to model the entire core in VIPRE. However, it is sufficiently accurate in the case of BWR analysis to

concentrate on a couple of assemblies individually. This takes advantage of the fact that each assembly is encased in an isolated duct and experiences no cross-assembly flow. Still, all assemblies share the same core-wide inlet and outlet plena and therefore have the same pressure drop.

In order to appropriately calculate the designated performance criteria, it was decided that MCPR would be calculated based on analysis of the hottest assembly in the core as, while calculation of the pressure drop would come from a core-averaged assembly model. The latter model is not intended to describe any "real" assembly within the core but rather serves as a best approximation of the expected core-wide pressure drop.

The process was as follows: a detailed model of a single assembly of the reference core was constructed using given geometrical parameters. Two input files were made from this geometry: one describing the power and coolant flow in a core-averaged assembly, and one for the hot channel of the core.

Core pressure drop was evaluated for the average assembly model using industry-standard operating conditions (Table 3.1); this pressure drop was then applied to the hot assembly as a fixed parameter before CPR was evaluated. Ultimately, this establishes a reference value for acceptable operating limits of our desired thermal-hydraulic measures. This process was introduced in previous work, including in a similar thermal-hydraulic analysis of annular fuel [6] for BWRs.

Margin for a power-density increase using Cross-Shaped Spiral fuel is therefore judged in comparison to the reference case, by developing unique CSS-VIPRE models. Likewise, one model is constructed for the hot assembly and one on the average assembly. Evaluation of pressure drop and CPR is found in the same manner, under the same operating conditions.

To quantify the power uprate potential, linear power and coolant mass flow are then raised proportionally for the average assembly input, to obtain the pressure drop at this

new power level. This ensures that the two-phase flow regime development along the core, as well as the outlet quality will be unchanged at this new power level. This is then imposed on the hot channel model, which has been elevated to the same new power level, and a new MCPR is found. This process is continued iteratively until hot channel MCPR for the CSS model is equal to that of the reference case.

3.1.2 Correlations

The accuracy of this investigation, and the uncertainty and conservatism associated with its results, are tied into the reliability of the two-phase flow and heat transfer models employed by VIPRE. Careful choice was given to the correlations used to model the effects of two-phase flow on hydraulic losses, rod-coolant heat exchange in various flow regimes, and the relationship between flow quality and void fraction.

Before the onset of nucleate boiling, the presence of single-phase forced convection allowed for use of the Dittus-Boelter [5] correlation for calculation of turbulent flow heat transfer. For subcooled and saturated nucleate boiling, the Chen correlation [5] was chosen due to its accuracy over a wide range of conditions. The Chen correlation takes the form:

$$q'' = h_{fc}(T_w - T_b) + h_{nb}(T_w - T_{sat}) \qquad \text{(Eqn. 3.1)}$$

In this way, it is able to correlate the mechanisms of forced convection and nucleate boiling separately, each as functions of quality, mass flux, core pressure, and geometry, enabling great accuracy over quite a span of conditions. Chen is generally recommended for qualities below 0.8, however all conditions presented for these models will reach CHF well below this limit.

To model critical heat flux, Hench-Gillis was used as the Critical Power Ratio (CPR) correlation for this "first-order" VIPRE model. This has well-established roots as a tool

for BWR analysis applications [6, 7, 8]. Hench-Gillis is a critical quality / boiling length correlation having the form:

$$x_{crit} = \frac{AZ}{B+Z}(2-J) + F_p \qquad \text{(Eqn. 3.2)}$$

$$A = \frac{0.5}{G^{0.43}}$$

$$B = 165 + 115G^{2.3}$$

$$Z = \frac{\pi \cdot d_{co} \cdot nL_B}{A_f}$$

J represents a subchannel peaking factor that depending on the position of the channel (central, side or corner), and is a function of the peaking factors of the surrounding nuclear rods, as well as mass flux, characteristic gap lengths, and total bundle flow area [5]. Hench-Gillis has a validity range of pressures between 600-1400 psi, inlet enthalpy between 0 - 233 kJ/kg, and mass flux between G = 340-2034 kg/m^{2}s.

Void fraction along the core height was predicted using the EPRI Drift-flux model, which is a state-of-the-art model which correlates local mass flux and quality to well-defined flow regimes. The friction model follows the VIPRE default Blasius correlation, with the additional of the EPRI two-phase friction multiplier.

For transition boiling, the default Condie-Bengtson correlation [5] was used; and finally for post-CHF heat transfer the default Groeneveld 5.7 tables [5] were adapted for use by VIPRE.

3.1.3 Reference VIPRE model

A VIPRE assembly analysis is conducted by writing an input file that provides full description of each individual coolant subchannel and fuel element, as well as extensive core operating parameters.

For a given subchannel, VIPRE accepts inputs for flow area, wetted and heated surface, neighboring channels, fuel rods in contact with the channel, and cross-flow to other channels, among other variables. These parameters were extracted from typical assembly geometry (Figure 2.1). Full sample input files can be found in Appendix A.

Local pin peaking factors was also based on industry-typical data, and for this analysis takes the form of seen in Figure 3.1. Peaking in the water rod region was taken at zero, meaning no heat generation within this region.

0.92	1.04	1.07	1.10	1.08	1.11	1.07	1.03	0.92
1.03	1.18	1.00	0.80	1.09	0.77	0.97	1.17	1.03
1.07	0.99	0.79	0.98	0.99	0.91	0.74	0.97	1.08
1.09	0.79	0.98			1.07	0.92	0.77	1.10
1.07	1.08	0.98				0.99	1.08	1.08
1.09	0.79	0.92	1.06			0.98	0.80	1.11
1.07	0.97	0.76	0.92	0.99	0.98	0.79	0.99	1.08
1.02	1.18	0.98	0.80	1.09	0.81	1.01	1.20	1.04
0.91	1.03	1.08	1.10	1.09	1.11	1.08	1.04	0.93

Figure 3.1: Reference Assembly pin peaking

Similarly, axial power peaking was defined using typical data (Figure 3.2).

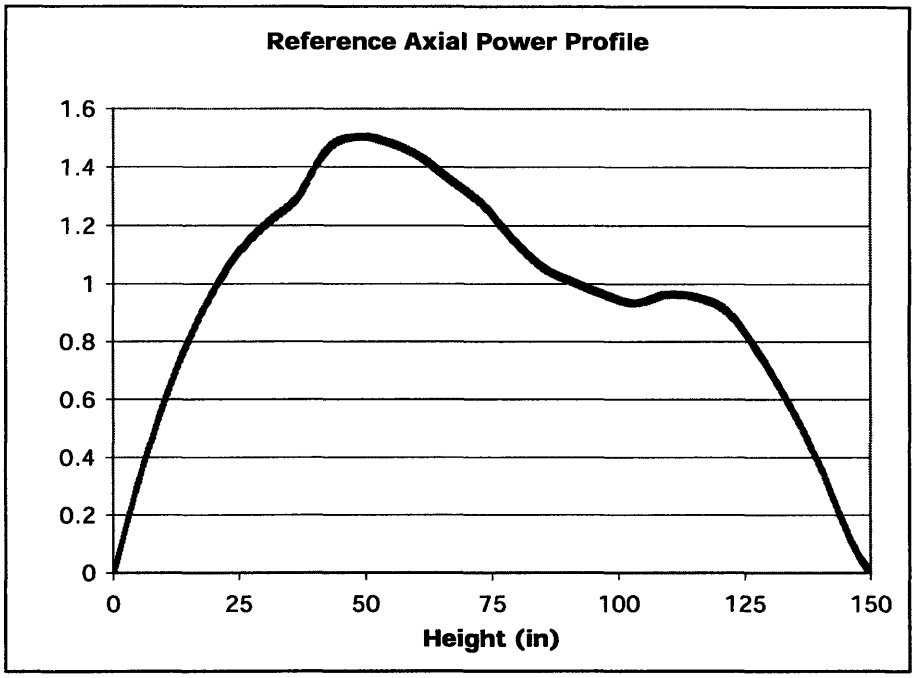

Figure 3.2. Reference Axial Peaking [1]

Operating conditions were based on standard BWR conditions; Table 3.1 summarizes much of this information:

Table 3.1: Reference Operating Parameters [1,9]

Parameter	Value
System pressure, MPa (psia)	7.136 (1035)
Core mass flow rate, kg/s (Mlbm/hr)	13670 (108.5)
Core inlet temperature, °C (°F)	278.3 (533)
Core thermal power, MW_{th}	3323
Fuel assembly axial length, m (in)	4.180 (164)
Fuel assembly heated axial length, m (in)	3.708 (146.0)
Hot assembly power, kW_{th}	6304.5
Hot assembly mass flow rate, kg/s (Mlbm/hr)	17.38 (0.1379)
Hot assembly linear-power-generation-rate, kW/m (kW/ft)	22.98 (7.00)
Average core exit quality	13.34%
Hot bundle exit quality	24.5%

Radial power peaking factor distribution with 4 zones	1.45,1.30,1.00 and 0.60
Axial power peaking factor	1.5
Maximum local peaking factor	1.2
H/HM ratio	4.3

This table also includes the values of average hot-assembly exit quality, which is not a fixed VIPRE input but serves to validate results.

Several pressure loss coefficients are fixed, in that they are not a function of our fuel choice but rather the core structure. These values were adapted from recommendations given in the VIPRE manual itself, seen in Table 3.2:

Table 3.2: Fixed Loss Coefficients [5]

Location	**Loss Coefficient (k)**
Orifice (average assembly)	24.28
Orifice (hot assembly)	23.37
Entrance plate	6.63
Exit plate	1.46
Grids	1.5 (each)

Loss coefficients, k, are a means of describing flow resistance of a given object, and are defined according to the formula:

$$\Delta p = k\frac{\rho v^2}{2} \qquad \text{(Eqn. 3.3)}$$

3.1.4 CSS VIPRE Model

In the absence of experimental friction-loss and CPR correlations specific to the cross-shaped spiral array geometry, the same set of correlations for the reference assembly was used in VIPRE calculations. That is, the core pressure-drop was effectively the same as that of a cylindrical fuel assembly with a smaller assembly hydraulic diameter, and lacking the 7 axial grid-spacers. The CPR is calculated using the Hench-Gillis correlation with a special equivalent diameter -- in order to account for the increased cooling surface, this diameter is obtained by equating the perimeter of a CSS rod to the equivalent perimeter of a cylinder.

Because VIPRE does not represent CSS rod geometry, further approximation was necessary. The input values for channel flow area, wetted perimeter, and heated perimeter were entered exactly as calculated for CSS geometry described thus far. However, the axial gap variation between neighboring coolant channels was approximated by averaging over the axial length between no gap (as in the case of touching pins) and the maximum gap at 45° apart. Dimensions of the coolant subchannels for the SP1 and SP2 assemblies can be seen in Tables 3.3, 3.4. Full input files for the SP1 and SP2 assemblies can be found in Appendix A.

These first-order approximations serve to capture the geometric description of a CSS fuel assembly, but do not yet incorporate other potential benefits of spiral fuel, including the additional component of radial velocity or its impact on flow conditions and subchannel mixing.

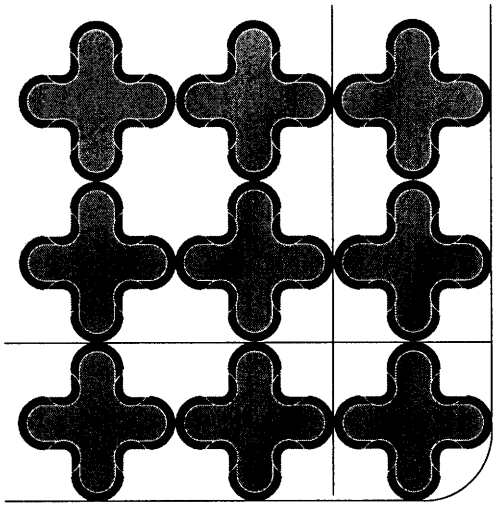

Figure 3.3: Central, Side and Corner subchannels are shown in greater detail.

Making the approximations listed in this section, the central, side, and corner subchannel geometry was evaluated and is listed below. As seen in Figure 3.3, a given central channel will have four neighbors with which direct exchange of mass, momentum, and energy; this number of crossflow channels drops to three for a side channel, and two for a corner channel.

The wetted and heated perimeters for the majority of central subchannels are identical. This is because they are not in contact with the duct wall, as is the case for the side and corner channels. Central channels adjacent to the central water rod cluster will not have this property, since the water rod cladded surface represents another cold wall.

Table 3.3: SP1 Assembly Subchannel input parameters

Channel location	Heated perimeter (cm)	Wetted perimeter (cm)	Flow Area (cm^2)	# of crossflow channels	Avg. channel gap width (cm)
Central	4.92	4.92	1.07	4	0.14
Side	2.46	3.93	0.53	3	0.07
Corner	1.23	2.39	0.15	2	0.07

Several observations can be made about the properties of the different characteristic channels for a CSS assembly. First, due to their proximity to the wall, the average channel gap widths for the side and corner channels are half of that of the central subchannels. The wall remains flat over the course of its height, whereas an adjacent CSS rods would twist away periodically. A reduction in a gap size could result in a decrease in exchange of enthalpy, creating a more probable hot spot.

Along with this reduction, the corner and side subchannels have disproportionately small flow areas in comparison to their wetted perimeter, resulting in a low subchannel hydraulic diameter which restricts flow to these border regions. In traditional rod bundles, this effect is not present. The duct wall is slightly further from side and corner rods than from other neighboring rods, in part, to alleviate this issue.

Table 3.4: SP2 Assembly Subchannel input parameters

Channel location	Heated perimeter (cm)	Wetted perimeter (cm)	Flow Area (cm^2)	# of crossflow channels	Avg. channel gap width (cm)
Central	4.74	4.74	1.13	4	0.15
Side	2.37	3.84	0.56	3	0.07
Corner	1.18	2.34	0.16	2	0.07

Because of the strong similarity in cross-sectional shape, many of the parameters for the subchannels of the SP2 assembly closely resemble those of the SP1 variant. The potential problem described for side and corner subchannels of the SP1 assembly is still an issue for this assembly geometry, though not to the same extent. In all cases, the flow area is slightly increased, whereas wetted perimeter is reduced.

It would be possible to endlessly speculate about the changes to thermal-hydraulic indicators, such as MCPR and core pressure drop, as a result of the changes in geometry shown here. However these questions can only be answered by performing a side-by-

side comparison of the VIPRE-modeled cores described above, under controlled operating conditions. The results of this analysis are presented in Section 4.1.

3.2 Thermal Conduction Model

Though the subchannel model detailed in Section 3.1 accurately accounted for changes in flow area and surface area due the fuel geometry, it was still unable to account for the specific CSS fuel cross-sectional shape, and resultant non-uniform heat-flux and temperature profiles laterally. This was accounted for with the creation of a thermal conduction analysis model, to the precise specifications of rod dimensions set forth in Chapter 2.

A thermal conduction analysis using the finite-element analysis package COSMOS [10] was essential to supplement the VIPRE modeling. The approach was to run VIPRE to find values for T_{bulk} and h_{co} at the most-limiting location of the assembly (as determined by the CSS VIPRE model), then to pass these results into the COSMOS model to predict maximum fuel temperature and surface heat flux distribution.

Because previous similar application of COSMOS for fuel rods was unknown, it was first necessary to attempt to validate its results. This could most easily be done using cylindrical rod geometry and constant, uniform heat transfer characteristics, as this scenario can be readily evaluated analytically as a 1D radial thermal resistance model.

3.2.1 Validation

The process of validation was set to take place as follows: a steady-state model would be developed with the help of the CAD software SolidWorks [11], then the results would be compared with a value given by the equation for overall thermal resistance of a fuel rod.

$$T_{\max} - T_{bulk} = q'\left[\frac{1}{4\pi k_f} + \frac{1}{2\pi R_g h_g} + \frac{1}{2\pi k_c}\ln\left(\frac{R_{co}}{R_{ci}}\right) + \frac{1}{2\pi R_{co} h_{co}}\right], \qquad [12] \quad \text{(Eqn. 3.4)}$$

These terms represent four thermal resistances in series: conduction within the fuel pellet, natural convection and radiation across the gap, conduction across the cladding, and a forced convection boiling resistance to the bulk temperature. For constant, uniform, and temperature independent thermal characteristics, the developed finite-element model should give results matching the above equation.

Using SolidWorks, a 1-mm thick cross-section was drawn to the specifications of the reference cylindrical GE11 fuel rod. A fine-mesh scheme was applied to the fuel rod cross-section for preparation for heat-conduction analysis (Figure 3.4). This scheme was subsequently imported into the finite-element analysis package COSMOS for a full steady-state thermal analysis.

In order to simulate anticipated BWR conditions, the coolant bulk temperature was set to the saturation temperature at the reference operating pressure, for this case T_{sat}(7.1 MPa) = 288°C. The outer surface of the cladding was supplied with a constant heat transfer coefficient typical of 2-phase forced convection, while the cladding and fuel pellet were defined with constant thermal conductivities appropriate for Zircalloy and Uranium dioxide.

The Helium gas gap between the fuel and clad was given a heat transfer coefficient typical of this resistance, without accounting for fuel relocation for conservatism. This initially required that the inner-cladding and outer fuel pellet surfaces would be defined as a contact-pair, as required in COSMOS wherever a heat transfer coefficient is applied. Finally, the fuel was assumed to generate uniform volumetric power, taken here as the

hot channel linear power specified in VIPRE models as 22.98 kW/m. A summary of the exact parameters used are given in Table 3.5.

Table 3.5: Reference Rod Thermal Study Input Parameters

Linear Heat Rate	$q' = 23$ kW/m
Coolant-Outer-Cladding Heat Transfer Coefficient	$h_{co} = 42{,}560$ W/m^2-K
Fuel-Cladding Gap Heat-Transfer Coefficient	$h_g = 8$ kW/m^2-K
Cladding Conductivity	$k_c = 16.96$ W/m-K
Fuel Conductivity	$k_f = 3.9$ W/m-K
Bulk Coolant Temperature	$T_{bulk} = 288$°C

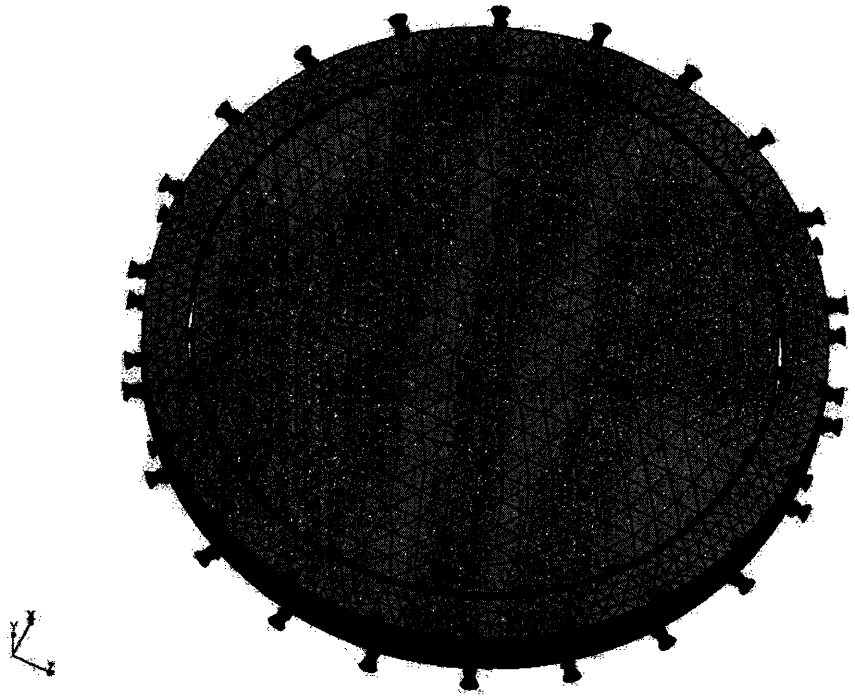

Figure 3.4: The GE11 Reference Fuel Pin, meshed for analysis in COSMOS.

A steady-state fuel thermal-conduction analysis using COSMOS was performed under the aforementioned conditions, for the reference cylindrical pin giving a maximum temperature of 1163K (Figure 3.5).

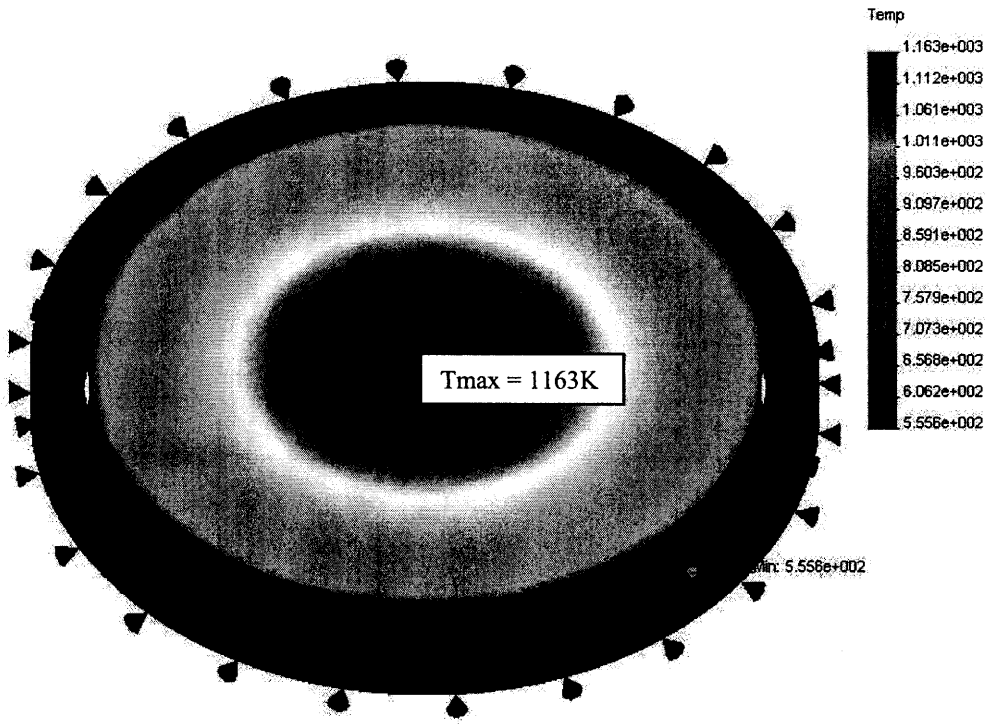

Figure 3.5: Initial COSMOS results for the Reference Fuel Rod.

However this model, solved analytically using Eqn. 3.4 for overall thermal resistance gives a slightly lower value, shown in Table 3.6.

Table 3.6: Thermal Study Validation Results

T_{max}, COSMOS	1163K
T_{max}, analytical	1100K

This error, though a small percentage difference, was larger than expected – the systems should have matched extremely well. The discrepancy was further dissected as follows, in Table 3.7.

Table 3.7: Temperature drop across each resistance between fuel and coolant.

ΔT_{drop} (K)	Analytical	COSMOS	Discrepancy
$T_{max} - T_{fo}$	469	480	11
$T_{fo} - T_{ci}$	47	95	48
$T_{ci} - T_{co}$	30	32	2
$T_{co} - T_b$	4	3	1

There seemed to be two distinct problem areas. First of all, the fuel region showed an 11 degree difference between COSMOS and predicted values for temperature drop. After a brief investigation it was discovered that this difference could be eliminated by adding increased meshing to the fuel-gap boundary region, where the temperature gradient is at its largest (Figure 3.6). Updating the mesh-scheme gives a new result: $T_{max} = 1153K$. The resultant temperature drops are shown in the updated Table 3.7.

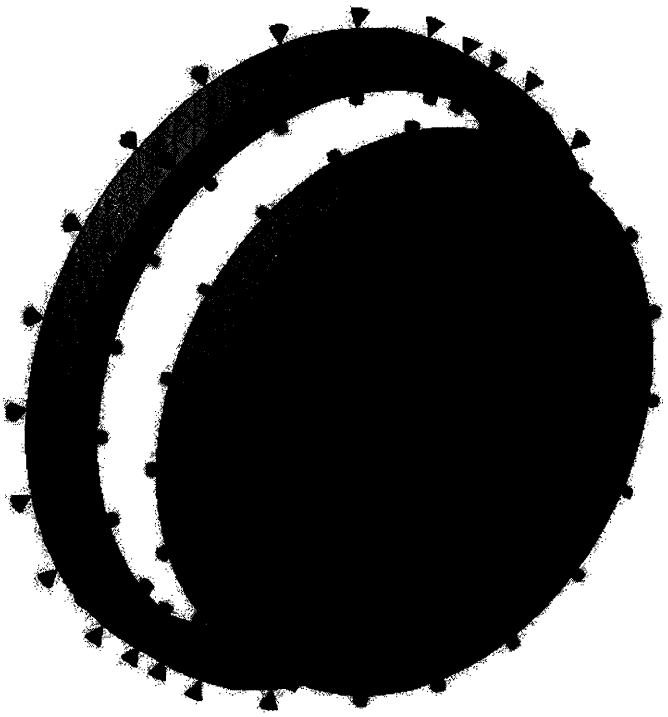

Figure 3.6: Increased meshing near the outer fuel pellet boundary.

Table 3.8: Temperature drop across each resistance; modified meshing.

ΔT_{drop} (K)	Analytical	COSMOS	Discrepancy
$T_{max} - T_{fo}$	469	470	1
$T_{fo} - T_{ci}$	47	95	48
$T_{ci} - T_{co}$	30	32	2
$T_{co} - T_b$	4	3	1

Comparing the temperature drops after this adjustment, the only problem region remaining is at the gas gap. In contrast with the analytical evaluation, the COSMOS model has a very large temperature drop across this region, meaning that heat generated in the fuel experiences an increased resistance in propagating across the gap. Here, selectively increasing meshing on the fuel outer surface and cladding inner surface had no effect on changing the temperature drop.

To combat this issue, a new model was created in SolidWorks. In this system, the gap is treated as a solid material wedge in between the fuel pellet and cladding, with an effective thermal conductivity (κ) found by equating

$$\frac{1}{2\pi R_g h_g} = \frac{1}{2\pi\kappa}\ln\left(\frac{R_{ci}}{R_{fo}}\right) \qquad \text{(Eqn. 3.5)}$$

The new COSMOS model, combined with increased meshing in the central region, alleviates the difference and predicts T_{max} = 1102 K.

It stands to reason that the method of defining the fuel outer-surface and cladding inner-surface as a contact pair was the ultimate cause of the temperature discrepancy, likely due to their difference in surface area. In the case of a thin slice, the "material-wedge" effective thermal conductivity approximation used here is not greatly different from the simplification that is normally used, which is to define the gas gap resistance as a convection resistance, h_g. The reality is that heat propagation across the gap is more complex than through other regions of the fuel rod, and cannot be fully described by any single mode of heat transfer. In principle, it should be modeled as three resistances in parallel: natural convection, radiation, and conduction within the gas. With this in mind, the approximation method introduced here does not seem outlandish.

While this resolves the cylindrical rod temperature issue, the process cannot be identically repeated for the cross-shaped rod, which has no analytical comparison to fall back on. For this purpose, the CSS model was supplied with the value of an effective conduction coefficient found for the cylindrical geometry as a good approximate for the value of the new geometry.

With a definite methodology established, it became possible to create a CSS fuel thermal analysis model for comparison with the reference. It also gave enough confidence in the model to begin adding a little more detail: temperature-dependent thermal conductivity was added to Uranium dioxide within the fuel pellet, using the curve taken in Figure 3.9.

The reference cylindrical rod model was finalized with the application of this conductivity, and was ready for introduction of the thermal conditions at the location of interest. For this study, it was decided that the temperature and heat-flux would be examined at the most limiting thermal location within the hot channel of each core model. This would be identified by examining the results of the steady-state VIPRE models to obtain bulk temperature, linear power, and the outer cladding heat transfer coefficient at the location closest to thermal limits.

With the reference model complete, 1-mm thick cross-sections were completed in SolidWorks for the SP1 and SP2 rod geometries, adapting the dimensions set forth in Chapter 2. A meshed model of SP1 can be seen in Figure 3.7. The thermal conditions imposed on each of these models are summarized in Table 3.10.

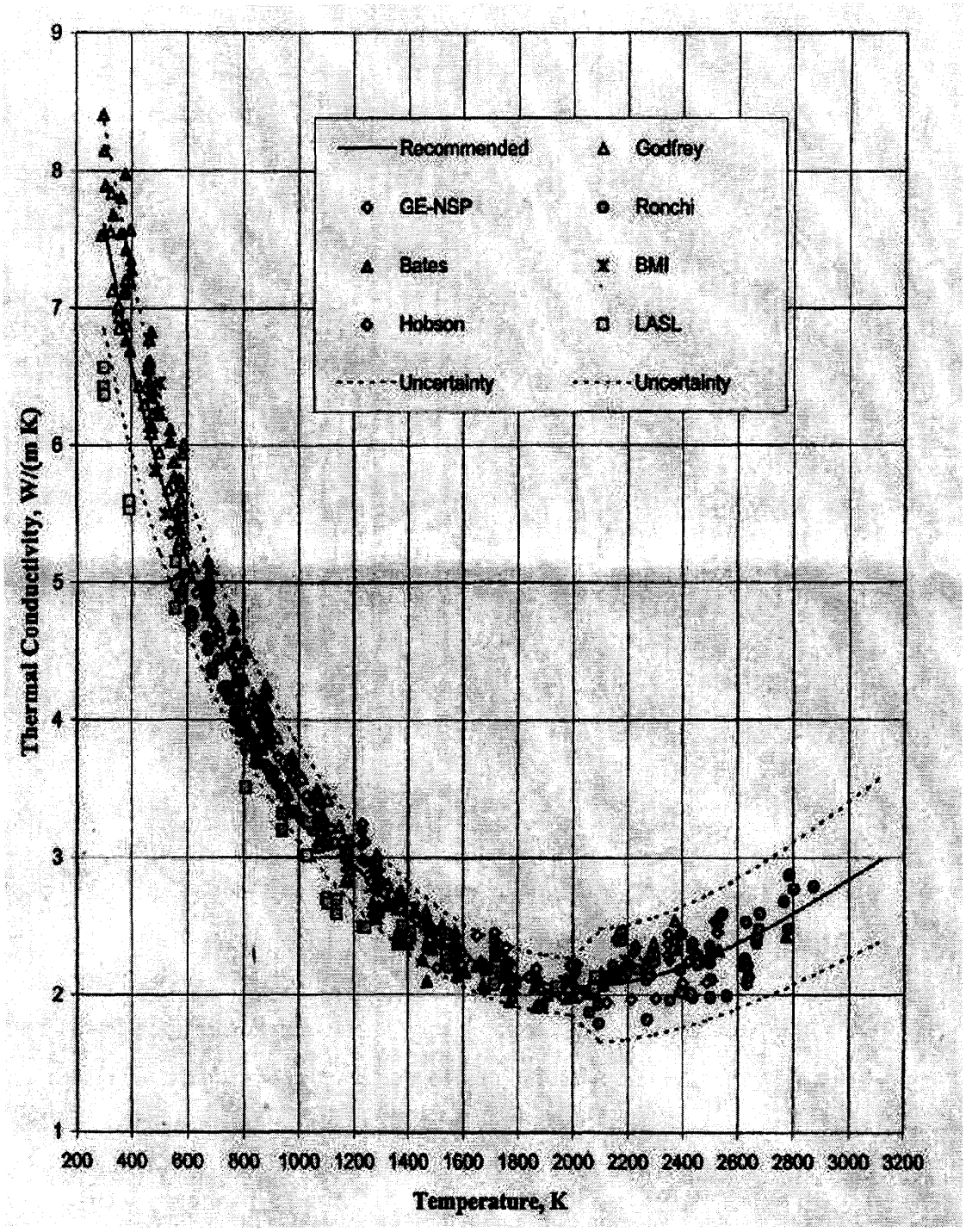

Figure 3.7: Temperature dependence of thermal conductivity of Uranium Dioxide [13].

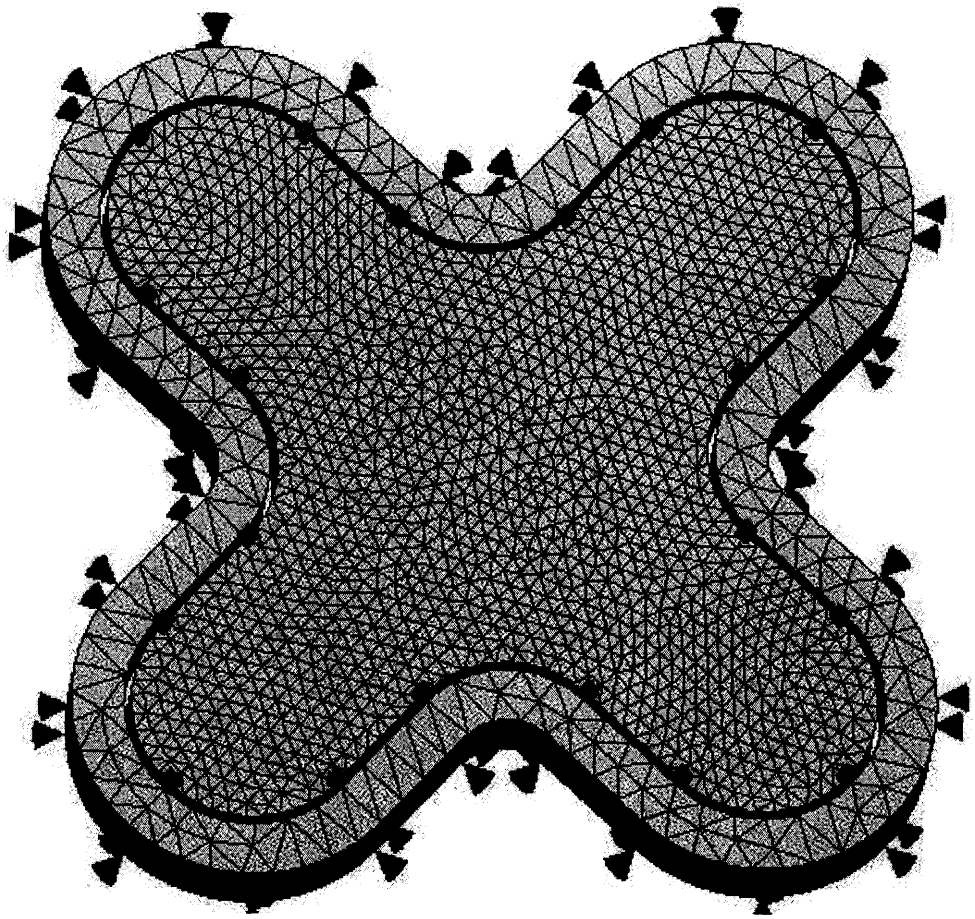

Figure 3.8: The CSS SP1 model, meshed for analysis in COSMOS.

Though the gap resistance is taken as a constant value, found for the effective conductivity, κ, using Eqn. 3.5. The thermal conductivity of Zircalloy is also taken as a constant over temperature, which makes sense given the limited temperature drop across this region (Tables 3.7 and 3.8). However, temperature dependence was introduced in the fuel region. The linear heat rate, outer cladding heat transfer coefficient, and bulk temperature at most limiting thermal condition were to be taken from VIPRE as previously described (Table 3.9).

Table 3.9: Operating Conditions defined for the Heat Conduction Study

Parameter	Reference	CSS Rods
Linear Heat Rate	Supplied by VIPRE output*	Supplied by VIPRE output*
Coolant-Outer-Cladding heat transfer coefficient (h_{co})	Supplied by VIPRE output*	Supplied by VIPRE output*
Fuel-Cladding Gap heat-transfer coefficient (h_g)	8 kW/m^2-K	8 kW/m^2-K
Fuel Conductivity	Temperature Dependent	Temperature Dependent
Cladding Conductivity	16.96 W/m-K	16.96 W/m-K
Bulk Coolant Temperature (T_b)	Supplied by VIPRE output*	Supplied by VIPRE output*

*As shown in Table 4.1

It was planned to compare the results from this analysis at the hottest location of the VIPRE run under nominal power and again at the maximum power uprate found in VIPRE analysis. These results are shown in Section 4.2.

3.3 Corrected Conduction Model

Undeniably, a model that aims to capture the effects of energy generation within an unusually shaped fuel pellet would be incomplete without an attempt to couple the thermal results with some form of neutronic study.

In this case, it was suspected that the unique shape of the CSS fuel might lead to significantly non-uniform energy generation within the pellet, due to extensive thermal-neutron shielding by the large petal-like extensions. Because of the large slow-neutron cross-section of uranium-235, a disproportionate amount of energy generation occurs close to the surface, where slow neutrons are first able to contact the fuel; this occurs to some extent in standard BWR and PWR fuel rods. For a fuel shape with a large surface-to-volume ratio as the CSS, this effect could force an even greater amount of power generation closer to the surface, especially in the outer lobes that would otherwise be relatively cool.

It was thought that for the case of diminished power at the center of the pellet, the potential issue of "elbow" heat flux peaking might be alleviated, since much of the peaking was believed be fed by power generated within the central region.

Another more detailed conduction model was therefore created in COSMOS, which segmented the fuel pellet of SP1 and SP2 into 88 different regions in which power generation could be defined individually (Figures 3.9, 3.10). It was recognized that the power in each of these regions could be found computationally by using a versatile neutronics code to set up representative models of SP1 and SP2. This code would also require the capability to allow definition of a meshing scheme to match that which was created manually in COSMOS in fuel rods SP1 and SP2.

Figure 3.9: The CSS SP1 model, manually meshed for coupling with MCNP.

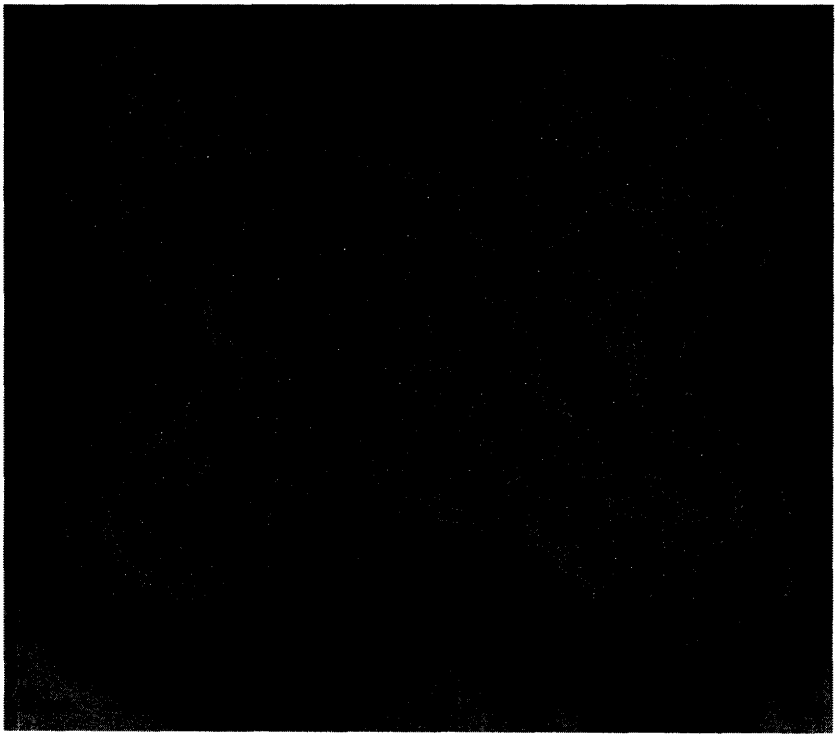

Figure 3.10: The CSS SP2 model, manually meshed for coupling with MCNP.

To this end, the neutronics code MCNP [14] (Monte Carlo N-Particle Transport Code) was selected. As in this study, MCNP is used primarily for the simulation of nuclear processes, such as fission, but has the capability to simulate particle interactions involving photons, and electrons in addition to neutrons.

A typical MCNP input is simple in concept, though the structure of an input file reads somewhat backwards. Using the first "deck", one divides all of three-dimensional space into material regions that are based upon general shapes defined in the second deck, and materials that are not specified until the third deck. Terms of the study, including the specifics regarding neutron sources and longevity of the study, are also specified within this third deck. While MCNP is most often used in determining the k-effective (criticality eigenvalue) for a given system, fission energy deposition within any desired region is a quantity that can be found indirectly using MCNP by setting up a volumetric flux tally.

MCNP models were constructed to the dimensions of Spiral Pin 1 and Spiral Pin 2 (shown in Figure 3.10, attached as Appendix B), with square-meshing along one of the petals and finer meshing near the center. This scheme exactly matches the level of detail shown in the conduction model, assuming that quarter-pin symmetry can be used effectively. Secondary models of SP1 and SP2 were constructed without any meshing; these models were used to obtain a value for the fission energy deposited within the entire pellet.

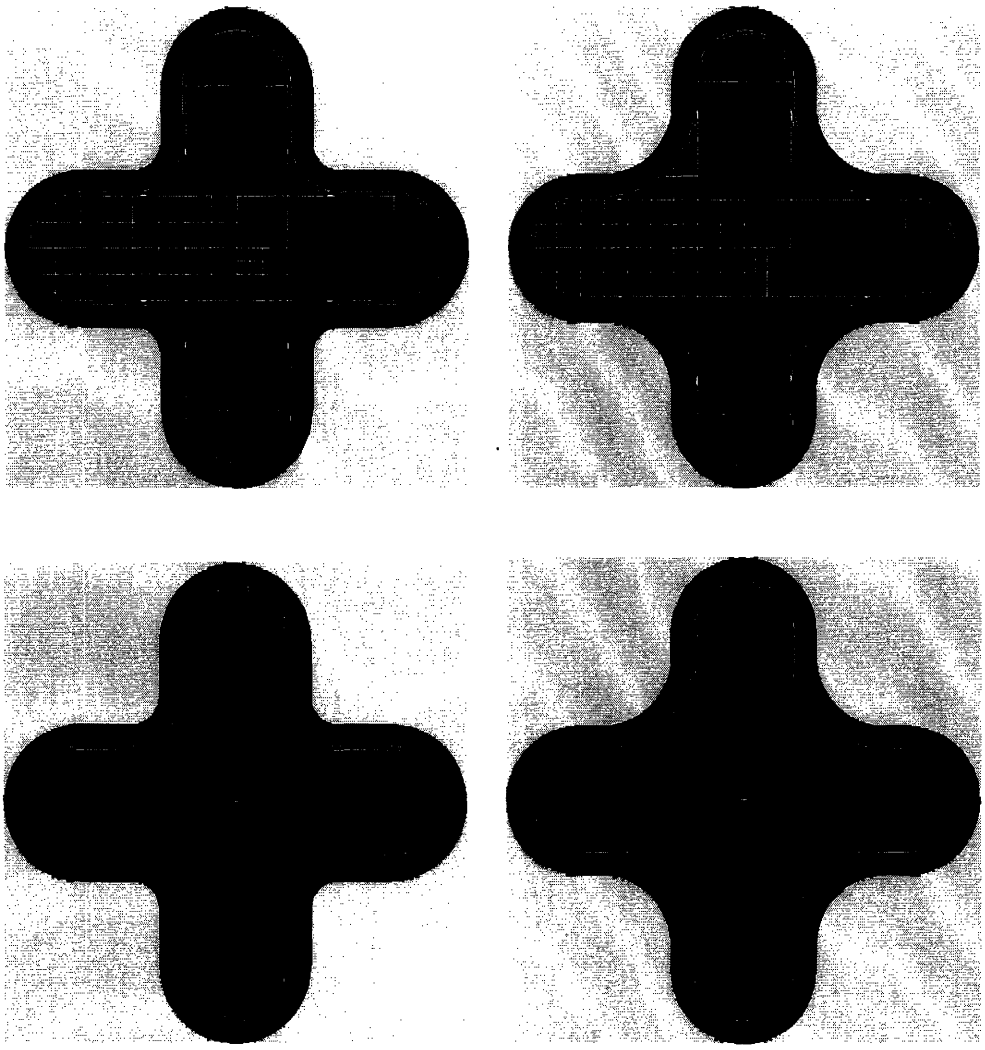

Figure 3.11: MCNP models of SP1 and SP2 with and without quarter-pin mesh.

The terms of the study were as follows: the two-dimensional single-rod models for SP1 and SP2 were constructed with fully-reflective boundary conditions, and used as unit-cell representations of the entire hot channel assembly (Figure 3.11). This is accomplished by evaluating an effective coolant density which matches the H/HM of an entire assembly, as calculated for assemblies CSS-SP1 and SP2 in Chapter 2. Maintaining this ratio ensures a similar neutron spectrum as would be expected for a full assembly, and therefore an accurate distribution in energy deposition. The effective density is much larger than that of even saturated water at BWR pressures because this density must account for water within the water rods and outside the assembly box in addition to that within the coolant, but must do so in a much smaller "flow" area. For the SP1 case, this

density is slightly larger due to its smaller flow area, and displacement of a larger number of water molecules from the coolant flow.

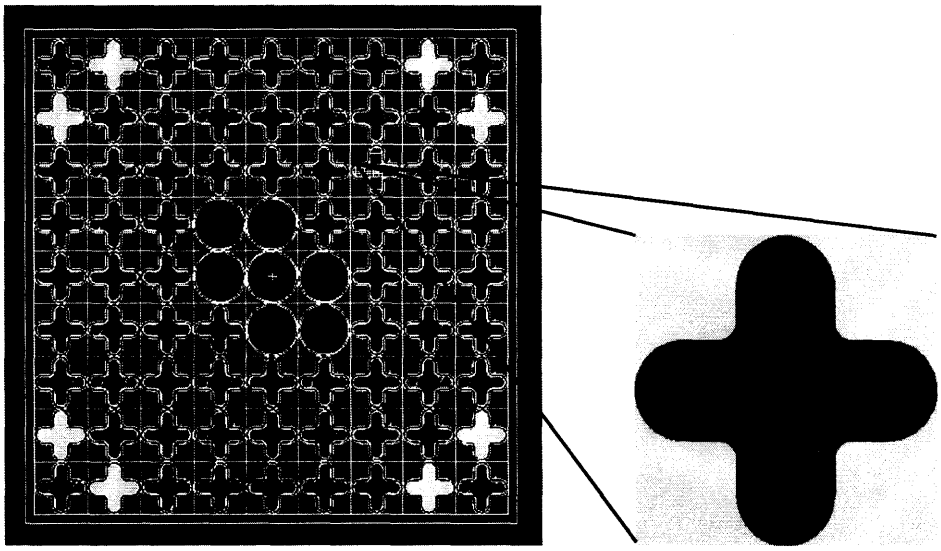

Figure 3.12: A single cell of equivalent H/HM is used to represent the CSS Assembly.

Fission energy density produced in each of the meshed-regions for MCNP input files SP1 and SP2 was to be simulated during MCNP runs of 10,000 neutrons and 120 active cycles, using the conditions and material properties set forth in Table 3.10.

When this was completed for all four models shown below, the energy density tallied in each region of the meshed model would be divided by the energy density found for the whole-pellet (non-meshed) case, allowing one to obtain the peaking factors across this lateral cross-section.

In order to convert these peaking factors into discrete heat loads to be placed into the COSMOS models depicted in Figures 3.8 and 3.9, information regarding the desired linear power must be specified. However, these Corrected-profile studies are designed to be conducted at the same conditions as the non-modified, uniform profile CSS rods for the purposes of conducting relevant comparisons. As a consequence, operating

conditions will the same as those taken in Table 3.9 for the uniform models, meaning that the linear power and outer-clad heat transfer coefficients will likewise be adopted from VIPRE results.

Table 3.10: Operating Conditions defined for MCNP study

	CSS – Spiral Pin 1	**CSS – Spiral Pin 2**
# of initial neutrons	10,000	10,000
# of active cycles	120	120
Fuel material	5% enriched UO_2	5% enriched UO_2
$\rho_{eff,\ water}$ (g/cc)	0.959	0.952
ρ_{UO2} (g/cc)	10.42	10.42
$\rho_{cladding}$ (g/cc)	6.44	6.44
$\rho_{gas\text{-}gap}$ (g/cc)	1.79E-04	1.79E-04

Once this linear power was obtained from VIPRE, it was converted into an average volumetric heat generation across the cross-section of fuel that was of interest. Total power in each meshed piece was found by multiplying this average volumetric heat generation by the lateral peaking factor unique to that piece, and then by its individual volume. It was then verified that the sum of the powers of the meshed piece is equal to what would be expected of the total fuel pellet.

With detailed data for power generation across a cross-section of the fuel imported from MCNP into COSMOS, temperatures and heat flux peaking was to be re-evaluated for comparison to results from the uniform profile; these results are explored in Chapter 4.

4. Computational Results and Analysis

4.1 Core Performance

4.1.1 VIPRE Reference Model

To begin comparative analysis, the reference core VIPRE model (outlined in Chapter 2) was closely examined to ensure that its behavior was similar to accepted BWR performance characteristics. This was done first through diagnostic comparisons with well-defined standards such as the axial distribution in pressure drop, flow quality, void fraction, and characteristic maximum temperatures.

First examined are the parameters that can be obtained from the reference core "average channel" VIPRE results. Modeling a single assembly with the average flow rate and average linear power was assumed to give a good indication of the total core pressure drop, as well as the core-averaged axial void fraction and quality distributions.

The pressure drop found here is passed along to the reference core "hot channel" VIPRE input as a fixed value boundary condition, conveniently allowing for accurate calculation of distributions within the hot channel itself. Important results include axial distribution equilibrium quality and void fraction, and the MCPR of the hot channel. This establishes two important characteristics of the reference core: the hot channel outlet quality, and the Minimum Critical Power Ratio.

4.1.1 (a) Average Channel Results

As shown in Figures 4.1, and 4.2, the reference VIPRE model agrees well with established parameter distributions. Core-averaged outlet quality and void fraction fall at 0.15 and 0.70 respectively. In addition, the core pressure drop reaches 22 psi, also not far off typical core pressure drop according to data provided by GE [15].

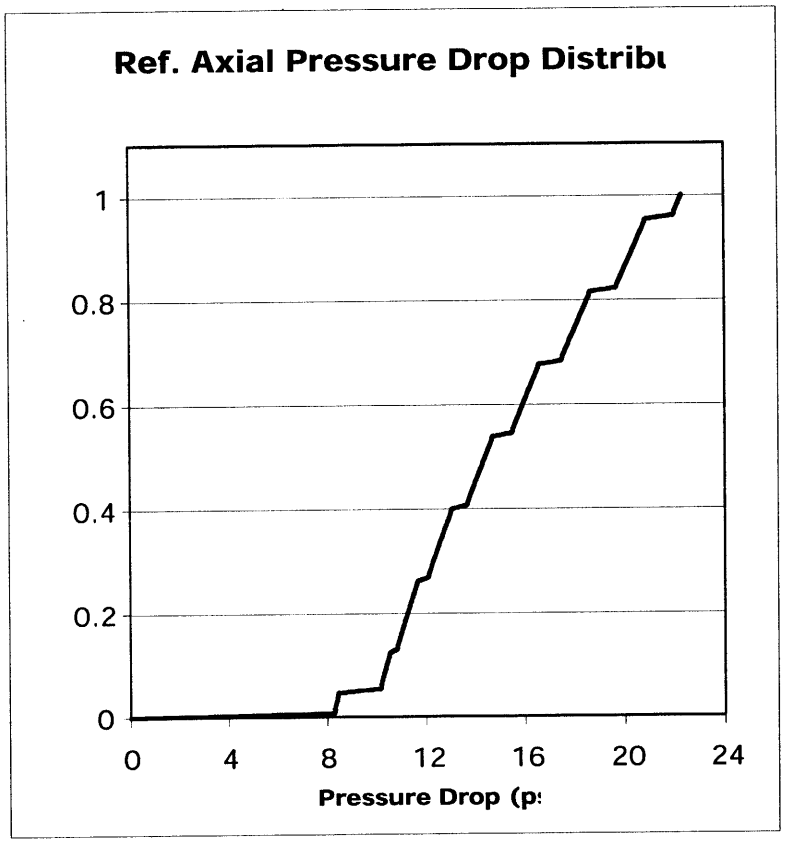

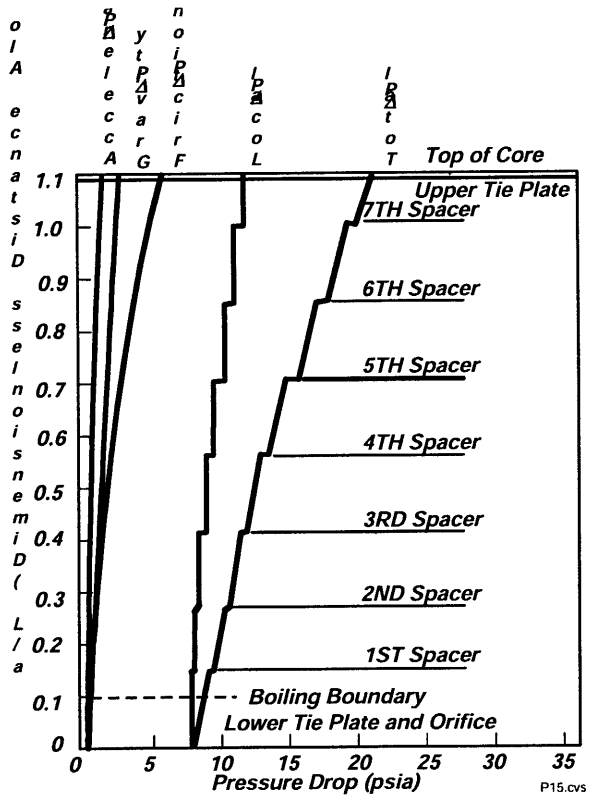

Figure 4.1: Comparison of reference core pressure drop in VIPRE to published results [15].

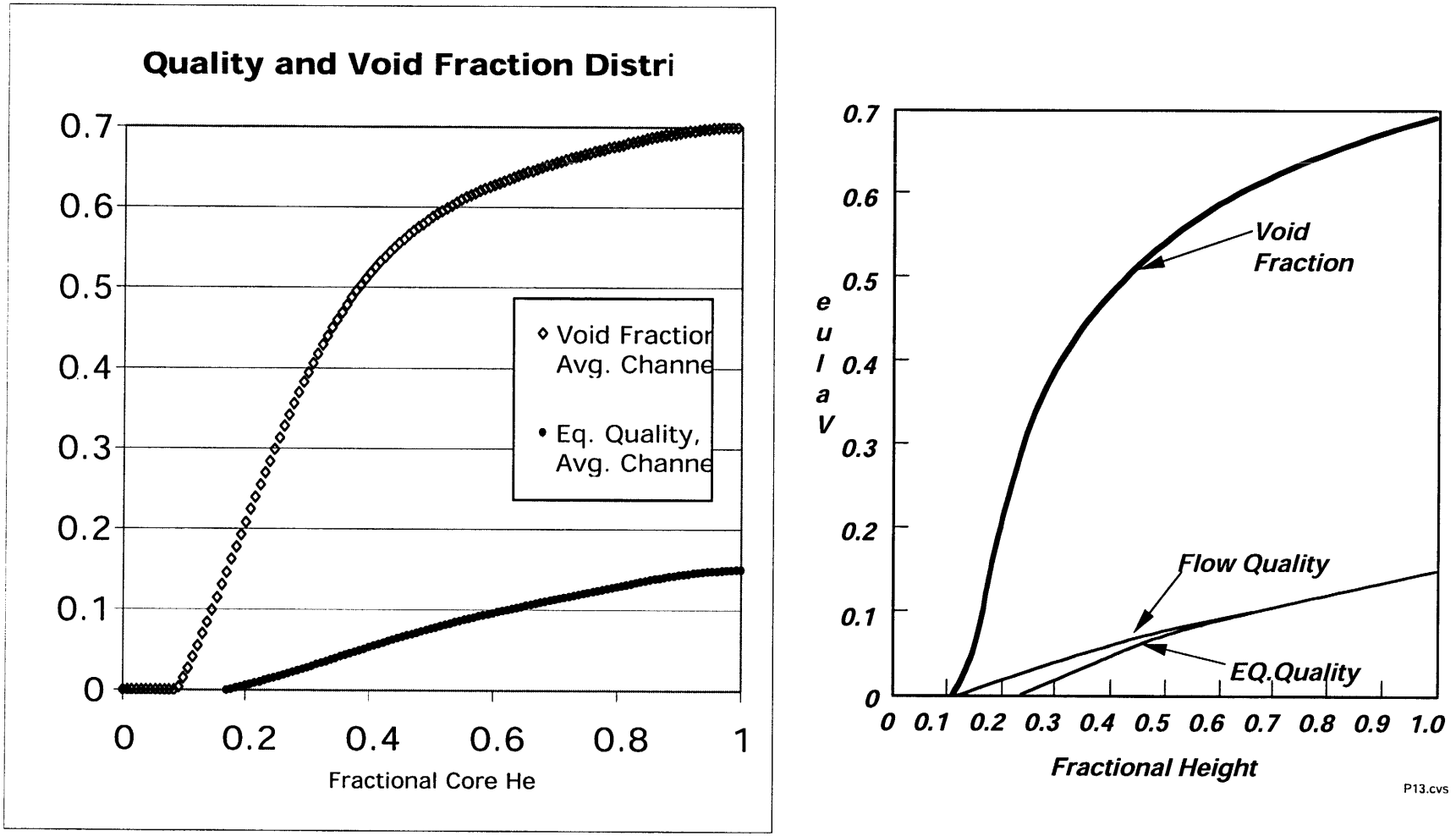

Figure 4.2: Comparison of reference core quality and void fraction in VIPRE to published results [15].

The pressure drop distribution within the channel also seems to follow qualitatively. This indicates that core height, mass flux, and hydraulic loss coefficients have taken on appropriate values, and other dimensions are otherwise reasonably accurate.

4.1.1 (b) Hot Channel Results

The hot channel in the reference core can be summarized by its quality, temperature results, and by the MCPR. First, it is shown that the outlet quality of the hot channel is at 0.245 (Figure 4.3); this is a key result in that it is sure to be maintained in all future comparative analysis. Maintaining a similar quality distribution is critical to ensuring that operation will occur in a flow-regime of well established stability.

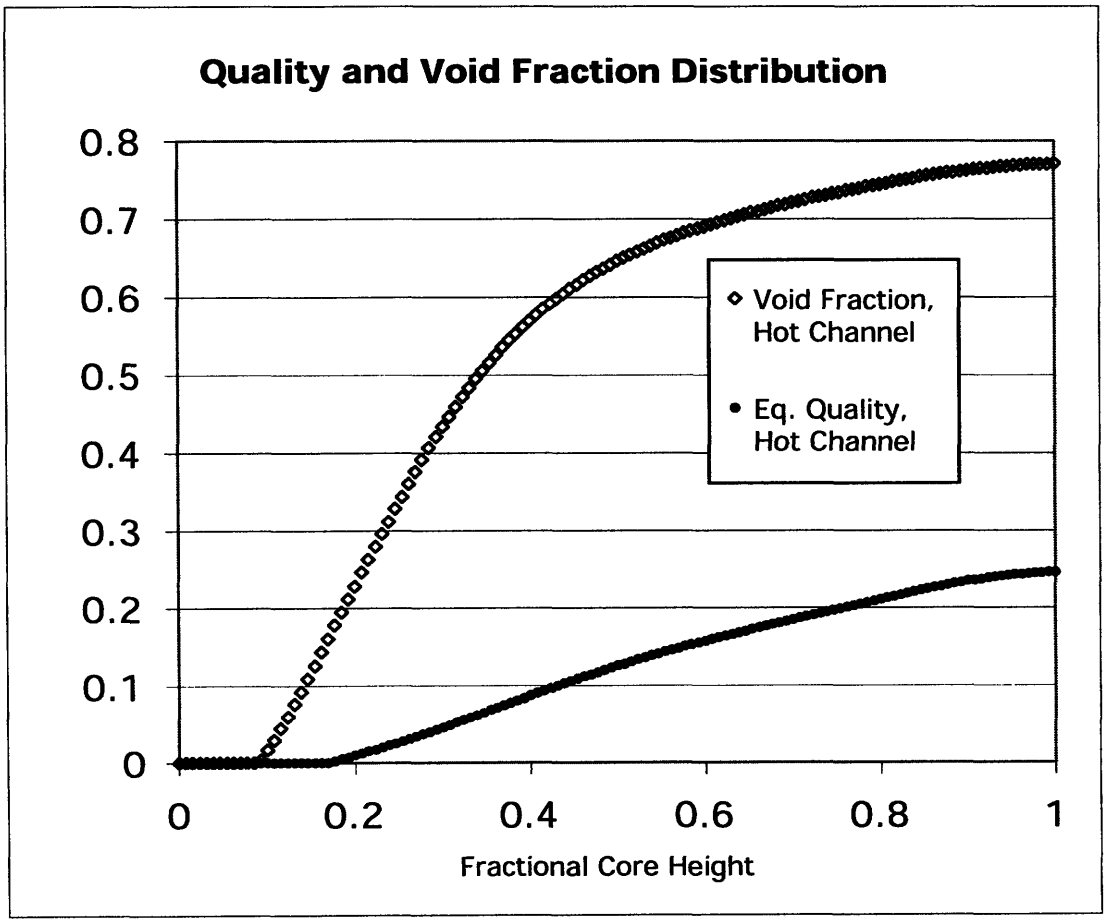

Figure 4.3: Reference hot channel quality and void fraction distributions.

The VIPRE reference hot channel model is a key indicator of performance because it serves to identify the subchannel and axial location within the hot assembly where dryout will occur first. Monitoring the margin to critical heat flux at this location, as well as the maximum temperatures experienced by the nuclear fuel rods adjacent to this limiting subchannel, is clearly one of the main aspects of this analysis.

Applying the core pressure drop shown in Figure 4.1, the reference hot channel MCPR was evaluated as described in Chapter 3. According to the VIPRE reference model output, critical quality was most nearly reached along Rod #64, in a central channel located near the fuel rod with the largest peaking factor. At this location, the heat transfer coefficient found by VIPRE according to the Chen correlation is calculated to be 54,170 W/m^2K, and the bulk coolant temperature is equal to T_{sat} = 288°C. The pin radial peaking factor and axial peaking factor are both multiplied to the nominal linear power provided to VIPRE, giving a linear heat rate of 26 kW/m.

Table 4.1: Conditions at Limiting Location

q' = 26 kW/m
T_{co} = 288°C
h_{co} = 54.2 kW/m^2K

These values are highlighted and shown in the table due to their importance for use in the heat conduction study, more fully described in Chapter 4.2.

For further diagnostic purposes, the rod adjacent to this limiting subchannel was examined in further detail, including detailed evaluation of the axial distribution in bulk temperature, outer cladding temperature, and maximum fuel temperature. Shown in Figures 4.4 and 4.5, the cladding temperature maxes out at 592°F and the fuel is predicted to reach a maximum near 2500°F. These are well below the limits placed on cladding and fuel materials during regular operation. Variation in the heat transfer coefficent is also shown (Figure 4.6).

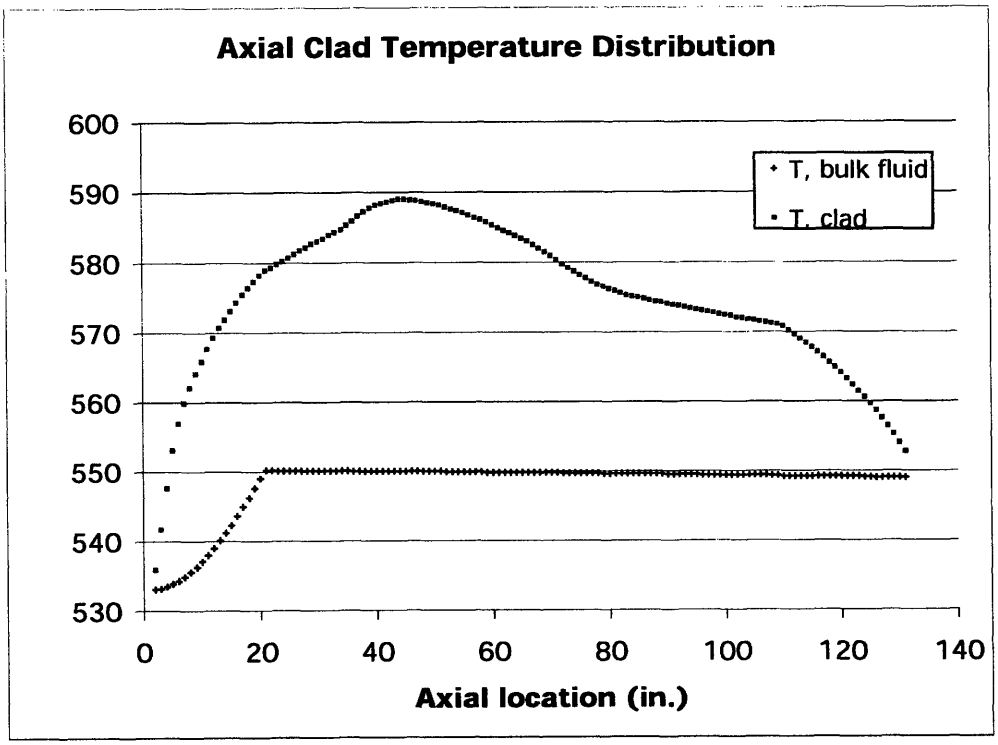

Figure 4.4: Axial distribution in clad and bulk coolant temperature.

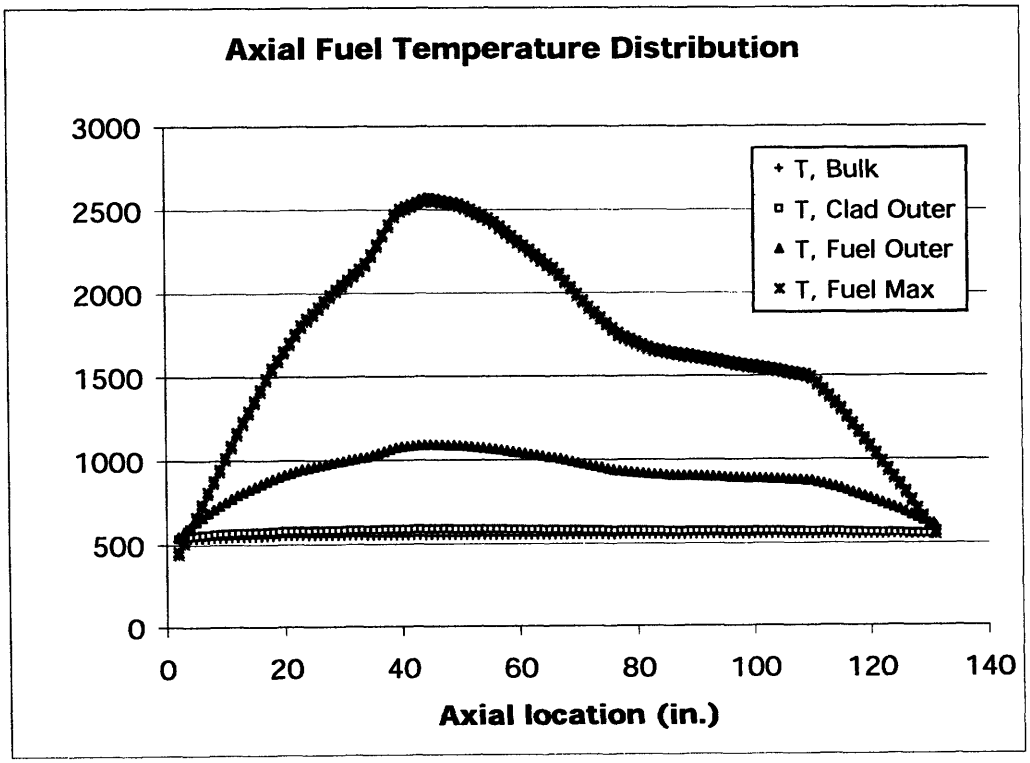

Figure 4.5: Axial distribution in fuel temperature.

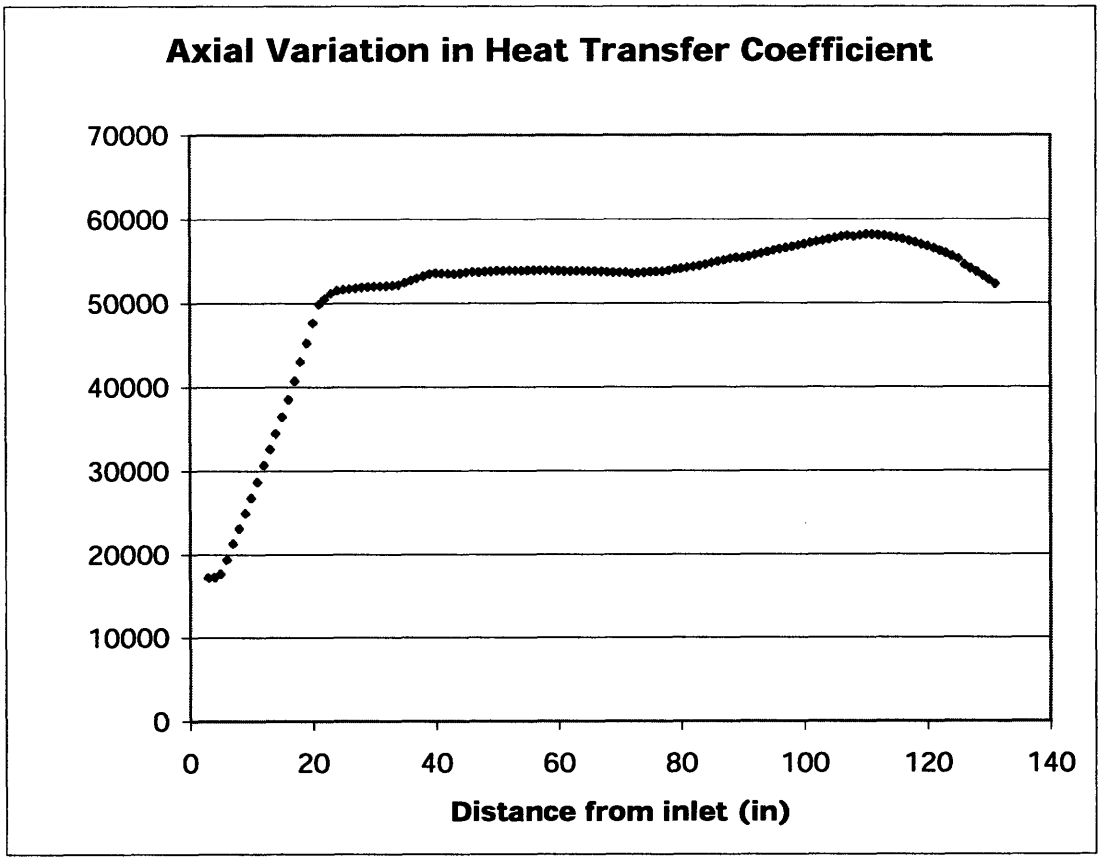

Figure 4.6: Axial distribution outer-cladding heat transfer coefficient.

For the given conditions, the Hench-Gillis critical quality correlation described in Chapter 3 predicts an MCPR of 1.142 for the reference input. This is further illustrated in Figure 4.7, which compare the critical quality predicted using Hench-Gillis at nominal power to the actual operating quality at nominal power. Figure 4.8 compares the critical quality (Hench-Gillis) at 114.2% power to the distribution of quality that would result from power increase to 114.2% (without adjusting mass flow rate). Note also that the two curves for critical quality differ – this is due to the fact that Hench-Gillis defines critical quality as a function of boiling length; boiling length is a value that increases as linear power is uniformly increased and saturation is more quickly reached.

Since the two curves of the latter figure approximately intersect, it can be said that 114.2% of full power represents the critical power, or CPR = 1.142. Since this

calculation has been performed at the most limiting condition, this CPR is necessarily the MCPR.

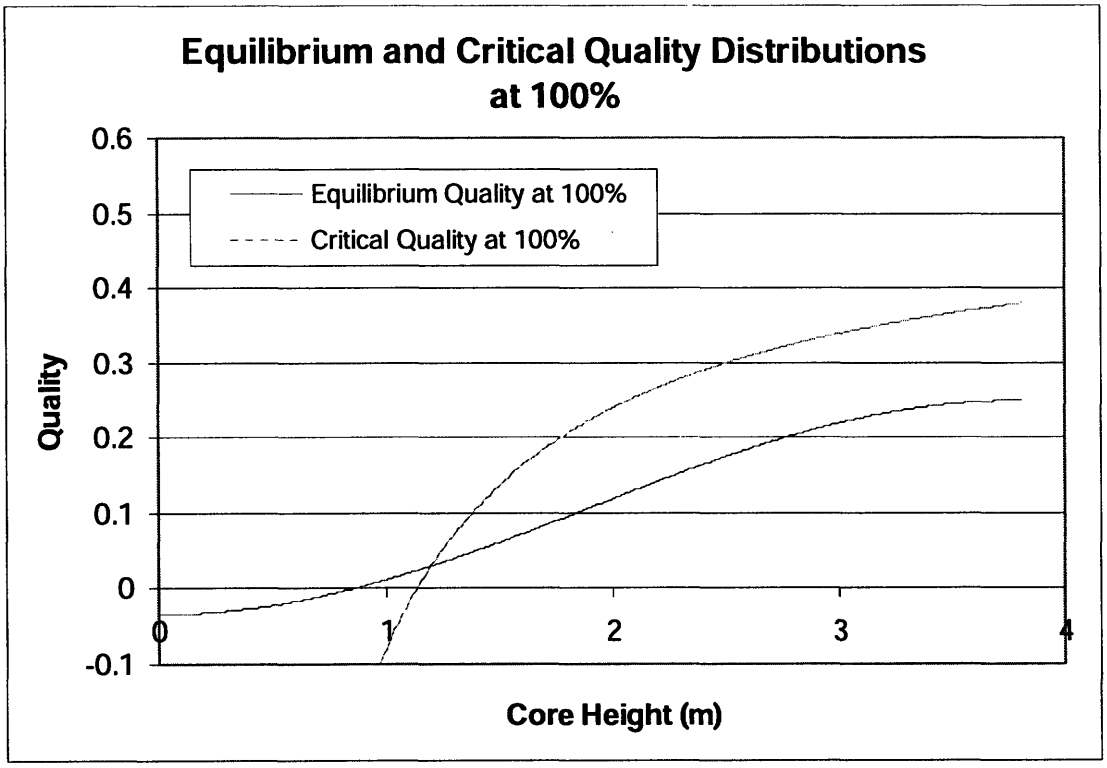

Figure 4.7: Critical quality in hot subchannel vs. equilibrium quality at nominal power.

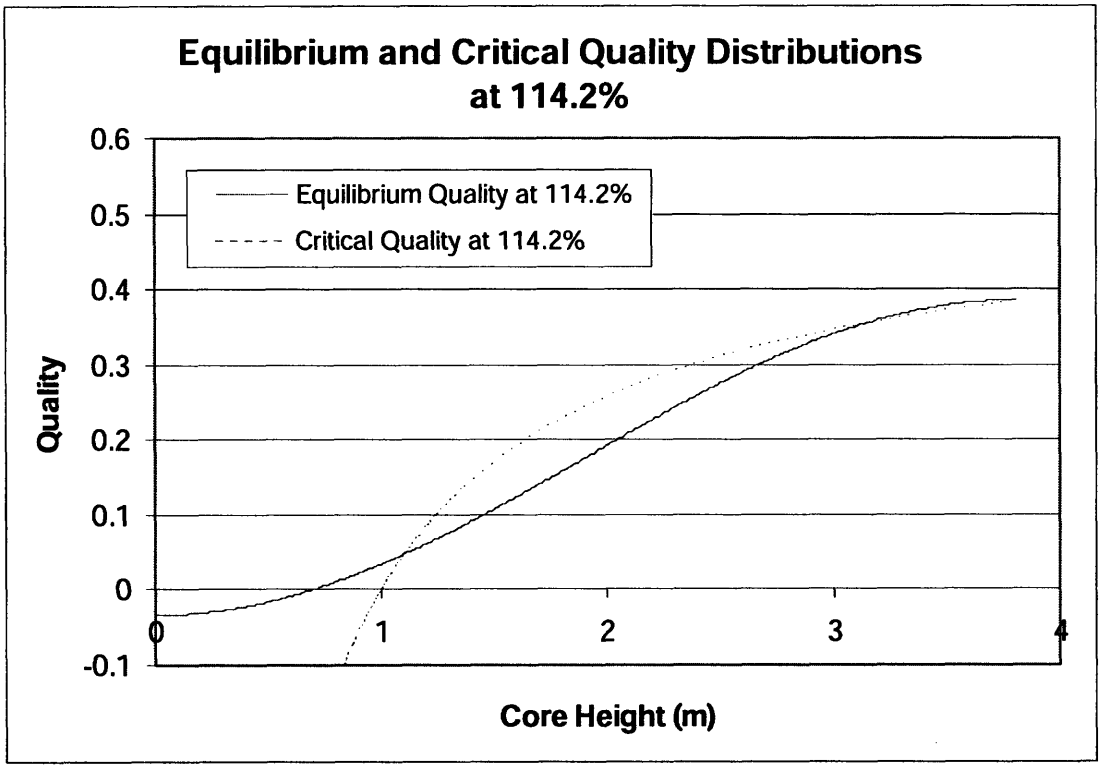

Figure 4.8: Critical quality matches equilibrium quality at 114% of nominal power.

In any case, establishment of this reference case gives a value for MCPR that can be directly compared with MCPR found for the CSS assemblies. The CSS models with an MCPR greater than 1.142 can be assumed to possess a margin for a power density increase, and the potential for core power uprate will be assessed according to the procedure set out in Chapter 3.

4.1.2 CSS Spiral Pin 1 Assembly

As with the reference fuel geometry, analysis for the CSS SP1 core began with the evaluation of the average channel assembly model. This model provided information about the axial distribution of quality, as well as the core pressure drop to be imposed on the hot channel CSS SP1 input file. As with the reference case, the hot channel model was then used to find the core MCPR.

4.1.2 (a) Average Channel Results

A quick look at Figure 4.9 reveals that the quality and void fraction distribution are very similar if not identical to that of the average channel. Of course, this is by design; two core designs with the same mass flow and total power, as well as the same axial power profile should result in the same distribution of these parameters. Still it is worth confirming in this case that the unusual geometry provided to VIPRE for this model does not distort the calculation.

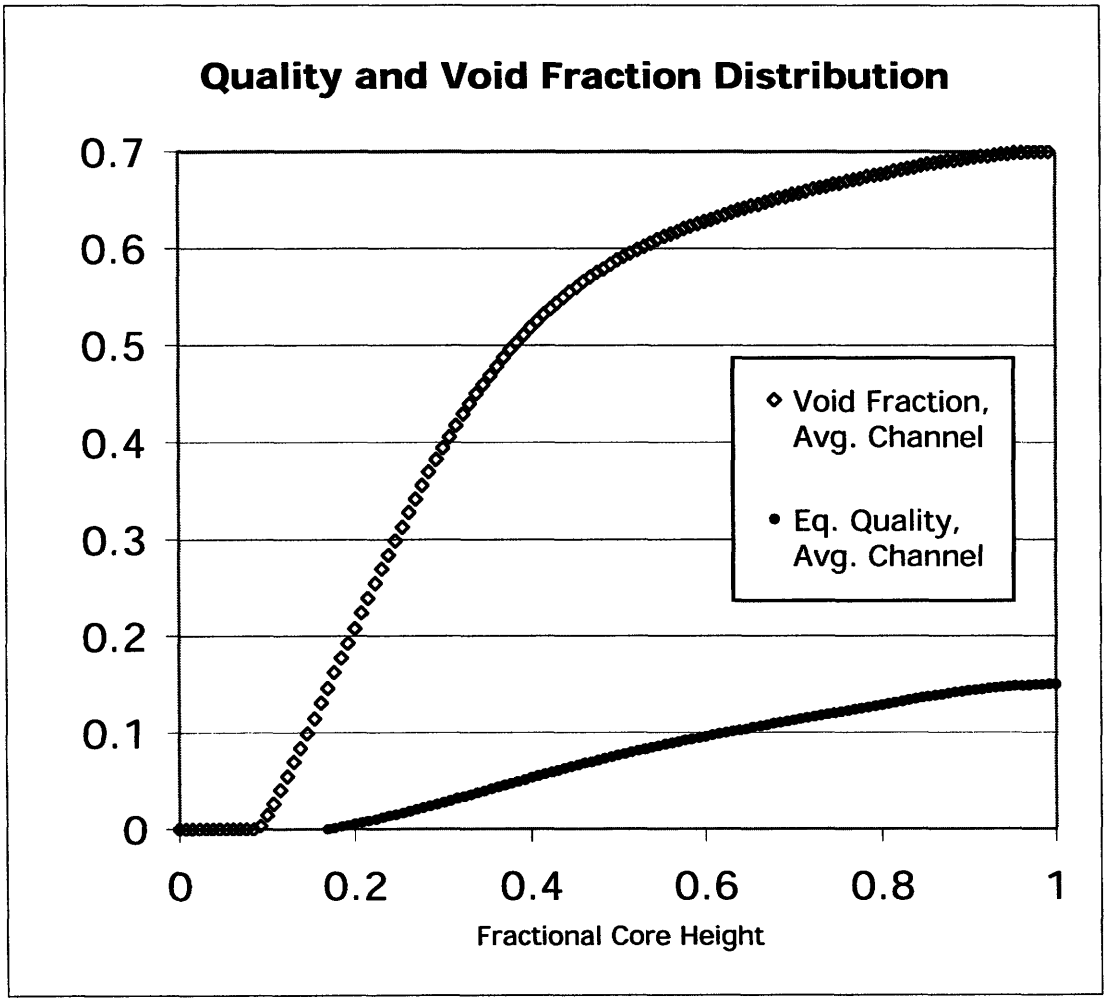

Figure 4.9: Quality,Void Fraction distribution for the SP1 average assembly.

The first major difference between the reference case and the CSS design can be seen in examining the distribution of pressures losses axially (Figure 4.10). Instead of a distribution with step losses at the location of each grid spacer, the CSS model shows an almost linear rate of loss, which slowly shifts towards a larger hydraulic loss rate as the two-phase quality increases.

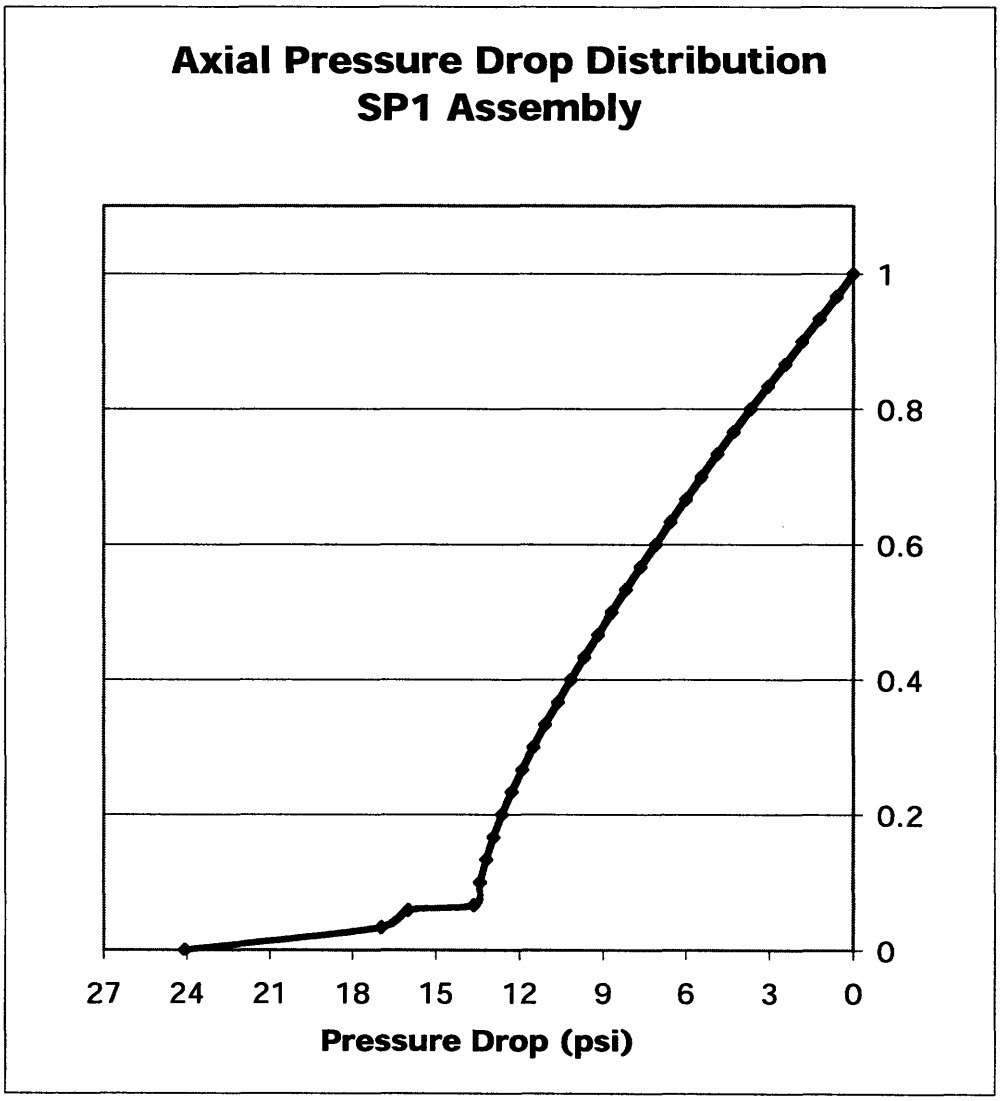

Figure 4.10: Core pressure drop distribution for CSS – SP1 VIPRE model.

4.1.2 (b) Hot Channel Results

Adapting the pressure drop shown in Figure 4.10 to the hot channel model gives qualities and void fractions that match up well with the reference model, as required by a basic heat balance (Figure 4.11). Again, this mainly serves to confirm that the CSS geometry is being correctly grasped by VIPRE as intended. This step should prove unnecessary for the CSS SP2 model.

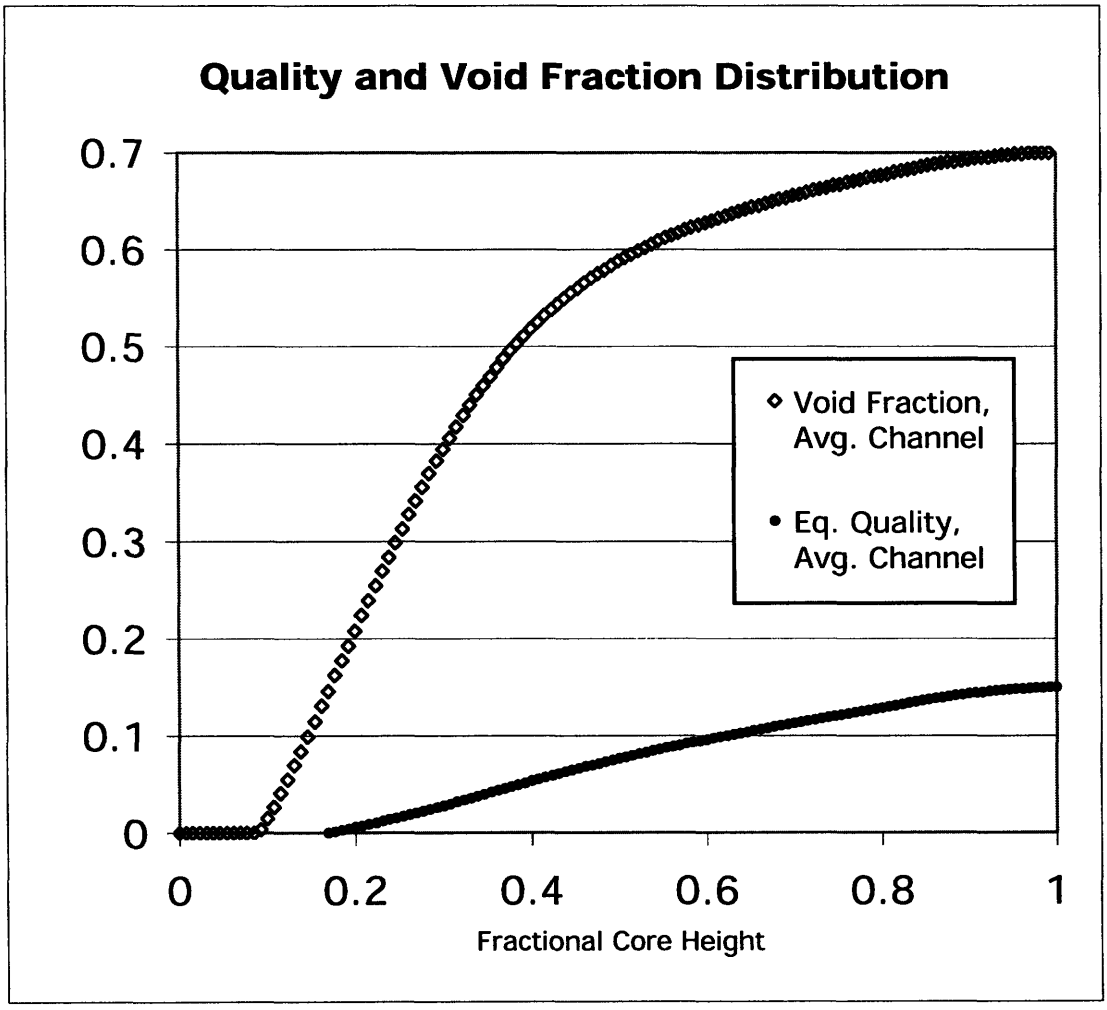

Figure 4.11: Quality and Void Fraction distribution for the CSS – SP1 hot channel.

The hot channel VIPRE results for CSS SP1 predicts CHF to occur at channel 53, an interior channel near one of the rods with the highest peaking factors. In this subchannel, VIPRE predicts an MCPR of 1.299 at nominal operating conditions.

In comparison to the reference MCPR of 1.142, this indicates significant potential for power uprate. The iterative process of determining the potential for power uprate was conducted, with results summarized in Table 4.2 below. Pressure Drops shown here are found by returning to the average assembly input file, increasing power and mass flow proportionally; taking this value and fixing it to the hot channel input file, and applying it to the same case in terms of percentage power uprate.

As described in Chapter 3, CSS pressure drops are modeled by using a friction correlation intended for use with cylindrical rod bundles, with the appropriate CSS hydraulic diameter, and without grid spacer losses. MCPR is calculated using Hench-Gillis, with an equivalent diameter to account for the increase in surface area.

Table 4.2: Effect of Power Uprate on T-H parameters

% Power increase, SP1	MCPR (H-G)	Pressure Drop (psi)
--	1.299	24.1
20	1.150	29.5
21	***1.143***	***30.0***
22	1.137	30.4

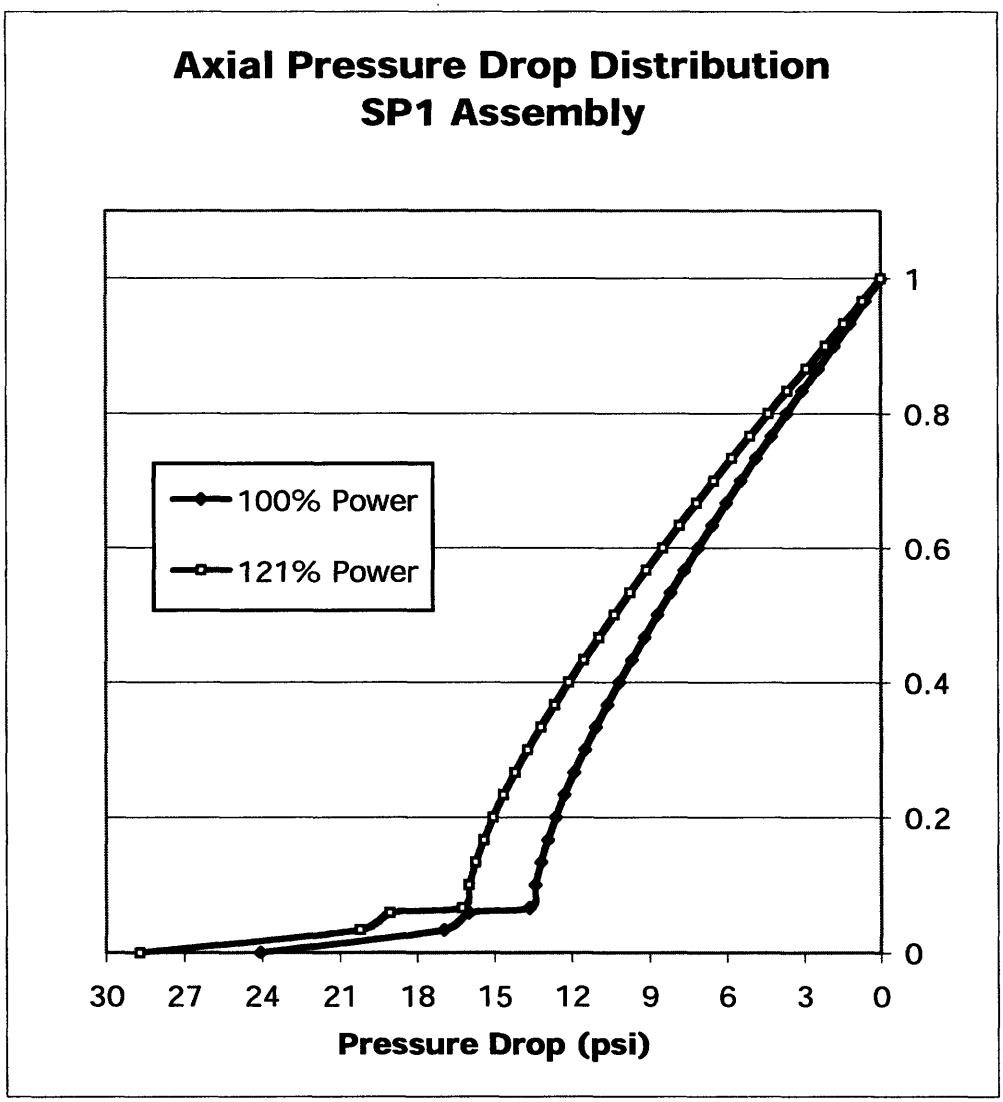

Figure 4.12: Comparison of pressure drop at nominal and uprated conditions, CSS –SP1.

These results show that the CSS – SP1 core can endure a 21% increase in power density before reaching the MCPR of the reference case. However, at this increase in power, the required mass flow results in velocities high enough that the pressure drop is increased to 30.0 psi (Figure 4.12). The pressure drop, which varies with the square of velocity, is highly sensitive to increases in mass flow. It should also be noted that the pressure drops are found using correlations for smooth cylindrical rods with equivalent hydraulic diameter; this is evaluated experimentally later.

4.1.3 CSS Spiral Pin 2 Assembly

4.1.3 (a) Average Channel Results

Analysis of the CSS SP2 fuelled-core closely mirrors that which was performed for the case of SP1. Maintaining assembly power and mass flow rate ensures the same distribution in quality axially as the average assembly for the reference case.

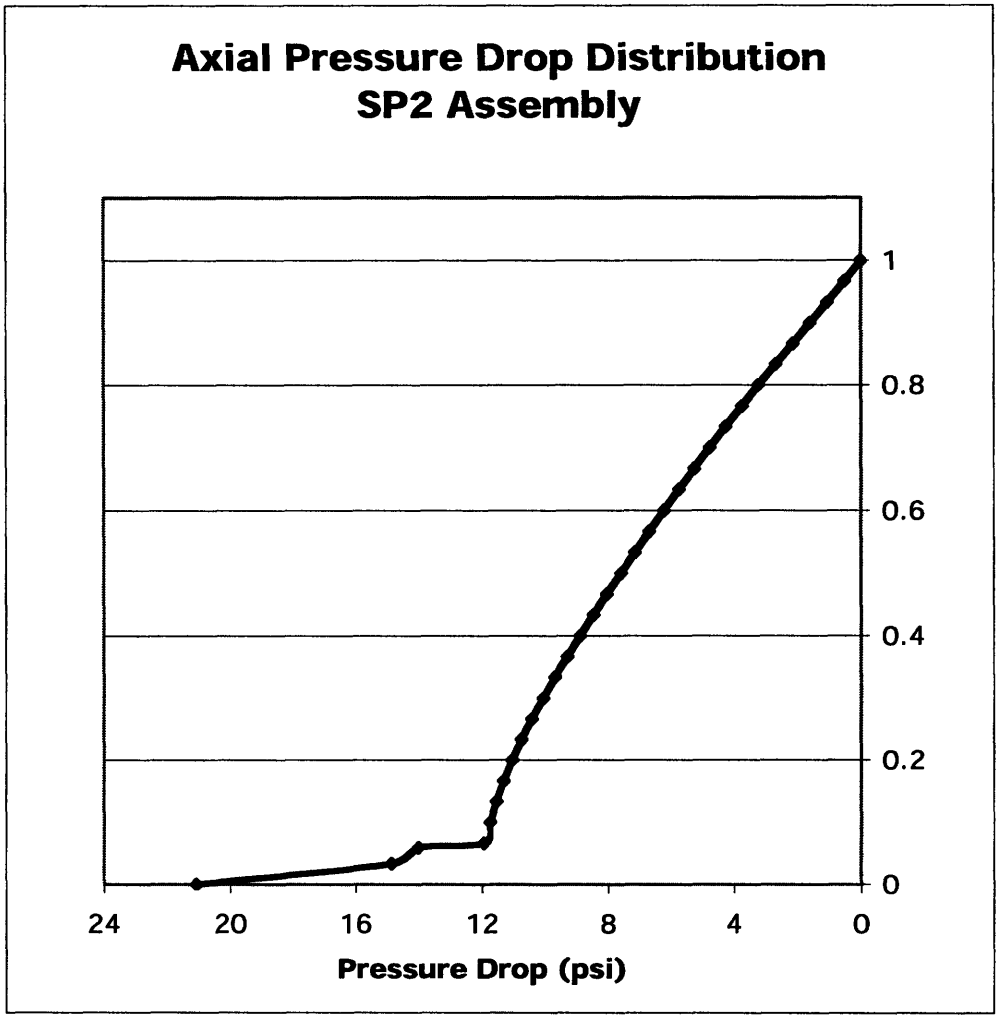

Figure 4.13: Core pressure drop distribution for CSS – SP2 VIPRE Avg. Assembly.

The distribution in hydraulic loss also closely resembles that for SP1. Lacking grid spacers, the distribution is continuous along the core height, and has a rate increasing as

quality rises within the core. However, with a slightly larger hydraulic diameter, the total pressure loss is not quite as large, maxing out at 21.7 psi, as compared with 24 psi for SP1 (Figure 4.13).

4.1.3 (b) Hot Channel Results

The hot channel VIPRE input file for CSS SP2 again predicts that CHF occurs at channel 53, an interior channel near one of the rods with the highest peaking factors. In this subchannel, VIPRE predicts an MCPR of 1.328 at nominal operating conditions. Evaluating the potential for core uprate as before, the CSS SP2 core is estimated to have margin for a 25% increase in core power (Table 4.3). Accounting for this increase in power, the resultant core pressure drop jumps above 28 psi (Figure 4.14).

Table 4.3: Effect of Power Uprate on T-H parameters

% Power increase, SP2	CPR (H-G)	Pressure Drop (psi) (*)
--	1.328	21.7
20	1.177	26.5
25	***1.145***	***28.7***
26	1.138	29.2

*P_{drop} assumes cylindrical rod bundle of equivalent D_h, with no spacers

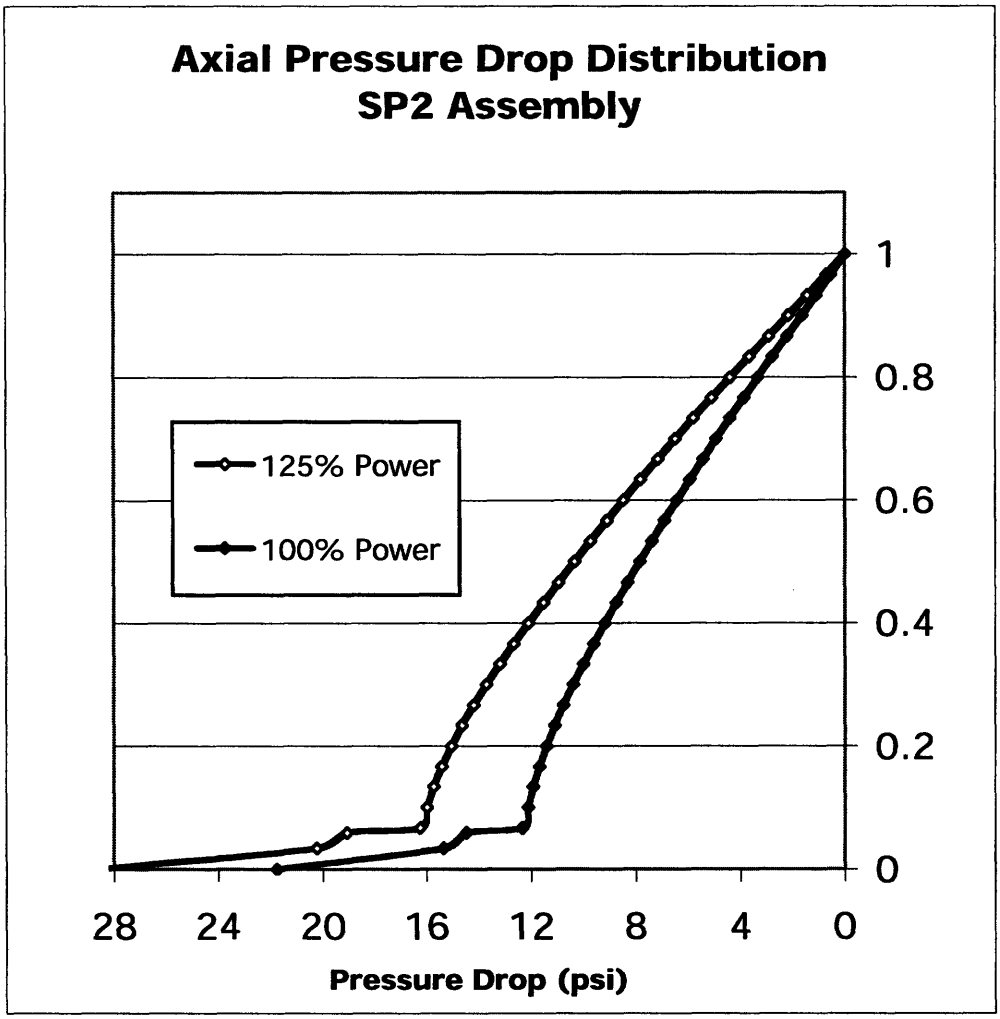

Figure 4.14: Comparison of pressure drop at nominal and uprate conditions, CSS – SP2.

4.1.4 Summary

Results detailed in Sections 4.1.1-3 are summarized in Table 4.4:

Table 4.4: First-order VIPRE Results for CSS SP1 and SP2

	MCPR (Hench-Gillis)	ΔP_{core} (psi)	% Uprate	ΔP_{core} (psi) After Uprate
Reference	1.142	22.3	--	22.3
SP1	1.299	24.1*	21	30.4*
SP2	1.328	21.7*	25	28.7*

*P_{drop} assumes cylindrical rod bundle of equivalent D_h, with no spacers

It's interesting to note here that, though SP1 has a larger surface area and consequently a lower surface-averaged heat-flux, the SP2 model allows for a larger uprate, and does so at a lower core pressure drop. This is due to the larger mass flux experienced in the SP1 core, as a result of its smaller flow area.

Examining the dominant terms of the Hench-Gillis Equation (Eqn. 3.2), it is no surprise that the critical quality decreases with mass flux. After all, nearly all terms vary inversely with G to some positive exponent. This is perhaps largely due to a more subtle flow effect on the liquid film at the fuel rod surface.

During annular flow, the thin circumferential flow is subject to constant attack, owing to entrainment of droplets by a highly dispersed vapor core. Of course, at times the vapor core is also a source of droplets, which deposit within the film to supplement the liquid layer. The existence of annular flow therefore depends on a delicate and often unstable balance between these mechanisms (as well as film evaporation, which will be temporarily neglected).

Both of these mechanisms can be expected to increase in intensity with an increase in coolant mass flux. However, experimental correlations show that the rate of entrainment of droplets from a given annular film (by turbulent wave undercut) is more sensitive to an increase in mass flux, increasing with $G^{1.632}$, whereas the rate of droplet deposition only increases with $\sim G^{0.8}$ [16]. Therefore dryout of annular flow occurs more readily in channels of higher mass flux, assuming all other parameters are fixed.

In this case, the SP2 core model must also overcome a larger surface-averaged heat flux to defeat the SP1 in terms of MCPR. This suggests that the MCPR is much more sensitive to increases in mass flux than surface heat flux. In fact, it is well-known that dryout is not heavily dependent on local heat-flux, but instead correlates better to total heat input, which does not reflect differences among the fuel assemblies for any given power level. That being said, clearly some advantage is gained by lowering average surface heat flux by a large margin (~35-40%), which explains why both SP1 and SP2 represent improvements over the reference case.

First order VIPRE modeling shows SP2 to be a superior design in terms of two major core performance indicators: MCPR and core pressure drop. Still, questions remain regarding the temperature and heat flux distributions; these are resolved in Section 4.2.

4.2 Heat Conduction Analysis

The validity of COSMOS modeling was established in (Chapter 3) by solving analytically for the maximum fuel temperature at a plane of a cylindrical fuel rod with uniform heat generation, and comparing the results to those of COSMOS. With this procedure accepted, the simplifying assumptions taken for analytical comparison were relaxed to create more accurate models, first by introducing temperature dependent thermal properties, then by accounting for non-uniformity in the lateral power profile. Predictions of temperature and heat flux distribution were obtained from the COSMOS model at the most limiting thermal location predicted by VIPRE under nominal operating conditions. Finally, the case of maximum central temperature given a 25% core power uprate was also explored.

4.2.1 Uniform Lateral Power Profile

4.2.1 (a) Reference

To provide a reference case, the cylindrical rod model was evaluated first. This COSMOS model was supplied with the operating conditions first given in Table 3.9, and the limiting location found using VIPRE models in Table 4.1, these are combined into Table 4.5 shown here. Significant results are given in Figure 4.15, and Table 4.6.

Table 4.5: Thermal Study Input Parameters

Linear Heat Rate	q' = 26 kW/m
Coolant-Outer-Cladding heat transfer coefficient	h_{co} = 54170 W/m^2-K
Fuel-Cladding Gap heat-transfer coefficient	h_g = 8 kW/m^2-K
Cladding Conductivity	Temperature Dependent
Fuel Conductivity	Temperature Dependent
Bulk Coolant Temperature	T_{bulk} = 288°C

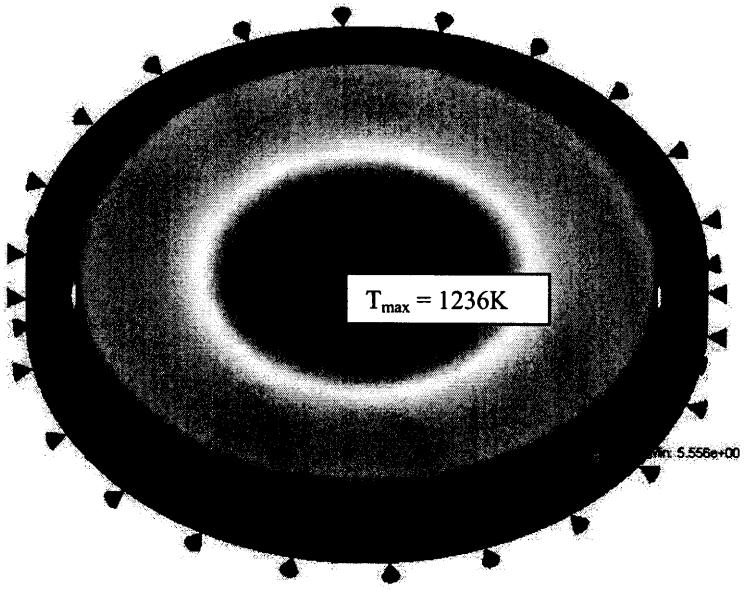

Figure 4.15: Temperature Distribution of the Reference Fuel, uniform heat generation.

Shown in Figure 4.15, the cylindrical fuel gave a maximum temperature of 1236 K. This value is noticeably higher than the temperature shown in Chapter 3, which used a constant thermal conductivity of 3.9 W/m-K, and resulted in a maximum fuel temperature of 1170K. However, the surface heat-flux value of q" = 0.89 MW/m^2 has not changed, as expected.

4.2.1 (b) Spiral Pin 1

The SP1 geometry was also evaluated under the conditions shown in Table 4.5. Parameters such as maximum linear power, heat transfer coefficient, and bulk temperature were taken at the limiting location of the reference VIPRE results. Though it is possible to calculate new parameters based on the limiting location of the SP1 VIPRE results, maintaining these values constant from one study to another ensures a more consistent comparison from one rod geometry to another.

In any case, it can be shown that the convection resistance between the bulk coolant and the outer surface of the cladding is insignificant compared to the conduction resistance within the fuel pellet itself, so this has little effect on the maximum temperature.

Key results from the SP1 study can be seen below in Figures 4.16 and 4.17, as well as in Table 4.6.

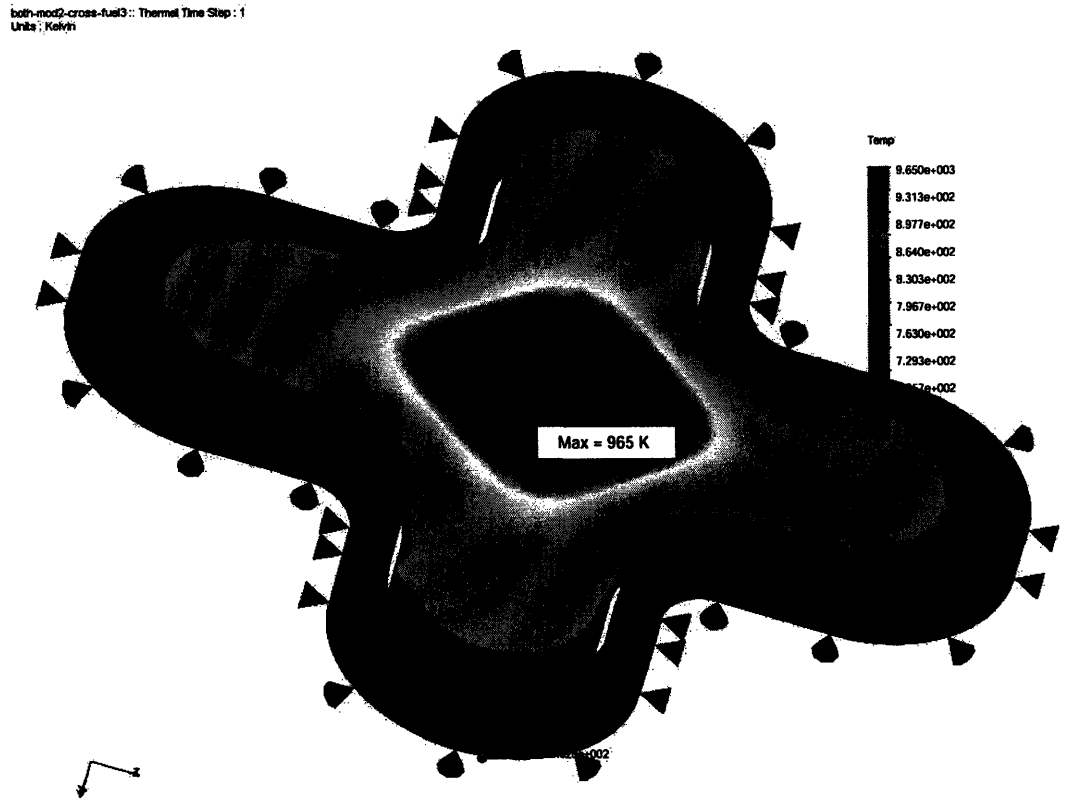

Figure 4.16: Temperature Distribution of the SP1 Design, uniform heat generation.

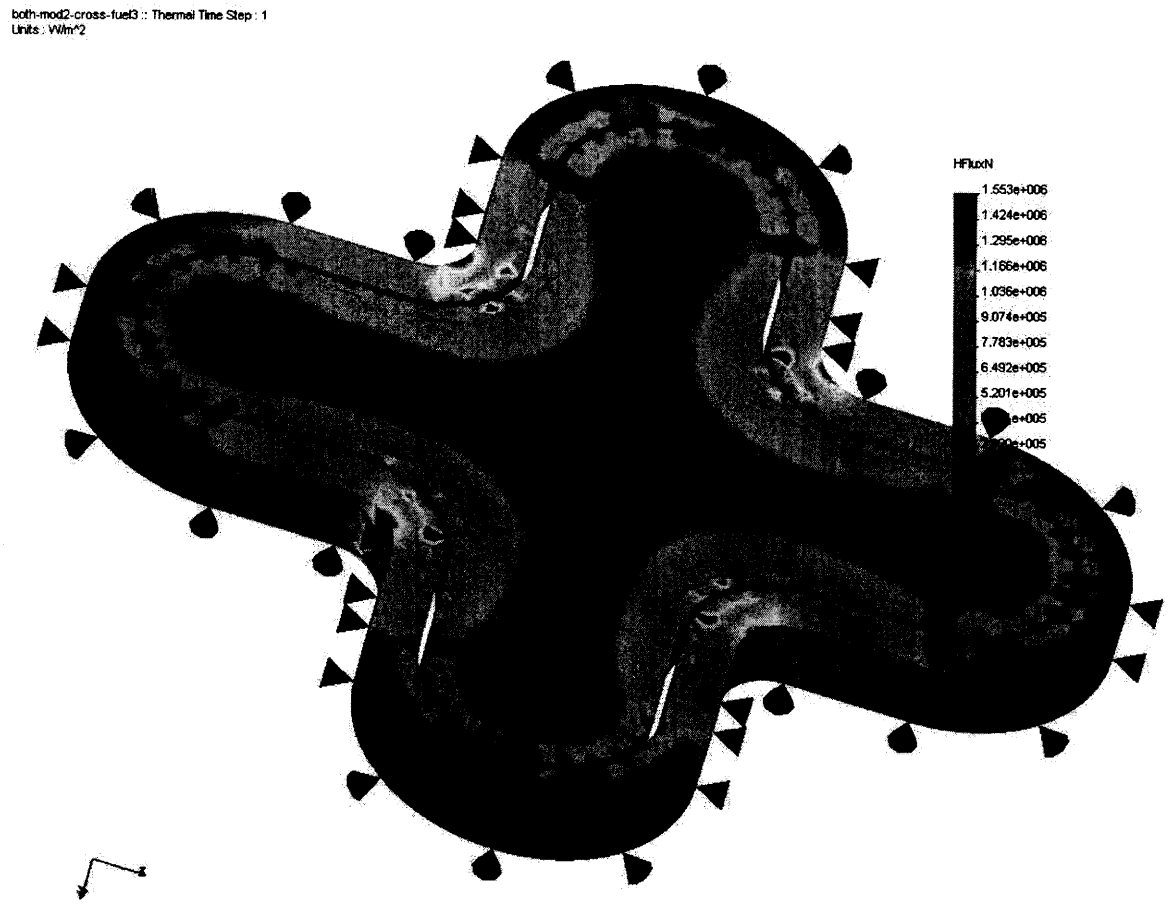

Figure 4.17: Heat Flux Distribution of the SP1 Design, uniform heat generation.

With respect to maximum temperature, SP1 fares well in comparison to the reference case, giving a reduction of 271 degrees K to 955 K under the same linear power. However, heat-flux is another story. Unlike the circumferentially-symmetric cylindrical rod, the cross-shape seen here gives rise to four prominent hot-spots at the cross-sectional "elbow" regions at the base of each fuel petal. Due to the low thermal conductivity of UO_2, heat overwhelmingly flows along the path of least resistance through these elbows, in favor of the out-stretched lobes which remain relatively cool. Though the larger wetted-surface gives way to a reduction in surface-averaged heat-flux, the maximum heat flux in these peaked regions (on the order of 1.53 MW/m^2) dwarves the heat-flux experienced by the cylindrical rod by a factor of 1.7.

This result was not wholly unexpected – in fact this concern was initially cited as the reason for the parallel investigation of the SP2 design. Still, it is not known whether or not the extent of peaking seen here can be considered excessive. Certainly the spike shown in Figure 4.18 is a cause for concern. This is further explored in a review of literature presented at the conclusion of this chapter.

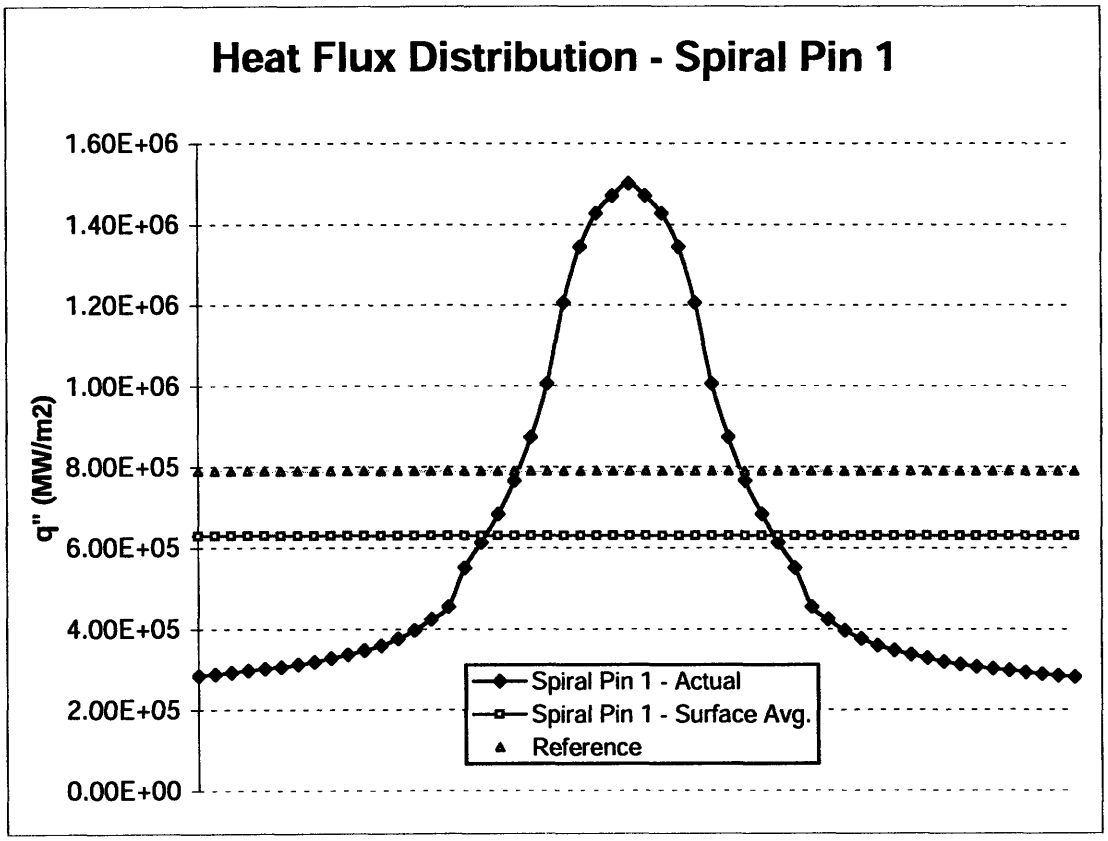

Figure 4.18: Surface Heat Flux at the problem "elbow" region of SP1.

4.2.1 (c) Spiral Pin 2

Similarly, the next CSS design – SP2, was tested in COSMOS under the conditions given in Table 4.5, with results shown in Figures 4.19 and 4.20. The increase in radius of curvature at the fuel elbow has resulted in a thicker central region in comparison to SP1, causing a 53 degree K increase in the central temperature to 1008 K. The moderate decrease in cooling surface area also contributes to this effect.

More importantly, the larger radius is a success in its intended effect -- to reduce heat-flux peaking. The increase in radius of curvature from 0.08 cm (for SP1) to 0.21 cm reduces the maximum surface heat flux to a more tolerable 1.24 MW/m^2, spreading and diminishing the peak predicted by the SP1 design (Figure 4.18).

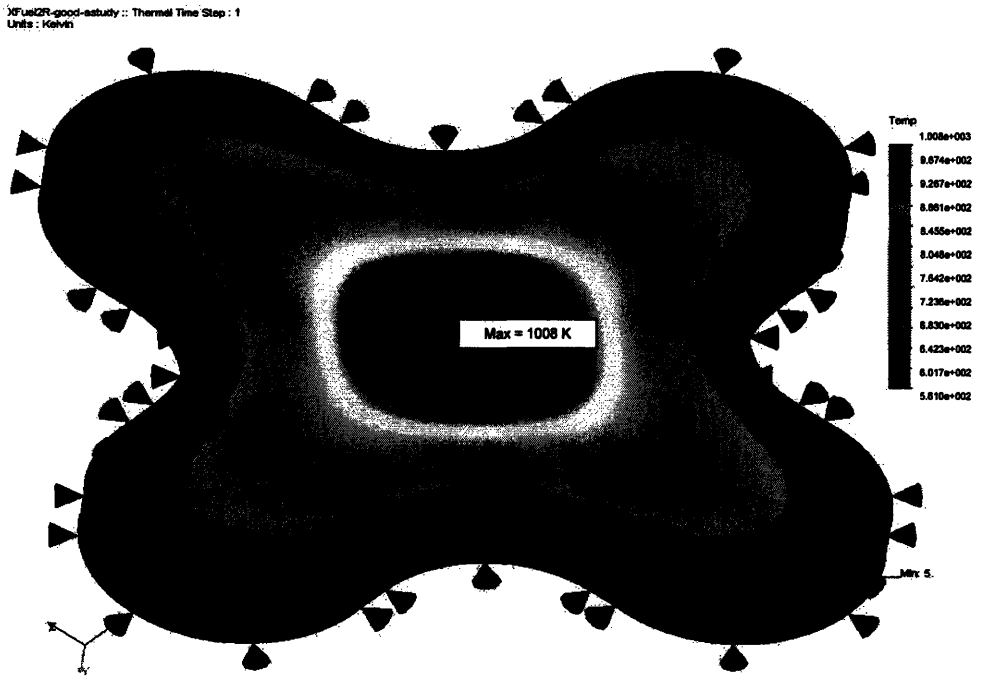

Figure 4.19: Temperature Distribution of the SP1 Design, uniform heat generation.

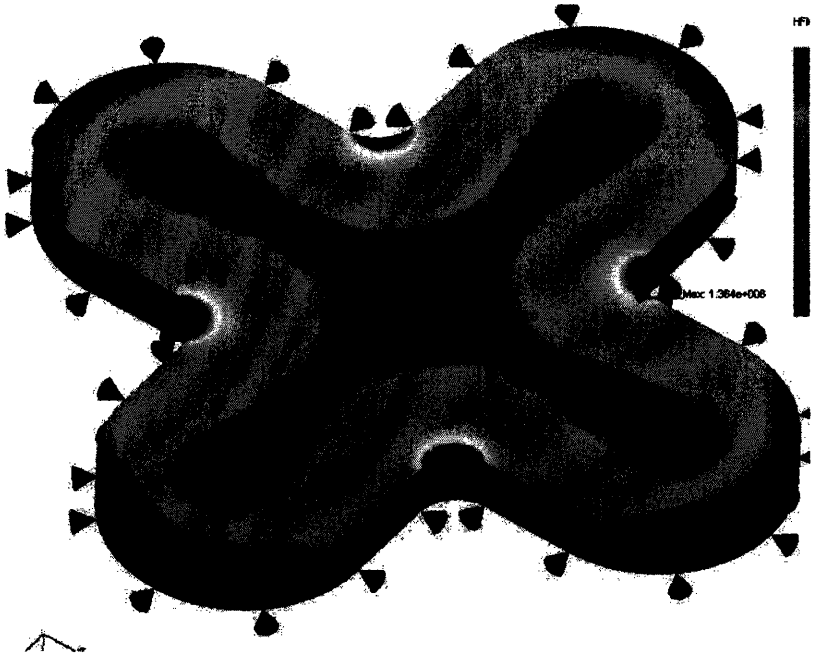

Figure 4.20: Heat Flux Distribution of the SP2 Design, uniform heat generation.

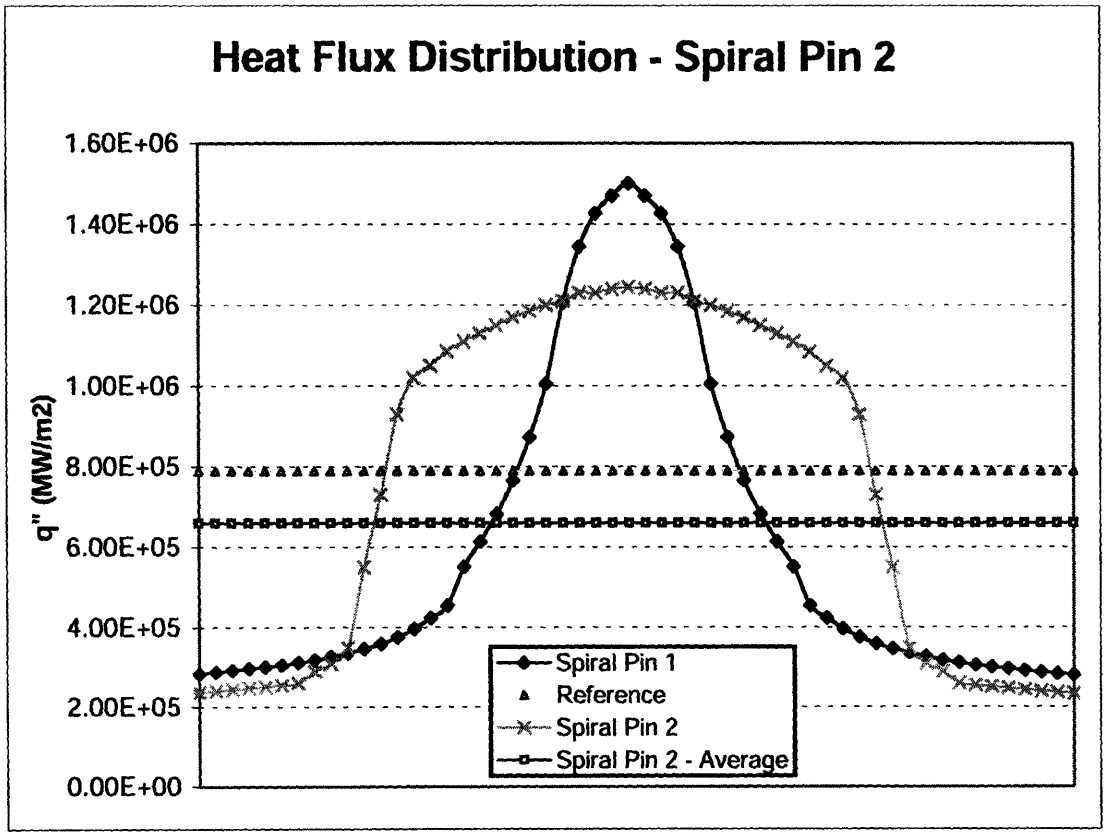

Figure 4.21: Surface Heat Flux at the problem "elbow" region of SP2.

4.2.1 (d) Summary

The insights gained from this study can be summarized in Table 4.6. Both CSS pins provide a significant reduction in central temperature at the expense of a circumferentially uniform surface heat-flux. Spiral Pin 2 fares better than SP1 in terms of maximum peaking, with a peak-to-average value of 1.88 compared to 2.42. However, a larger portion (28%) of the surface becomes elevated significantly above the average surface heat-flux.

Table 4.6: Summary of COSMOS Results for CSS SP1 and SP2

Pin	Surface area increase	Max fuel Temp. (K)	"Elbow" radius of curvature (cm)	Max surface q" (MW/m^2)	Avg surface q"	Peak-to-average	% of surface > Avg
Reference	--	1236	--	0.89	0.89	1.00	--
SP1	+40%	956	0.08 cm	1.53	0.63	2.42	10%
SP2	+35%	1008	0.21 cm	1.24	0.66	1.88	28%

4.2.2 Corrected Lateral Power Profile

For simplicity, the simulations described to this point were performed under the assumption of uniform power generation within the fuel pellet. Though adequate for a first order approximation, this is not actually the case. Even in ordinary cylindrical fuel pellets, power generation is known to occur more intensely on the outer surface due to a phenomenon known as thermal neutron shielding. In the case of an azimuthally symmetric shape, such as a cross-sectional slice of a cylinder, this will have no impact on surface heat-flux. As long as the heat load varies only radially, all heat will be removed uniformly, regardless of the distribution.

However this assumption cannot be made for the circumferentially non-uniform CSS design. Also, due to the unique shape, a significantly larger portion of the fuel volume is nearer to the surface, especially that which is within the large fuel petals. Because heat generation within the central region most directly feeds the peaked elbow heat-flux, the lateral power profile of the two CSS fuel designs was evaluated to determine whether using a "corrected", more-realistic lateral power profile might alleviate the peaking. This was carried out using detailed COSMOS models supported by MCNP, as described in Chapter 3.

4.2.2 (a) Spiral Pin 1

The study was first conducted on Spiral Pin 1. This pin was characterized by very large, sharp heat-flux peaking, but also has the largest surface to volume ratio. Because of these factors, gains made by incorporating this effect should be most evident for this case.

The results are summarized in Figure 4.22, represented by normalized power peaking factors. As expected, evaluating the lateral distribution shows a reduction in power density near the center of the rod, with the largest power generation in a shallow region near the pellet surface. However the disparity, which maximizes at 1.09, and falls as low as 0.92, is seemingly not large enough to cause any major changes in the heat-flux distribution.

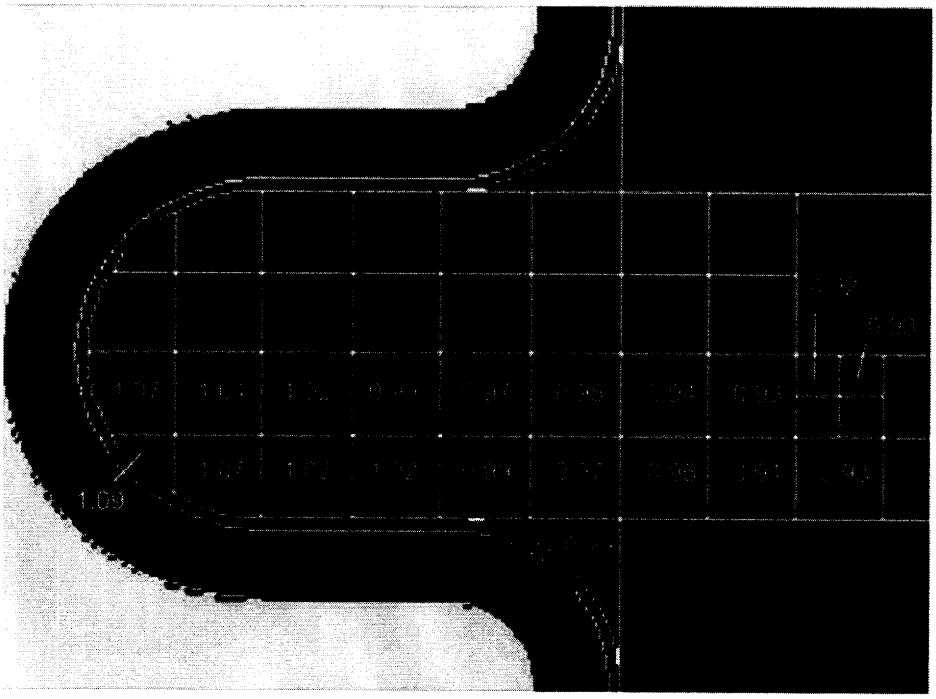

Figure 4.22: Normalized Lateral Power Generation Peaking for SP1, $\rho_{water} = 0.959$ g/cc

This suspicion is confirmed by the thermal analysis results in Figure 4.23 and 4.24. The maximum heat-flux along Spiral Pin 1 is reduced to some degree (around 5% of peak value), but this appears to be only a minor effect. Interestingly, the maximum central temperature does improve by 56 degrees, to reach the value of 909 K. These results tip the balance further in favor of SP2, which inherently has a peak 20-25% heat flux below the SP1 peak. Still, SP1 fares better than SP2 in terms of its maximum fuel temperature.

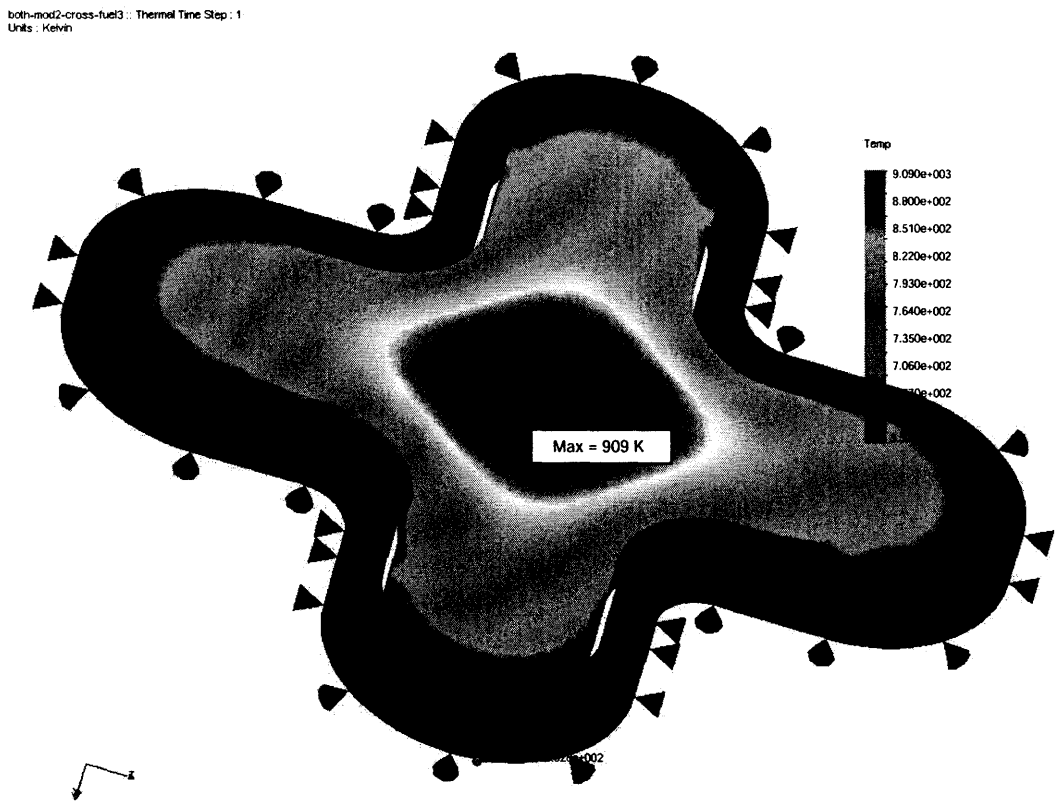

Figure 4.23: Temperature Distribution for SP1, corrected lateral profile.

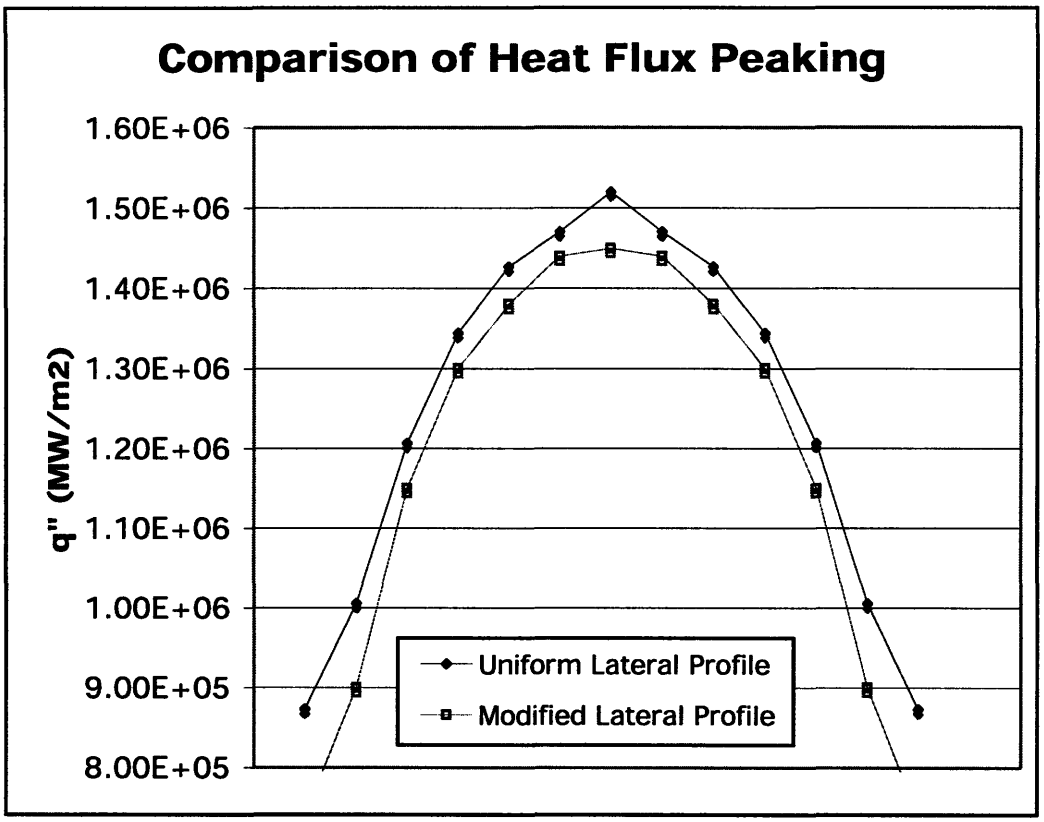

Figure 4.24: Heat Flux Peaking for SP1, Uniform vs. Corrected Profile.

4.2.2 (b) Spiral Pin 2

Though the previous analysis shows that thermal neutron shielding has little bearing on this study, the SP2 design was next examined in the interest of completeness. An MCNP study using the same parameters was performed, yielding very similar results, including matching values for the maximum and minimum lateral peaking factor values of 1.09 and 0.92 respectively (Figure 4.25).

Resultant heat flux and temperature distributions (Figure 4.26) also showed very similar improvements: maximum surface heat flux dropped by 4% to a value of 1.21MW/m^2, and maximum centerline dropped 48 degrees from its uniform profile calculation to a peak of 960 K.

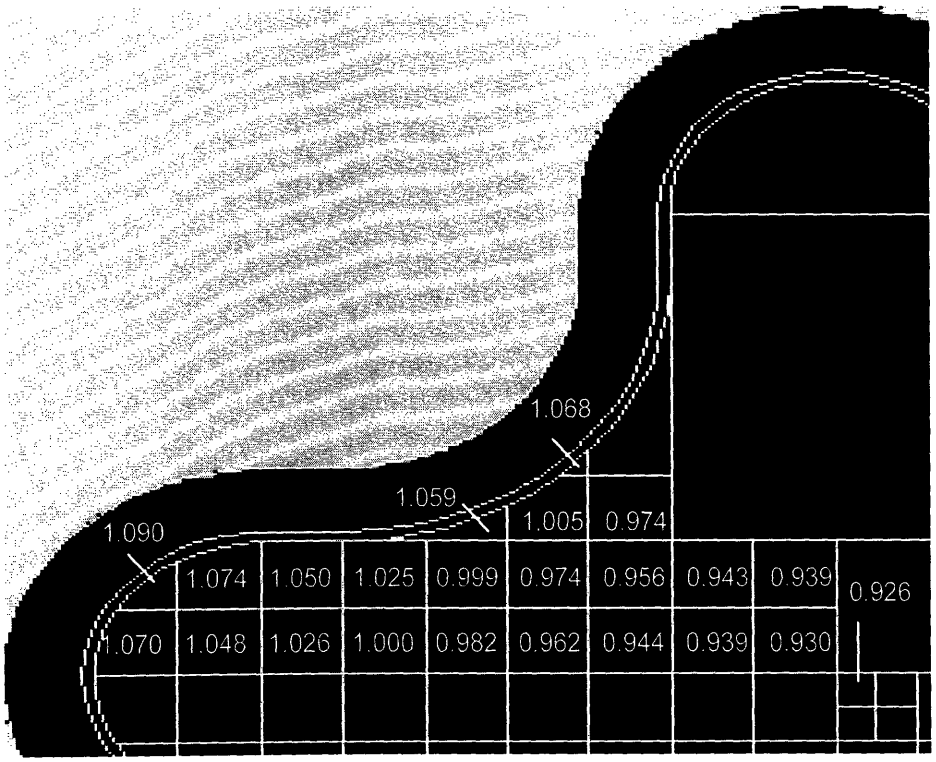

Figure 4.25: Normalized Lateral Peaking for SP2, $\rho_{water} = 0.952$ g/cc

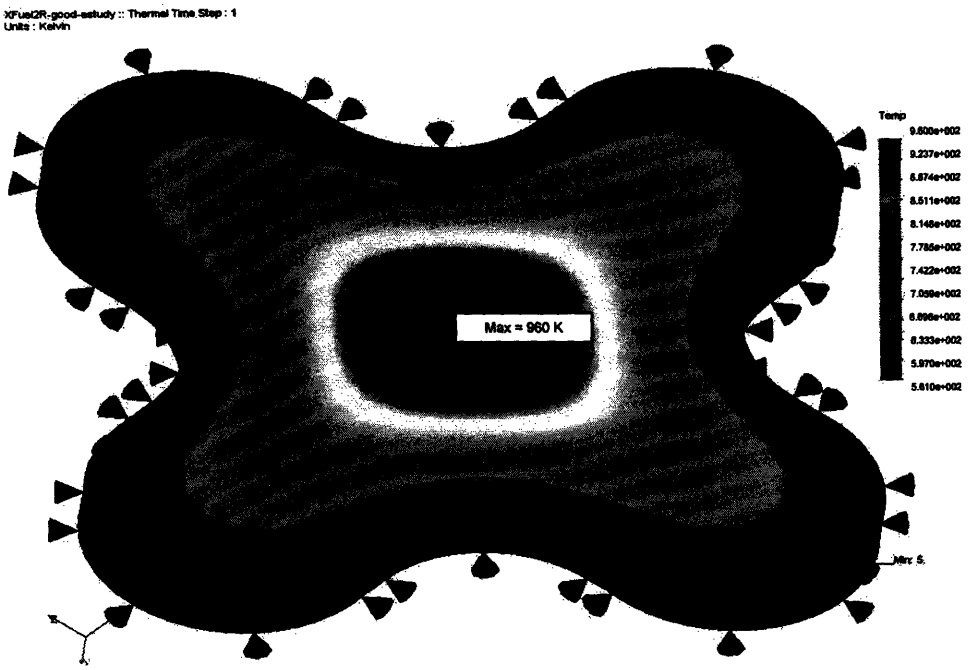

Figure 4.26: Temperature Distribution for SP1, corrected lateral profile.

Table 4.7: Summary of Corrected COSMOS Results for CSS SP1 and SP2

Lateral Power Profile	J_{min}*	T_{max} (K)	% difference	q''_{max} (MW/m^2)	% difference
Uniform, SP1	1.00	965		1.53	
Corrected, SP1	0.92	909	-5.8	1.47	-4.4
Uniform, SP2	1.00	1008		1.25	
Corrected, SP2	0.92	960	-4.8	1.21	-3.6

*The quantity J_{min} represents the lowest peaking factor in the cross-section

4.2.3 Power Uprate Performance

Core performance models in Section 4.1 indicate that using CSS fuel may very well allow for a core power uprate of 25% judging by purely thermal-hydraulic considerations. In this case, linear power would be 25% larger, requiring a proportional increase in coolant mass flow to maintain flow conditions within the core. Still, it is not clear how the fuel temperature might be affected by these adjustments. Using Chen's correlation for 2-phase flow heat transfer, for fixed quality, one can only expect an increase in heat transfer coefficient from 54.2 to 55.8 kW/m^2K, as calculated by VIPRE for the uprated reference input file. At this location, boiling heat transfer dominates over forced convection contributions, and increasing flow velocity therefore has only a small impact on h_{co}.

Thus, as the linear heat rate is increased to raise power density by 25%, the overall thermal resistance between the fuel centerline and the bulk coolant temperature does not change much in comparison to the nominal case, and remains dominated by the conduction resistance within the fuel pellet. From this assumption, one could estimate that the value of $T_{CL} - T_b$ for the reference cylindrical fuel rod would increase roughly proportionally.

In fact, the COSMOS results show that, this holds fairly closely: Figure 4.27 shows this increase in Temperature to 1407K. The discrepancy is likely due to temperature dependent properties with the fuel pellet which cause a lower thermal conductivity for the higher temperature case, further raising centerline temperature.

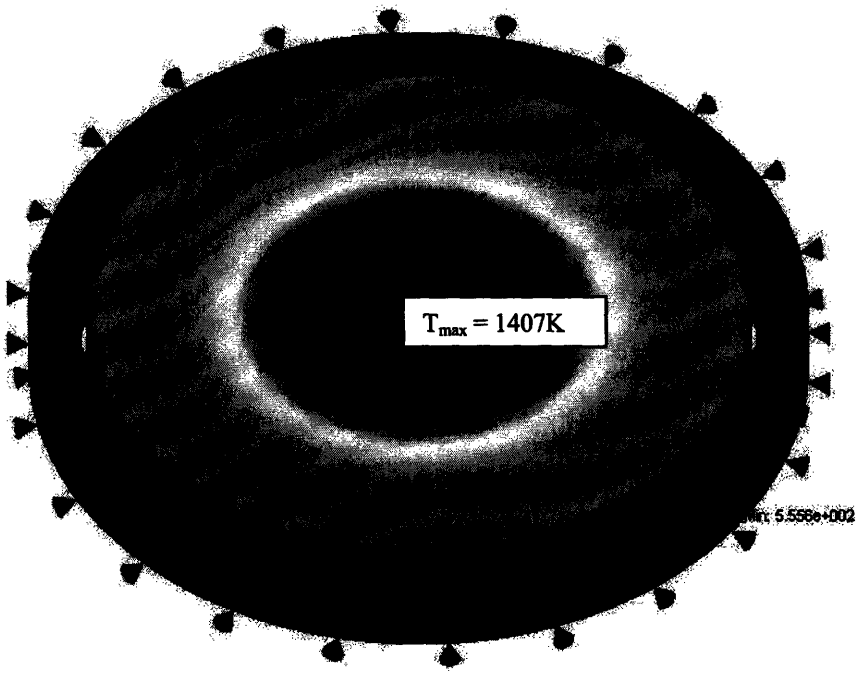

Figure 4.27: Temperature Distribution in Reference Fuel, 25% uprate in linear power.

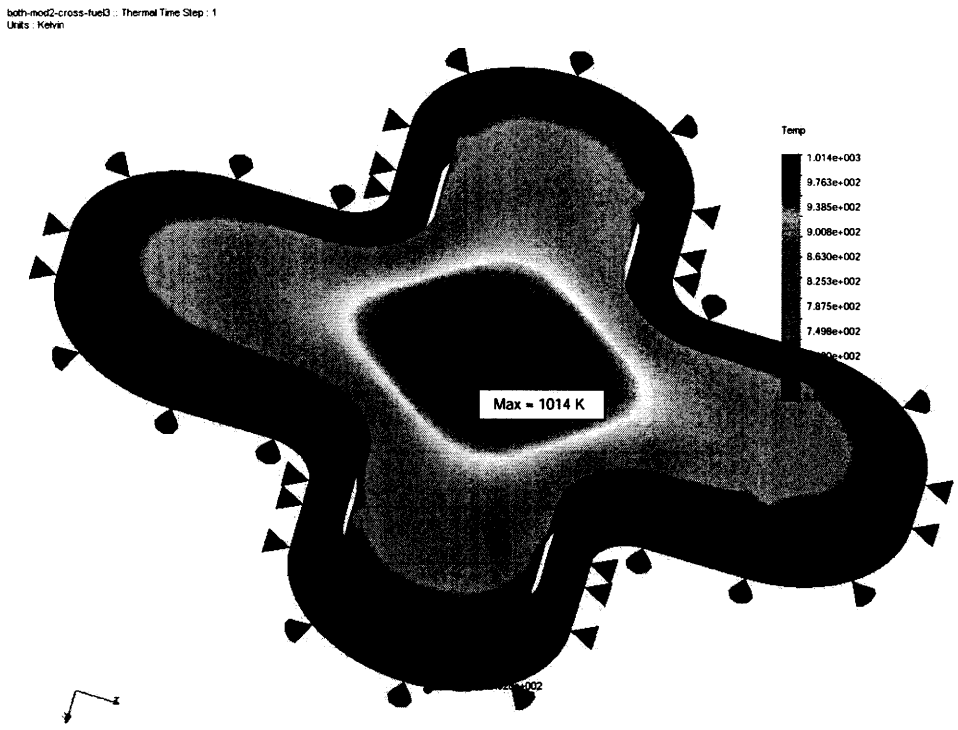

Figure 4.28: Temperature Distribution for the SP1 Design, 25% uprate in linear power.

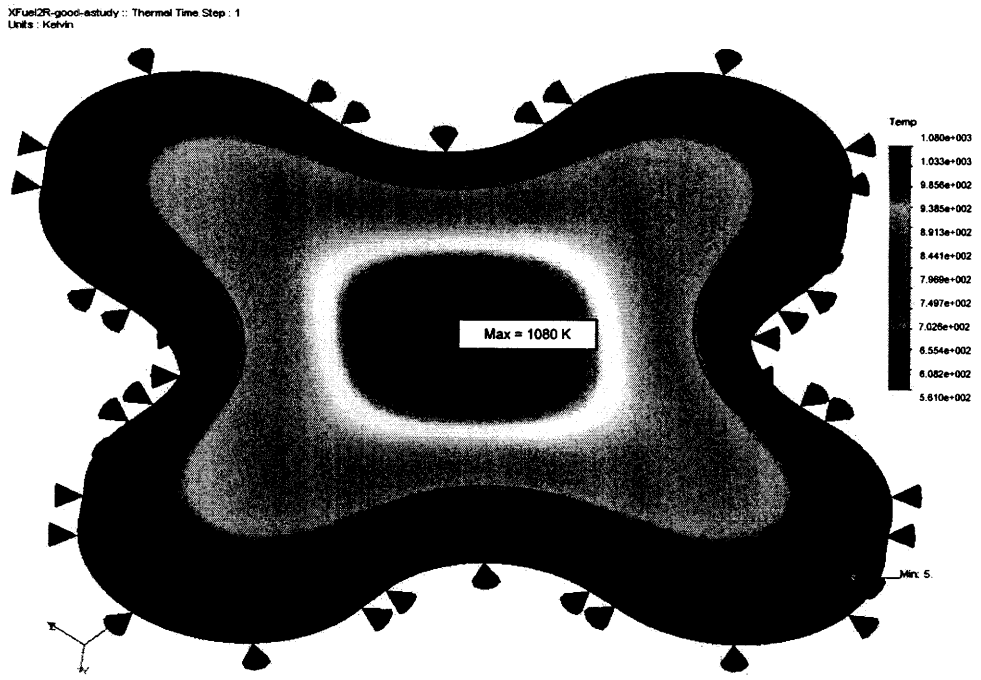

Figure 4.29: Temperature Distribution for the SP2 Design, 25% uprate in linear power.

Meanwhile, the CSS rod geometries seem to be able to achieve a lower rate of temperature increase with linear power uprate (Figures 4.28, 4.29). Clearly the shape does not lend itself to a 1-dimensional linear extrapolation in the same manner. From this standpoint, the CSS design is a more efficient shape for heat conduction purposes, heat-flux peaking looms as an issue.

Table 4.8: Summary of COSMOS Results for CSS SP1 and SP2, 25% uprate

Fuel Geometry	Maximum Temp. (K)
Reference	1407
SP1	1014
SP2	1080

A summary of the maximum fuel temperatures predicted for the three rod geometries is shown in Table 4.8. At 25% uprated conditions, the CSS rod geometry predicts an improvement on the order of 350°C. In this regard, SP1 performs better than SP2, though the difference is not huge.

4.3 Review on Non-Uniform Circumferential Critical Heat-Flux

With the issue of heat-flux peaking proving to be persistent through finite-element analysis, a review of previous research into critical heat-flux under similar peaked conditions.

Kitto and Wiener (1982): Adequate literature was found to exist on the effect of non-uniform circumferential critical heat-flux, though mainly for single tube-channels rather than rod bundles. One particularly useful study [17] compared the critical heat-flux of uniformly heated channels to channels with a peak-to-average heat flux of 2.05. These 3.8 cm outer-diameter tubes enclosed high pressure two-phase vertical flow at 18.5 MPa, 950 kg/m^{2}s, and were peaked on one side (Figure 4.30), representing an application for certain edge-tubes in the bundle of a fossil boiler.

Figure 4.30: Comparison of uniform and peaked heated tubes, a peak-to-avg of 2.05 [17]

Experiments into non-uniformly heated tubes introduce a couple of terms that are worth defining explicitly here for the sake of clarity. The term "average critical heat flux" refers to the circumferentially-averaged heat flux at the axial location where critical heat flux has occurred. "Maximum critical heat flux" refers to the maximum value of the heat flux along the tube inner-circumference at the same axial location. Clearly, the maximum critical heat flux is equal to the average critical heat flux, multiplied by the peak-to-average factor applied by the experiment. For uniformly heated tubes, there is no difference between these two values.

Data showed that for subcooled CHF events, the peaked tubes had a large reduction in average critical heat flux, in comparison to the uniform case. This indicates that the peak

is having a strong effect on curtailing CHF points below that for uniform circumferential data. However for high quality CHF events, the experimental data consistently shows no difference between uniform tube CHF and the averaged critical heat flux (Figure 4.31).

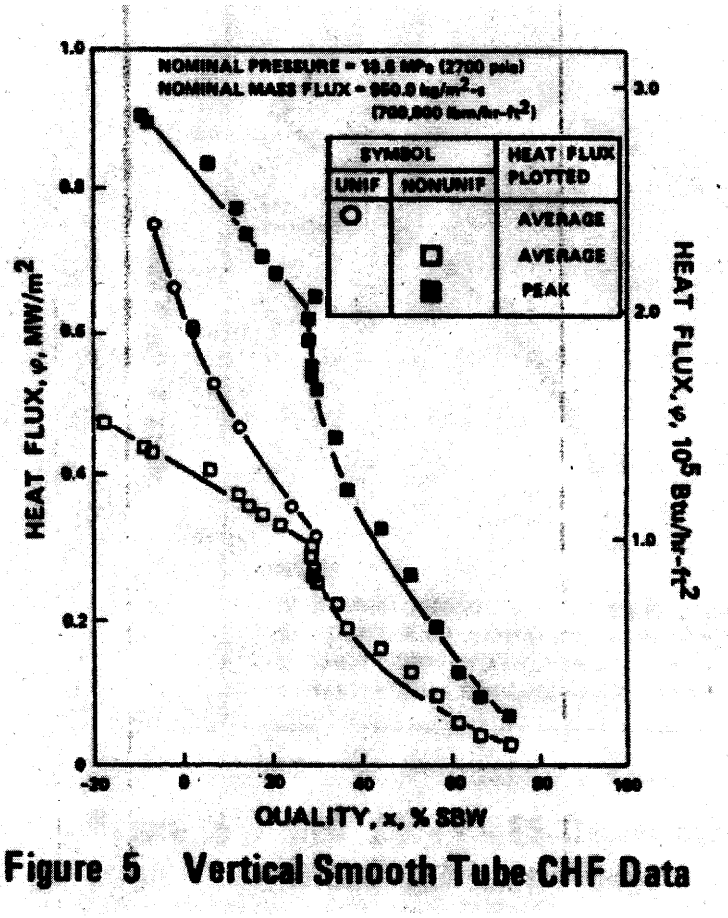

Figure 5 Vertical Smooth Tube CHF Data

Figure 4.31: Average and Maximum CHF vs. critical quality, [17]

This behavior is reasonable in view of the differences between the mechanism leading to low quality and high quality CHF. Low quality CHF, or departure from nucleate boiling, is wholly dependent on local conditions: the local heat flux, local mass flux, and local quality at a given operating pressure. It is not hard to imagine that a given heat-flux spike adjacent to nearly limiting thermal conditions might force that location into DNB. In contrast, high quality CHF (dryout) is a function of total heat input, and is usually correlated as a critical quality – boiling length relationship, as with Hench-Gillis. In this

case, CHF data more closely follows the curve of the uniform case, since these two curves have the same total heat input -- integrated along the whole tube -- at the location of CHF.

It is curious that throughout the study, even in the low quality CHF region, the maximum CHF is significantly higher than in the uniform case, indicating that some other unusual phenomenon is taking hold in this region; the author does not propose a reason for this enhancement, this is discussed in Butterworth.

Alekseev *et al.* (1964): Similar results were found in another study involving non-uniformly heated tubes, conducted by Alekseev [18]. Critical heat flux data was taken for vertical, single-channel tubes of ID = 10mm, with peak-to-average heat flux variation of 1.0 (uniform), 1.12, 1.28, and 1.50. For a fixed mass flux of 2000 kg/m^2s, inlet subcooling was varied to give variation of the average CHF with critical quality (Figure 4.32). This experiment was conducted at pressures of 5.9 MPa, 9.8 MPa, and 17.7 MPa.

Again, in all cases, the data shows that the value for average critical heat flux for the peaked channels begins lower than the uniform channel CHF, then approaches this value at high quality. The figure shows that peaking hampers subcooled CHF (DNB), and that the degree of this limitation is dependent on the severity of heat-flux peaking. Yet for high quality CHF, the difference between uniform and non-uniform tubes is diminished, or has vanished altogether in some cases.

Once more, the author cites that these experiments confirm the "local" nature of the critical condition at high subcoolings and the tendency to an "overall power" condition in the higher steam critical regions.

The fact that data is seen to show a pressure dependence, especially in the low quality region, gives some further insight into the mechanism of CHF in this region. At lower pressure, boiling occurs more readily and therefore one would expect boiling to occur at a lower equilibrium quality; this is consistent with the trend shown.

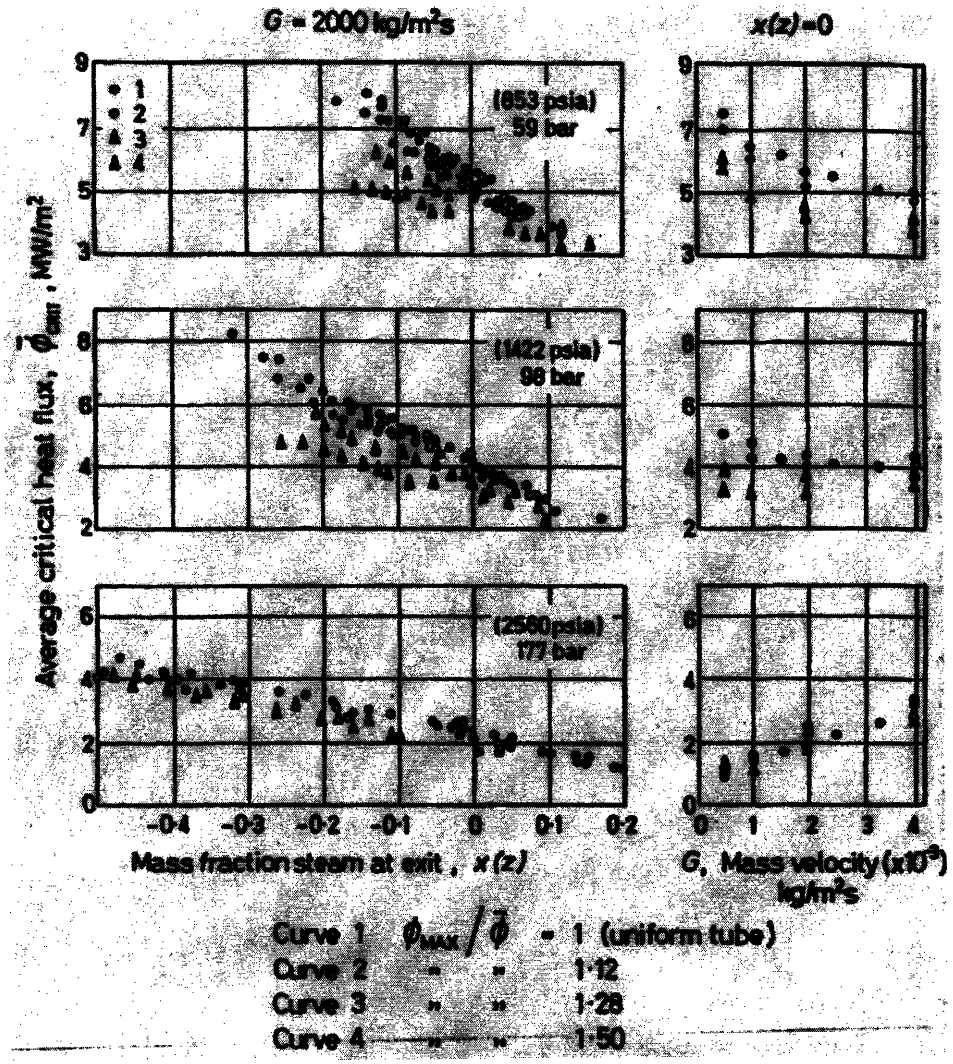

Figure 4.32: Average CHF vs. critical quality, due to Alekseev [18]

Butterworth (1972): In a purely analytical study, Butterworth also examined non-uniform heating within vertical tubes [19]. The difference between high and low quality CHF data was already well-documented; his work instead developed a theory to explain why maximum CHF for non-uniform tubes consistently tops CHF for uniform tubes over all ranges of quality. The author suggested that non-uniform heating has the effect of initiating a side-to-side, circumferential flow within the liquid film on the heated surface.

This additional circumferential flow, superimposed on the axial annular flow, makes it more difficult for a stable vapor film to take hold on the tube wall.

The author examined a circumferential film spreading model for the annular flow regime, devising the following relations:

$$\frac{q''_{nu-avg}}{q''_{u}} = \frac{1}{1+(D_i^2/Kz)\alpha} \qquad \text{(Eqn. 4.1)}$$

$$\alpha = \frac{(q''_{nu-\max})}{q''_{nu-avg}} - 1 \qquad \text{(Eqn. 4.2)}$$

In this case, $q''_{nu\text{-}avg}$ and $q''_{nu\text{-}max}$ represent average and maximum heat fluxes for non-uniform tubes, q''_{u} is the heat flux for uniform tubes, D_i is the tube inner-diameter, and K is the spreading coefficient for the proposed secondary circumferential flow, assumed to be 0.9 mm by Butterworth.

At critical conditions, these can be equated to:

$$\frac{q''_{chf,nu-\max}}{q''_{chf,u}} = \left(\frac{\alpha+1}{1+D_i^2 Kz\alpha}\right) > 1 \qquad \text{(Eqn. 4.3)}$$

$$\frac{q''_{chf,nu-avg}}{q''_{chf,u}} = \left(\frac{1}{1+D_i^2 Kz\alpha}\right) \leq 1 \qquad \text{(Eqn. 4.4)}$$

Kitto and Weiner found qualitative agreement with this model, but noted that the value for α is highly dependent on quality as well, as seen in their work and that of Alekseev. Butterworth's model does not offer any dependence on critical quality.

Fusion Divertor Research: Extensive research has been performed for non-uniform heating of cooling tubes for application to fusion divertor heat removal systems [20,21].

In this situation, the divertor experiences a strong heat flux from the side of the tube exposed to the hot plasma, but little to no heat-flux from the other side.

Such research is performed only for subcooled CHF, and shows the same trends as other studies as far as subcooled CHF events. This research is mentioned mainly to provide a starting point for those interested in investigating literature for PWR analysis applications.

4.3.1 Summary

The data presented above shows that for high quality CHF within single tubes, peaking as substantial as a 2.05 peak-to-avg ratio can be endured with no reduction in average critical heat flux. Still, there is likely an upper-bound to how much peaking can be tolerated, even for dryout limited CHF. There is no way of knowing this limit without further experimentation.

Furthermore it is impossible to quantify the added effect of non-uniform geometry that is present for the CSS fuel shape, or the effects of CHF along a rod-bundle cluster rather than a single-tube, without performing a series of specific experiments. Nevertheless, it is reassuring to note that the peaking calculated for the SP2 fuel type in the conduction studies falls within the tested range at 1.88, so it is not unreasonable to assume as a first-order assessment that this can be neglected, as has been done for VIPRE core analysis thus far.

4.4 Spiral Rod CHF Correlation

Computational VIPRE models show that the SP1 and SP2 cores will allow for an uprate of 21 and 25% in core power, respectively, as predicted using the Hench-Gillis correlation. Still, it's not clear that simply adapting this correlation to CSS rods of an equivalent surface area should provide meaningful results. For a drastically different rod geometry such as the CSS, only representative experimental data can truly be reliable.

Experiments on a similar type of fuel were recently conducted at the Kurchatov Institute in Russia. Some of these results are available in a limited distribution report. In this study, the rods were of a slightly different 3-petal variety, and were heated uniformly circumferentially, and axially. Though conducted at high pressure (16 MPa), these tests were run at a wide range of inlet subcooling and coolant mass flux conditions. As a result, among the largely subcooled CHF data provided, the report included a significant amount of high-quality CHF data (above x=0.3) that could be particularly useful in correlating Critical Power for BWR application. Furthermore the data offered a side-by-side comparison of the performance of traditional cylindrical-rod fuel assemblies to twisted fuel assemblies under the same conditions.

A full analysis of this data was conducted as part of the body of work for this thesis, however it cannot be fully documented here due to the limitation on further distribution under which it was obtained. A brief summary reads as follows: A VIPRE model was constructed to the reference cylindrical-rod geometry set forth in this report. The model was able to match critical heat flux values reported by the experimental data, at a wide range of critical qualities. This required discarding the Hench-Gillis CPR correlation in favor of the EPRI-1 Critical Heat Flux (CHFR) correlation [5], which proved to be capable of predicting limiting conditions over a wide range of critical qualities. VIPRE was also able to match reported pressure drops with good accuracy, once supplied with an appropriate rough-channel friction factor correlation.

A second VIPRE model was constructed, to model the twisted fuel assembly dimensions, using similar approximations as used in Chapter 3 for CSS-VIPRE modeling. This included appropriately accounting for the increase in surface area, adjustment of subchannel flow areas and gaps, and other minor changes. In this case, the EPRI-1 correlation was able to predict an enhancement in CHFR for the twisted fuel, in comparison to the reference, at the same operating conditions.

However this enhancement did not fully match the experimental data. At low critical qualities the model was fairly accurate as-is. But at high critical qualities, the increase predicted by VIPRE was not nearly as large as the increase seen experimentally, which was on the order of a 30-35% improvement. It was hypothesized that this difference in behavior had to do with the unique fluid dynamical conditions in high-quality rod-bundle flow. This could suggest that the twisted rod shape promotes a secondary vapor flow, which serves to sustain annular flow beyond what can be envisioned by a code such as VIPRE. It's also likely that the increase in mixing between neighboring subchannels can act to prevent the occurrence of hotspots, allowing for higher bundle-averaged critical qualities.

A new twisted-fuel CHFR Correlation dubbed "EPRI-Spiral" was developed accordingly, using the EPRI-1 correlation as a baseline, and applying an enhancement factor to drive up the CHFR in order to compel VIPRE to match the Kurchatov experimental Critical Power data. Since the data indicated a large-scale increase in CHFR for high quality dryout conditions rather than for subcooled DNB, this factor attempted to capture the mechanism of critical heat flux itself. This is not necessarily an easy task, especially when considering that this correlation should adequately cover the 16 MPa pressure range of the correlated data, as well as the 7 MPa pressure, for the purposes of our BWR analysis.

This was accomplished in the following way: in simple terms, one can usually differentiate between DNB and dryout by the relative effect of mass flux (G) on the critical heat flux for a particular critical quality. For the case of DNB, increasing G will

delay the onset of subcooled boiling, serving to postpone DNB and enhance CHF. For dryout, increasing G will primarily serve to increase the rate of droplet entrainment from the rod surface, thereby decreasing CHF.

There is also likely a transition region, between the high and low quality CHF, in which no clear effect of G will be noted. For the purposes of this study, this was called the "hybrid" region. It might also be expected that, at high pressure, dryout would only take hold as the dominant mechanism of CHF for inordinately large qualities, since pockets of vapor would be far more difficult to sustain. These general trends can be verified in examining the Figures 4.33 and 4.34, adapted from the AECL CHF Lookup Tables [22].

Two key figures have been selected for inspection, which show this shift from DNB to dryout with increase in quality, and "hybrid" region lingering between.

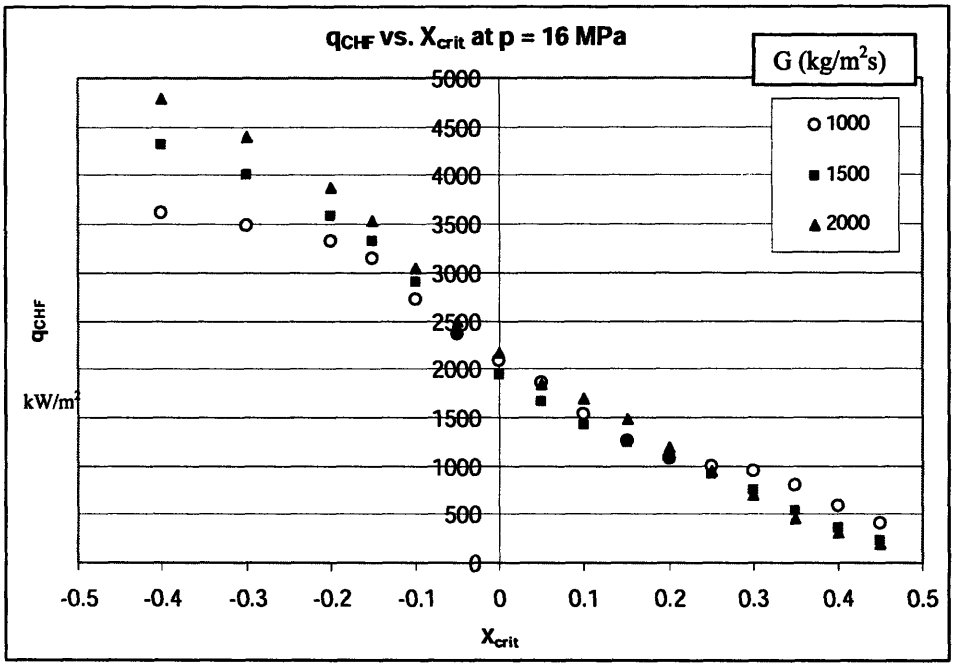

Figure 4.33: AECL '95 CHF tube studies at 16 MPa. [22]

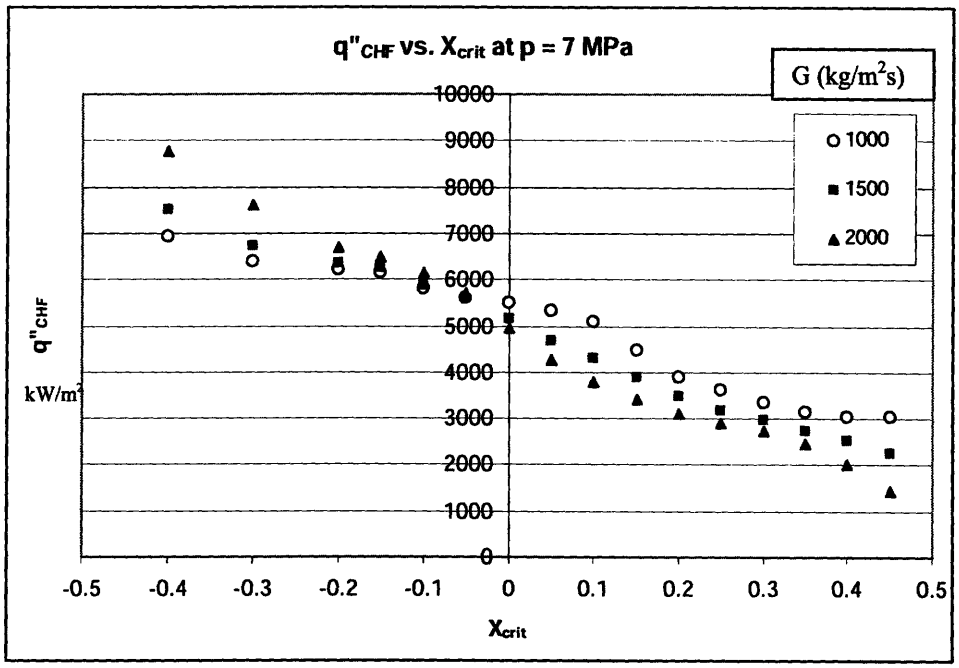

Figure 4.34: AECL '95 CHF tube studies at 7 MPa. [22]

From Figures such as these, one is able to extract the so-called "Minimum dryout quality" for two-phase CHF data at any given pressure, as determined by the reversal of the trend of mass flux (Figure 4.35). For a pressure of 16 MPa, Figure 4.33, this appears to occur at a quality of 0.3, while this occurs near x=0 for the lower pressure data shown in Figure 4.34. This reversal point is examined for the whole range of pressure, to be developed into a function of pressure.

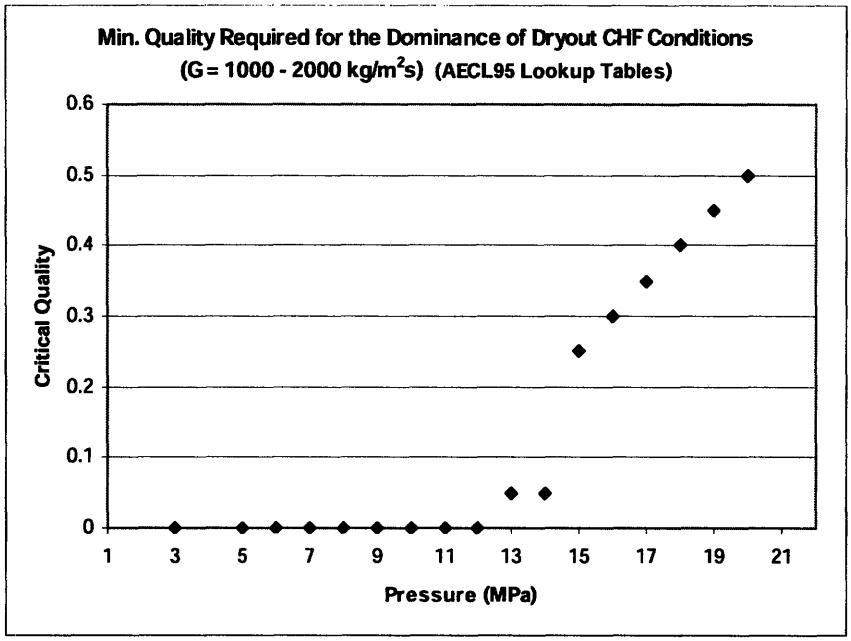

Figure 4.35: Minimum dryout quality for a range of pressures.

For a given operating pressure, the factor developed for CHF enhancement was set at 1 (no change) for data below this point of minimum dryout quality, and beyond this point, increased as a function of quality and mass flux in a manner than agreed with the provided experimental data. In this way, the high pressure CHF data was adapted for use into a more general twisted-rod CHF correlation.

The next logical step was to apply this new information to the 9x9 BWR CSS models described in Chapter 3, by replacing only the Hench-Gillis CPR correlation with the newly developed EPRI-Spiral CHFR correlation. This was performed for the case of the SP2 Assembly model, which had proved to be the more successful of the two in earlier studies.

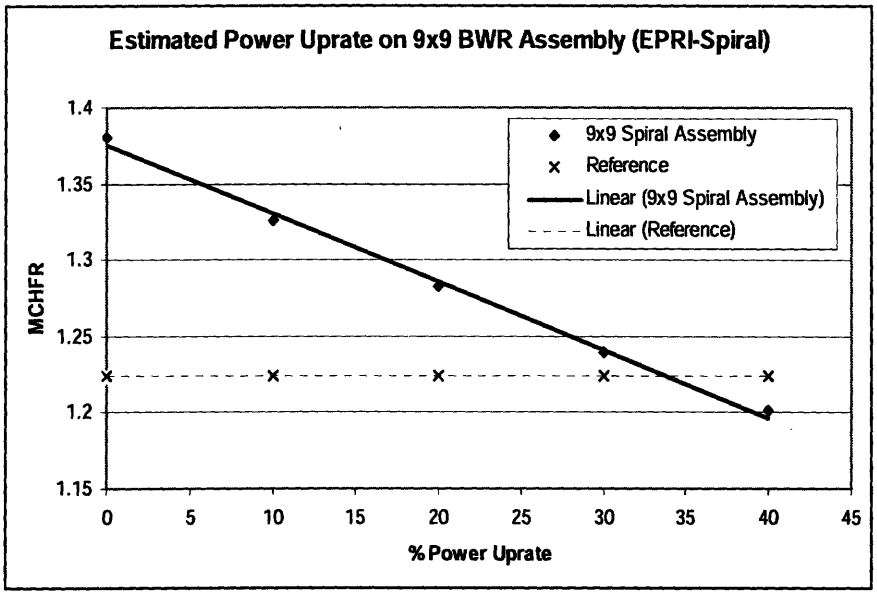

Figure 4.36: CSS SP2 Power Uprate predicted by EPRI-Spiral

As seen in Figure 4.36, the CSS SP2 core was predicted to be able to sustain a 34% power uprate in comparison to the reference case.

Despite the numerous differences between this data and the desired conditions for the BWR CSS Core – the higher pressure, the smaller number of fuel petals, the lack of non-uniform circumferential heating, etc. – this work seems to confirm that twisted rods of this geometry are able to maintain a circumferential flow in high quality two-phase flow.

Detailed in Chapter 4.3, the argument can be made that heat-flux non-uniformity on the order of what is expected for this fuel type can be tolerated in high-quality flow, provided that steady circumferential flow is maintained along the periphery of the rods. Coupled with the results from the unpublished data source, this suggests that circumferential heat-flux peaking should not be an issue for the CSS fuel proposed here.

5. Pressure Drop Investigation

Thermal-hydraulic results for the CSS core based on computational models detailed in Chapter 4 are indicators of the potential for higher power using such assemblies. Still, these models rely on correlations that have been developed for cylindrical rod bundles, and are unlikely to accurately capture effects of the geometry of CSS rods.

In fact, unpublished experimental tests at the Kurchatov Research Institute using similar bundles of twisted fuel have shown the friction factor at the same flow velocity to be lower than that for a bare assembly of cylindrical rods. Therefore, an experiment has been performed to investigate the validity of previous tests using our own fuel design, and will seek to reach a greater understanding of the effect that cross-shaped spiral rods may have on hydraulic resistance.

An experimental facility was constructed in order to measure the single-phase pressure drop resulting from 4x4 square lattice bundles of the proposed CSS rod design. This facility produces a range of highly turbulent water flow velocities at room temperature and pressure. In total, the test matrix included three CSS rod assemblies of different twist pitch, as well as a reference cylindrical rod model. Ultimately, data from this experiment was to be used to compare turbulent CSS friction factor to cylindrical rod friction factors, and yield an approximate hydraulic loss correlation.

5.1 Test Rod Design Criteria

CSS fuel rods were originally designed to fit into a GE BWR/6 assembly box as a closely packed 9x9 bundle; this defined the cross-section of CSS experimental test rods, denoted Spiral Pin 2 in Chapter 2 (Figure 2.4). The Spiral Pin 2 fuelled core proved to be a more promising design to meet thermal-hydraulic constraints in Chapter 4. In BWR fuel assemblies, these rods would match the 4.1 m height of standard BWR fuel rods. A

minimum twist pitch of 2 meters, would ensure at least 8 contact points along the rod height, the same as in the grid-supported assemblies of today.

For the purposes of this hydraulic experiment, it was judged that a smaller 1.5m tall, 4x4 array of rods would serve as a sufficient test-section, minimizing inlet/outlet and wall effects and allowing the cross-shaped spiral effect to be clearly investigated. These test rods match the CSS SP2 cross-sectional dimensions from Figure 2.4, and were manufactured as three individual sets of 16 test rods (Figure 5.1), each set with a different twist pitch (Table 5.1). An early schematic of one such rod is shown in Figure 5.2, with a photograph showing all sets of test rods in Figure 5.3.

An additional set of 16 cylindrical rods of the same 1.5 meter height were to be tested for comparison purposes, as well as for validation of the facility with current accepted bundle pressure drop correlations. The dimensions and other characteristics of all test rod types are detailed in Tables 5.1, 5.2, and 5.3.

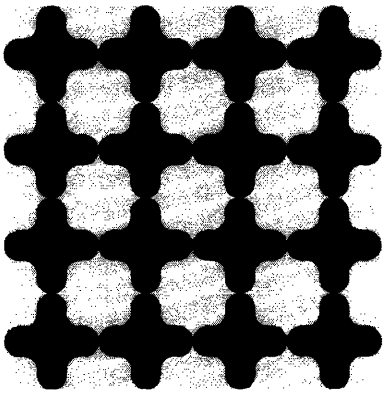

Figure 5.1: A cross-cut of the 4x4 test-section.

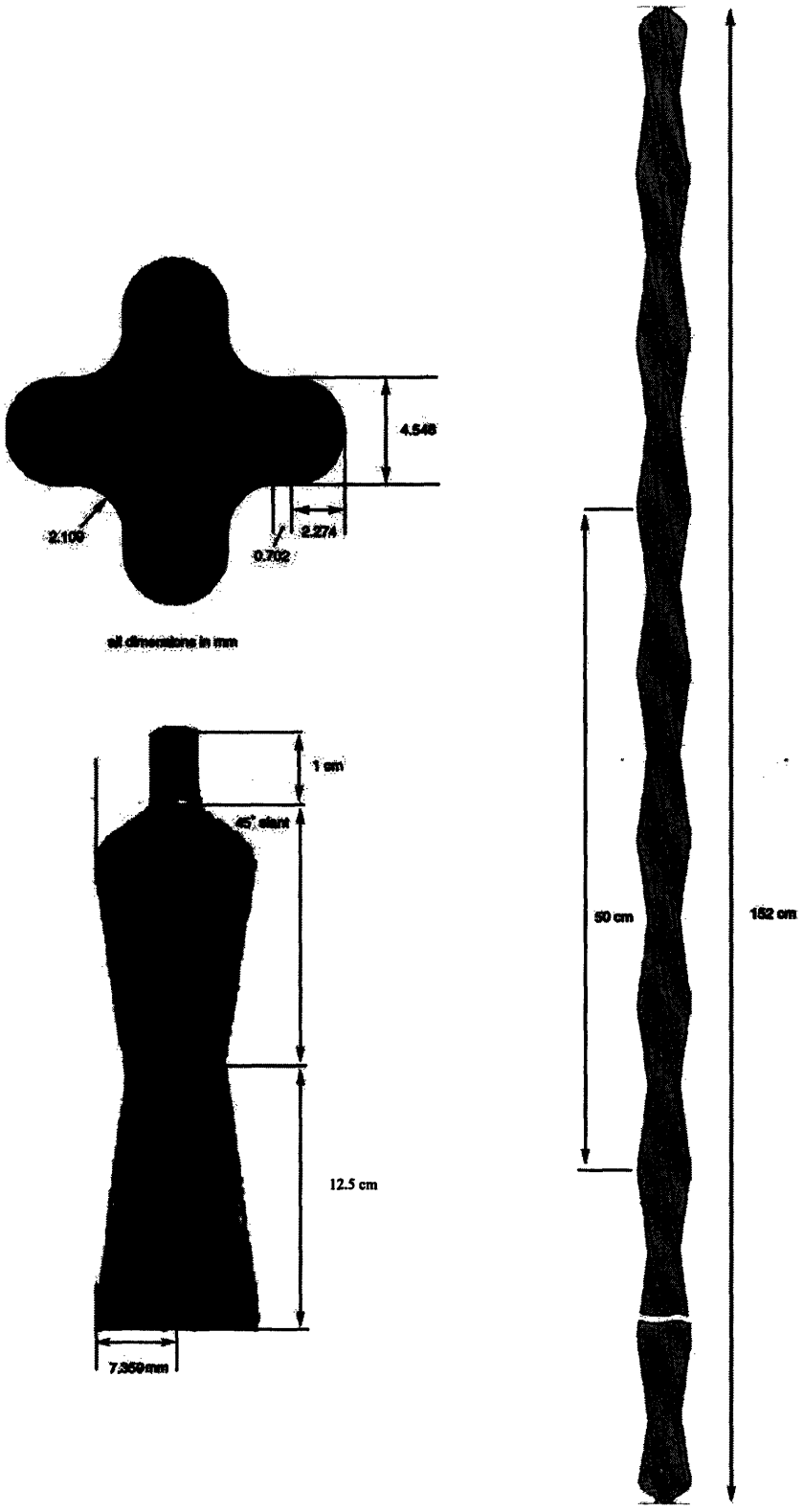

Figure 5.2: Design parameters of the cross-shaped spiral fuel pin (CSS Type 3 is shown, with a 50 cm twist pitch); not to scale.

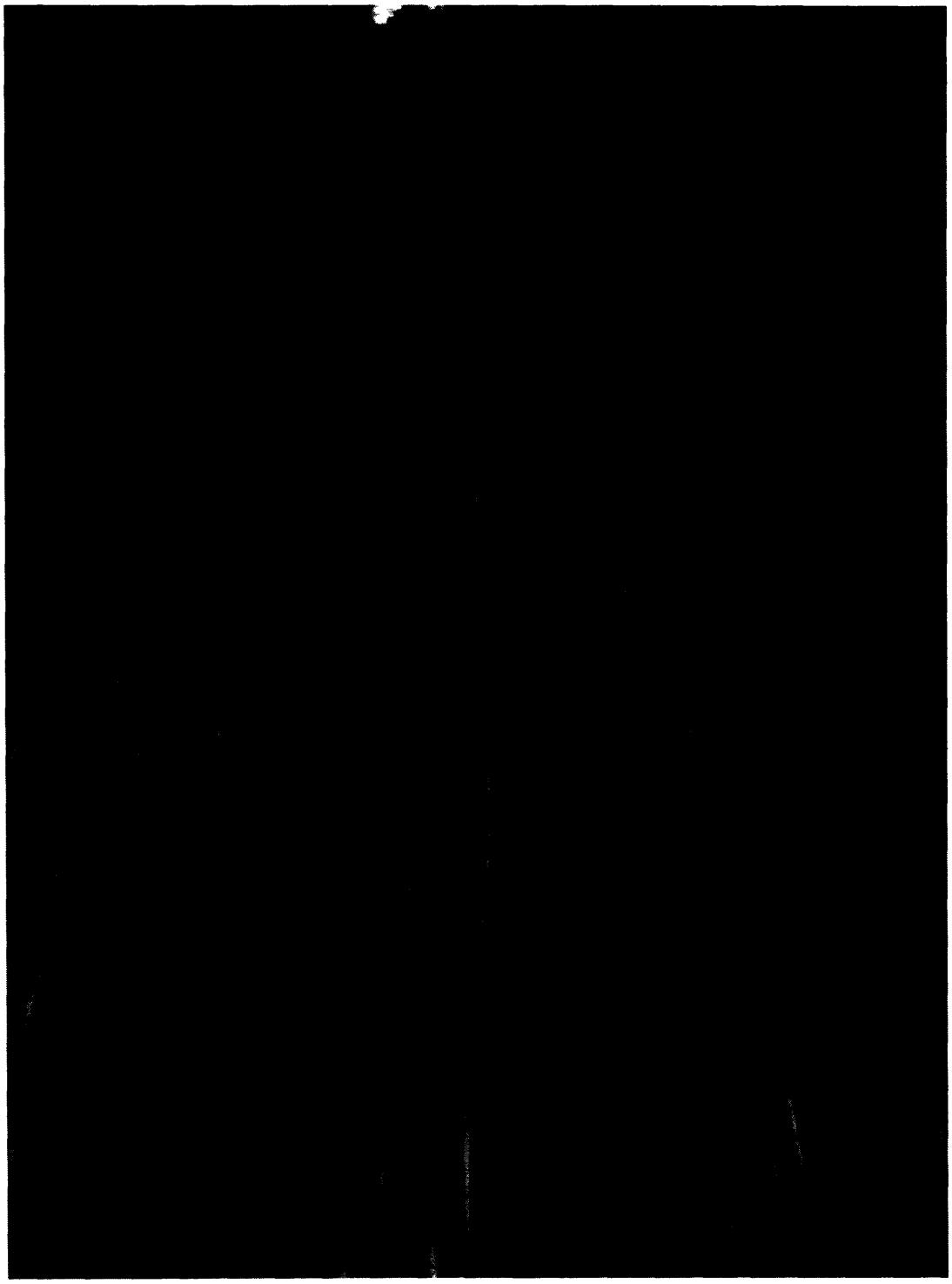

Figure 5.3: Photograph showing, from L to R, CSS Rod Types 3, 2, 1 and the Reference.

Table 5.1: Summary of CSS rod bundle parameters

Parameter	Value
Pin pitch	1.47 cm
Rod test height	1.1 m
Assembly flow area	19.4 cm^2
Assembly size	4 x 4, 16 rods
Hydraulic diameter	0.77 cm
Spiral twist pitch*	See Table 3

*defined as the distance required to make one complete turn.

Table 5.2: Summary of reference rod bundle parameters

Parameter	Value
Pin pitch	1.47 cm
Rod test height	1.1 m
Assembly flow area	21.6 cm^2
Assembly size	4 x 4, 16 rods
Hydraulic diameter	1.08 cm

Table 5.3: Test Rod Types

Fuel Type	Fuel Cross-Section	Twist Pitch
1	Cross-shape*	200 cm
2	Cross-shape	100 cm
3	Cross-shape	50 cm
Reference	Cylinder, D=11.11 mm (7/16")	--

* See Figure 2.4

5.2 Flow Conditions in Assembly

Desired water flow through the assembly was determined by matching nominal operating BWR inlet flow velocities (typically near 2.1 m/s), though under room temperature and pressure. Flow conditions range from 50% of this nominal velocity to 150% (Table 5.5). This ensures that data will be correlated for a significant range of Reynolds numbers (10,000 - 40,000), including on the order of highly turbulent flow typical of reactor core coolant subchannels. The properties of water are significantly different at room temperature and pressure, shown in Table 5.4:

Table 5.4: Variation in Water Properties at BWR and Room Temperature, Pressure.

	BWR conditions	Room Temp, Pressure
Density (kg/m^3)	750.3	997.1
Dynamic Viscosity (μPa-s)	93.5	954.4

Water at BWR operating conditions (saturated at 280°C) is less viscous than water at room temperature by an order of magnitude. But it is also less dense, resulting in typical **Re** exceeding 100,000. For this experiment, making a direct comparison at matching **Re** would require greatly exceeding typical flow velocities, increasing requirements in pumping power and facility infrastructure. However, friction factors tend to flatten out considerably as flow becomes significantly turbulent. Seen in Figure 5.4 is the Blasius turbulent friction correlation, used as the default setting in the reactor core thermal-hydraulics code VIPRE. Also shown is the well-known McAdams correlation, for use in smooth tubes and highly turbulent flow which gives its range as 30,000 to 100,000. This suggests that established trends at 40,000 or 50,000 will not greatly change over this range. In rough channels, this flattening effect should occur at even lower **Re**.

In a study that is meant to establish a comparative relationship between frictional factors of CSS rods and cylindrical rods, pushing flow **Re** near the 40,000 regime should be sufficient to establish comparison. For each test rod type, the pressure drop will be

measured for 9 flow rates, from 11 to 99.7 gallons per minute (gpm) in increments of 11 gpm (Table 5.6).

Table 5.5: Test Loop Operating Conditions

Parameter	Value
Operating Temperature	22°C
Operating Pressure	0.1 MPa
Velocity Range (at flow meter)	0.15 – 1.35 m/s
Velocity Range (within the bundle)	0.38 – 3.5 m/s
→ corresponding $\dot{m}$	0.72 kg/s – 6.3 kg/s
→ corresponding Re	~5,000 – 40,000

Table 5.6: Flow Velocity Test Matrix

Test flow m/s at FM (gpm)	**Reference** m/s (gpm)	**CSS Type 1** m/s (gpm)	**CSS Type 2** m/s (gpm)	**CSS Type 3** m/s (gpm)
1	0.15 (11.1)	0.15 (11.1)	0.15 (11.1)	0.15 (11.1)
2	0.30 (22.2)	0.30 (22.2)	0.30 (22.2)	0.30 (22.2)
3	0.45 (33.2)	0.45 (33.2)	0.45 (33.2)	0.45 (33.2)
4	0.60 (44.3)	0.60 (44.3)	0.60 (44.3)	0.60 (44.3)
5	0.75 (55.4)	0.75 (55.4)	0.75 (55.4)	0.75 (55.4)
6	0.90 (66.5)	0.90 (66.5)	0.90 (66.5)	0.90 (66.5)
7	1.05 (77.5)	1.05 (77.5)	1.05 (77.5)	1.05 (77.5)
8	1.20 (88.6)	1.20 (88.6)	1.20 (88.6)	1.20 (88.6)
9	1.35 (99.7)	1.35 (99.7)	1.35 (99.7)	1.35 (99.7)

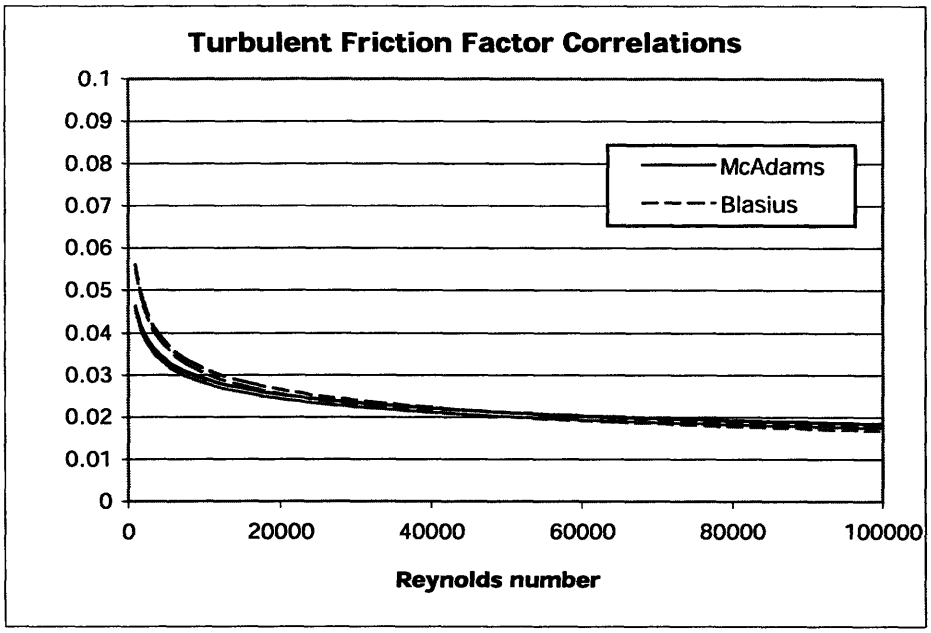

Figure 5.4: Comparison of common turbulent friction correlations

At the velocity of water required, the large Reynolds number puts flow in the highly turbulent regime. Fully developed flow requires an undisturbed length of 25 times the assembly hydraulic flow diameter; this comes out to approximately 20 cm (which differs with rod-type). A rod height of 1.5 m limits this developing region to 25% of the rod length, allowing a 1.1 m total test-length at well-developed conditions.

6. Test Facility Overview

The pressure drop test facility (Figure 6.1, 6.2) is comprised of a large reservoir which supplies a powerful pump. PVC piping is used to deliver water to the test-section and back to the reservoir tank. The set-up is supported by two main unistrut support structures, and is bolted to a wooden platform.

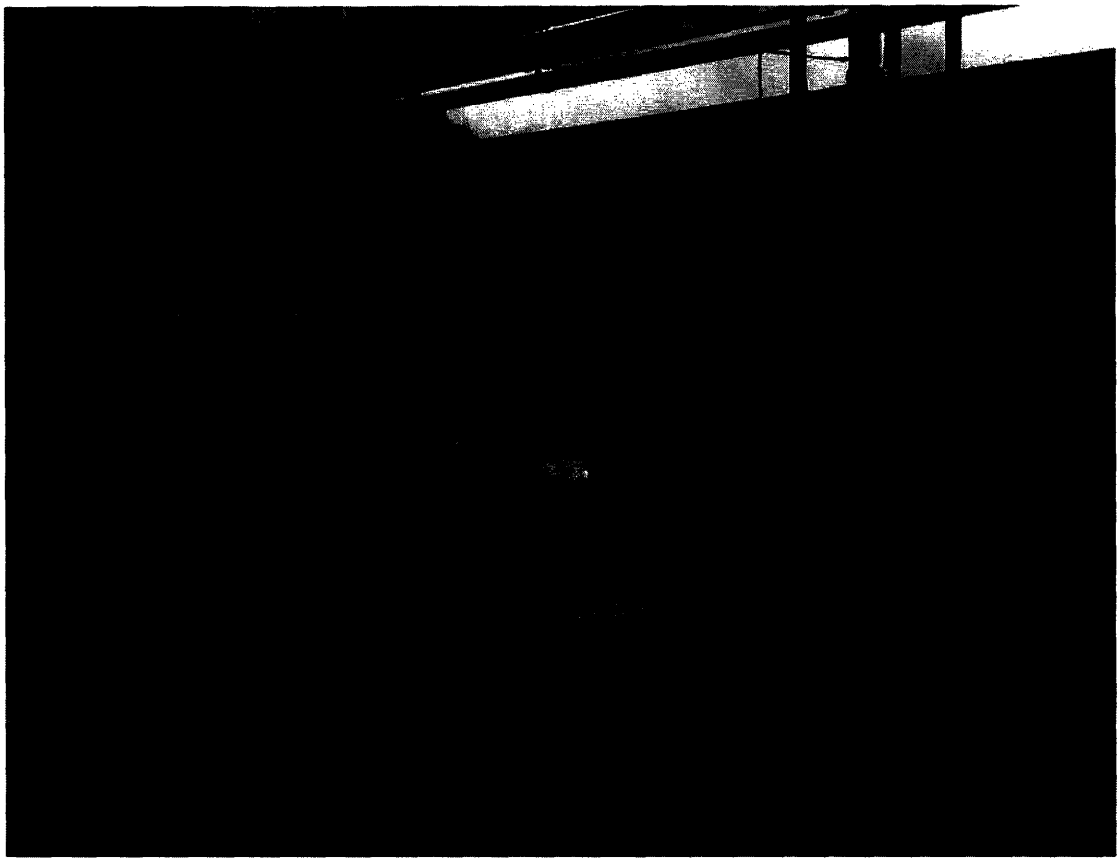

Figure 6.1: Photograph of the pressure drop facility showing outlet piping descending into water reservoir at left, the test-section (upper-right), data acquisition station (lower-right).

Pressure Drop Test Facility

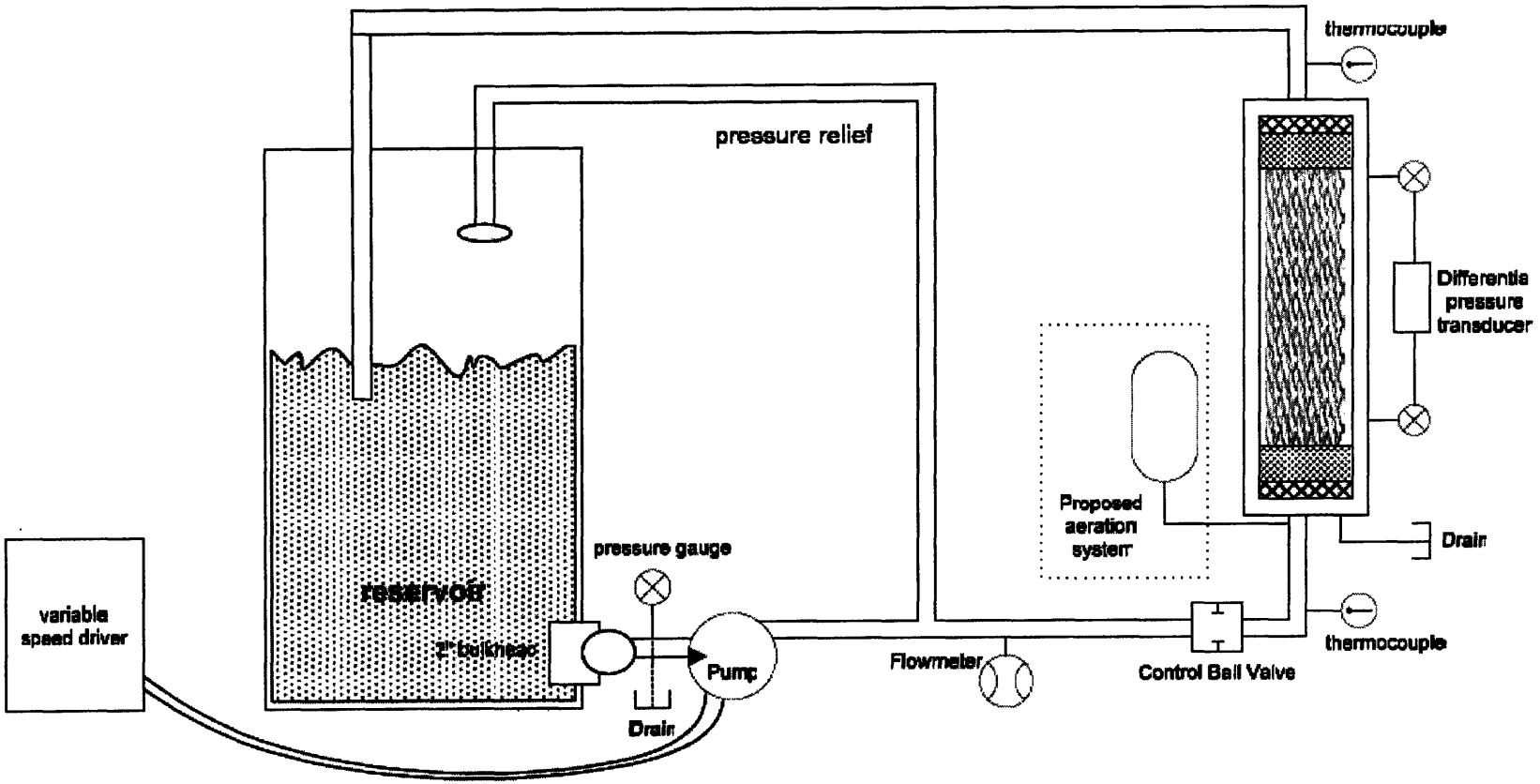

Figure 6.2: Schematic of the test facility (not to scale).

6.1 Pumping and Flow Control

Circulation is forced through the system through the use of a centrifugal pump (Ebara Model 3U), designed with impeller diameter and horsepower suited to provide our maximum desired flowspeed at our expected system head loss, shown in Table 6.1 (99.7 gpm, 12.2 psi head). Flow variability is introduced through the use of a variable speed driver, which can be adjusted for the desired flow output while maintaining the pump near its best efficiency point (Figure 6.3). The pump is shown in Figure 6.4.

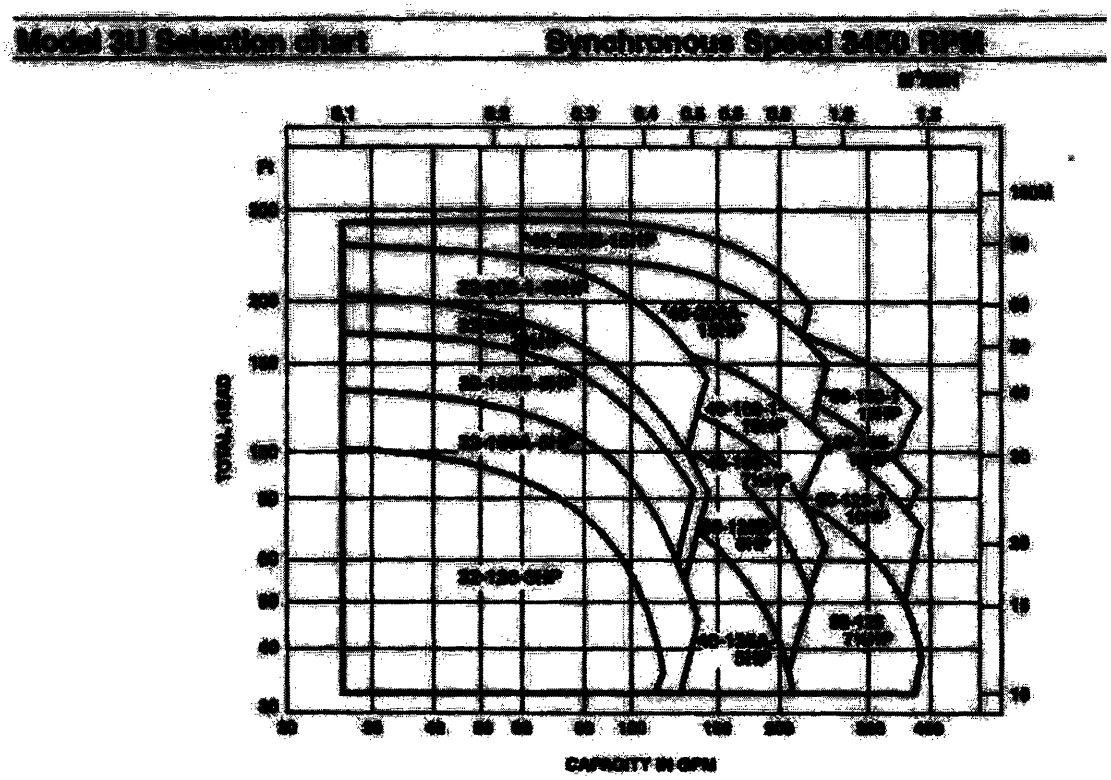

Figure 6.3: Characteristic Curve for the Ebara 3U Pump

Figure 6.4: The pump, as it is installed beside the reservoir tank.

Fine-tuning of flow control is established through the use of a 3" proportional control ball valve to further restrict and drive down the flow rate. This resembles an ordinary ball valve, but the port is extended with a triangular slit allowing for small flow adjustments. Union connections at both ends of the valve allow installation and repair without disrupting piping connections.

Table 6.1: Estimated Hydraulic Losses

For frictional losses: $\Delta p = f \frac{L}{D} \frac{\rho v^2}{2}$

Other minor losses: $\Delta p = k \frac{\rho v^2}{2}$

	Irreversible Losses k or f(L/D)	Max flow velocity m/s	ΔP – kPa
Along Piping			
Friction, 10 m	0.03 x (15m /7.6cm)	1.35	5.4
Elbow x 4	2.0	1.35	7.3
Tee x 1	0.9	1.35	0.8
Gravity (2 m)	--	1.35	19.6
Ball valves (open)	0.1	1.35	0.1
Pump outlet	6.0	1.35	5.1
Assembly			
Friction	0.03 x (1.5m/0.77cm)	3.6	37.9
Upper plate	1 -> 0.5	3.6	3.3
Lower plate	0.5 -> 1	3.6	3.3
Total Head			**82.7 kPa (12.0 psi)**

Reference: [23]

6.2 Assembly Test Section

To simulate a BWR-style assembly channel, a square duct was designed to firmly enclose the rod bundle, though an exterior cylindrical tube acts as the ultimate pressure boundary. The rod bundle was fitted with an inlet plate, perforated with holes (Figure 6.5) in order to cleanly direct flow into the bundle subchannels. The test section was to include inlet

and outlet plena, extending several inches at either side of the test-section to further ease flow development.

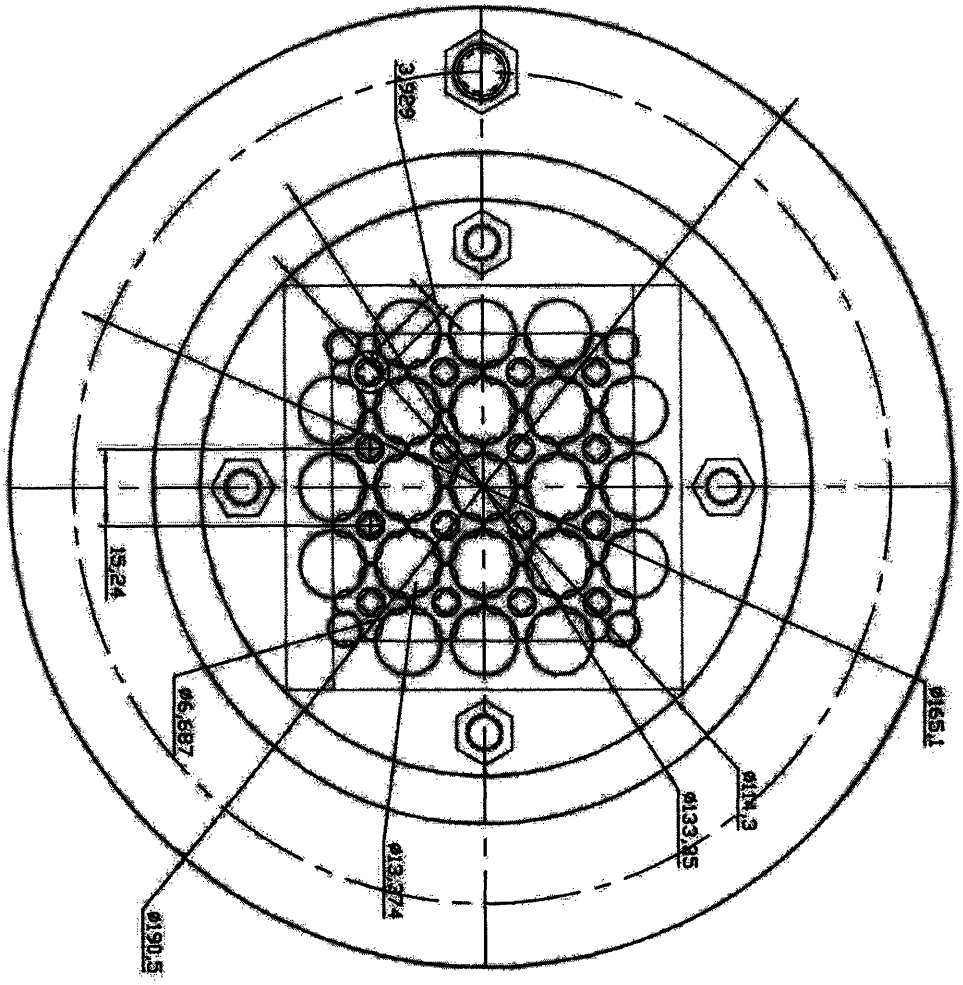

Figure 6.5: A schematic of the lateral cross-section of the assembly.

Structural rigidity requirements placed upon the test-section assembly were accomplished by securely fitting the rods into grid plates from above and below. This necessitated machining of the ends of the rods to fit carefully into special slots as seen in Figure 6.5. The array was enclosed between two plates of 90-degree angle stock, screwed tightly together, surrounding the rods into a tall cylindrical box (Figure 6.7). These stock plates are clamped between the grid plates as well, which are fastened together with 4 threaded rods extending the entire length of the assembly tube. This construction is surrounded by

a flanged aluminum tube, which is capped by plena at the top and bottom. From the plena, the assembly transitions smoothly to PVC piping, attaching it to the rest of the piping system. Here, union attachments (Figure 6.8) allowed for easy removal when loading and unloading the assembly.

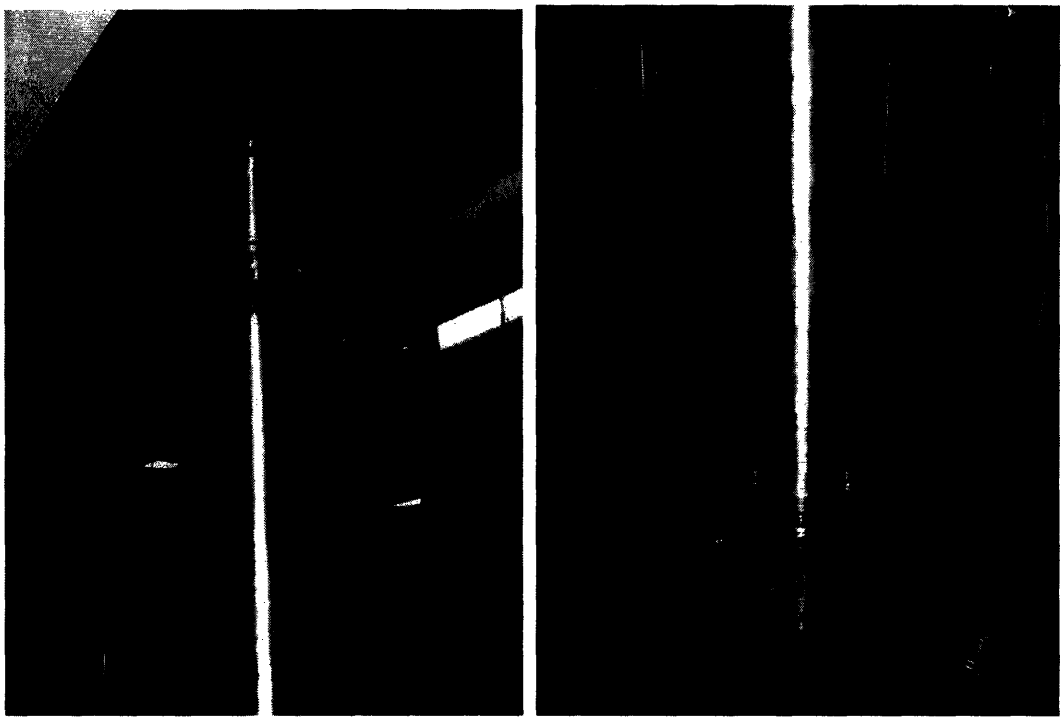

Figure 6.6: (L) The top of the assembly test section, showing plenum and union connections. (R) bottom of the test-section.

The rod assembly tube, which exceeds 100 pounds when fully loaded, is mounted on a sturdy unistrut support. As seen, the outer aluminum tube is tightly caged to prevent motion during operation (Figure 6.6). Significant effort was made to ensure that the assembly components and pressure drop tubing were configured in such a way as to simplify the difficult loading and unloading process of the test bundles.

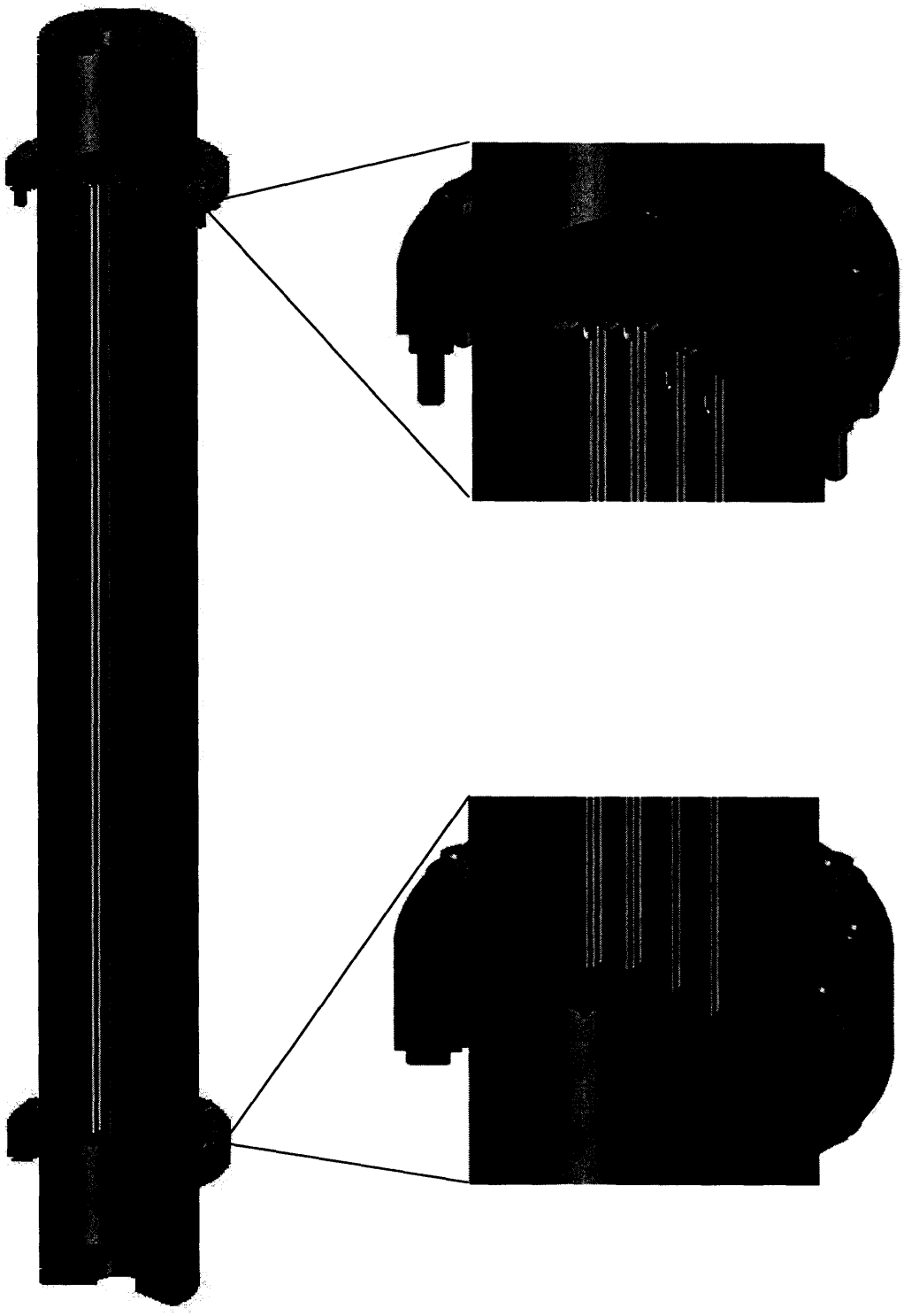

Figure 6.7: Isometric drawing of the test-assembly.

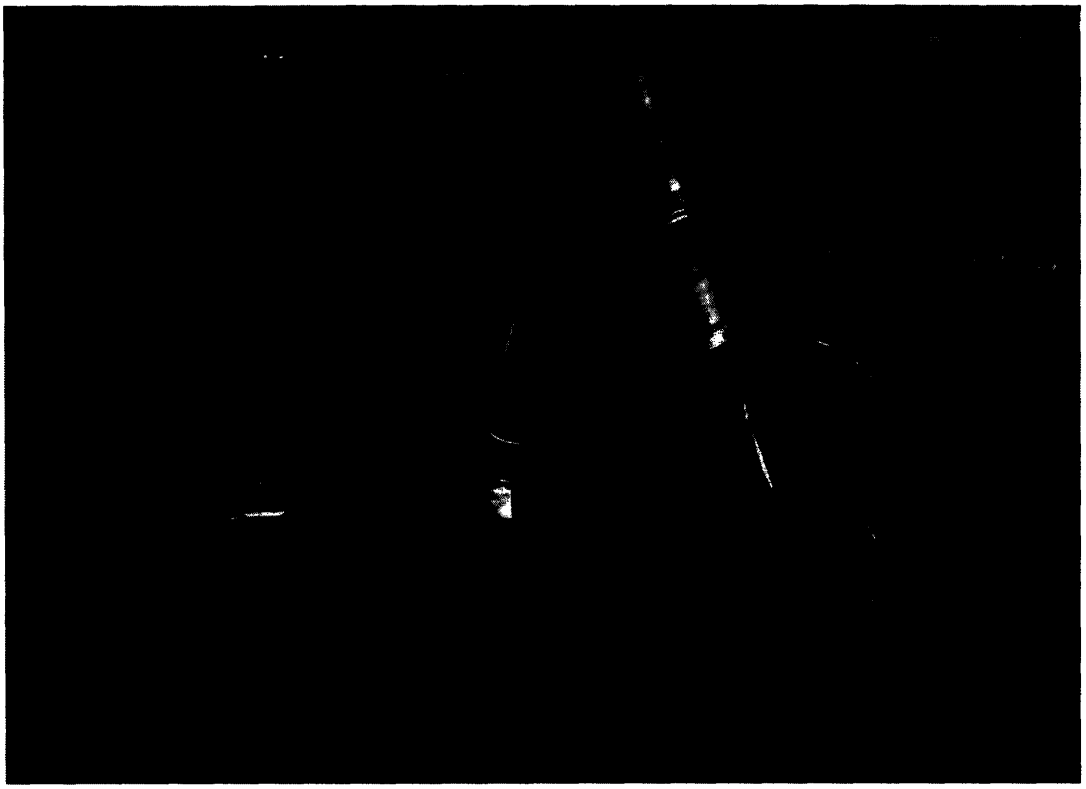

Figure 6.8: Test assembly is shown with union valves unattached.

6.3 Piping

For pumping of water at room temperature and pressure, the easy choice of piping was PVC. However piping manufacturers recommend a maximum linear flow speed in schedule 80 PVC piping of 5 feet/sec (1.52 m/s). Flow above this speed increases the rate of deterioration of walls, a phenomenon known as scrubbing.

The piping system must be able to deliver 6.3 kg/s of water to the assembly as dictated by the desired maximum flow speed, shown in Table 28. A 3" pipe diameter limits linear speed to 1.35 m/s at the maximum necessary flow conditions. Choosing a large 3" diameter sets the overall size of the facility, since 20-25 diameters are required to allow flow to settle before and after the flowmeter. This translates to 10 -12 feet of undisturbed horizontal flow surrounding the flowmeter.

6.4 Flow-meter

The flow meter chosen (Burkert Electromagnetic Flow Transmitter Type 8401) was designed for use with large pipes, ranging in diameter from ½" to 16". It uses a magnetic insertion sensor (Figure 6.9), composed of an electronic module and stainless steel electrode sensors. Operation is based on Faraday's Law, which states that the voltage induced across a conductor as it moves normal to a magnetic field is proportional to the velocity of that conductor. The flowmeter is fitted with a 4-20 mA output, a pulse rate output, and a relay output.

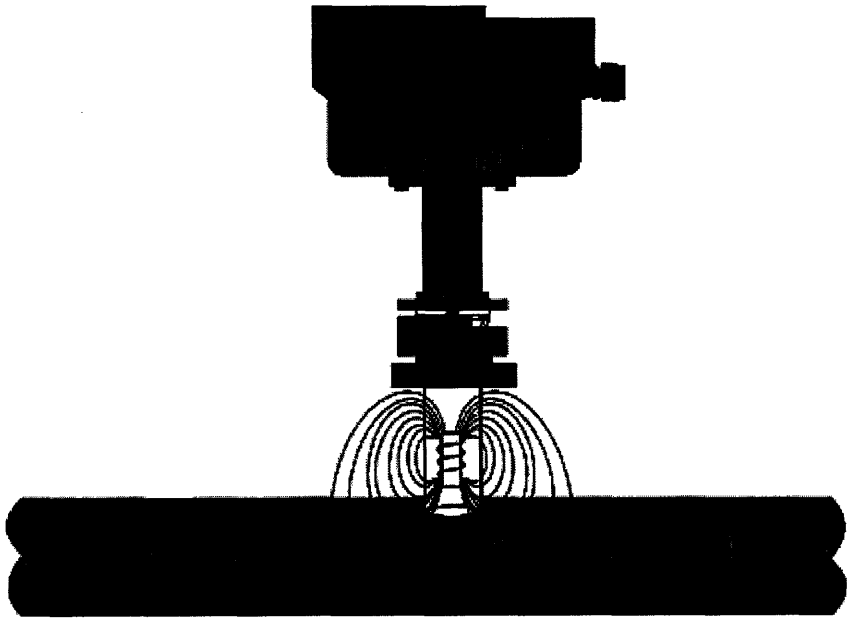

Figure 6.9: Schematic of Omega Magnetic Insertion Flowmeter [24]

The device was positioned 20 hydraulic diameters (5 feet) downstream from the nearest flow disturbance, as well as 10 diameters upstream of the nearest disturbance, as recommended to ensure a stable measurement. With a rated range of 0.3 – 32.8 ft/sec, it advertises an accuracy of ± 2% of the measured flow speed, with a repeatability of 0.25% and a linearity of ± 1% of measured value.

6.5 Differential Pressure Measurement

Pressure drop was measured using a unidirectional wet/wet differential pressure transmitter (Omega Model PX23000-5DI). This functions by converting pressure difference into an analog electrical signal by the physical deformation of a diaphragm, which introduces stress to attached strain gages. The resultant strain produces an electrical resistance change proportional to the pressure difference. The device takes a power supply at 24 volts DC and outputs a 4-20 mA signal.

Minimum sensitivity of the differential pressure transmitter was determined by the expected pressure drop at the low end of the flow test range, estimated to be 1.5 kPa (0.2 psid), though it should have the ability to detect pressure drops at the higher range as well, expected to be around 4 psi. For this application the selected transmitter measures a maximum of 5 psi. The transmitter boasts an accuracy of ±0.25% of full-scale measured value, which includes linearity, repeatability, and hysteresis.

Pressure taps were located 20 hydraulic diameters from the top of the gridplates. A small elbow fitting, with one side exposed to the flow channel, leads to 1/8" nylon piping (Figures 6.10, 6.11), which transitions to ¼" stainless steel piping at the assembly tube boundary (Figures 6.12, 6.13), then continues to the pressure measurement device (Figure 6.12).

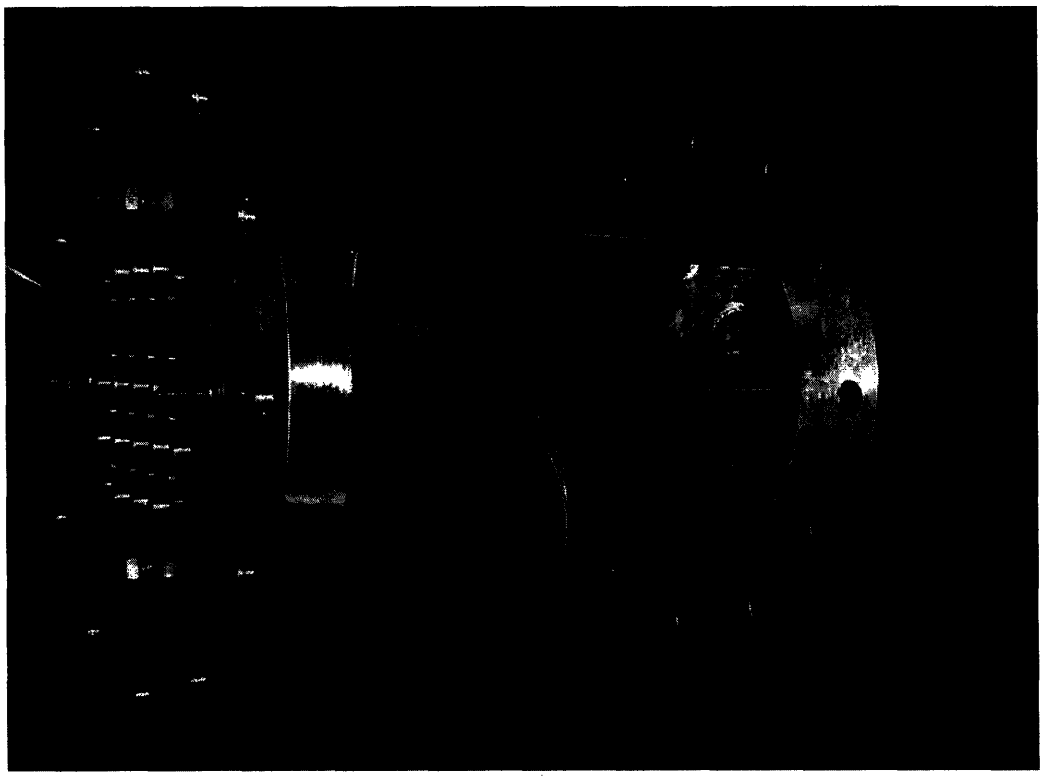

Figure 6.10: Nylon tubing leading from the pressure tap elbow through bottom gridplate.

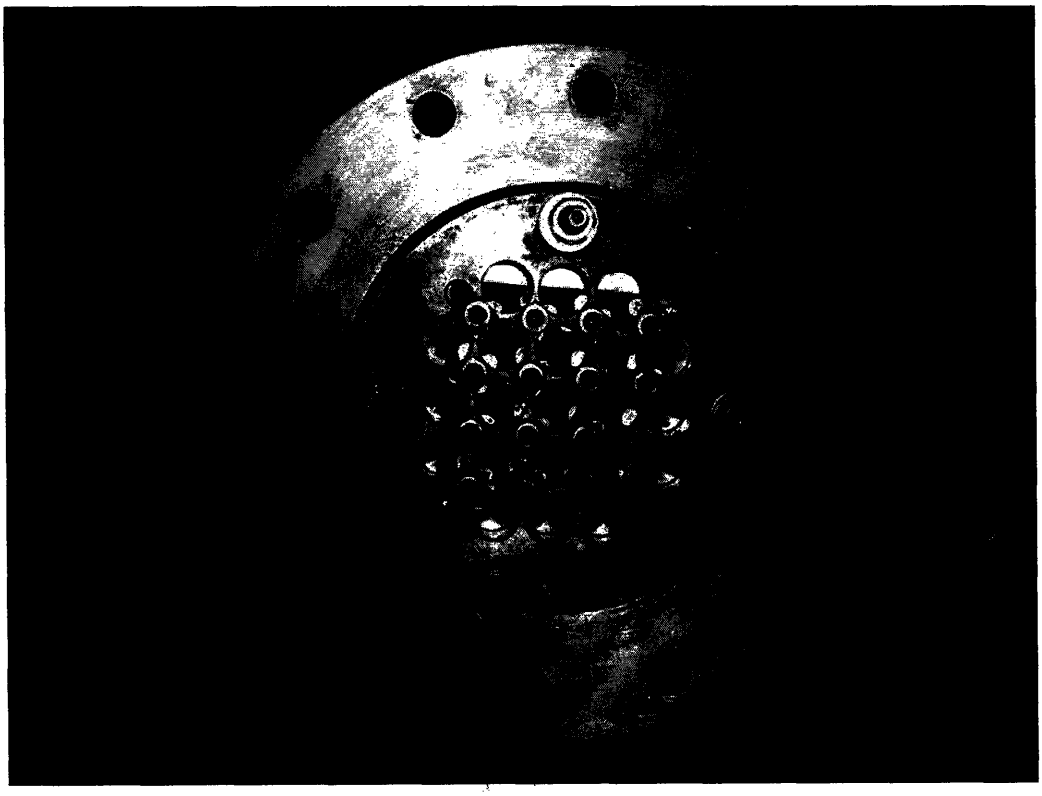

Figure 6.11: Nylon tubing leading from the pressure tap elbow through top gridplate.

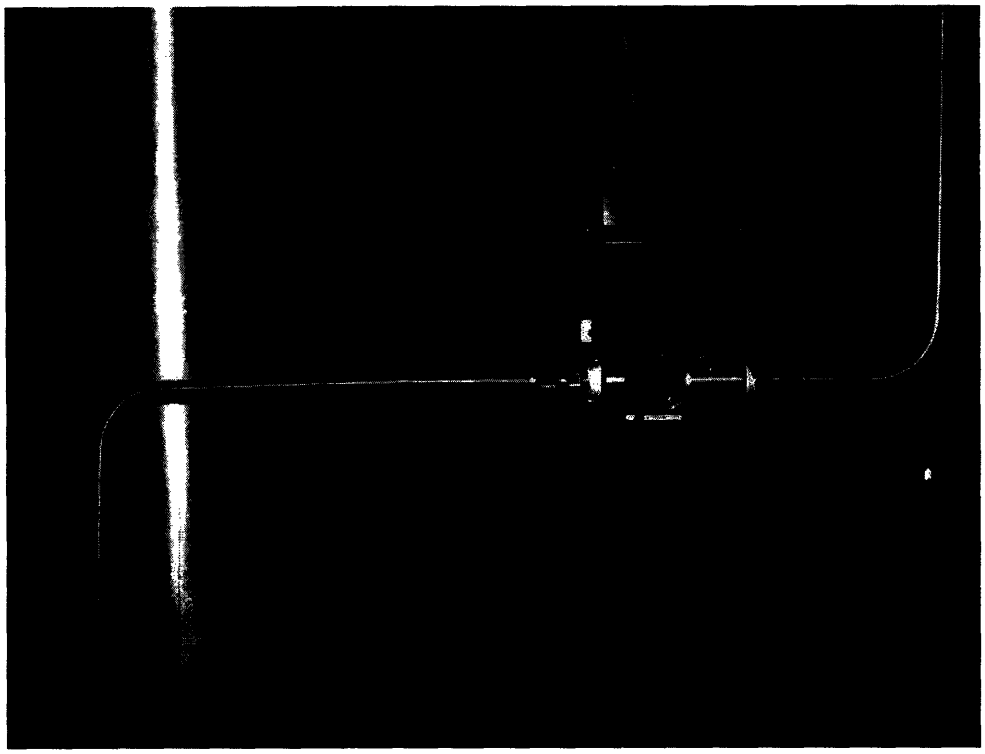

Figure 6.12: High and low side tubing leading into the differential pressure transmitter.

Figure 6.13: Pressure tubing outside the assembly, heading out of the upper plenum.

6.6 Temperature Measurement

Heat introduced by viscous resistance within the pump and other pressure losses within the system drive the water above room temperature over time. Two stainless-steel sheathed and grounded K-type thermocouples are used (McMaster-Carr Air/Immersion Thermocouple Probes with Flat-Pin Mini Connector, #3) – one at the test-section input and one close to its output. These monitor the change in water temperature during operation, and therefore the changes to the fluid dynamic viscosity. The probe is a 1/8" stainless steel pipe which protrudes an inch into the pipe though use of a PVC mounting saddle.

6.7 Water Reservoir

With a maximum flow rate near 100 gpm, the water reservoir should accommodate a large volume. Natural convection of air off of the top of the reservoir will do little to remove the added heat, at around 10 W/m^2C, with a 2-5 degree temperature difference across the interface. In order to limit temperature rises (and resultant changes in density and viscosity), an inventory of at least 200 gallons should be maintained in the reservoir. As far as weight loading of the full tank, this was estimated to be well below structural limits on the lab floor. The tank, with a 500 gallon capacity, is seen on the left hand side of Figure 6.1.

6.8 Pressure Relief Line

The pressure relief system was intended to protect the system from being subjected to pressures exceeding design limits. The system was unlikely to be deployed in the case of pipe overpressure, but instead needed to protect the pump from motor damage resulting from excessive head (pump is rated for zero flow at 90 ft, or 200 psi). The burst pressure for Schedule 80 PVC fittings is well above this level, at 280 psi.

A Tee from the main flow branch was fitted with a rupture disc (Figure 6.14). For conditions exceeding 60 psi, the disc was designed to burst, rejecting flow into the reservoir tank at a point above the water level to allow for an audible response to overpressure conditions.

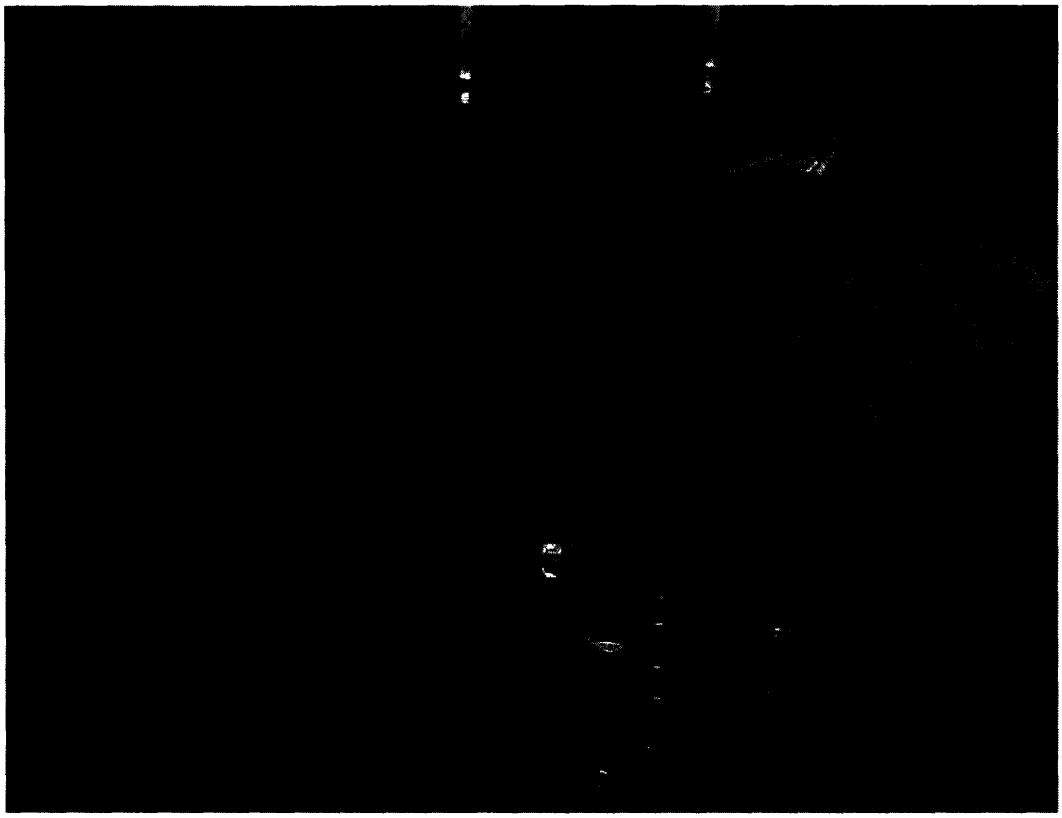

Figure 6.14: Pressure relief valve, hanging above the operating reservoir line.

6.9 Aeration

The introduction of bubbles to the inlet of the assembly can be done in the lower plenum using an in-house laboratory aeration system (Figure 6.15). The feasibility of obtaining meaningful two-phase flow data requires further investment of time and equipment before proceeding.

Figure 6.15: Aeration system connected to laboratory in-house air system.

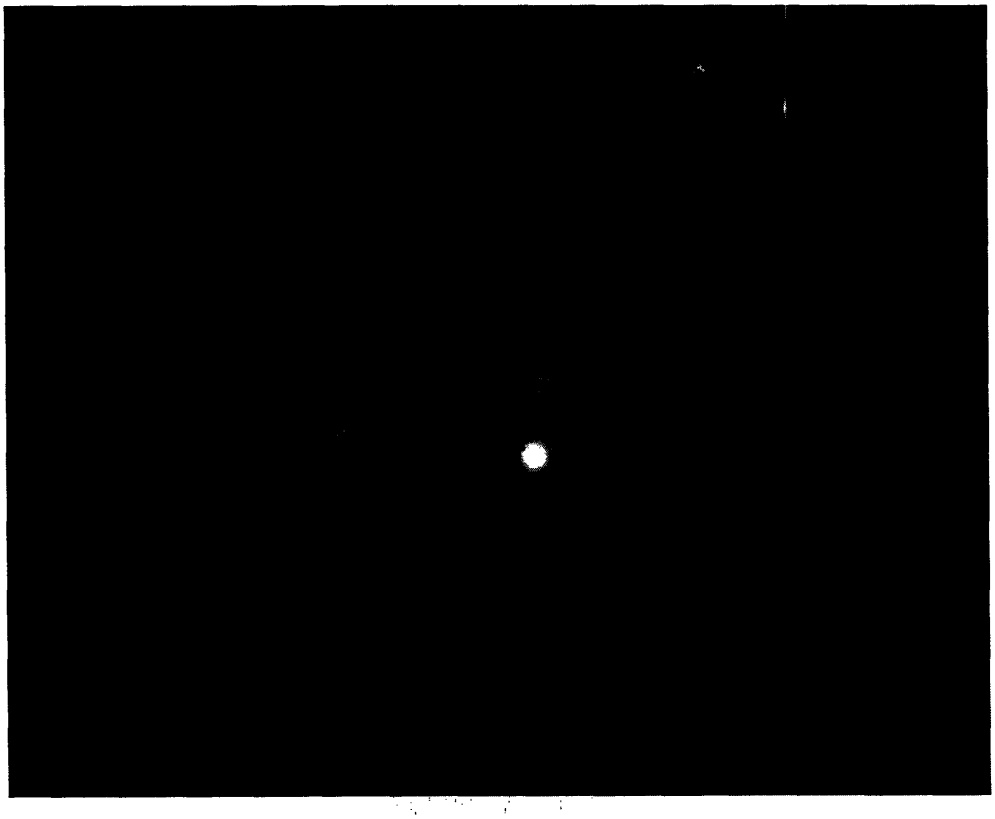

Figure 6.16: Agilent Data Acquisition system

6.10 Data Acquisition system

The data acquisition system (Figure 6.16) consists of a Digital Multi-Meter (DMM), Agilent Technologies Model 24280A, to scan the instrumentation and directly acquire current, voltage, and temperature. Offset and gain for pressure and flow velocity measurements were read by the DMM and output to a connected Dell desktop computer, where data reduction was performed.

6.11 Materials

Wherever possible, materials selection was intended to minimize corrosion and rust issues by limiting susceptible metals, dissimilar metal contact, and maximizing the use of stainless steel in wetted components including: pump head and flanges, thermocouple and flowmeter probes, and pressure measurement tubing. A limited number of brass fittings were used as needed. PVC was used for the main pipeline, for reasons mentioned above. All test-rods and the assembly structure itself were made of aluminum.

7. Validation of Measurements

Though instruments came with certification of calibration, independent confirmation was conducted to verify accuracy.

7.1 Pressure Transmitter

The differential pressure transmitter was tested by filling the loop with stagnant water and sealing off the test section using the control valve. The output of the pressure transmitter was compared with the expected hydrostatic pressure difference of known height differences within the assembly, to a good degree of accuracy, seen in Table 7.1.

Table 7.1: Pressure measurement verification

Expected dp (psi)	Measured dp (psi)	Error
0	-0.024	--
1.56	1.58	+1.3%

Expected pressure drop was defined as the quantity ρgh, "h" being the difference in elevation between the high and low side of the differential pressure measurement.

7.2 Flow meter

The flowmeter was delivered with a factory-certified guarantee of calibration. However the conditions during this calibration (pipe size, flow rate, temperature and pressure) were unknown, and therefore was assumed to confirm only repeatability.

A flow velocity verification was conducted by measuring time required to fill a bucket of known volume (5 gallons).

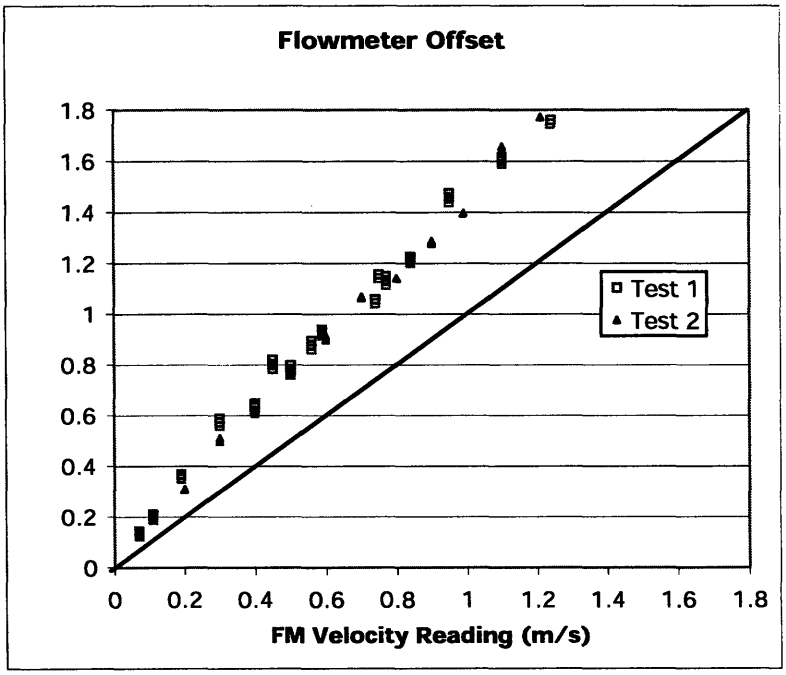

Figure 7.1: Flowmeter verification trials 1 and 2.

This seemed to show that the flowmeter was consistently underestimating flow velocity by a large margin. The test was repeated to verify repeatability (Figure 7.1), the two tests matched up well, considering the method employed here. The discrepancy between the empirical "bucket" velocity, and that which was read from the flowmeter, was large enough that a significant factor would have to be applied. The correction factor is defined by (Figure 7.2):

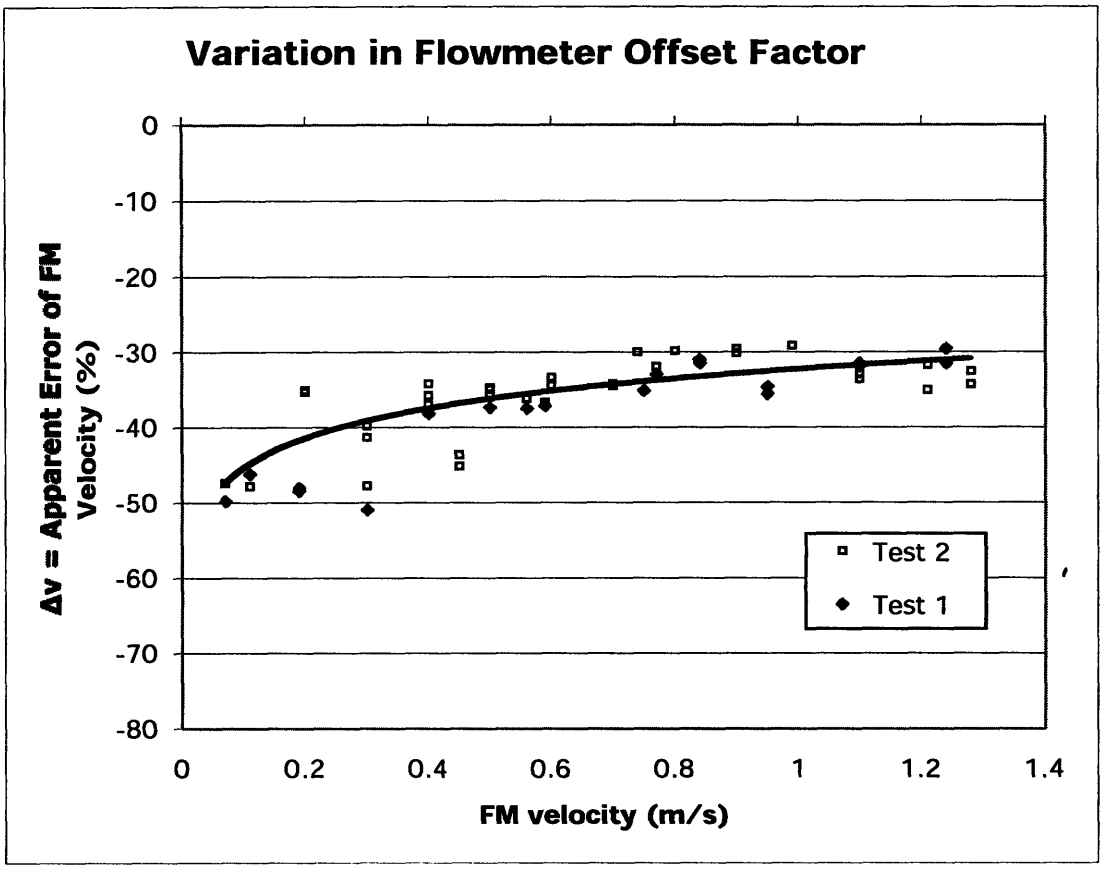

Figure 7.2: Flowmeter offset is shown as a function of measured velocity.

$$\Delta v \equiv \left(\frac{v_{fm} - v_{meas}}{v_{meas}} \right) < 0 \qquad \text{(Eqn. 7.1)}$$

$$v = v_{meas} = \frac{1}{(1+\Delta v)} v_{fm} = f_c(v_{fm}) \cdot v_{fm} \qquad \text{(Eqn. 7.2)}$$

with $f_c(v_{fm})$ being the flowmeter correction factor.

The offset factor cannot be represented as a constant to be applied over all ranges of flowmeter velocity. Seen in Figure 7.2, the factor is very large (about 50%) at very low velocities, but improves steadily. Near the high end of velocities, at which the most important data will be taken, the correction factor stabilizes. Here, the velocity is still underestimated at the flowmeter by around 30%.

7.3 Comparison to Published Correlations

With pressure and velocity measurement accuracy determined, it became possible to perform a quick check of the reference cylindrical rod bundle data to established correlations. This was accomplished by selecting a cylindrical tube correlation, then applying an appropriate multiplication factor to account for the rod-bundle geometry. Still, there is a spread among the correlations that might be selected for tube. The Blasius Relation (Eqn. 7.3) is common for smooth tube turbulent losses, for Re<30,000:

$$f_{tube} = 0.316\mathrm{Re}^{-0.25} \qquad \text{(Eqn. 7.3)}$$

The McAdams correlation (Eqn. 7.4) is used for smooth tubes in even more highly turbulent flow, Reynolds numbers of 30,000 to 100,000.

$$f_{tube} = 0.184\mathrm{Re}^{-0.2} \qquad \text{(Eqn. 7.4)}$$

Finally, the Altschull correlation (Eqn. 7.5) [23], more commonly given in Russian texts, is correlated to rough tube data, and takes the form:

$$f_{tube} = 0.11\left(\frac{\Delta}{D_e} + \frac{68}{\mathrm{Re}}\right)^{0.25} \qquad \text{(Eqn. 7.5)}$$

where Δ/D is the relative roughness of the flow channel walls (with absolute roughness, Δ, is usually ~10 microns).

These three correlations are compared in Figure 7.3 below. Also in this diagram, the Altschull correlation is compared to points from the more commonly used Moody chart. These points were solved for using MATLAB to evaluate the Colebrook equation (Eqn. 7.6), of which the Moody diagram is a graphical representation.

$$\frac{1}{\sqrt{f}} = -2\log_{10}\left[\frac{\Delta/D_e}{3.70} + \frac{2.51}{\mathrm{Re}\sqrt{f}}\right] \qquad \text{(Eqn. 7.6)}$$

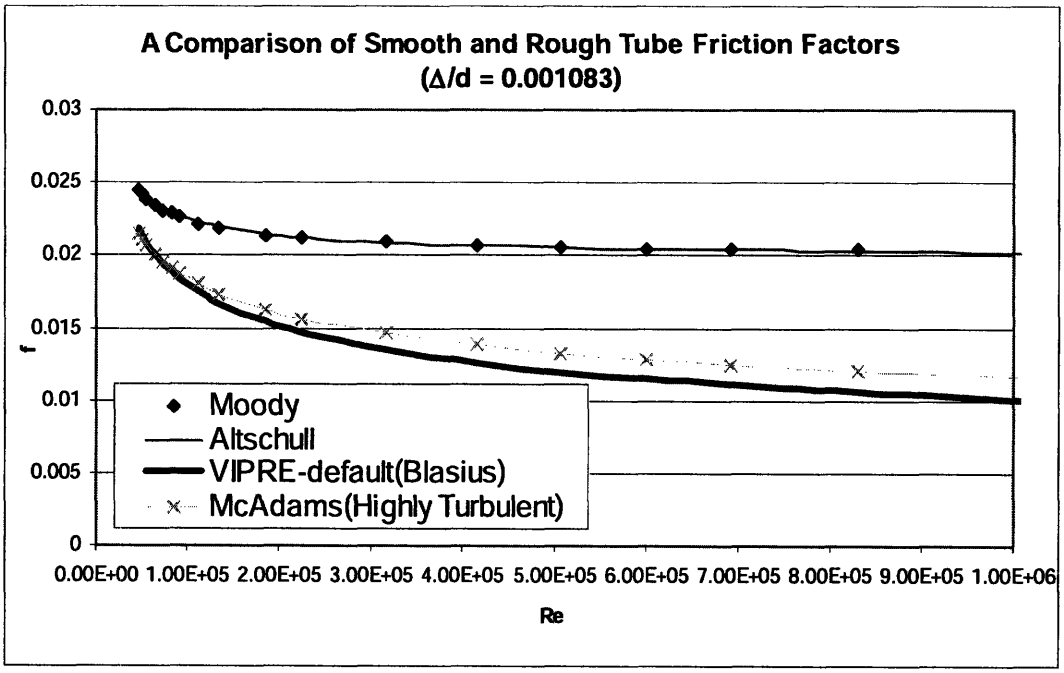

Figure 7.3: A comparison of various friction factor correlations over a wide range of Re.

Agreement between the Altschull and Moody rough cylindrical tube factors is dead-on. Because the test rods are engineering-grade surfaces with a roughness close to 10 microns, the Altschull correlation was selected as the base-line tube friction factor. This was fitted with a 1.055 rod bundle factor (based on Rehme [25]), for cylindrical tube rod bundles with the reference case P/D. This is done in concert with the effective-assembly-diameter approach, using a hydraulic diameter defined as $4A_f/P_w$ for the assembly as a whole. The result is given in Equation 7.7.

$$f_{assembly} = 1.055 \cdot 0.11\left(\frac{\Delta}{d_h} + \frac{68}{\mathrm{Re}}\right)^{0.25} \qquad \text{(Eqn. 7.7)}$$

From this point, the friction factor can be extracted from preliminary data taken for the cylindrical rod bundle, according to Equation 7.8.

$$f = \frac{2D_e}{\rho L}\left(\frac{\Delta p}{v^2}\right) \qquad \text{(Eqn. 7.8)}$$

This is compared with the friction factor developed from published correlations (Figure 7.4), using two different velocity definitions. First the experimental friction factor is shown, calculated as if the flowmeter velocity is accurate as read (a), and second, the friction factor is calculated using the correction factor developed in Figure 7.2 and Equations 7.1 and 7.2.

Deviation from the correlation which results from treating the flowmeter velocity as accurate, as well as the good agreement that is obtained using the corrected-velocity data, serves to further confirm the corrective factor.

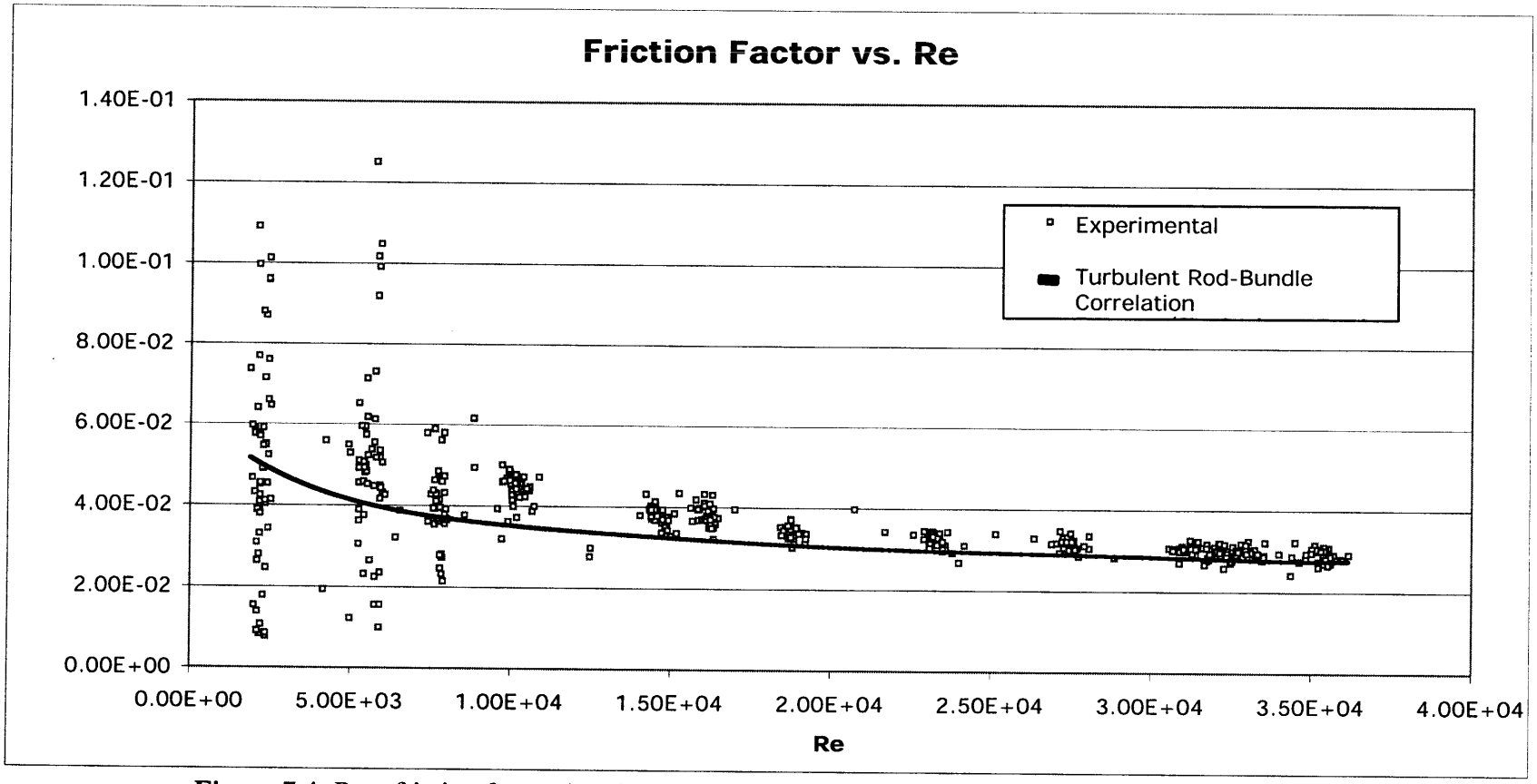

Figure 7.4: Raw friction factor data for cylindrical test rods, compared with established correlation.

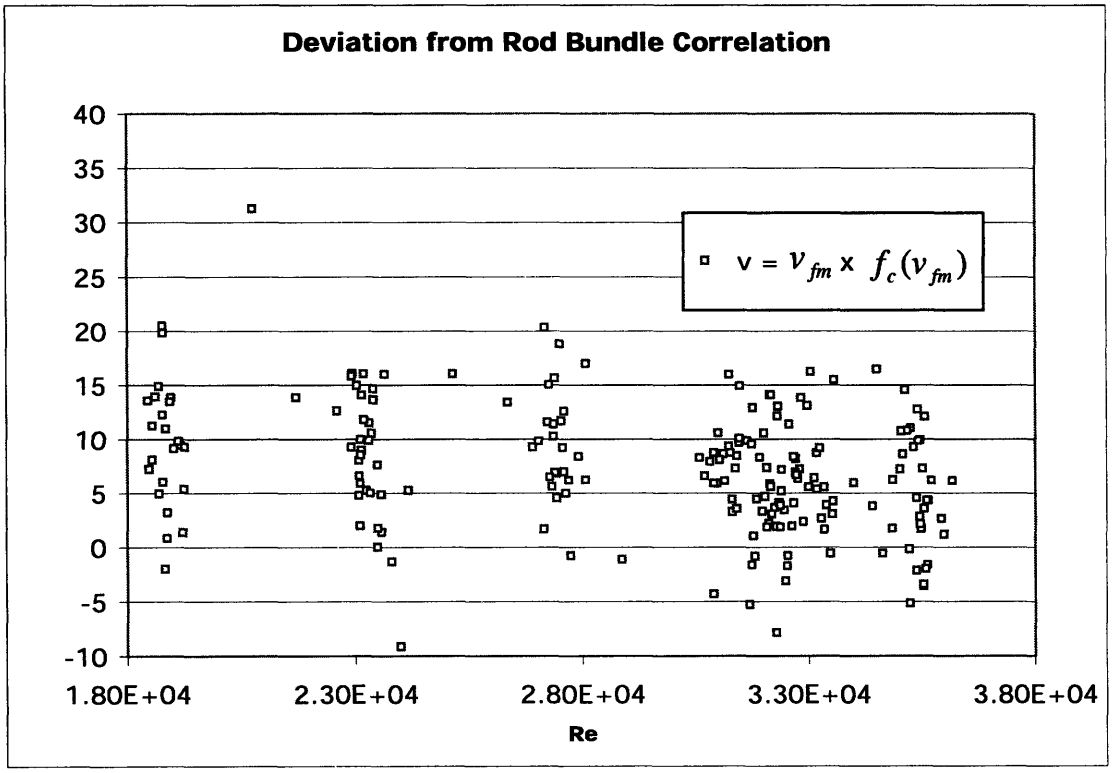

Figure 7.5: Fractional deviation from the Altschull correlation, with the velocity corrective factor (Eqn. 7.7)

Figure 7.5 shows the fractional deviation of the experimental friction factor from the published bundle correlation used. Most of the data seems to lie within +/- 15% of the correlation described above. This figure also acts to confirm necessity of the correction factor introduced to the flow velocity earlier on.

7.4 Viscosity Measurement

Due to heat input by viscous losses within the 3 horsepower pump, water temperature within the loop was expected to rise, at least several degrees over the operation time of a given test. At room temperature, water viscosity is known to vary significantly with temperature. But, it was initially uncertain whether or not the tap-water used in this test facility could be expected to have the same viscosity as published values for water.

Using a capillary viscometer, the viscosity of a sample of our test fluid (Cambridge water) was measured. Kinematic viscosity of the fluid at room temperature was found, and compared to published values for pure water; $\nu_{H2O} = 0.8926\ mm^2/s^2$, in Table 7.2.

Table 7.2: Tap-water kinematic viscosity measurement

	ν (mm^2/s^2) Test Bulb 1	**% Difference from published value**	**ν (mm^2/s^2) Test Bulb 2**	**% Difference from published value**
Trial 1	0.8930	+ 0.45	0.8942	+ 0.18
Trial 2	0.8896	- 0.34	0.89875	+ 0.69

With very good comparison to pure water, it was decided that the known variation of viscosity with temperature for pure water could be applied to our test data. This was calculated for subcooled water at atmospheric pressure for a temperature range of 0 to 40°C using the Steam Table application SteamPro [26].

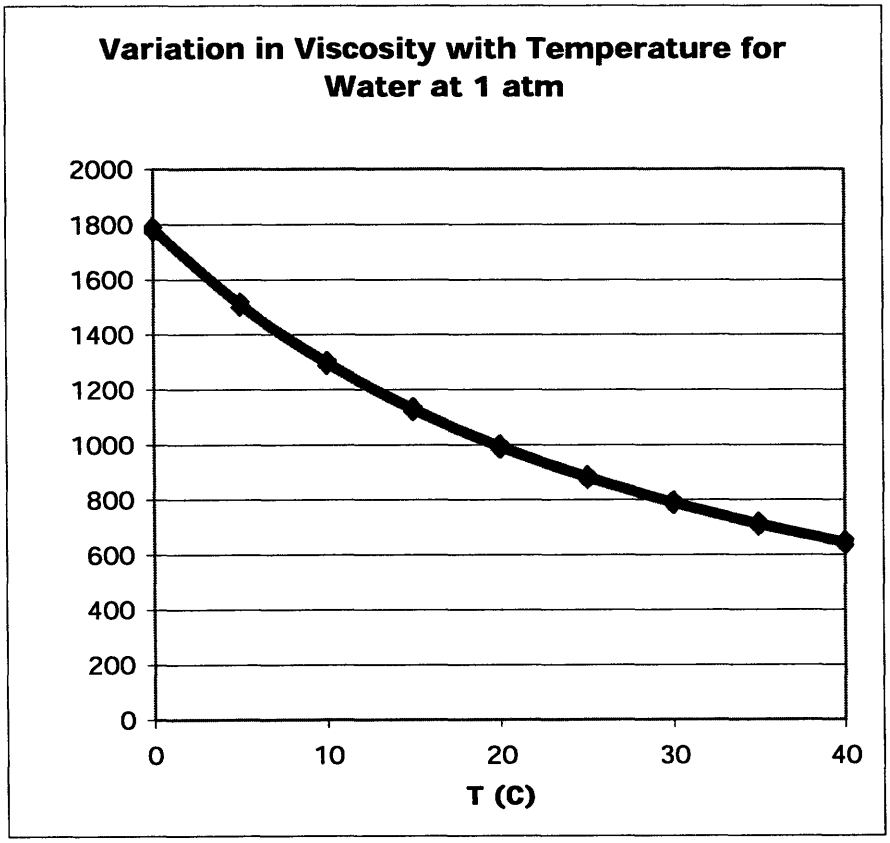

Figure 7.6: Variation in dynamic viscosity with Temperature.

As seen in Figure 7.6, viscosity does change significantly over a 5°C range for water at room temperature. Over the 20-25°C range of operation of our tests, this variation in viscosity can be linearized as:

$$\mu(T) = 1508.8 - 24.747T \qquad \text{(Eqn. 7.9)}$$

with $\mu(T)$ in μPa-s and T in °C.

8. Data Analysis

8.1 Data Reduction

Once all data collection was complete for a rod bundle test as described in the Procedure (Appendix C), raw data taken from the memory buffer was saved to file. This was converted into a neat 4-column format in Microsoft Excel, corresponding to the four measurements taken for each scan: flow velocity at the flowmeter (m/s), the corresponding frictional pressure drop (psi), and water temperatures (°C) at the inlet and outlet of the test section.

The process of data reduction was in converting these raw numbers into a dimensionless friction factor vs. Reynolds number plot for each rod type. These conversions were performed using the following definitions:

$$\mathrm{Re} = \frac{\rho v D_e}{\mu} \qquad \text{(Eqn. 8.1)}$$

$$f = \frac{2D_e}{\rho L}\left(\frac{\Delta p}{v^2}\right) \qquad \text{(Eqn. 8.2)}$$

In terms of values measured for the purposes of this experiment, which were the system temperature (T), flow velocity (v_{fm}), and pressure drop (Δp), the dimensionless numbers of Eqns 8.1 and 8.2 can be extracted according to the equations below. This requires the use of the relation $v = v_{fm} f_c(v_{fm})(A_{f_1}/A_{f_2})$ to determine the flow velocity within the assembly itself, which account for the difference in flow areas between the pipe and test section as well as the flowmeter correction factor.

$$\mathrm{Re}(v_{fm}, T, A_{f_2}, D_e) = \frac{\rho(T)\left[v_{fm} f_c(v_{fm})(A_{f_1}/A_{f_2})\right] D_e}{\mu(T)} \qquad \text{(Eqn. 8.3)}$$

$$f(\Delta p, v_{fm}, A_{f_2}, D_e, T) = \frac{2D_e(\Delta p)}{\rho(T)L\left[v_{fm} f_c(v_{fm})(A_{f_1}/A_{f_2})\right]^2} \qquad \text{(Eqn. 8.4)}$$

$T \equiv$ measured inlet temperature (°C)
$\mu(T) \equiv$ viscosity as a function of measured inlet temperature (kg/ms)
$\rho(T) \equiv$ density as a function of measured inlet temperature (kg/m^3)
$A_{f_1} \equiv$ pipe flow area (m^2)
$A_{f_2} \equiv$ test section flow area (m^2)
$v_{fm} \equiv$ flow velocity, measured at the flow meter (m/s)
$f_c(v_{fm}) \equiv$ correction factor to v_{fm}, which also varies as a function of v_{fm} (unitless)
$\Delta p \equiv$ measured frictional pressure drop (Pa)
$L \equiv$ test length (m)
$D_e \equiv$ equivalent hydraulic diameter of the test-section (m)

For a series of data scans that are taken for a given flow-velocity, as prescribed by the test-matrix (Table 5.6), all of the data during 3 minutes of continuous scanning is averaged together into a single data point. A 100-second sample of data from a cylindrical rod bundle test, at $v_{fm} = 1.2$ m/s, is shown in Table 8.1.

Table 8.1: Reduction of Sample Data at 1.2 m/s

t (sec)	T1 (°C)	T2 (°C)	dp (psid)	v_{fm} (m/s)	μ (μPa-s)		Re	f
0	23.30	23.30	2.130	1.196	932.2		37760	0.0261
5	23.30	23.29	2.008	1.217	932.4		38430	0.0263
10	23.29	23.30	2.146	1.197	932.2		37780	0.0258
15	23.29	23.29	2.039	1.207	932.5		38020	0.0254
20	23.30	23.30	2.202	1.211	932.1		38220	0.0259
25	23.31	23.30	2.014	1.200	932.1		37880	0.0252
30	23.32	23.31	2.024	1.213	931.9		38300	0.0260
35	23.31	23.30	2.028	1.233	932.1		38930	0.0262
40	23.32	23.31	2.011	1.218	932.0		38440	0.0257
45	23.33	23.33	1.971	1.192	931.5		37650	0.0260
50	23.34	23.33	2.062	1.214	931.4		38350	0.0264
55	23.34	23.33	2.161	1.213	931.5		38310	0.0259
60	23.33	23.33	2.057	1.220	931.4		38530	0.0252
65	23.34	23.34	2.091	1.207	931.2		38130	0.0254
70	23.34	23.33	2.193	1.230	931.6		38870	0.0259
75	23.34	23.35	2.122	1.197	930.9		37850	0.0263
80	23.35	23.36	1.970	1.209	930.8		38210	0.0258
85	23.35	23.35	2.166	1.218	931.0		38480	0.0260
90	23.35	23.35	2.009	1.219	931.0		38520	0.0256
95	23.36	23.37	2.094	1.214	930.5		38390	0.0262
100	23.37	23.36	2.068	1.217	930.8		38470	0.0259
Avg.							**37580**	**0.0257**

When this process is completed for each velocity in the test matrix, the graph of friction factor f vs. Re can be readily plotted for a given rod type.

8.2 Error Analysis

An analysis of the uncertainty present in the data was conducted in order to characterize the error due to equipment, and in the process, investigate possible instability in the low flow data that was detected during initial testing (Figure 7.4). Steady state readings were taken for pressure and velocity at several typical velocities (Figures 8.1-4), including in the region of apparent instability.

The study was performed by comparing error expected by equipment, using manufacturer-provided accuracies, with noise level seen in the data for given steady state conditions.

Table 8.2: Manufacturer Provided Equipment Error

Flowmeter velocity	2% of measured value; Range: 0.2 – 10 m/s
Differential Pressure Transmitter	0.25% of Full-Scale (5 psi); fixed at ± 0.0125 psi

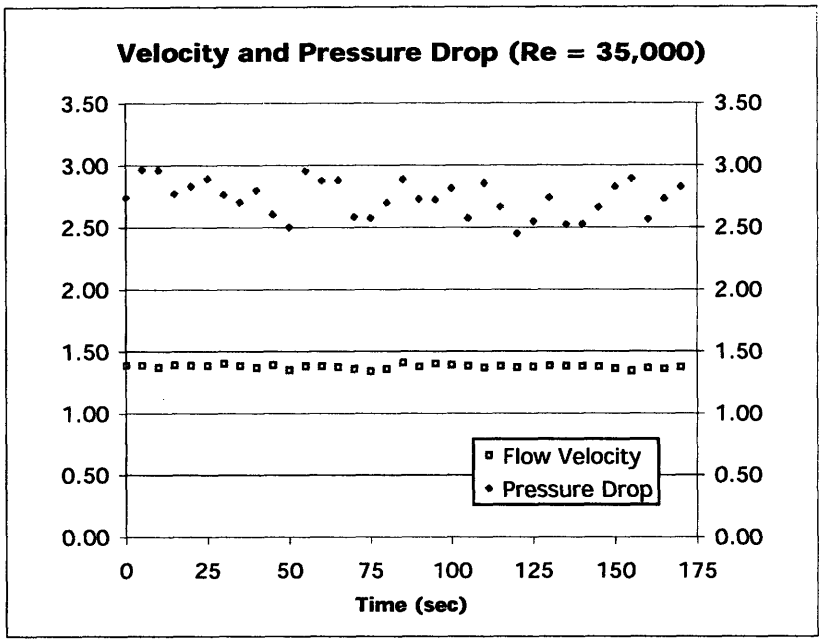

Figure 8.1: Variation in measured velocity, pressure drop with time; Re = 35,000.

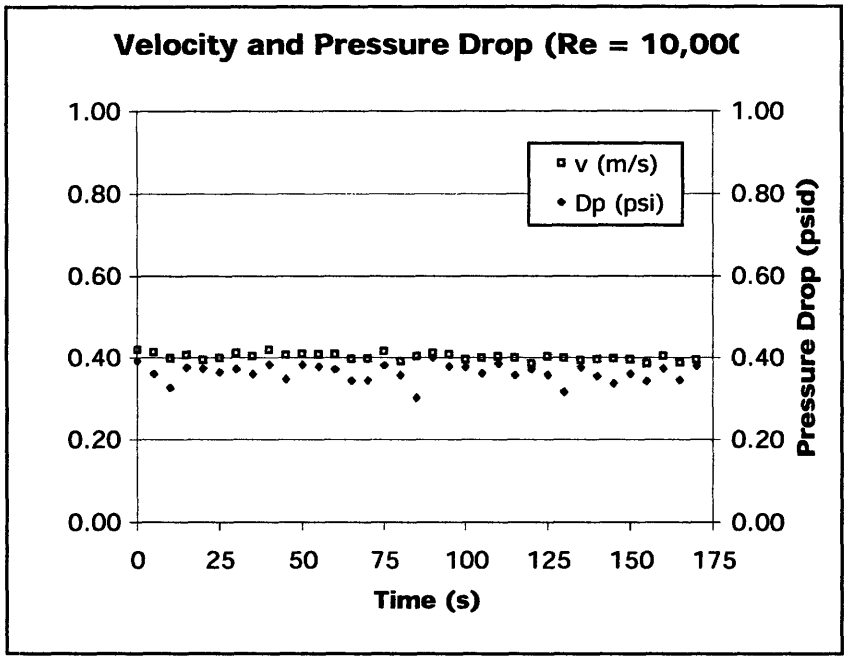

Figure 8.2: Variation in measured velocity, pressure drop with time; Re = 10,000.

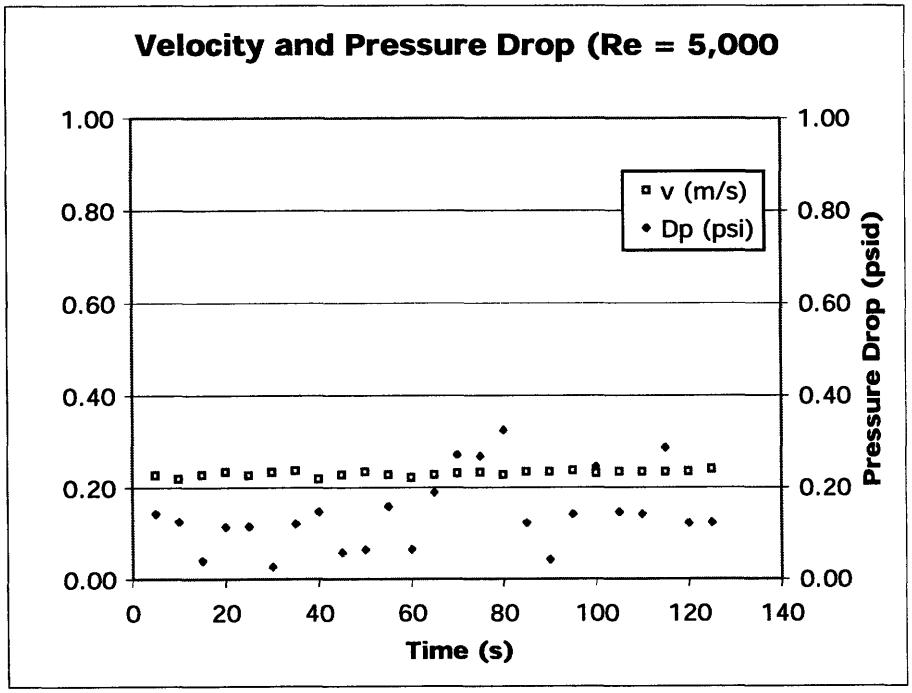

Figure 8.3: Variation in measured velocity, pressure drop with time; Re = 5,000.

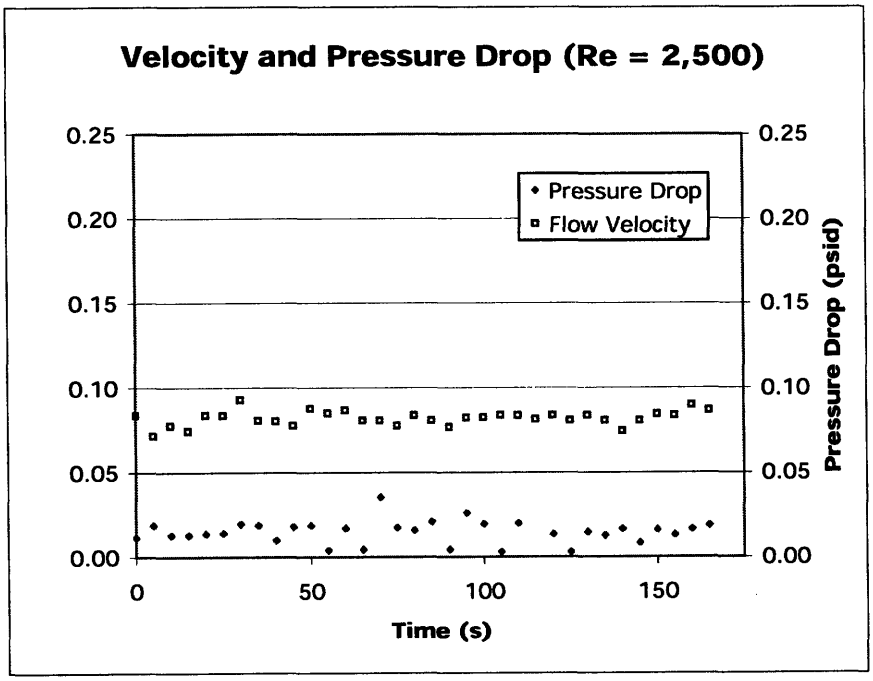

Figure 8.4: Variation in measured velocity, pressure drop with time; Re = 2,500.

In all ranges of data shown, the flow velocity seems fairly stable. Differential pressure does not show the same level of stability, instead exhibiting a higher level of noise. Evaluating standard deviations from the mean, it appears that fractional variance $(\sigma_x / \bar{x})$ becomes much larger at low Re (Table 8.3):

Table 8.3: Fractional Variance in Velocity and Pressure Differential Data, Compared to Equipment Error

Re	(σ_v / v_{avg})	Equip. Error	$(\sigma_{dp} / \Delta p_{avg})$	Equip. Error
2,500	0.0527	0.02	0.498	0.831
5,000	0.0235	0.02	0.558	0.092
10,000	0.0217	0.02	0.059	0.053
35,000	0.0112	0.02	0.053	0.040

For velocity, variance in the data is close to the given equipment error, except at low Re = 2500 (v = 0.07 m/s), which is below the prescribed range of the flowmeter.

For pressure drop, variance in the data is close to the equipment error for the higher velocities, but again not at the lower velocities. At Re = 2500, Δp_{avg} is ~0.015 psi, very close to the given differential pressure transmitter accuracy of ±0.0125 psi, leading to a very high equipment error.

The more important question is how this error propagates into error in the friction factor. Here, measurement error can be developed as follows:

For an equation $f = f(x,y)$, one can approximate total variance for two variables [27]:

$$\sigma_f^2 \approx \left(\frac{\partial f}{\partial x}\right)^2 \sigma_x^2 + \left(\frac{\partial f}{\partial y}\right)^2 \sigma_y^2 \qquad \text{(Eqn. 8.1)}$$

For $f = A\frac{x}{y^2}$;

$$\frac{\partial f}{\partial x} = \frac{A}{y^2};\ \frac{\partial f}{\partial y} = -\frac{2Ax}{y^3};$$

$$\sigma_f^2 = \left(\frac{A}{y^2}\right)^2 \sigma_x^2 + \left(-\frac{2Ax}{y^3}\right)^2 \sigma_y^2$$

$$\left(\frac{\sigma_f}{f}\right)^2 = \left(\frac{\sigma_x}{x}\right)^2 + \left(\frac{2\sigma_y}{y}\right)^2 \qquad \text{(Eqn. 8.2)}$$

Therefore, for the equation for friction factor, given by $f = \frac{2D}{\rho L}\left(\frac{\Delta p}{v^2}\right)$;

The error can be estimated from:

$$\sigma_f = f\left(\left(\frac{\sigma_{\Delta p}}{\Delta p}\right)^2 + \left(\frac{2\sigma_v}{v}\right)^2\right)^{1/2},\quad \left(\frac{\sigma_f}{f}\right)^2 = \left(\frac{\sigma_{\Delta p}}{\Delta p}\right)^2 + \left(\frac{2\sigma_v}{v}\right)^2 \qquad \text{(Eqn. 8.3)}$$

which assumes that error in density, as a function of error in Temperature measurement, can be neglected. The resulting cumulative error is given in Table 8.4.

Table 8.4: Error in derived friction factor

Re	σ_f	(σ_f / f)	Equip. Error
2,500	0.0332	0.509	0.831
5,000	0.0462	0.560	0.100
10,000	0.0048	0.073	0.066
35,000	0.0025	0.058	0.057

The fluctuations in data at Re = 2500 could be meaningless, since in this regime, uncertainty in the measured value is quite large. However for the Re = 5000 data, equipment error is limited to around ±10%, yet the noise in data is still very large, which leads to a fractional variance of ±56% (Figure 8.5).

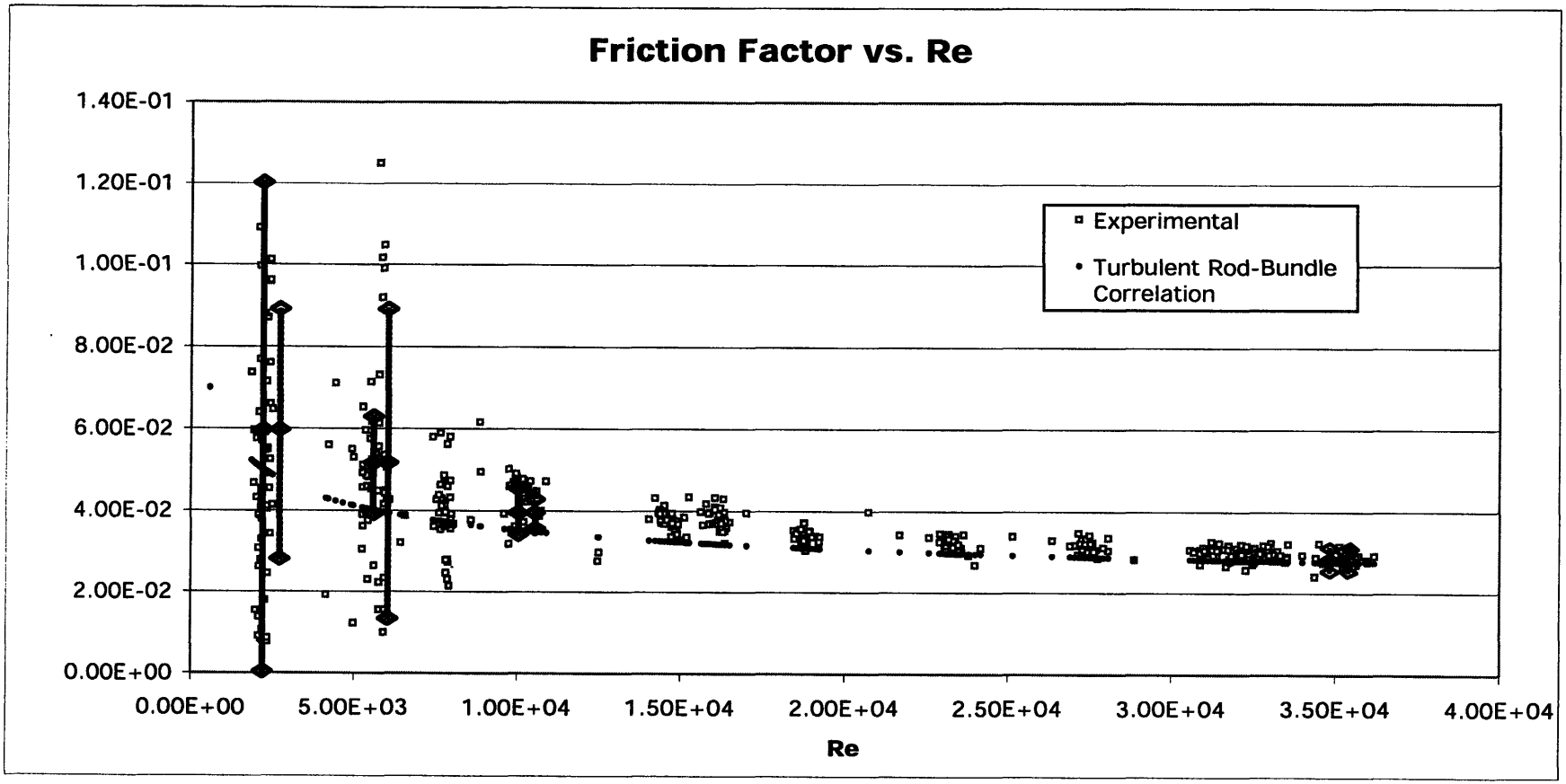

Figure 8.5: Here the solid lines represent expected uncertainty due to the equipment, and the dotted lines represent the noise level in the data.

According to Preger [27], for internal pipe flow instability can occur near log(Re) = 3.6, or Re=4000, for a roughness of D_e/Δ = 1000 (Δ=10 microns). In our case, the abnormal data occurs at Re=5000 or slightly higher, so it is not unreasonable to think that this could be the same phenomenon.

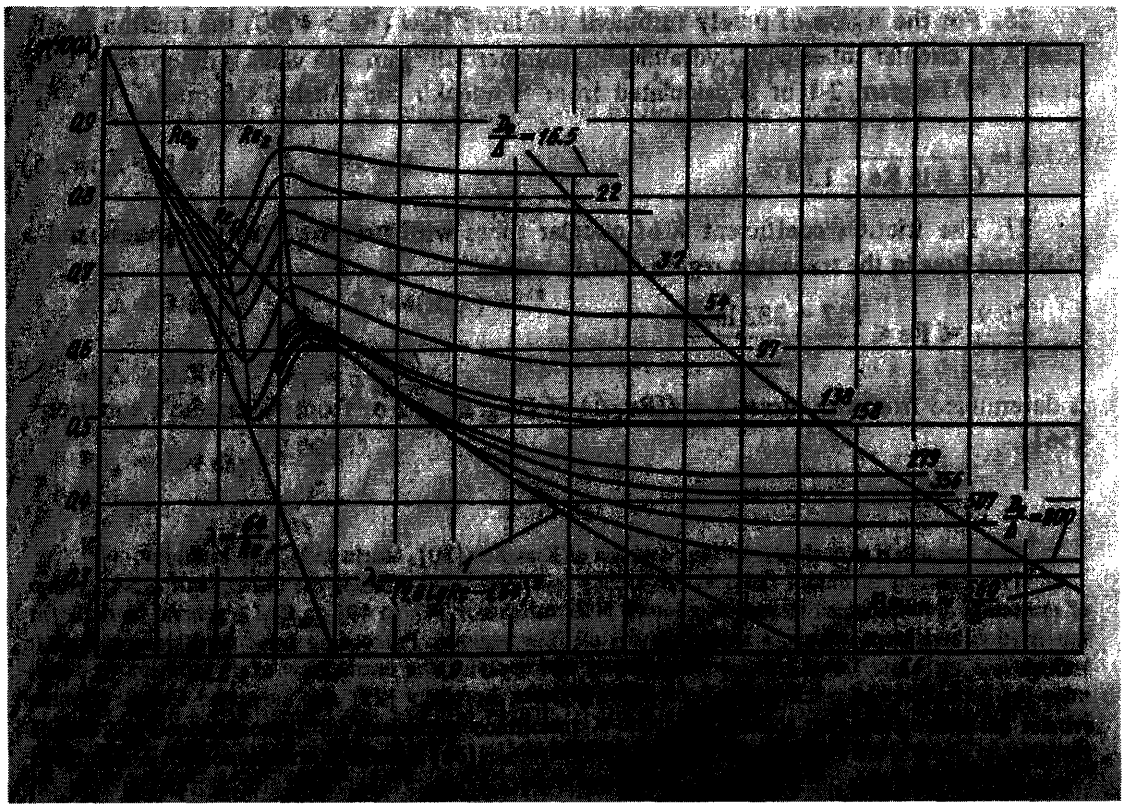

Figure 8.6: Variation of friction factor with Re, including the transition region [28].

In any case, though data is taken in this region due to curiosity, valuable information regarding the CSS/reference rod comparative friction factors can only be obtained from the high range of Re, where data has a much higher degree of certainty.

9. Results and Analysis

After testing was completed on all rod-types, over all velocities in the test matrix, the trends of pressure drop with increase in velocity were well-established. However, this left plenty of room for further analysis, including (but not limited to) the extraction of the CSS friction factor from its frictional pressure loss data, development of a unique friction factor correlation, and analysis of the overall impact of CSS rods on irreversible hydraulic losses within the core.

Additionally, using information obtained from the experiment, a correction was extended to the 2-phase core pressure drops estimated by VIPRE in Chapter 4. This led to more confident predictions of the CSS-rod core pressure drop, and how it would be affected by a core power density uprate.

9.1 Presentation of Data

In order to fully examine all information that can be obtained from this data, results are offered in several different forms, including in terms of non-dimensional parameters. It is also important to examine the uncertainty with which each data point is presented; an effort was made to clearly show this aspect as well.

First shown here is a comparison of frictional pressure drop with mass flow for each rod type (Figure 9.1). This is as close to a representation of raw, unmanipulated data as can be shown for a given test. The cross-shaped twisted rods are shown to have pressure losses that are significantly higher than for the reference rods at the high range of velocities, though there appears to be little to distinguish data for the different CSS rods. Figure 9.2 below confirms that this can be considered to have a fairly high degree of certainty. However this representation does not tell the full story.

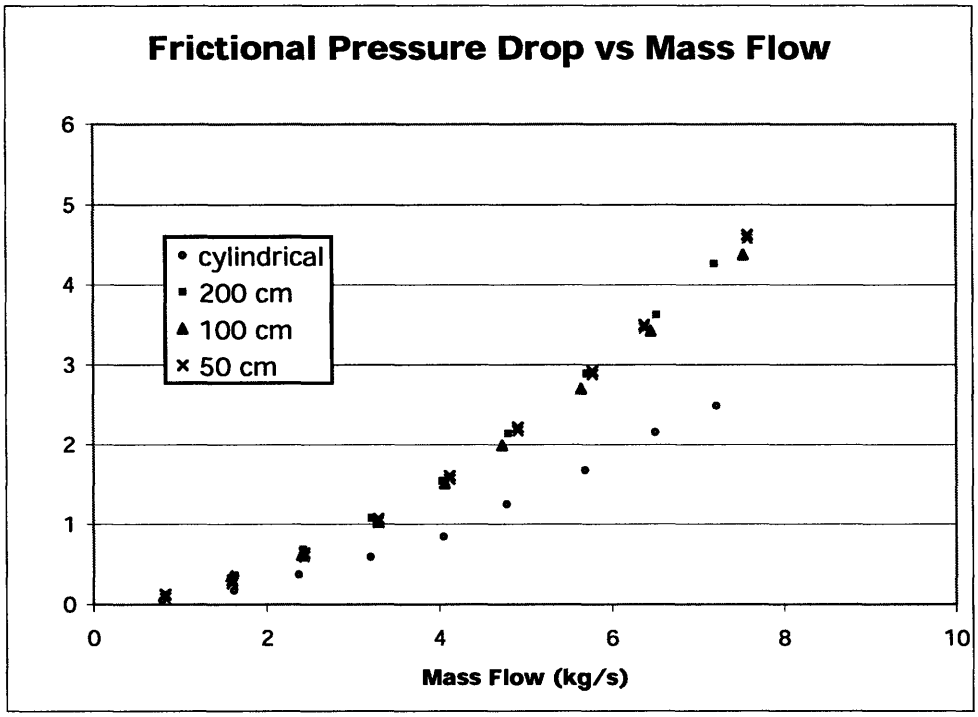

Figure 9.1: Frictional pressure drop for all rod types.

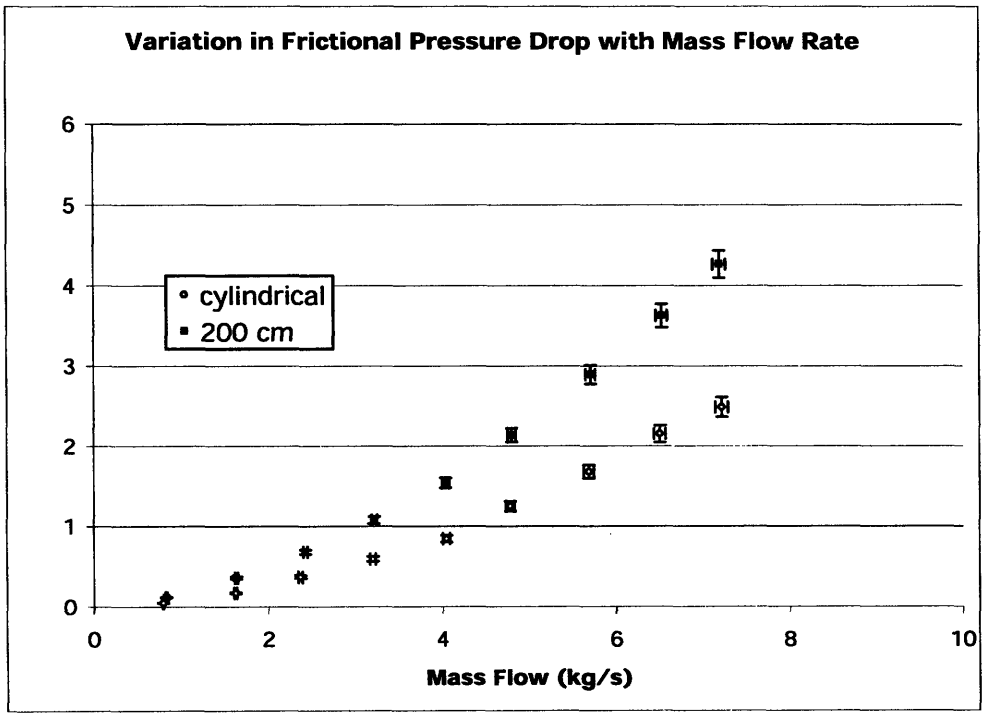

Figure 9.2: Frictional pressure drop for Reference and CSS Rod Type 1; error shown.

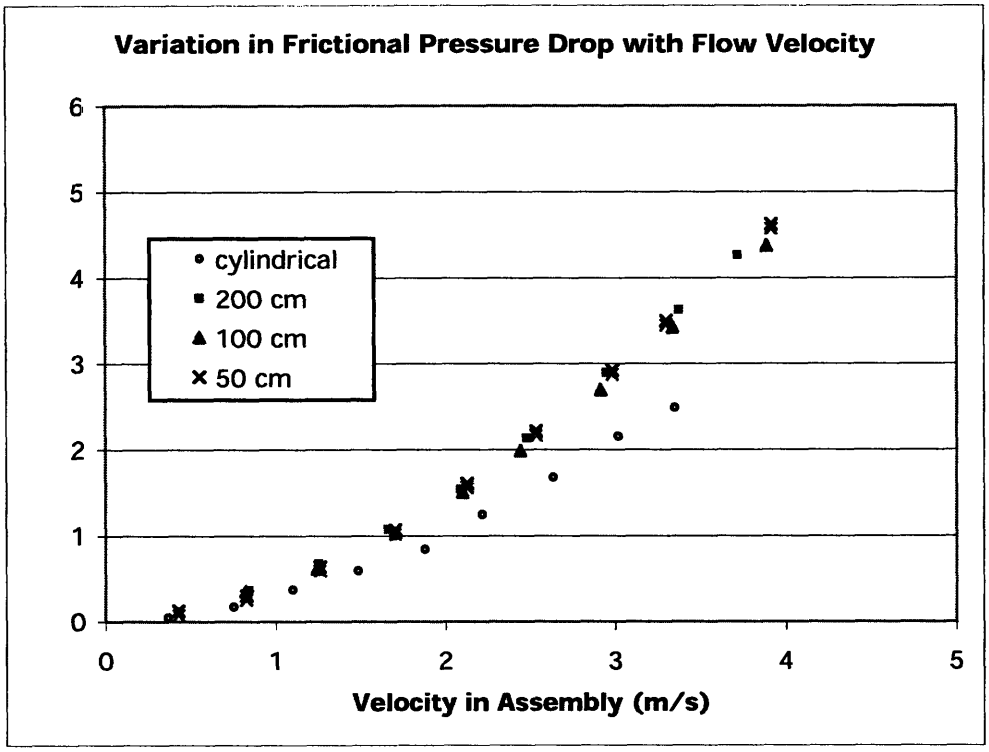

Figure 9.3: Frictional pressure drop for all rod types.

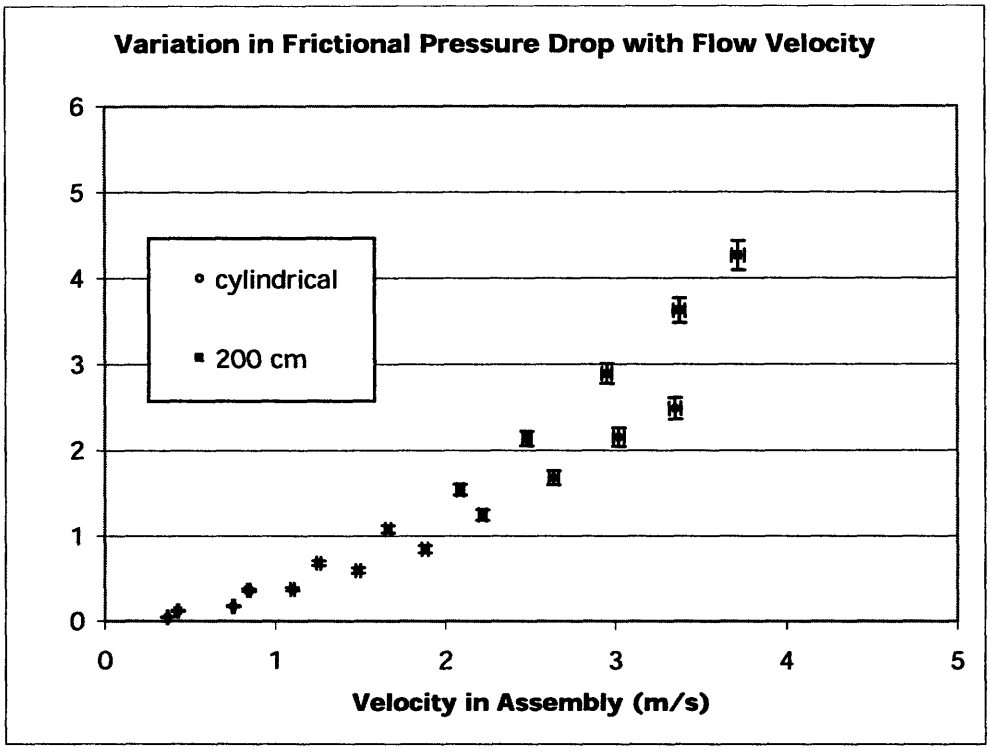

Figure 9.4: Frictional pressure drop for reference and CSS Rod Type 1; error shown.

While one would in general expect an assembly with a smaller hydraulic diameter to give rise to a larger pressure drop, the reference and CSS assemblies also have an 11% disparity in flow area, meaning that CSS assemblies face a proportionally higher flow velocity. Thus, the pressure drop, which is proportional to the square of velocity, will be higher still.

In order to de-couple the effect of flow area, it is also useful to examine the frictional pressure drop as a function of flow velocity itself, which is analogous to mass flux. Shown in Figure 9.3, the CSS twisted rods maintain a pressure drop noticeably larger than the reference case, but the gap has narrowed. Uncertainty is kept to a fairly low level in this case (Figure 9.4). This is based on analysis detailed in Chapter 8, and should be quite similar for each rod type. Data in this form more clearly shows the effect of the larger CSS surface area in comparison to the reference rod geometry, rather than the effects of flow area changes. Again, not much difference can be seen between the various CSS rod twists.

In order to gain further insight into the data, one can remove the effect of increase in surface area, and instead express each assembly as a single non-dimensional channel of hydraulic diameter D_e. Using this diameter, one can reduce the pressure drop data for each assembly into friction factors, and each measured velocity into a characteristic Reynolds number. This picture strips away all information aside from the fundamental geometrical effect distinguishing the cross-shaped spiral geometry from cylindrical rod geometry (Figure 9.5).

Remarkably, the friction factor for the CSS rods is shown to be below the friction factor for a bundle of cylindrical rods, for Re larger than 10,000. Again, little effect can be seen due to the twist pitch of the CSS rods, though CSS rods of all twist pitch seem to produce friction factors that lie comfortably below the reference case. Admittedly, data outside of the highest range of Re should be treated with care due to large uncertainty, based on manufacturer provided accuracy limits of the equipment (Figure 9.6).

However, one trend seems to be that the more tightly twisted CSS serve to turbulize the flow at lower Reynolds numbers. This is in line with what would be expected from this scenario. Previous research into eddy promoters shows a similar transition to turbulent flow at lower Reynolds numbers for set-ups with a tighter lateral pitch of cylindrical eddy promoters placed in the crossflow [29]. The pitch of eddy promoters can be seen as analogous to the twist pitch of the CSS test rods, in this case.

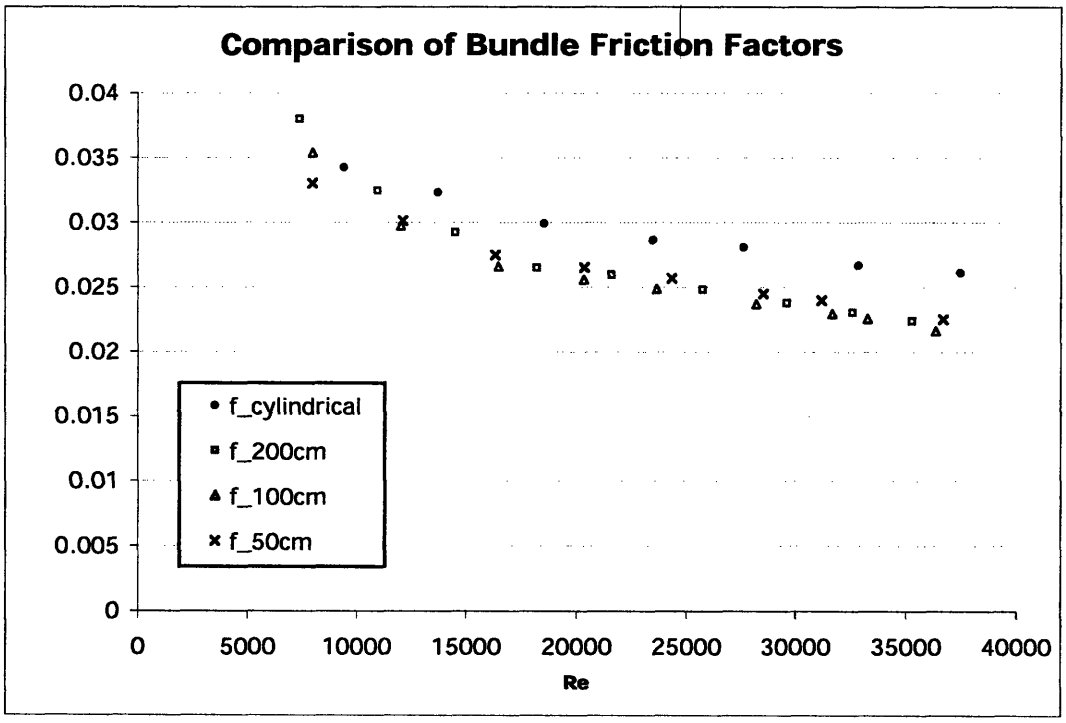

Figure 9.5: Comparison of Reference, CSS bundle friction factors.

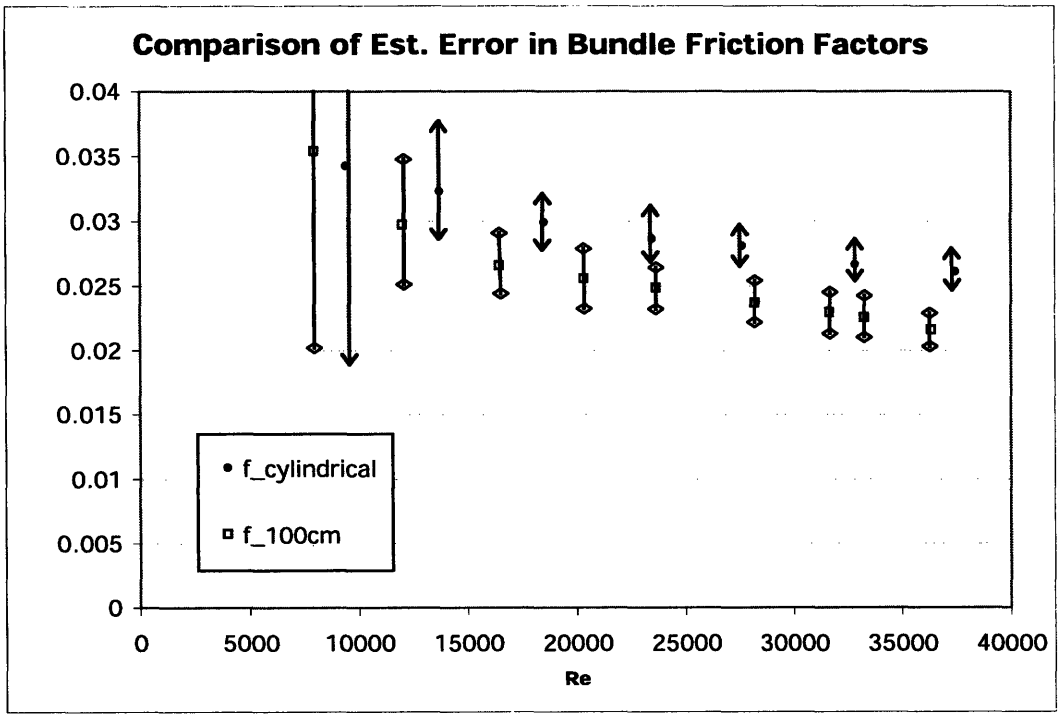

Figure 9.6: Uncertainty in reference and CSS bundle friction factors.

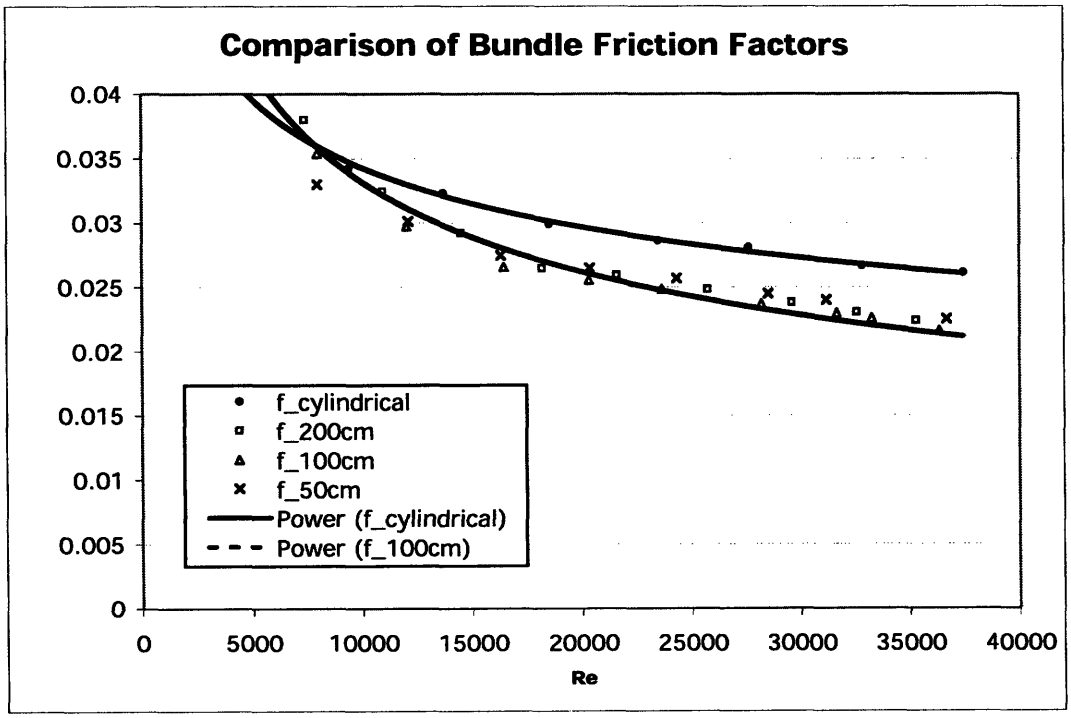

Figure 9.7: Comparison of Reference, CSS bundle friction factors; logarithmic trendlines shown.

Another small effect lies hidden in the definition of Reynolds number. For a given value of Re, data presented in Figures 9.5 and 9.7 for the CSS rods has a higher flow velocity on average than that for the reference, due to a smaller hydraulic diameter. In light of this, it is more impressive still that the CSS assembly has a lower friction factor. This is an effect that is discussed when extrapolating these results onto predictions for changes to the greater flow system.

Yet another useful manner in which to display the data is by means of a non-dimensional pressure drop term versus the flow Reynolds number. This non-dimensional friction pressure drop is, for these purposes, termed the total assembly hydraulic loss, and is represented by the expression:

$$\frac{\Delta p}{\frac{1}{2}\rho v^2} = f\frac{L}{D_e} \qquad \text{(Eqn. 9.1)}$$

This plot (Figure 9.7) enables one to clearly see the frictional pressure drop, while keeping the generality allowed by the use of non-dimensional groups. Whereas Figure 9.7 is somewhat misleading in that it suggests better friction characteristics for the CSS rods, Figure 9.8 shows that the net effect of the CSS rods is in fact an increase in pressure drop over the reference case at equivalent Reynolds numbers. The margin between these two cases, however, appears to diminish significantly at high Reynolds numbers.

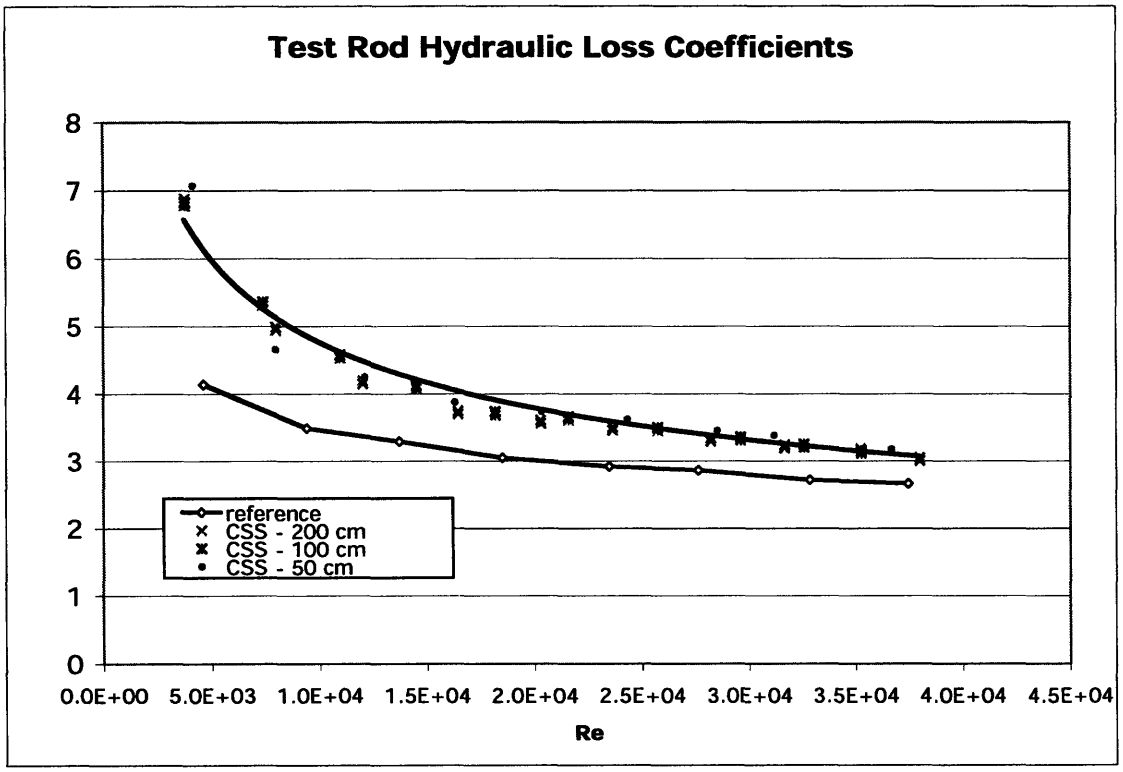

Figure 9.8: Comparison of Reference, CSS test rod hydraulic loss coefficients.

9.2 Correlating Friction Factor Data

In correlating the data for cross-shaped spiral rods, one might first note the similarity in geometry to close-packed wire-wrapped rods or even to twisted-tape tubes. These channels are known to give rise to a centrifugal swirl flow, significantly affecting local flow velocity. An extensive review of single and two-phase flow and heat transfer correlations for twist-tape swirl flow can be found in a literature review by Buongiorno [30].

For single-phase swirl flow along wire-wrapped fuel or in twisted tape channels, the author recommends that pressure drop can be found using the following relations due to Gambill [31]:

$$\Delta p_{fric} = f_{sw} \frac{L_s}{D_h} \frac{\rho v'^2}{2} \qquad \text{(Eqn. 9.2)}$$

where:

$$L_s = L\sqrt{1+\frac{\pi^2}{4y^2}};\ v' = v\sqrt{1+\frac{\pi^2}{4y^2}};\ y = \frac{H}{2D_i} \qquad \text{(Eqn. 9.3)}$$

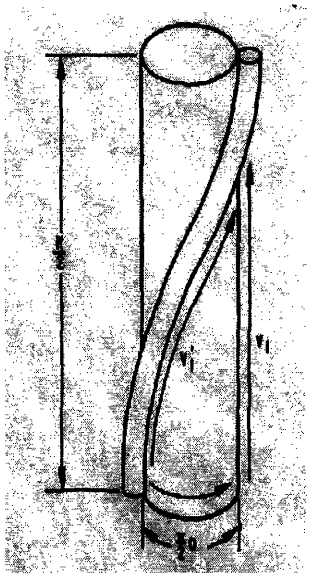

Figure 9.9: A Helical wire is shown wrapped around a cylindrical rod [30].

For CSS rods, the dimensions would are defined in Figure 9.10:

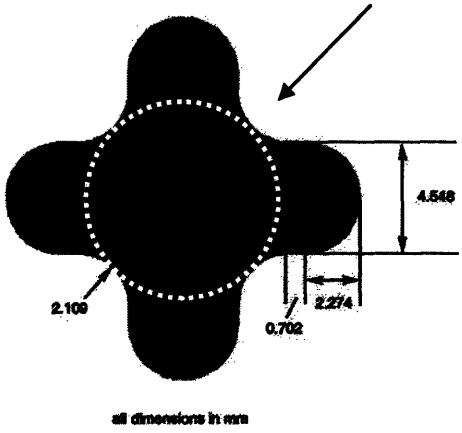

Figure 9.10: CSS Rod dimensions, as compared to dimensions more commonly defined for wire-wrapped fuel.

D_i is the internal diameter, defined with respect to the internal cylinder high-lighted above (by disregarding the outer-lobes). For our test rods, D_i=0.81 cm; P/D_i=1.8.

Table 9.1:

Twist Ratio and Non-dimensional Twist Length for Experimental Rod Types

CSS Rod Type	H/D_i	y	$\sqrt{1+\frac{\pi^2}{4y^2}}$
200 cm	246.6	123.3	1.00008
100 cm	123.3	61.6	1.00032
50 cm	61.6	30.8	1.00130

Typically swirl flow friction factors for wire-wrapped rods and for internal twisted-taped tubes are found to be higher than those of bare rods, this is attributed to three effects; (1) increased flow per unit path length due to the resultant helical flow lines, (2) increased local velocity as a result of the imposed tangential component, and (3) increased fluid-wall contact area.

Therefore, the difficulty in using this type of correlation for the purpose of our CSS data becomes quite apparent: None of the CSS data shows much of any effect of twist pitch, and therefore centrifugal effects are seemingly negligible.

It's interesting to note that this may be due to the limited range of twist pitches explored in this study. For example, data for wire-wrapped fuel rods shows increase over cylindrical rods for H/D_i above 50 (Figure 9.11) [32]. Though the CSS experiment cannot necessarily be assumed to follow the same trend as wire-wrapped rods, the tightest twist of any CSS rod tested was near a 62 cm H/D_i ratio (Table 9.1). At this twist ratio, the factor that amplifies helical path length, and increases local velocity, is very nearly equal to 1 in all cases (Column 3, Table 9.1).

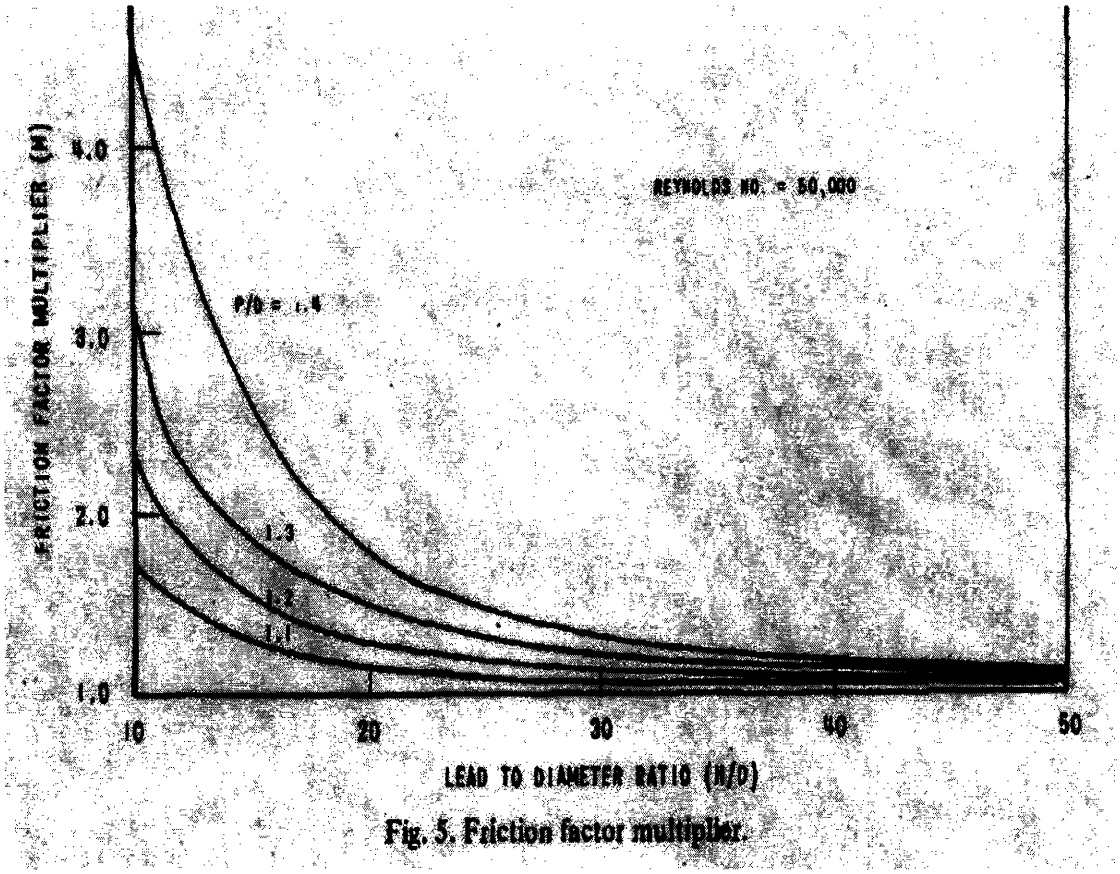

Figure 9.11: Wire-Wrapped Fuel Bundle Data Fit:
Friction Factor Multiplier vs. H/D_i for Re=50,000 and P/D 1.1-1.4 [31]

Combined with the highly turbulent flow typical of this experiment, the effect of twist appears to have become washed out. Successful correlation of the data in this experiment, therefore, requires a different approach.

9.3 Correlating with a Constant Geometrical Factor

Because no consequence is seen due to the change in twist, it seems that the low friction factor can only be linked to a cross-shaped geometrical effect, rather than any centrifugal effect of the spiraling fin. Instead of trying to develop a complicated correlation depending on any other factors, it was judged that correlating via a single, geometry-related factor would make the most sense.

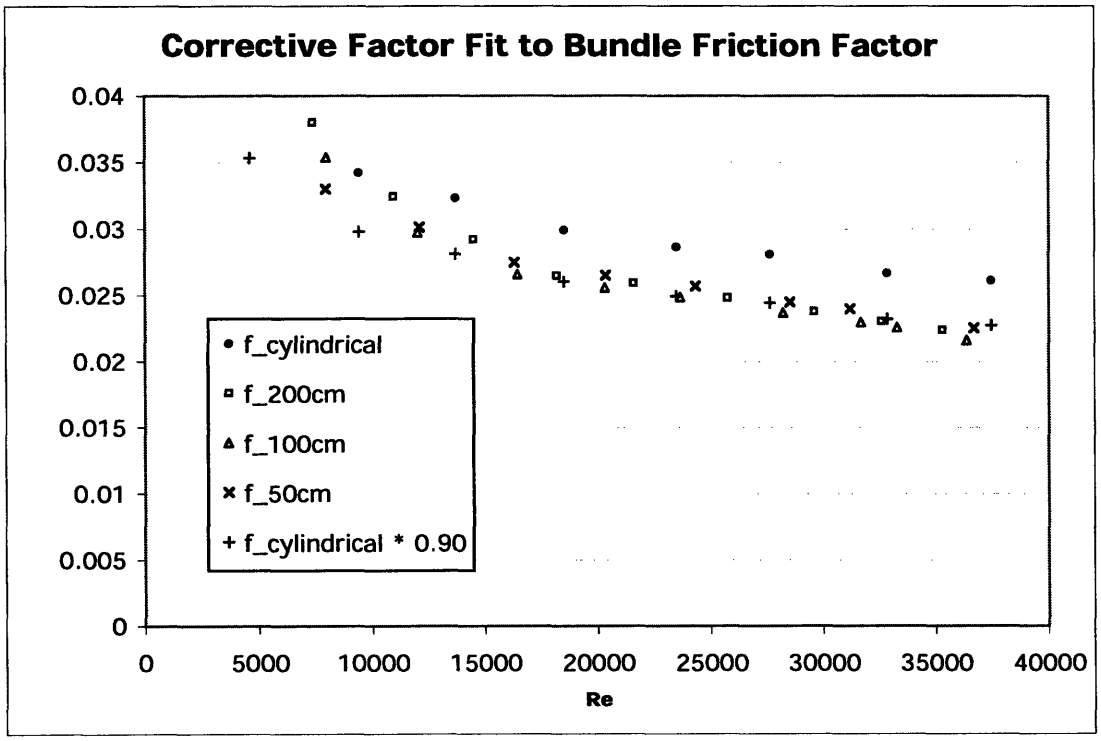

Figure 9.12: Comparison of Reference, CSS bundle friction factors; corrective factor shown.

Using the construction:

$$\Delta p = k_{CSS} \frac{f_{ref} L}{D_e} \frac{\rho v^2}{2} \qquad \text{(Eqn. 9.1)}$$

The CSS data seems best correlated when fitted with a factor of $k_{css} = 0.9$, or 90% of that expected from a bundle of cylindrical rods (Figure 9.12). This scenario does have precedence [23], in that a limited number of tube geometries are shown to have k factors less than 1 -- even in turbulent flow, when boundary conditions are typically unimportant. This reduction in expected friction factor can occur, for instance, if the flow does not equally contact all of the wetted-perimeter. This occurs most notably in the case of more sharply-angled triangular flow channels.

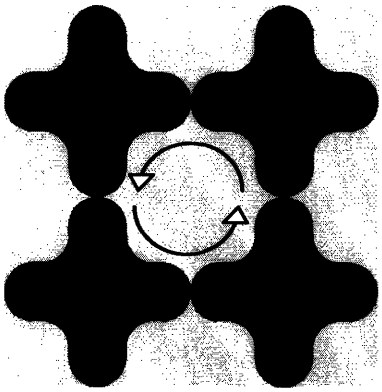

Figure 9.13: A typical CSS Test Assembly subchannel.

Upon examining a subchannel typical of flow within the CSS test assembly, it does not seem unreasonable to think that a similar effect might take hold at the point of contact between the petals of neighboring CSS test rods. In this small crevice, it is theorized that flow is pinched off and slowed significantly, resulting in a fluid-wall contact that is fundamentally different from that between the bulk axial flow and the majority of the rod surface. Furthermore, it appears that the affected region over an entire subchannel is on the order of what would be required to diminish the friction factor by 10%.

With the measured data well-correlated using this factor, the door was opened to further analysis, including estimation of the effect of CSS rods on full-core pressure drop.

9.4 Application to the BWR Core

9.4.1 Improvement to Core Hydraulic Loss Coefficient

To this point much has been made of the comparative bare-rod friction factors. However, the primary advantage of the CSS assembly has not yet been treated: elimination of the grid spacers. In order to express this, a comparison analogous to that shown in Figure 9.8 was developed with several corrections:

First, the dimensionless frictional pressure drop term, $f(L/D_e)$, was adjusted to account for the full-BWR-assembly hydraulic diameter and height. This increases length by a factor

of 4, to 4.1 meters, and takes D_e for a full assembly rather than the 4x4 test bundle. Expanding to a 9x9 array drops the hydraulic diameter of the CSS assembly from 0.77 to 0.73 cm; this increase is due to the unique central water rod structure (Figure 2.5), which possesses a large amount of surface and takes up a good deal of flow area, but is necessary to keep H/HM near the reference value. The hydraulic diameter of the reference assembly itself inches up from 1.08 to 1.13 cm. This is a result of the weakening effect of the assembly wall, as it becomes a smaller fraction of the total wetted surface, overcoming any effects from the water rods.

For the CSS rods, this bundle resistance is the whole resistance; the reference rods, however, require the addition of losses at 7 spacers along the 4.1-meter height. Each spacer is given an irreversible hydraulic loss coefficient "k" characteristic of this type of restriction. Computational analysis in Chapter 4 took a value of 1.5 as suggested by VIPRE. The end result was plotted in a graph displaying the total core hydraulic loss, (excluding the inlet and outlet plates).

Shown in Figure 9.14, the hydraulic loss for the CSS assembly slopes down below that of a reference BWR assembly. The additional losses introduced by the presence of grid spacers are enough to reverse the disadvantages of the CSS assembly, which had posted a higher loss in the bare-rod case in Figure 9.8. Taking the recommended value of k=1.5, this represents a greater-than 40% reduction in total hydraulic loss in the high range of Reynolds numbers.

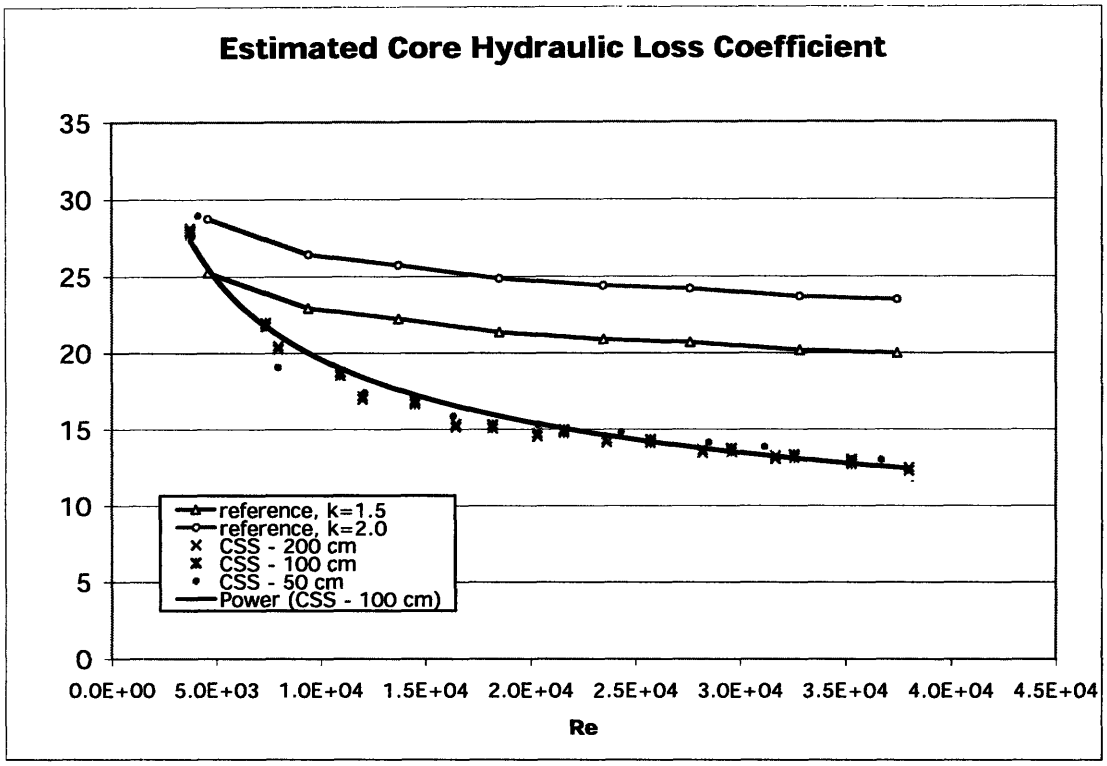

Figure 9.14: Comparison of Reference and CSS core hydraulic loss coefficients.

Though the BWR CSS assembly can claim a 40% reduction in the core hydraulic loss coefficient, not all of this can be recouped in the form of reduced pressure drop. In fact, a good deal of this pressure drop margin will be spent on the fact that the CSS assembly flow area is 11% smaller, and will therefore require a higher flow velocity at the same power level. In any case, the results here provide a good idea of the total resistance faced in an assembly of each fuel type.

9.4.2 Improvement to Core Pressure Drop

The issue of how to adjust pressure drop data of VIPRE, displayed in Chapter 4 (Table 4.4) remains. Two-phase pressure drop across the core can be modeled according to the following equations:

$$\Delta p = \Delta p_{fric} + \Delta p_{grav} + \Delta p_{acc} + \Delta p_{form} \qquad \text{(Eqn. 9.5)}$$

where:

$$\Delta p_{fric} = f_{lo} \frac{L}{D_e} \frac{G^2}{2\rho_l} \frac{1}{L} \int_0^L \phi_{lo}^2 dz$$

$$\Delta p_{grav} = \int_0^L \rho_m g dz = \int_0^L (\alpha\rho_v + (1-\alpha)\rho_l) g dz$$

$$\Delta p_{acc} = G^2 \left(\frac{1}{\rho_m^+(L)} - \frac{1}{\rho_m^+(0)} \right); \quad \frac{1}{\rho_m^+} = \frac{x^2}{\alpha\rho_v} + \frac{(1-x)^2}{(1-\alpha)\rho_l}$$

$$\Delta p_{form} = \Delta p_{form,acc} + k \frac{G^2}{2\rho_l} \frac{1}{L} \int_0^L \phi_{lo}^2 dz$$

and ϕ_{lo}^2 represents the local 2-phase multiplier.

First, the frictional loss term is examined. The two-phase friction multiplier selected for use in VIPRE was the default EPRI correlation. This form decouples the two-phase friction factor, and enables the direct use of the single-phase liquid-only friction factor shown in Figure 9.7. The resultant two-phase frictional pressure drop will therefore be smaller than the frictional pressure drop predicted by VIPRE in Chapter 4 (Table 4.4) by the same factor of 0.9, estimated from Figure 9.12.

In order to accept this result, one must recall that, for the CSS VIPRE models, pressure drop was originally calculated using a traditional cylindrical bundle correlation in combination with the actual CSS hydraulic diameter. This has also made use of the fact that the axial distribution of flow conditions (mass flux, quality, void fraction) through the core has remained the same, and therefore the integrated friction multiplier is unchanged.

However given the non-uniform profile in axial heating, and therefore quality and void fraction, it is difficult to analytically isolate the fraction of the core pressure drop that is due only to friction; Table 4.4 has reported only total core pressure drop. Instead, the change to pressure drop can most easily be found by performing a minor edit to the CSS VIPRE input file, adjusting the friction factor by multiplying through with the 0.9 correction factor.

It should be noted that transitioning from the VIPRE predicted CSS core pressure drop of 21.7 psi, to a more accurate model which uses the experimentally developed correlation, will not be a large improvement. This is due to the fact that the coolant mass flux, as well as the distribution in quality and void fraction will be unaffected, meaning acceleration, gravity and form pressure losses will remain the same; only frictional pressure drop will be altered, and by only a small amount.

Analysis from this point proceeds only for the CSS-SP2 model for which the CSS friction factor correlation has been developed experimentally. Shown in Figure 9.15, pressure drop reduces here by 7%, from 21.7 to 20.2 psi.

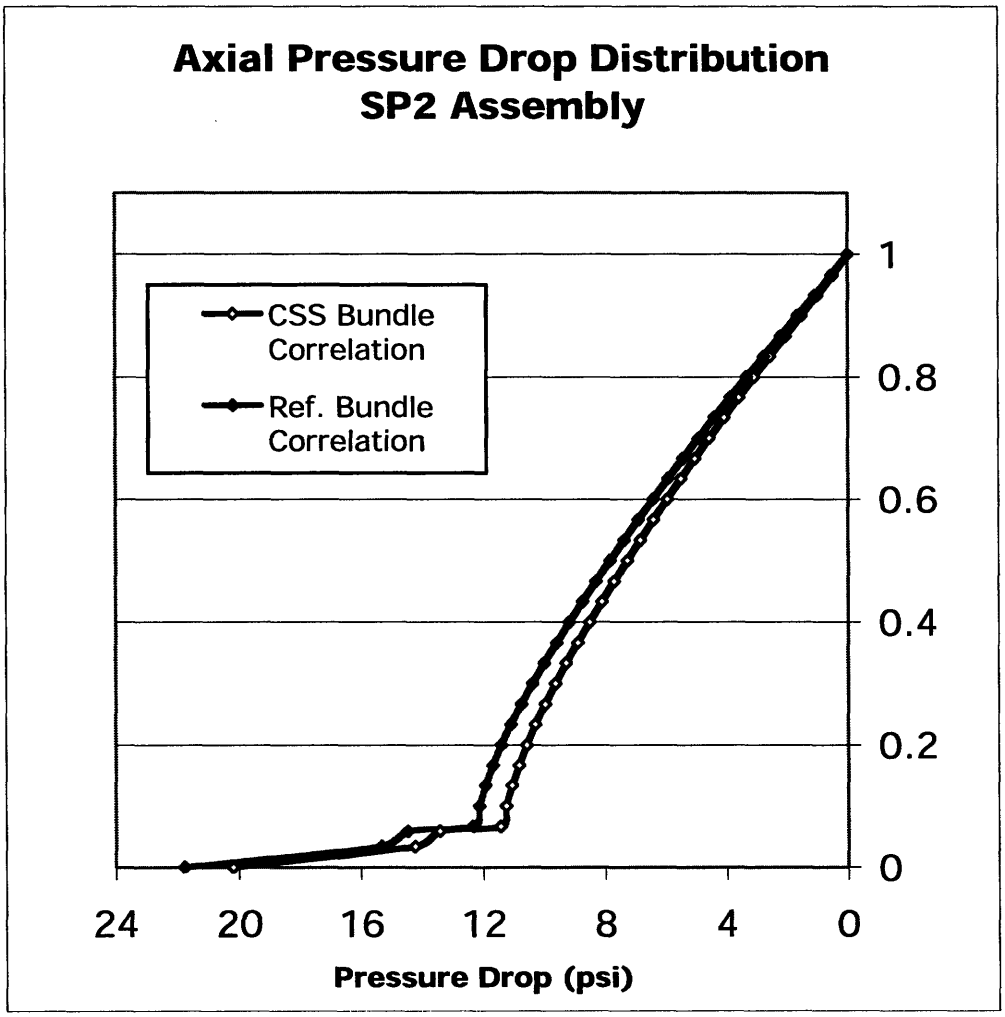

Figure 9.15: CSS-SP2 core pressure drop: Reference Correlation vs. CSS Correlation.

The 1.5 psi (or 7%) reduction in core pressure drop for the CSS core, achieved by using the experimental correlation, implies that 1.5 psi has been shaved off of the frictional pressure drop by way of the 90% multiplicative factor; this seems to be on the order of what would be expected.

The new calculated pressure drop, based on experimental data as well as the more complex two-phase VIPRE model, gives more accurate pressure drop which can be compared to the reference pressure drop found in Chapter 4. This comparison is shown in Figure 9.16; here the CSS model come out ahead of the reference core, but only by a reduction in pressure drop of 9% from 22.3 psi to 20.2 psi.

The 40% drop in hydraulic resistance mentioned earlier can only be converted into a 9% decrease in core pressure drop because of the increase in flow velocity required by the smaller assembly flow area. Unfortunately this is unavoidable for advanced fuel geometries which seek to exploit an increase in cooling surface, and are saddled with a proportional increase in cladding volume within the assembly.

Perhaps a more clever future design can take full advantage of the potential shown in Figure 9.14 by maintaining the reference coolant flow area, though this has proven to be difficult using traditional oxide-pellet clad fuel rods. One possibility might be to relax the requirement of maintaining the reference fuel volume, as is done in the case of internally-cooled annular fuel design studies [6], which would allow for a reduction in the cross-sectional "footprint" of each CSS fuel rod. This however would require an extensive neutronics sensitivity study. It is also likely to require a higher fuel enrichment for the reduced fuel volume to provide the same fuel cycle length. Therefore, it is not obvious that is would be more economic than the CSS-SP2 core described here.

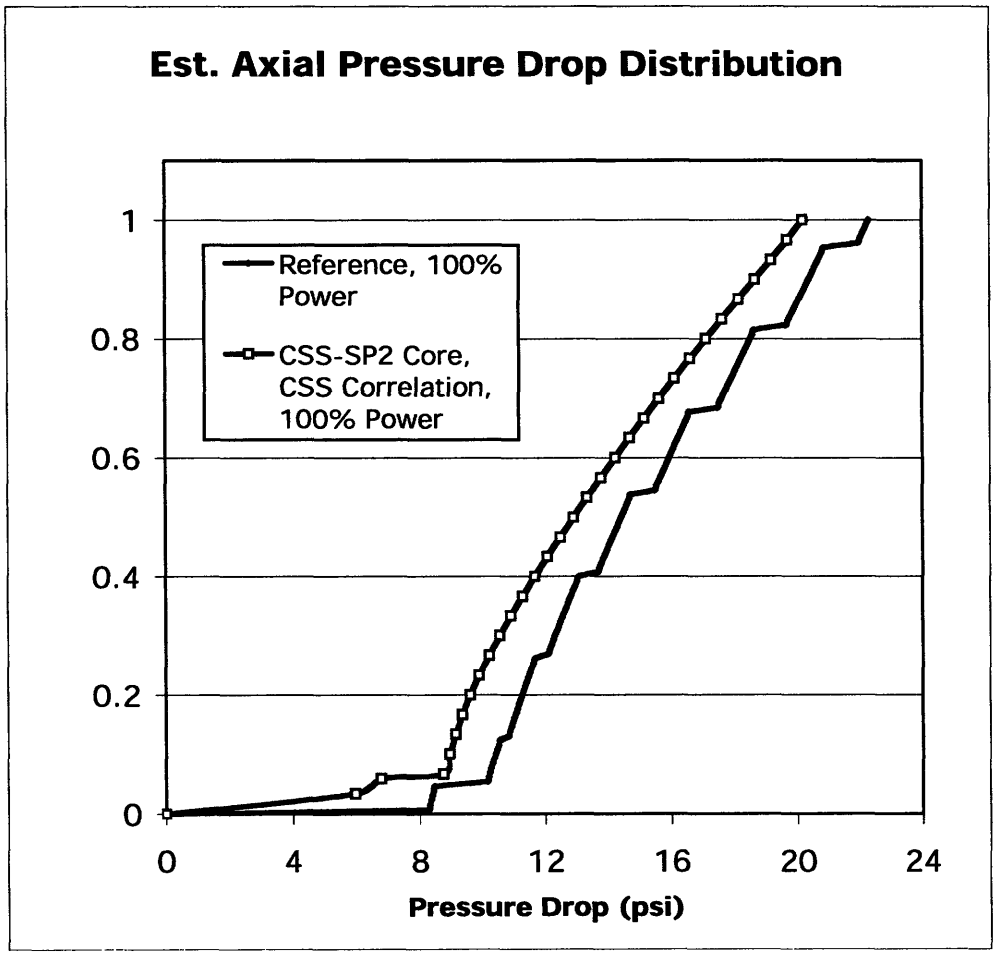

Figure 9.16: Comparison of Reference and CSS core pressure drop at nominal power.

9.4.3 Pressure Drop at 125% Power

Figure 9.16 still focuses on a comparison of the CSS core to the reference core at nominal power level. Increasing the CSS core to 125% of the nominal power level, as was calculated to be safe in Chapter 4 Core Performance analysis, results in a pressure drop that increases 16% beyond the reference core pressure drop at nominal power, to 25.9 psi.

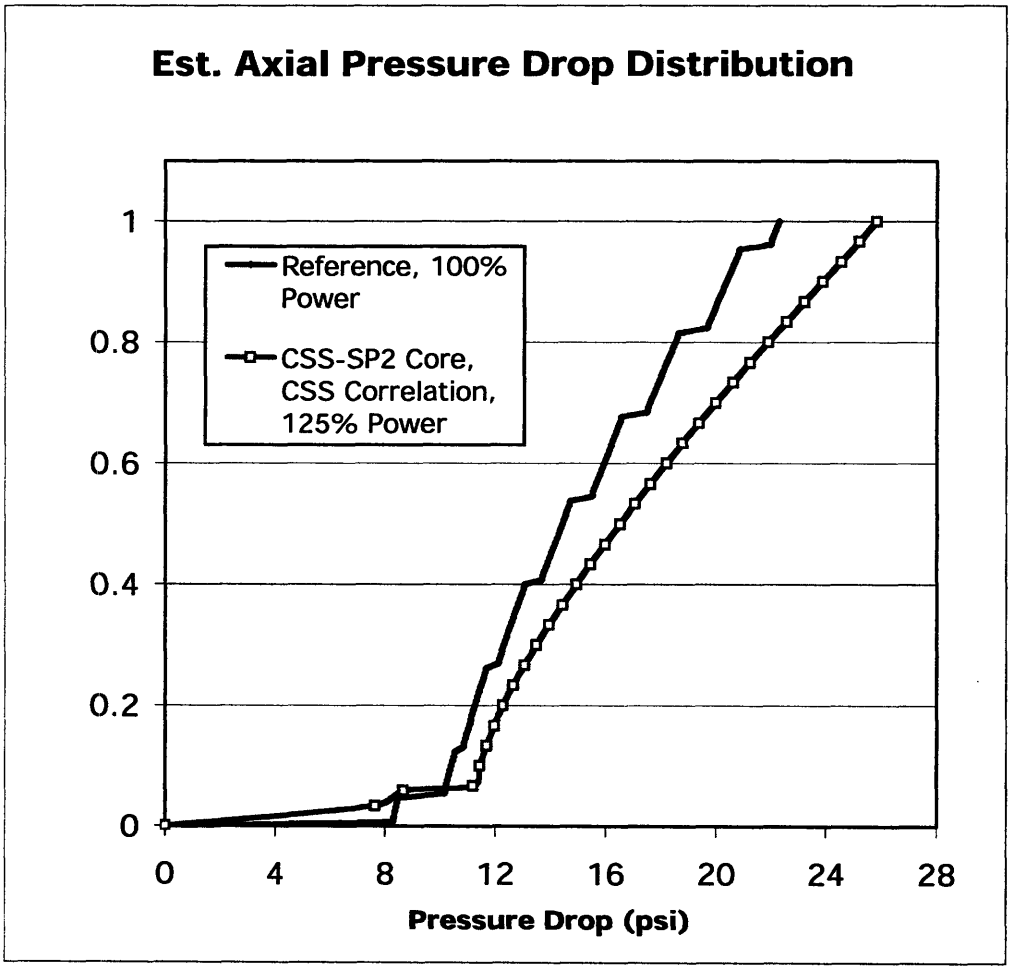

Figure 9.17: Core Pressure Drop Comparison: Reference core at nominal power compared with CSS core at 125% of nominal power.

Illustrated in Figure 9.17, power-uprated pressure drop was obtained in the same manner as previously. Again, this involves multiplying the frictional pressure drop distribution within VIPRE by the experimental 0.9 factor. In this case, mass flow, and therefore flow velocity, is 25% higher within the core than at nominal power. This substantially increases not only the frictional pressure drop, but also acceleration and form losses.

Table 9.2 summarizes core performance from Chapter 4, reflecting changes brought about through the incorporation of experimental data:

Table 9.2: Updated Pressure Drop Comparison for the CSS and Reference Rods

	P-drop (psi)	% Uprate Allowed	P-drop after Uprate (psi)
Reference	22.3	--	22.3
CSS – SP2	20.2	25	25.9

10. Summary and Conclusions

The objective of this study was to provide a first-order steady-state thermal-hydraulic analysis of the use of Cross-Shaped Spiral (CSS) fuel in a high-power-density BWR core; in this aim it was successful, and gives an optimistic view of this potential application.

As described in Chapter 2, two CSS rod models were designed: Spiral Pin 1 (SP1), which maximized surface area for this shape, at 40% greater than the reference rods, and Spiral Pin 2 (SP2), which maximized the "elbow" radius of curvature, but maintained a 35% larger surface. These rods were designed to fit into a 9x9 GE BWR fuel assembly, and to match this reference fuel mass. A comparative analysis was conducted between these assembly types, and the reference assembly with cylindrical rods.

First, each assembly was examined as a full-core VIPRE model, which is to say that each was modeled with a hot channel assembly and an average channel assembly. This allowed for determination of the core pressure drop as well as the MCPR of each case. At nominal operating conditions, the CSS-SP2 core held an edge over the reference core and the CSS-SP1 core, in both pressure drop and MCPR, as detailed in Chapter 4.1. This increase in MCPR over the reference case, from 1.142 to 1.328, enables a power uprate of 25% based purely on thermal-hydraulic considerations. The corresponding MCPR for the SP1 model is 1.299, allowing an uprate of 21%. This advantage of the SP2 model over the SP1, which possesses a larger heated surface, was attributed to the larger flow area allowed in SP2. Both geometries, designed with the intent to increase surface perimeter, consequently increase the fraction of cladding within a given fuel assembly at the expense of flow area. This gives rise to an increase coolant mass flux at a given power rating, diminishing the margin to dryout.

Correcting only for the decrease in hydraulic diameter and the elimination of gridspacers along the core, VIPRE models predict a 21.7 and 24.1 psi core pressure drop for the SP2 and SP1 core respectively, in comparison to a reference value of 22.3 psi.

These initial predictions are no more than a first order model, which account for the appropriate changes in surface perimeter and flow area, but none of the more detailed effects that were thought to pose potential problems. This includes a potential disruption of the circumferential film typical of high-quality rod-bundle flow due to the twisted fuel shape. Also, though an increase in heated surface will be accompanied by a lower average surface heat-flux, the non-uniform shape leads to a possible lower critical dryout quality due to large heat-flux peaking. Even the effects of the twisted shape on the exchange of mass, momentum, and energy are not addressed. These are issues that really cannot be dealt with analytically but can be examined in more detail, and are resolved to some degree in Chapter 4.

Non-uniformity in the CSS fuel cross-section could give rise to several abnormalities. Primarily, the concern was that heat-flux peaking at the elbow region of a fuel rod (the central intersection of fuel petals) would be too large; it was feared that the drop in the central fuel thickness at this region, as well as the low thermal conductivity of UO_2, would cause a majority of heat from the fuel to be drawn out in a relatively small fraction of the surface. The reduction in fuel thickness was also assumed to significantly lower the maximum fuel centerline temperature, due to the same effect. Combating this, the large fuel surface perimeter was thought to create a rise in thermal neutron shielding of the central fuel region, creating a larger-than-normal gradient of volumetric power generation within the pellet. This would limit the amount of power generated in the pellet center, and could therefore diminish the heat-flux peaking in comparison to a fuel pellet with uniform volumetric power generation.

These effects were quantified using coupled finite-element analysis and MCNP models to give the following results, at hot-channel limiting conditions predicted by VIPRE: The SP1 model, with the lowest central fuel thickness and largest surface perimeter, fared the best in terms of fuel centerline temperature, at 909K, but had the elbow heat-flux peaking at 1.47 MW/m^2 (2.42 peak-to-average) at nominal power. The SP2 model predicted a maximum temperature of 960K, but lowered the surface heat-flux experienced to 1.21 MW/m^2 (a 1.88 peak-to-average ratio). These values are in comparison to a reference

fuel maximum temperature of 1236 K and a circumferentially uniform heat flux of 0.89 MW/m^2, at the same conditions.

Though these values of peaking were large, Chapter 4.3 reviews several papers that have investigated a similar phenomenon. Kitto [17], and well as Alekseev [18], have experimented with critical heat flux on tubes of non-uniform circumferential heating on the order of 2.0 and 1.5 peak-to-average heat flux respectively. Both have noted that in the case of high-quality critical heat flux, the circumferentially-averaged critical heat flux of a tube with peaking was equal to that of a uniformly heated tube with the same total heat input axially. Whereas, for subcooled CHF events, data showed that the peaked tubes had a large reduction in average critical heat flux in comparison to the uniformly heated case.

This behavior is reasonable in view of the differences between the mechanisms leading to low quality and high quality CHF: departure from nucleate boiling is wholly dependent on local conditions, while high quality CHF (dryout) is instead a function of total heat input, and is usually correlated as a critical quality – boiling length relationship. Still, the ability of these experimental tube-channels to endure peaked heating conditions was predicated on the assumption that annular flow is allowed to continue unabated. This may not necessarily be the case for a bundle of twisted rods, as annular flow could be destabilized by the additional component of radial velocity that is imposed upon the axial flow.

However, a set of experimental data (as yet unpublished), suggests otherwise. A recent Kurchatov Institute study that was not widely distributed reported on high-quality critical heat-flux tests on similarly twisted rod assemblies. These tests confirmed that a significant power uprate might be allowed by the use of such a rod assembly. A correlation devised from this data suggests a potential power-uprate of 34% over the reference BWR detailed in Chapter 3. Additionally, this study reports values of critical quality for twisted rod bundles that are well-beyond the transition to the regime of

annular flow, as predicted by most two-phase transition models. This suggests that annular flow is indeed able to exist and thrive along such rods.

Still, differences remain between the rods examined, as well as the test conditions of the unpublished experimental study, and those optimized for the BWR core in Chapter 3 of this study. Though it was not immediately possible to conduct a similar CHF test with the exact dimensions described for CSS SP1 or SP2, a facility was constructed to perform this feat for pressure drop and friction factor data. For the test rods, the SP2 cross-section was selected, as this rod type proved to be advantageous in previous analysis. Sixteen rods of 50 cm, 100 cm, and 200 cm twist pitches were manufactured , along with a set of reference rods

Experimental measurements of hydraulic losses along 1.5-meter-long model CSS-SP2 rods in 4x4 bundles show a significantly larger pressure drop at the same mass flow, as compared to bare cylindrical rods. This increase was mainly due to the reduction in flow area as a result of the larger SP2 cross-section. The SP2 rods also show a larger pressure drop at the same flow velocity, in comparison to bare cylindrical rods; this was attributed to their larger frictional wetted-surface. However, the SP2 bundle turbulent friction factor is only 90% of the expected value given its hydraulic diameter. It was theorized that this has to do with a flow-pinching occurrence at the contact point between the petals of neighboring CSS rods, effectively lowering the surface area. The effect of increasing twist pitch on this pressure drop and friction factor was negligible in all cases, in the range of twists examined.

This bare-rod, 4x4 assembly result can be extended to a full BWR core comparison with the addition of grid spacer losses to the reference case, the use of 9x9 BWR assembly hydraulic diameters, and the extension of all results to full-length BWR rods. This results in a 40% reduction in core hydraulic loss at the same Reynolds number, for the CSS rod assemblies in comparison the reference case (neglecting entrance and exit plates in both cases). Nevertheless, this does not yet account for the increase in flow velocity required to maintain nominal power conditions at this reduced flow area. All told, the use of CSS

rods should decrease total core pressure drop at nominal power by 9%, in spite of the 8% reduction in assembly flow area. At 125% of nominal power, this becomes a 16% increase in pressure drop in comparison to the reference core at nominal power.

Based on the preliminary analysis outlined in this work, the CSS core, in particular fuelled with the SP2 rod model, is able to provide a lower pressure drop at nominal power while significantly raising safety margins including the MCPR and maximum fuel temperature, and should be viewed as a successful design from this standpoint. At 25% uprated conditions, the CSS-SP2 core is predicted to match the reference MCPR, with only a 16% pressure drop increase, and further improve the reduction in central fuel temperature. From this perspective, it should be considered as an advanced fuel design candidate for high-power-density BWRs of the future.

Appendix A: Sample VIPRE Input

```
**************************************************************************
*
*GE9by9 CSS SP2 BWR with 7 water rods
1,0,0,                                                                  *vipre.1
Bwr solid fuel                                                          *vipre.2
*
**************************************************************************
*
geom,100,100,50,0,0,0,                                                  *geom.1
*
145.98,0.0,0.5,                                                         *geom.2
*
1, 0.025369, 0.922056, 0.466962, 2, 2, 0.029319, 0.434583, 11, 0.029319, 0.434583,
2, 0.086764, 1.513368, 0.933923, 2, 3, 0.029319, 0.579444, 12, 0.058638, 0.434583,
3, 0.086764, 1.513368, 0.933923, 2, 4, 0.029319, 0.579444, 13, 0.058638, 0.434583,
4, 0.086764, 1.513368, 0.933923, 2, 5, 0.029319, 0.579444, 14, 0.058638, 0.434583,
5, 0.086764, 1.513368, 0.933923, 2, 6, 0.029319, 0.579444, 15, 0.058638, 0.434583,
6, 0.086764, 1.513368, 0.933923, 2, 7, 0.029319, 0.579444, 16, 0.058638, 0.434583,
7, 0.086764, 1.513368, 0.933923, 2, 8, 0.029319, 0.579444, 17, 0.058638, 0.434583,
8, 0.086764, 1.513368, 0.933923, 2, 9, 0.029319, 0.579444, 18, 0.058638, 0.434583,
9, 0.086764, 1.513368, 0.933923, 2, 10, 0.029319, 0.434583, 19, 0.058638, 0.434583,
10, 0.025369, 0.922056, 0.466962, 1, 20, 0.029319, 0.434583,
11, 0.086764, 1.513368, 0.933923, 2, 12, 0.058638, 0.434583, 21, 0.029319, 0.579444,
12, 0.173529, 1.867846, 1.867846, 2, 13, 0.058638, 0.579444, 22, 0.058638, 0.579444,
13, 0.173529, 1.867846, 1.867846, 2, 14, 0.058638, 0.579444, 23, 0.058638, 0.579444,
14, 0.173529, 1.867846, 1.867846, 2, 15, 0.058638, 0.579444, 24, 0.058638, 0.579444,
15, 0.173529, 1.867846, 1.867846, 2, 16, 0.058638, 0.579444, 25, 0.058638, 0.579444,
16, 0.173529, 1.867846, 1.867846, 2, 17, 0.058638, 0.579444, 26, 0.058638, 0.579444,
17, 0.173529, 1.867846, 1.867846, 2, 18, 0.058638, 0.579444, 27, 0.058638, 0.579444,
18, 0.173529, 1.867846, 1.867846, 2, 19, 0.058638, 0.579444, 28, 0.058638, 0.579444,
19, 0.173529, 1.867846, 1.867846, 2, 20, 0.058638, 0.434583, 29, 0.058638, 0.579444,
20, 0.086764, 1.513368, 0.933923, 1, 30, 0.029319, 0.579444,
21, 0.086764, 1.513368, 0.933923, 2, 22, 0.058638, 0.434583, 31, 0.029319, 0.579444,
22, 0.173529, 1.867846, 1.867846, 2, 23, 0.058638, 0.579444, 32, 0.058638, 0.579444,
23, 0.173529, 1.867846, 1.867846, 2, 24, 0.058638, 0.579444, 33, 0.058638, 0.579444,
24, 0.173529, 1.867846, 1.867846, 2, 25, 0.058638, 0.579444, 34, 0.058638, 0.579444,
25, 0.173529, 1.867846, 1.867846, 2, 26, 0.058638, 0.579444, 35, 0.058638, 0.579444,
26, 0.173529, 1.867846, 1.867846, 2, 27, 0.058638, 0.579444, 36, 0.058638, 0.579444,
27, 0.173529, 1.867846, 1.867846, 2, 28, 0.058638, 0.579444, 37, 0.058638, 0.579444,
28, 0.173529, 1.867846, 1.867846, 2, 29, 0.058638, 0.579444, 38, 0.058638, 0.579444,
29, 0.173529, 1.867846, 1.867846, 2, 30, 0.058638, 0.434583, 39, 0.058638, 0.579444,
30, 0.086764, 1.513368, 0.933923, 1, 40, 0.029319, 0.579444,
31, 0.086764, 1.513368, 0.933923, 2, 32, 0.058638, 0.434583, 41, 0.029319, 0.579444,
32, 0.173529, 1.867846, 1.867846, 2, 33, 0.058638, 0.579444, 42, 0.058638, 0.579444,
33, 0.173529, 1.867846, 1.867846, 2, 34, 0.058638, 0.579444, 43, 0.058638, 0.579444,
34, 0.148160, 1.855979, 1.400885, 2, 35, 0.045000, 0.579444, 44, 0.045000, 0.579444,
35, 0.122791, 1.844112, 0.933923, 1, 36, 0.045000, 0.579444,
36, 0.148160, 1.855979, 1.400885, 2, 37, 0.058638, 0.579444, 46, 0.045000, 0.579444,
37, 0.173529, 1.867846, 1.867846, 2, 38, 0.058638, 0.579444, 47, 0.058638, 0.579444,
38, 0.173529, 1.867846, 1.867846, 2, 39, 0.058638, 0.579444, 48, 0.058638, 0.579444,
39, 0.173529, 1.867846, 1.867846, 2, 40, 0.058638, 0.434583, 49, 0.058638, 0.579444,
40, 0.086764, 1.513368, 0.933923, 1, 50, 0.029319, 0.579444,
```

41, 0.086764, 1.513368, 0.933923, 2, 42, 0.058638, 0.434583, 51, 0.029319, 0.579444,
42, 0.173529, 1.867846, 1.867846, 2, 43, 0.058638, 0.579444, 52, 0.058638, 0.579444,
43, 0.173529, 1.867846, 1.867846, 2, 44, 0.058638, 0.579444, 53, 0.058638, 0.579444,
44, 0.122791, 1.844112, 0.933923, 1, 54, 0.045000, 0.579444,
45, 0.072054, 1.820378, 1.820378,
46, 0.097423, 1.832245, 0.466962, 1, 47, 0.045000, 0.579444,
47, 0.148160, 1.855979, 1.400885, 2, 48, 0.058638, 0.579444, 57, 0.045000, 0.579444,
48, 0.173529, 1.867846, 1.867846, 2, 49, 0.058638, 0.579444, 58, 0.058638, 0.579444,
49, 0.173529, 1.867846, 1.867846, 2, 50, 0.058638, 0.434583, 59, 0.058638, 0.579444,
50, 0.086764, 1.513368, 0.933923, 1, 60, 0.029319, 0.579444,
51, 0.086764, 1.513368, 0.933923, 2, 52, 0.058638, 0.434583, 61, 0.029319, 0.579444,
52, 0.173529, 1.867846, 1.867846, 2, 53, 0.058638, 0.579444, 62, 0.058638, 0.579444,
53, 0.173529, 1.867846, 1.867846, 2, 54, 0.058638, 0.579444, 63, 0.058638, 0.579444,
54, 0.148160, 1.855979, 1.400885, 2, 55, 0.045000, 0.579444, 64, 0.058638, 0.579444,
55, 0.097423, 1.832245, 0.466962, 1, 65, 0.045000, 0.579444,
56, 0.072054, 1.820378, 1.820378,
57, 0.122791, 1.844112, 0.933923, 2, 58, 0.058638, 0.579444, 67, 0.045000, 0.579444,
58, 0.173529, 1.867846, 1.867846, 2, 59, 0.058638, 0.579444, 68, 0.058638, 0.579444,
59, 0.173529, 1.867846, 1.867846, 2, 60, 0.058638, 0.434583, 69, 0.058638, 0.579444,
60, 0.086764, 1.513368, 0.933923, 1, 70, 0.029319, 0.579444,
61, 0.086764, 1.513368, 0.933923, 2, 62, 0.058638, 0.434583, 71, 0.029319, 0.579444,
62, 0.173529, 1.867846, 1.867846, 2, 63, 0.058638, 0.579444, 72, 0.058638, 0.579444,
63, 0.173529, 1.867846, 1.867846, 2, 64, 0.058638, 0.579444, 73, 0.058638, 0.579444,
64, 0.173529, 1.867846, 1.867846, 2, 65, 0.058638, 0.579444, 74, 0.058638, 0.579444,
65, 0.148160, 1.855979, 1.400885, 2, 66, 0.045000, 0.579444, 75, 0.058638, 0.579444,
66, 0.122791, 1.844112, 0.933923, 2, 67, 0.045000, 0.579444, 76, 0.058638, 0.579444,
67, 0.148160, 1.855979, 1.400885, 2, 68, 0.058638, 0.579444, 77, 0.058638, 0.579444,
68, 0.173529, 1.867846, 1.867846, 2, 69, 0.058638, 0.579444, 78, 0.058638, 0.579444,
69, 0.173529, 1.867846, 1.867846, 2, 70, 0.058638, 0.434583, 79, 0.058638, 0.579444,
70, 0.086764, 1.513368, 0.933923, 1, 80, 0.029319, 0.579444,
71, 0.086764, 1.513368, 0.933923, 2, 72, 0.058638, 0.434583, 81, 0.029319, 0.579444,
72, 0.173529, 1.867846, 1.867846, 2, 73, 0.058638, 0.579444, 82, 0.058638, 0.579444,
73, 0.173529, 1.867846, 1.867846, 2, 74, 0.058638, 0.579444, 83, 0.058638, 0.579444,
74, 0.173529, 1.867846, 1.867846, 2, 75, 0.058638, 0.579444, 84, 0.058638, 0.579444,
75, 0.173529, 1.867846, 1.867846, 2, 76, 0.058638, 0.579444, 85, 0.058638, 0.579444,
76, 0.173529, 1.867846, 1.867846, 2, 77, 0.058638, 0.579444, 86, 0.058638, 0.579444,
77, 0.173529, 1.867846, 1.867846, 2, 78, 0.058638, 0.579444, 87, 0.058638, 0.579444,
78, 0.173529, 1.867846, 1.867846, 2, 79, 0.058638, 0.579444, 88, 0.058638, 0.579444,
79, 0.173529, 1.867846, 1.867846, 2, 80, 0.058638, 0.434583, 89, 0.058638, 0.579444,
80, 0.086764, 1.513368, 0.933923, 1, 90, 0.029319, 0.579444,
81, 0.086764, 1.513368, 0.933923, 2, 82, 0.058638, 0.434583, 91, 0.029319, 0.579444,
82, 0.173529, 1.867846, 1.867846, 2, 83, 0.058638, 0.579444, 92, 0.058638, 0.434583,
83, 0.173529, 1.867846, 1.867846, 2, 84, 0.058638, 0.579444, 93, 0.058638, 0.434583,
84, 0.173529, 1.867846, 1.867846, 2, 85, 0.058638, 0.579444, 94, 0.058638, 0.434583,
85, 0.173529, 1.867846, 1.867846, 2, 86, 0.058638, 0.579444, 95, 0.058638, 0.434583,
86, 0.173529, 1.867846, 1.867846, 2, 87, 0.058638, 0.579444, 96, 0.058638, 0.434583,
87, 0.173529, 1.867846, 1.867846, 2, 88, 0.058638, 0.579444, 97, 0.058638, 0.434583,
88, 0.173529, 1.867846, 1.867846, 2, 89, 0.058638, 0.579444, 98, 0.058638, 0.434583,
89, 0.173529, 1.867846, 1.867846, 2, 90, 0.058638, 0.434583, 99, 0.058638, 0.434583,
90, 0.086764, 1.513368, 0.933923, 1, 100, 0.029319, 0.434583,
91, 0.025369, 0.922056, 0.466962, 1, 92, 0.029319, 0.434583,
92, 0.086764, 1.513368, 0.933923, 1, 93, 0.029319, 0.579444,
93, 0.086764, 1.513368, 0.933923, 1, 94, 0.029319, 0.579444,
94, 0.086764, 1.513368, 0.933923, 1, 95, 0.029319, 0.579444,
95, 0.086764, 1.513368, 0.933923, 1, 96, 0.029319, 0.579444,
96, 0.086764, 1.513368, 0.933923, 1, 97, 0.029319, 0.579444,

```
97, 0.086764, 1.513368, 0.933923, 1, 98, 0.029319, 0.579444,
98, 0.086764, 1.513368, 0.933923, 1, 99, 0.029319, 0.579444,
99, 0.086764, 1.513368, 0.933923, 1, 100, 0.029319, 0.579444,
100, 0.025369, 0.922056, 0.466962,
101,0.189932,1.544912,1.544912,
102,0.189932,1.544912,1.544912,
103,0.189932,1.544912,1.544912,
104,0.189932,1.544912,1.544912,
105,0.189932,1.544912,1.544912,
106,0.189932,1.544912,1.544912,
107,0.189932,1.544912,1.544912,
*
**********************************************************************
*
prop,0,1,2,1   *internal EPRI functions                                  *prop.1
*
**********************************************************************
*
rods,1,81,1,2,1,0,0,0,0,0,0                                              *rods.1
145.98,0.0,0,0                                                           *rods.2
*
*
25
*                                                                        *rods.3
*                                                                        *rods.4
0.,0.,?
6.0825,0.38,?
12.165,0.69,?
18.2475,0.93,
24.33,1.1,?
30.4125,1.21,?
36.495,1.3,?
42.5775,1.47,
48.66,1.51,?
54.7425,1.49,?
60.825,1.44,?
66.9075,1.36,
72.99,1.28,?
79.0725,1.16,?
85.155,1.06,?
91.2375,1.01,?
97.32,0.97,?
103.4025,0.94,?
109.485,0.97,?
115.675,0.96,
121.65,0.91,?
127.7325,0.77,?
133.815,0.59,?
139.8975,0.38,
145.98,0.12,
*
*rods geometry input                                                     *rods.9
1,1,.92,1,1,0.25,2,0.25,11,0.25,12,0.25,
2,1,1.04,1,2,0.25,3,0.25,12,0.25,13,0.25,
3,1,1.07,1,3,0.25,4,0.25,13,0.25,14,0.25,
4,1,1.10,1,4,0.25,5,0.25,14,0.25,15,0.25,
```

5,1,1.08,1,5,0.25,6,0.25,15,0.25,16,0.25,
6,1,1.11,1,6,0.25,7,0.25,16,0.25,17,0.25,
7,1,1.07,1,7,0.25,8,0.25,17,0.25,18,0.25,
8,1,1.03,1,8,0.25,9,0.25,18,0.25,19,0.25,
9,1,.92,1,9,0.25,10,0.25,19,0.25,20,0.25,
*
10,1,1.03,1,11,0.25,12,0.25,21,0.25,22,0.25,
11,1,1.18,1,12,0.25,13,0.25,22,0.25,23,0.25,
12,1,1.0,1,13,0.25,14,0.25,23,0.25,24,0.25,
13,1,0.80,1,14,0.25,15,0.25,24,0.25,25,0.25,
14,1,1.09,1,15,0.25,16,0.25,25,0.25,26,0.25,
15,1,0.78,1,16,0.25,17,0.25,26,0.25,27,0.25,
16,1,0.97,1,17,0.25,18,0.25,27,0.25,28,0.25,
17,1,1.17,1,18,0.25,19,0.25,28,0.25,29,0.25,
18,1,1.03,1,19,0.25,20,0.25,29,0.25,30,0.25,
*
19,1,1.07,1,21,0.25,22,0.25,31,0.25,32,0.25,
20,1,0.99,1,22,0.25,23,0.25,32,0.25,33,0.25,
21,1,0.79,1,23,0.25,24,0.25,33,0.25,34,0.25,
22,1,0.98,1,24,0.25,25,0.25,34,0.25,35,0.25,
23,1,0.99,1,25,0.25,26,0.25,35,0.25,36,0.25,
24,1,0.91,1,26,0.25,27,0.25,36,0.25,37,0.25,
25,1,0.74,1,27,0.25,28,0.25,37,0.25,38,0.25,
26,1,0.97,1,28,0.25,29,0.25,38,0.25,39,0.25,
27,1,1.08,1,29,0.25,30,0.25,39,0.25,40,0.25,
*
28,1,1.09,1,31,0.25,32,0.25,41,0.25,42,0.25,
29,1,0.79,1,32,0.25,33,0.25,42,0.25,43,0.25,
30,1,0.98,1,33,0.25,34,0.25,43,0.25,44,0.25,
31,1,1.07,1,36,0.25,37,0.25,46,0.25,47,0.25,
32,1,0.92,1,37,0.25,38,0.25,47,0.25,48,0.25,
33,1,0.78,1,38,0.25,39,0.25,48,0.25,49,0.25,
34,1,1.10,1,39,0.25,40,0.25,49,0.25,50,0.25,
*
35,1,1.07,1,41,0.25,42,0.25,51,0.25,52,0.25,
36,1,1.08,1,42,0.25,43,0.25,52,0.25,53,0.25,
37,1,0.98,1,43,0.25,44,0.25,53,0.25,54,0.25,
38,1,0.99,1,47,0.25,48,0.25,57,0.25,58,0.25,
39,1,1.08,1,48,0.25,49,0.25,58,0.25,59,0.25,
40,1,1.08,1,49,0.25,50,0.25,59,0.25,60,0.25,
*
41,1,1.09,1,51,0.25,52,0.25,61,0.25,62,0.25,
42,1,.79,1,52,0.25,53,0.25,62,0.25,63,0.25,
43,1,.92,1,53,0.25,54,0.25,63,0.25,64,0.25,
44,1,1.06,1,54,0.25,55,0.25,64,0.25,65,0.25,
45,1,0.98,1,57,0.25,58,0.25,67,0.25,68,0.25,
46,1,0.80,1,58,0.25,59,0.25,68,0.25,69,0.25,
47,1,1.11,1,59,0.25,60,0.25,69,0.25,70,0.25,
*
48,1,1.07,1,61,0.25,62,0.25,71,0.25,72,0.25,
49,1,0.97,1,62,0.25,63,0.25,72,0.25,73,0.25,
50,1,0.76,1,63,0.25,64,0.25,73,0.25,74,0.25,
51,1,0.92,1,64,0.25,65,0.25,74,0.25,75,0.25,
52,1,0.99,1,65,0.25,66,0.25,75,0.25,76,0.25,
53,1,0.98,1,66,0.25,67,0.25,76,0.25,77,0.25;
54,1,0.79,1,67,0.25,68,0.25,77,0.25,78,0.25,

```
55,1,0.99,1,68,0.25,69,0.25,78,0.25,79,0.25,
56,1,1.08,1,69,0.25,70,0.25,79,0.25,80,0.25,
*
57,1,1.02,1,71,0.25,72,0.25,81,0.25,82,0.25,
58,1,1.18,1,72,0.25,73,0.25,82,0.25,83,0.25,
59,1,0.98,1,73,0.25,74,0.25,83,0.25,84,0.25,
60,1,0.80,1,74,0.25,75,0.25,84,0.25,85,0.25,
61,1,1.09,1,75,0.25,76,0.25,85,0.25,86,0.25,
62,1,0.81,1,76,0.25,77,0.25,86,0.25,87,0.25,
63,1,1.01,1,77,0.25,78,0.25,87,0.25,88,0.25,
64,1,1.20,1,78,0.25,79,0.25,88,0.25,89,0.25,
65,1,1.04,1,79,0.25,80,0.25,89,0.25,90,0.25,
*
66,1,0.91,1,81,0.25,82,0.25,91,0.25,92,0.25,
67,1,1.03,1,82,0.25,83,0.25,92,0.25,93,0.25,
68,1,1.08,1,83,0.25,84,0.25,93,0.25,94,0.25,
69,1,1.10,1,84,0.25,85,0.25,94,0.25,95,0.25,
70,1,1.09,1,85,0.25,86,0.25,95,0.25,96,0.25,
71,1,1.11,1,86,0.25,87,0.25,96,0.25,97,0.25,
72,1,1.08,1,87,0.25,88,0.25,97,0.25,98,0.25,
73,1,1.04,1,88,0.25,89,0.25,98,0.25,99,0.25,
74,1,0.93,1,89,0.25,90,0.25,99,0.25,100,0.25,
*
75,2,0.0,1,34,0.25,35,0.25,44,0.25,45,0.25,
76,2,0.0,1,35,0.25,36,0.25,45,0.25,46,0.25,
77,2,0.0,1,44,0.25,45,0.25,54,0.25,55,0.25,
78,2,0.0,1,45,0.25,46,0.25,55,0.25,56,0.25,
79,2,0.0,1,46,0.25,47,0.25,56,0.25,57,0.25,
80,2,0.0,1,55,0.25,56,0.25,65,0.25,66,0.25,
81,2,0.0,1,56,0.25,57,0.25,66,0.25,67,0.25,
*
0                                                    *rods.9
*
1,  2,  3,  4,  5,  6,  7,  8,  9,                  *rods.57
10, 11 ,12, 13, 14, 15, 16, 17, 18,
19, 20, 21, 22, 23, 24, 25, 26, 27,
28, 29, 30, 31,         32, 33, 34,
35, 36, 37,             38, 39, 40,
41,42,43,           44, 45, 46, 47,
48, 49, 50, 51, 52, 53, 54, 55, 56,
57, 58, 59, 60, 61, 62, 63, 64, 65,
66, 67, 68, 69, 70, 71, 72, 73, 74,
* blank line above necessary /rods.57 -HG CPR corr
81,0.579444,0.056946,1.23303,14.042698,              *rods.58
*
0                                                    *rods.59
*fuel
1,nucl,1.23303,1.105032,12,0.0,0.028                 *rods.62
0,0,0,0,0,1056.66,0.955,0,                           *rods 63
*constant radial power in the pellet, no power in the clad
*
*water tube
2,tube,0.5794444,0.4917607,1                         *rods.68
3,1,0.03,1.0,                                        *rods.69
*wall
*3,wall,5.415,0.0,1
```

```
*3,1,0.1,1.0,
*
*
1,1,409.7,clad,
662,0.076,10.05,
**************************************************************************
*P,T
oper,1,1,0,1,0,1,0,0,0,                                                    *oper.1
-1.0,0.0,2.0,0.005,                                                        *oper.2
0                                                                          *oper.3
1035.0,533.0,33.39,85.2506,0.0                                             *oper.5
*
*Rod power got from total power divided total number of rods
0,              *no forcing functions                                      *oper.12
**************************************************************************
*correlations
corr,1,2,0,                                                                *corr.1
epri,epri,epri,none,                                                       *corr.2
0.2,                                                                       *corr.3
ditb,chen,chen,epri,cond,g5.7,    *correlation for boiling curve           *corr.6
1,0,0.0,
hnch,                                                                      *corr.16
*
mixx,0,0,0,
0.8,0.0048,0.0,
**************************************************************************
grid,0,7,                                                                  *grid.1
9.4609,1.203,0.3751,21.089,182.049,305.,710.0,
100,3,                                                                     *grid.4
1,2,3,4,5,6,7,8,9,10,11,12,13,14,15,16,                                    *grid.5
17,18,19,20,21,22,23,24,25,26,27,28,29,30,31,32,
33,34,35,36,37,38,39,40,41,42,43,44,45,46,47,48,
49,50,51,52,53,54,55,56,57,58,59,60,61,62,63,64,
65,66,67,68,69,70,71,72,73,74,75,76,77,78,79,80,
81,82,83,84,85,86,87,88,89,90,91,92,93,94,95,96,
97,98,99,100,
*
0.0,4,7.3,1,160.748,3,
*2,1
*99,100,
*0.0,6,
7,1
101,102,103,104,105,106,107,
0.0,7,
0,
**************************************************************************
cont,                                                                      *cont.1
0.0,0,500,100,3,0,   *iterative solution                                   *cont.2
0.10,0.00001,0.001,0.05,0.01,0.9,1.5,1.0,                                  *cont.3
5,0,0,0,0,0,1,1,0,0,0,1,1,0,                                               *cont.6
100.,0.0,0.0,0.0,0.0,0.0,0.0,                                              *cont.7
endd
*
*end of data input
0
**************************************************************************
```

Appendix B: Sample MCNP Input

```
Crossfuel_SP1
c
c  single-cell model, fully meshed
c
10 1 -10.42 -1 2 -13 7 imp:n=1
100 1 -10.42 -7 104 -107 2 imp:n=1     $center square, top left(C1), upper left
140 1 -10.42 -7 104 -101 107 imp:n=1   $center square, top left(C1), upper right
141 1 -10.42 2 -107 -104 100 imp:n=1   $center square, top left(C1), lower left
142 1 -10.42 -104 100 -101 107 imp:n=1 $center square, top left(C1), lower right
103 1 -10.42 101 -1 -7 100 imp:n=1     $center square, top right
101 1 -10.42 -100 105 -107 2 imp:n=1   $center square, bottom left (C2), upper
143 1 -10.42 -100 105 -101 107 imp:n=1 $center square, bottom left (C2), upper
144 1 -10.42 -105 8 -107 2 imp:n=1     $center square, bottom left (C2), lower
153 1 -10.42 -105 8 -101 107 imp:n=1   $center square, bottom left (C2), lower
102 1 -10.42 101 -108 -100 109 imp:n=1 $center square, bottom right (C4), top left
107 1 -10.42 -100 109 -106 108 imp:n=1 $center square, bottom right, top left,
108 1 -10.42 -109 105 -108 101 imp:n=1 $center square, bottom right, top left,
109 1 -10.42 108 -106 -109 105 imp:n=1 $center square, bottom right, top left,
104 1 -10.42 -100 105 106 -1 imp:n=1   $center square, bottom right, top right
105 1 -10.42 101 -106 -105 8 imp:n=1   $center square, bottom right, bottom left
106 1 -10.42 106 -1 -105 8 imp:n=1     $center square, bottom right, bottom right
110 1 -10.42 -1 2 -8 14 imp:n=1
120 1 -10.42 -7 104 -112 16 imp:n=1    $left square, top left(L1), upper left
126 1 -10.42 -7 104 -103 112 imp:n=1   $left square, top left(L1), upper right
127 1 -10.42 -112 16 -104 100 imp:n=1  $left square, top left(L1), lower left
128 1 -10.42 -104 100 -103 112 imp:n=1 $left square, top left(L1), lower right
121 1 -10.42 -7 104 -111 103 imp:n=1   $left square, top right (L3), upper left
129 1 -10.42 -7 104 -113 111 imp:n=1   $left square, top right (L3A), upper right
1299 1 -10.42 -7 104 -2 113 imp:n=1    $left square, top right (L3B), upper right
131 1 -10.42 -104 100 -111 103 imp:n=1 $left square, top right (L3), lower left
132 1 -10.42 -104 100 -113 111 imp:n=1 $left square, top right (L3), lower right
1322 1 -10.42 -104 100 -2 113 imp:n=1  $left square, top right (L3), lower right
122 1 -10.42 -100 105 -112 16 imp:n=1  $left square, bottom left (L2), upper left
133 1 -10.42 -100 105 -103 112 imp:n=1 $left square, bottom left (L2), upper right
134 1 -10.42 -105 8 -112 16 imp:n=1    $left square, bottom left (L2), lower left
136 1 -10.42 -105 8 -103 112 imp:n=1   $left square, bottom left (L2), lower right
123 1 -10.42 -100 105 -111 103 imp:n=1 $left square, bottom right (L4), upper left
137 1 -10.42 -100 105 111 -113 imp:n=1 $left square, bottom right (L4), upper right
1377 1 -10.42 -100 105 113 -2 imp:n=1  $left square, bottom right (L4), upper right
138 1 -10.42 -111 103 -105 8 imp:n=1   $left square, bottom right (L4), lower left
139 1 -10.42 8 -105 -113 111 imp:n=1   $left square, bottom right (L4), lower right
1399 1 -10.42 8 -105 -2 113 imp:n=1    $left square, bottom right (L4), lower right
130 1 -10.42 1 -15 -7 8 imp:n=1
115 1 -10.42 (-20 13)  imp:n=1
125 1 -10.42 (-23 -14) imp:n=1
135 1 -10.42 (-26 15)  imp:n=1
145 1 -10.42 (-29 -110 104) imp:n=1    $left semicircle top, upper left
150 1 -10.42 (-29 110 104 -16) imp:n=1 $left semicircle top, upper right
151 1 -10.42 (-29 -104 100 -110) imp:n=1 $left semicircle top, lower left
152 1 -10.42 (-104 100 -16 110) imp:n=1 $left semicircle top, lower right
146 1 -10.42 (-29 -16 -105 110) imp:n=1 $left semicircle bottom, lower right
147 1 -10.42 (-29 -110 -105) imp:n=1    $left semicircle bottom, lower left
```

```
148 1 -10.42 (-29 105 -100 -110) imp:n=1   $left semicircle bottom, upper left
149 1 -10.42 (-100 105 110 -16) imp:n=1    $left semicircle bottom, upper right
40 1 -10.42 (40 -400 7 1 -420) imp:n=1
50 1 -10.42 (43 -400 -111 7 430) imp:n=1
51 1 -10.42 (43 -17 111 -113 7 430 -400) imp:n=1
53 1 -10.42 (43 17 111 -113 7 430 -400) imp:n=1
52 1 -10.42 (43 -400 113 -2 7 430 -17) imp:n=1
54 1 -10.42 (43 -400 113 -2 7 430 17) imp:n=1
60 1 -10.42 (46 -8 1 -420 410) imp:n=1
70 1 -10.42 (49 -8 -2 410 430) imp:n=1
3 3 -6.55 (-22 21 13):(-25 24 -14):(-28 27 15):(-31 30 -16):(400 -13 -5 3)&
:(-15 420 -11 9):(-15 420 -10 12):(-5 3 -410 14):(14 -410 6 -4)&
:(-430 16 12 -10):(16 -430 -11 9):(400 -13 -4 6):(-50 51 -8 -2 410 430)&
:(-47 48 -8 1 -420 410):(-41 42 -400 7 1 -420):(-44 45 -400 -2 7 430) imp:n=1
2 2 -2.63282E-03 (-21 20 13):(-24 23 -14):(-27 26 15):(-30 29 -16)&
:(400 -13 -3 1):(-15 420 -9 7):(-15 420 -8 10):(-3 1 -410 14):(14 -410 4 -2)&
:(-430 16 10 -8):(16 -430 -9 7):(400 -13 -2 4):(-49 50 -8 -2 410 430)&
:(-46 47 -8 1 -420 410):(-40 41 -400 7 1 -420):(-43 44 -400 -2 7 430)  imp:n=1
4 4 -0.94 (#10 #100 #110 #120 #130 #115 #125 #135 #145 #40 #50 #60 #70 #2&
 #3 #146 #122 #101 #121 #123 #103 #102 #104 #105 #107 #108 #109 #144 #153 #142&
 #106 #147 #148 #149 #150 #151 #152 #126 #133 #134 #136 #137 #138 #139&
 #127 #128 #129 #131 #132 #140 #141 #143 #1299 #1322 #1377 #1399 #51&
 #53 #52 #54) (-502 503 -500 501) imp:n=1
999 0 #(501 -500 503 -502 -601 600) imp:n=0
c 502:-503:500:-501 imp:n=0

1 px  0.1460966
2 px -0.1460966
3 px  0.1562566
4 px -0.1562566
5 px  0.2273766
6 px -0.2273766
7 py  0.1460966
8 py -0.1460966
9 py  0.1562566
10 py -0.1562566
11 py  0.2273766
12 py -0.2273766
17 py 0.2191449
c
100 py 0
101 px 0
103 px -0.3635466788
104 py 0.0730483
105 py -0.0730483
106 px 0.0730483
107 px -0.0730483
108 px 0.03652415
109 py -0.03652415
110 px -0.581561698
111 px -0.2910633192
112 px -0.4360300384
113 px -0.2185799596
117 px -0.2921932
c
13 py  0.508513398
```

```
14 py -0.508513398
15 px  0.508513398
16 px -0.508513398
c
20 c/z  0  0.508513398 0.1460966
21 c/z  0  0.508513398 0.1562566
22 c/z  0  0.508513398 0.2273766
23 c/z  0 -0.508513398 0.1460966
24 c/z  0 -0.508513398 0.1562566
25 c/z  0 -0.508513398 0.2273766
26 c/z  0.508513398 0  0.1460966
27 c/z  0.508513398 0  0.1562566
28 c/z  0.508513398 0  0.2273766
29 c/z -0.508513398 0  0.1460966
30 c/z -0.508513398 0  0.1562566
31 c/z -0.508513398 0  0.2273766
400 py  0.4382898
410 py -0.4382898
420 px  0.4382898
430 px -0.4382898
40 c/z  0.4382898 0.4382898 0.2921932
41 c/z  0.4382898 0.4382898 0.2820332
42 c/z  0.4382898 0.4382898 0.2109132
43 c/z -0.4382898 0.4382898 0.2921932
44 c/z -0.4382898 0.4382898 0.2820332
45 c/z -0.4382898 0.4382898 0.2109132
46 c/z  0.4382898 -0.4382898 0.2921932
47 c/z  0.4382898 -0.4382898 0.2820332
48 c/z  0.4382898 -0.4382898 0.2109132
49 c/z -0.4382898 -0.4382898 0.2921932
50 c/z -0.4382898 -0.4382898 0.2820332
51 c/z -0.4382898 -0.4382898 0.2109132
*500 px  0.73589
*501 px -0.73589
*502 py  0.73589
*503 py -0.73589
*600 pz -0.73589          $ lower boundary
*601 pz  0.73589          $ upper boundary
KCODE 10000 1.0 30 150
ksrc 0.01 0.01 0.1  .2 .2 .2
c
m1 8016.53c -0.11853 92238.15c -0.83740 92235.15c -0.044074 $ 3.15
m2 2004.42c 1.0 $ helium Gap
m3 26000.42c -0.005 40000.58c -0.9791 &
50000.42c -0.0159 $zirc-4
m4 1001.53c 2.0 8016.53c 1.0
mt4 lwtr.04t
c
f7:n 50 51 52 53 145 151 150 152 120 127 126 128 121 131 129 132 &
1299 1322 100 141 140 102 107 108 109
sd7 .00183784 .00444576 .005294786 .000318339 .001681565&
.004873044 .004873044 .005336054 .005294786 .005294786&
.005294786 .005294786 .005294786 .005294786 .005294786&
.005294786 .005294786 .005294786 .005336054 .005336054&
.005336054 .001334013 .001334013 .001334013 .001334013
print
```

Appendix C: Test Procedure

This section is written in a detailed manner so that future students might easily test other rod geometries using the same test facility:

C.1 Start-up and Set-up for Data Collection

(1) Fill the reservoir tank until pipe outlet is submerged below the tank water level (~200 gallons).

(2) Turn on the variable speed driver at the wall, via the large lever-switch. Turn on the data acquisition system via the front panel, and recall the state SETUP_1, for easy monitoring of flow velocity and pressure drop during start-up.

(3) With top bleed valve closed, pressure-relief valve open, and control valve open, pump turn on the pump by clicking the "Pump On" button within the Loop.exe interface (See Figure 75).

(4) Start up the pump at a medium speed by clicking "Up On", and then "Up Off" when the flowmeter velocity reads 0.5 m/s. Close the pressure relief bleed valve when a jet of water is produced, meaning the majority of air has been bleed out of the system.

(5) Ramp up the pump to a high speed (0.8 m/s) and run until air bubbles are no longer present at the outlet.

(6) Lower pump speed (to 0.4m/s) by clicking "Down On", then "Down Off" when the flowmeter reads 0.4 m/s; quickly shut the control valve, trapping static water in the test section. Shut off the pump.

(7) Open the top bleed valve, and bleed the pressure drop measurement by way of opening the bleed screws in the differential pressure transmitter until droplets of water are produced.

(8) On the data acquisition system, verify that the channel representing pressure drop is at or within ±25 mPSI of 0 PSID (as in, zero static pressure difference).

(9) Close the top bleed valve. Simultaneously, turn on the pump at a low speed (around 0.4 m/s), and open the main control valve in such a way that minimal air is allowed back into the system.

(10) With the loop and pressure measurement system sufficiently clear of air, enter instructions to initialize the data scan at the command line interface of the data acquisition software as follows:

Open the Agilent™ Connection Expert application. When it has loaded, click on the LAN(TCP/IP) icon, and then right-click the icon for the Data Acquisition System, which should be labeled "34980A"; choose the option "Send Commands to Instrument". When the prompt loads, enter:

TRIG:SOURCE TIMER
TRIG:TIMER 5
TRIG:COUNT INFINITY
INIT

These commands will initiate a scan which will save data to the memory buffer every 5 seconds; the count is infinite in that it must be manually terminated.

(11) Adjust flow velocity according to the desired test matrix (See "Operation"). When chosen velocity has been reached, hold for 3 minutes to collect data. Once all data collection is complete for a rod bundle test, proceed to "Shutdown" instructions.

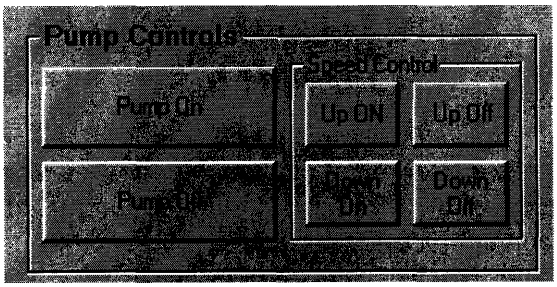

Figure C1: Variable speed driver control interface.

C.2 Operation

Pump operation is relatively simple: For large changes in flow velocity, the variable speed drive should be used by way of the user interface in the application "Loop.exe", shown above. Usually at higher speeds (above 0.6 m/s) clicking "Up On" followed by "Up Off" immediately, will raise the flow speed by 0.1 m/s, as there is some time delay in execution of the commands.

Data for velocities below 0.6 m/s should be taken by dropping pump to a 0.6 m/s flow velocity using the "Down On" and "Down Off" buttons; then throttling flow using the control valve. For fine control at these lower flow velocities (0.2 – 0.4 m/s), the control valve is essential but must be moved slowly and carefully. When adjusting the control valve in the direction of flow constriction, it is important to keep careful note of the system pressure gauge. For normal operation, there is no need to exceed 15 psi, though the burst disk is rated much higher at 60 psi.

C.3 Shutdown and Data Retrieval

(1) When measurement period is complete: within the data acquisition system command line interface, enter:

ABORt – scan is ended manually
FETCh? – retrieves data stored in the data acquisition buffer memory

(2) The pump should be allowed to slowly ramp down in speed to avoid damage. This is done by clicking "Down On", pausing for a second or two, then clicking "Down Off" (within the Loop.exe interface).

(3) When the pump has reached a sufficiently low level (around 0.2 m/s): close the control valve, and shut off the the pump (by clicking Pump Off), again trapping static water within the test section.

(4) Check the front panel of the data acquisition system to verify that static pressure still reads within ±20 mPSI of 0 PSID.

(5) Drain the system below the height of the bottom of the test assembly, and leave valves open to allow all components to dry off.

(6) Turn off the variable speed driver at the wall via the lever arm.

C.4 Disassembly

(1) Drain water from the system until tank level is below the height of the pump outlet.

(2) Loosen the top union using a 3" strap wrench.

(3) With a water pan ready, use the strap wrench to loosen and unscrew the bottom union. Make sure that the water pan is positioned to capture any remaining water during the process of unmounting the test assembly.

(4) Disconnect the stainless steel pressure measurement piping from the top and bottom plena at the respective 1/8" compression fittings.

(5) Remove the top crossbar by way of 4 screws along the bar, and slide it out of the unistrut frame using a rubber mallet if necessary. At this point, a second person should be on hand to help support the test assembly unit.

(6) Similarly, remove the bottom crossbar.

(7) The test section should now be completely free to be unmounted, and should be carefully lifted by two people from its support frame onto its wooden stands for further disassembly.

(8) On the test section, remove the bolts from the top flange and detach the nylon pressure line by unscrewing it at the nylon compression fitting by the interior of the top plenum. Set the top plenum aside.

(9) Remove the bolts from the bottom flange; Slide the assembly box, with rods inside, out from the bottom of the tube and detach nylon tubing at the quick-connect elbow. Set the bottom plenum aside.

(10) One-by-one, remove the long threaded rods, which hold together the top and bottom gridplates.

(11) Pry off the bottom gridplate and set it aside; unscrew the individual test rods at the top using an Allen wrench.

(12) Slide the box out from the top, and detach the nylon tubing at the quick-connect junction; set aside the top gridplate.

(13) Disassemble the box at the three threaded rods on each side. Remove the rods and bundle them together for storage.

C.5 Reloading

(1) Using a marker tag the 16 rods by row and column, at the top and bottom faces of the rods, to ensure that they are properly lined up.

(2) Set the bottom grid plate onto two 2x4's, so that the area underneath can later be easily accessed for tightening of the long threaded rods.

(3) Fit the rods into the slots one-by-one, carefully attending to the row and column markings.

(4) Re-assemble the assembly box around the rods by matching up the faces engraved as C & D on the box to the C & D engraving on the grid plate.

(5) Attach the top grid plate by matching the A & B engravings on the box to the markings on the grid plate. Be sure that the corners of the box do not extend beyond the area of the top plate.

(6) Insert the four long threaded rods, and tighten them by reaching beneath the bottom grid plate. The box with grid plates and rods should now be a solid bundle.

(7) Slide a rubber stopper onto the box, down to the bottom grid plate; then attach the top nylon pressure measurement tubing through the top grid plate and into its quick-connect fitting. Load this bundle into the assembly tube from the bottom, carefully looping the nylon tubing at the top.

(8) Hold a second rubber stopper to the bottom face of the grid plate. Attach the bottom nylon tubing first at the quick-connect fitting, pull it through the grid plate and stopper, then attach at the compression fitting within the bottom plenum.

(9) Attach and tighten the bottom plenum.

(10) Back at the top, pull the nylon tubing through the last rubber stopper, and attach the tubing at the compression fitting inside the top plenum.

(11) Tighten on the top plenum; the test unit should now be complete.

(12) With two people, lift this unit back onto its unistrut structure mounting.

(13) Slide the top and bottom crossbars into place, and tighten in the screws.

(14) Finish reassembly by tightening the union fittings at the top and bottom of the plenum, then tightening the 1/8" stainless steel compression fittings to re-attach the test unit to the differential pressure transmitter.

References

[1] Kazimi, M.S., et. al., "Core Design Options for High Power Density BWRs", MIT-NFC-PR-089 (December 2006).

[2] Ponomarev-Stepnoi, N.N., Kevrolev, V., Kuzentsov, V.V., Kuzentsov, V.F., Morosov, A., "Non-Proliferative Light Water Thorium Reactor: Final Report", Kurchatov Institute Research Center (1998).

[3] Feng, D., Kazimi, M. S., and Hejzlar, P., "Innovative Fuel Designs for High Power Density Pressurized Water Reactors", MIT-NFC-TR-075 (September 2005).

[4] Kazimi, M. S., et. al., "Core Design Options for High Power Density BWRs", Appendix F (Hejzlar), MIT-NFC-PR-089 (December 2006).

[5] Cuta J.M., et. al., VIPRE-01 A Thermal-Hydraulic Code for reactor Cores, Volumes 1-3, EPRI, NP-2511-CCM (July 1985).

[6] Morra, P., Xu, Z., Hejzlar, P., Saha, P., and Kazimi, M.S., "Neutronic and Thermal-Hydraulic Designs of Annular Fuel For High Power Density BWRs", MIT-NFC-PR-071 (December 2004).

[7] Ferroni, P., Todreas, N. E., "Steady State Thermal Hydraulic Analysis of Hydride Fueled BWRs", MIT-NFC-TR-079 (May 2006).

[8] Handwerk, C., "Preliminary Thermal Hydraulic Analysis of a Hydride Fueled Boiling Water Reactor", NERI02-189-MIT-9 (January 2005).

[9] Nine Mile Point Unit 2, Updated Safety Analysis Report (USAR), Rev.16, (October 2004).

[10] Structural Research and Analysis Corp, "COSMOS/M: a Finite Element Analysis Tool", Santa Monica, CA (2005).

[11] SolidWorks,"SolidWorks 3D Mechanical Design Software", Santa Monica, CA (2004).

[12] Todreas, N.E. and Kazimi, M.S., Nuclear Systems I: Thermal-Hydraulic Fundamentals, Hemisphere Publishing Corp., New York, (1990).

[13] Fink, J.K., "Thermal Conductivity and Thermal Diffusivity of Solid UO_2", http://www.insc.anl.gov/matprop/uo2/cond/solid/thcsuo2.pdf, (July 1999).

[14] Los Alamos National Laboratory, "MCNP 4c3 Software", Los Alamos National Laboratory LLC, Los Alamos, NM (1995).

[15] Shiralkar, B.S., "BWR Systems and Steady State Operation", Presentation to the MIT-INPO Reactor Technology Course for Utility Executives, MIT NSE Department, (June 2006).

[16] Collier, J.G. and Thome, J.R., "Convective Boiling and Condensation", 3rd Edition, Oxford Science Publications, London, (1994).

[17] Kitto, J.B., Jr. and Weiner, M., "Effects of nonuniform circumferential heating and inclination on critical heat flux in smooth and ribbed bore tubes", Paper Presented at 7th International Heat Transfer Conference, Munich, 4, 297-302, (1982).

[18] Alekseev, G.V., Zenkevich, B.A., Peskov, O.L., Sergeev, N.D., and Subbotin, V.I., "Burnout heat fluxes under forced flow", Paper A/CONF.28/P/327a presented by USSR at the Third International Conference on Peaceful Uses of Atomic Energy, Geneva (August, 1964).

[19] Butterworth, D., "A model for predicting dryout in a tube with circumferential variation on heat flux", UKAEA Report No. AERE M2436, (1972).

[20] Kinoshita, H. and Yoshida, T., "Study on the Mechanism of Critical Heat Flux Enhancement for Subcooled Flow Boiling in a Tube with Internal Twisted Tape under Nonuniform Heating Conditions", Journal of Heat Transfer -- Japanese Research, 25 (5) (1996).

[21] Leontiev, A.I., Mostinsky, I.L., Polonsky, V.S., Styrikovich, M.A., and Chernika, I.M., "Experimental Investigation of the Critical Heat Flux in Horizontal Channels with Circumferentially Variable Heating", Journal of Heat and Mass Transfer, Vol.24, No.5, pp. 821-828, (1981).

[22] Groeneveld, D.C., et. al., "The 1995 look-up table for critical heat flux in tubes", Nuclear Engineering and Design, Volume 163, Number 1, pp. 1-23(23), (June 1996).

[23] Idelchik, I. E., "Handbook of Hydraulic Resistance", 2nd Edition, Hemisphere Publishing Corp., New York, (1986).

[24] OMEGA Engineering Technical Reference, "Product Info: Magnetic Insertion Flowmeters", Figure 2. http://www.omega.com/prodinfo/magmeter.html, (2006).

[25] Rehme, K., "Simple method of predicting friction factors of turbulent flow in non-circular channels", International Journal of Mass Transfer, 16:933, (1973).

[26] ChemicaLogic, "SteamPro Version 2 - ChemicaLogic SteamTab Companion", ChemicaLogic Corporation, Burlington, MA (2003).

[27] Bevington, P. and Robinson, D., "Data Reduction and Error Analysis for the Physical Sciences" 3rd Edition, McGraw-Hill Publishing, Boston, MA, (2003).

[28] Preger, E. A. and Samoilenko, L. A., "Investigation of hydraulic resistance of pipelines in the transient mode of flow of liquids and gases", Issled. Vodosnabzhen, Kanalizatsii (Trudy LISI), no. 500, 27-39, Leningrad, (1966).

[29] Mikic, B.B., Kapat, J., Ratnathicam, J., "Transition to turbulence in systems with eddy promoters: Implication for the question of transition", Physics of Fluids A: Fluid Dynamics, Vol. 4, Issue 8, p. 1854-1855, (August 1992).

[30] Buongiorno, J., "A Brief Report on Heat Transfer Mechanisms, Pressure Drop and Available Correlations in Twisted Tape Swirl Flow", MIT NSE Department, Internal Memo (March 1998).

[31] Gambill, W.R., et. al., "Heat transfer, burnout and pressure drop for water in swirl flow through tubes with internal twisted tapes", Chemical Engineering Prog. Symposium Series, 57, (32), 127; (1961).

[32] Novendstern, E.H., "Turbulent Flow Pressure Drop Model for Fuel Rod Assemblies Utilizing a Helical Wire-Wrap Spacer System", Nuclear Engineering and Design, 22, 19:27, (1972).